Dissertation

submitted to the

Combined Faculty of Mathematics, Engineering and Natural Sciences

of Heidelberg University, Germany

for the degree of

Doctor of Natural Sciences

Put forward by

Leon Lettermann

born in: Paderborn

Oral examination: 21.01.2026

Modeling Malaria Parasite Motility: From Chiral Active Particles to Complex Shapes with Surface Flow

Referees: Prof. Dr. Ulrich Schwarz
Prof. Dr. Peer Fischer

Zusammenfassung

Aktive Materie nutzt lokale Energiequellen, um Kräfte und Bewegung zu erzeugen. Ein wichtiges Beispiel ist die Fortbewegung von Mikroorganismen, die sich als aktive Brownsche Teilchen modellieren lassen. Ein physikalisch besonders interessanter Spezialfall sind chirale aktive Teilchen, die einer bevorzugten Rotationsrichtung folgen. In dieser Arbeit zeige ich mittels theoretischer Analysen über alle relevante Skalen, dass Malaria-Parasiten aufgrund ihrer hohen Geschwindigkeit und gekrümmten Form ein ausgezeichnetes Modellsystem dafür darstellen.

Zunächst habe ich eine automatisierte Bildverarbeitungspipeline aufgebaut, um experimentell gemessene Trajektorien in einem dreidimensionalen Hydrogel zu analysieren. Dabei wurde eine rechtshändige Chiralität nachgewiesen, die auch Übergänge zwischen zwei- und dreidimensionalen Umgebungen kontrolliert.

Weiterhin formulierte ich eine stochastische Theorie für chirale aktive Teilchen auf Basis eines Ornstein–Uhlenbeck-Prozesses für die Rotation und zeigte, dass helikale Bewegung robuster gegenüber Fluktuationen ist und statistisch zu größerer Nettoversetzung führen kann—sodass eine Helix gewissermaßen „gerader als eine Gerade“ sein kann.

Schließlich entwickelte ich eine Theorie für den selbstorganisierten Oberflächenfluss von Adhäsionsmolekülen, der die Bewegung antreibt. Diese legt nahe, dass die gekrümmte Form der Parasiten eine evolutionäre Anpassung ist, um Rotationen auf der Stelle zu vermeiden. Eine Erweiterung der Theorie um mechanischen Deformationen führt die beobachtete Rechtshändigkeit auf eine asymmetrische Freisetzung der Adhäsionsmoleküle zurück; diese Vorhersage wurde experimentell bestätigt.

Abstract

Active matter taps local energy sources to generate forces and motion. A key example is the locomotion of microorganisms, which can be modeled as active Brownian particles. A particularly intriguing case involves chiral active particles that follow a preferred sense of rotation. Working across relevant scales, I show theoretically that malaria parasites, owing to their high speeds and curved shape, provide an excellent model system for this class.

First, I built an automated image-processing pipeline to analyze experimentally measured trajectories in a three-dimensional hydrogel. This established proof of uniformly right-handed chirality, which also controls transitions between two- and three-dimensional environments.

I then formulated a stochastic theory for chiral active particles based on an Ornstein–Uhlenbeck process for rotational dynamics, demonstrating that helical motion is more robust to fluctuations and can, statistically, yield larger net displacements—so that a helix can be "straighter than a straight line".

Finally, I developed a theory for the self-organized surface flow of adhesins, driving the motion. This suggested that the parasites' curved shape is an evolutionary adaptation to avoid on-the-spot rotations. An extension of the theory that incorporates mechanical deformations attributes the observed right-handedness to an asymmetric release of adhesion molecules; this prediction was corroborated experimentally.

Contents

Introduction

Motion is fascinating—from children's toys like spinning tops or marble runs to watching sporting events, or throwing an American football or a Frisbee yourself to test how rotation stabilizes the path. This fascination has long been applied to studying the microscopic realm: Motion at microscopic scales follows its own rules, with inertial effects irrelevant compared to viscous drag, captured by the concept of a low Reynolds number [1]. While we can throw a ball and watch it fly, a swimming *E. coli* bacterium has to constantly propel itself forward, barely able to compete with the thermal diffusion randomly moving everything around [2]. Evolution has engineered many different solutions to generate the constant propulsion force necessary for continuous movement: microswimmers may have a few flagella or many cilia, whereas crawling mammalian cells utilize actin turnover to move through tissue, and certain bacteria fire grappling hooks called type IV pili to pull themselves forward. Certain parasites, including those causing the disease malaria, have developed their own specific solution, enabling them to outrun the immune system. In this thesis, we explore the motion machinery and motility of these parasites in a series of theoretical models, motivated and supported by analyzing experimental data from collaborators.

Over 250 million people contract malaria each year, which causes 600 000 deaths, mainly children in sub-Saharan Africa [3]. The disease is caused by infection with a unicellular parasite from the genus *Plasmodium*, which contains hundreds of known species, five of which infect humans. All species share a complicated life cycle, alternating between a mosquito and a vertebrate host. During different stages of this life cycle, the parasite takes a number of different forms. Humans, as the vertebrate host, are infected by sporozoites, a long and slender stage of the parasite that is transmitted during a mosquito blood meal. The sporozoite moves through skin tissue, finds a blood vessel and rides the bloodstream to the liver. There, it eventually morphs into the blood stage of malaria, and starts infecting red blood cells (RBCs). This is where the disease becomes symptomatic, and with a few percent to nearly half of RBCs infected, it can cause a number of life-threatening conditions [4].

The starting point of each infection is the migration of a relatively small number (few tens) of sporozoites through the skin. Because stopping these would prevent infection, understanding their migration is of high medical relevance and is the target of recent vaccine approaches [5–11]. But also for

themselves, *Plasmodium* sporozoites present very rewarding research targets. Their gliding motility is empowered by an ingenious machinery, called the glideosome. Adhesins in the parasite's membrane are pulled backward by a distributed actomyosin motor assembly. While they are linked to the extracellular matrix, this rapidly propels the parasite forward, such that it beats the speed of the immune cells it wants to outrun by a factor of 10.

The rapid motility is not the only intriguing physical property of *Plasmodium* sporozoites. They have a well-maintained, high-aspect-ratio, curved shape. At about 10 µm long, and with a diameter below 1 µm, they form a crescent shape with a radius of curvature of about 5 µm (see the cover of Chapter 1). The cell is not only highly polarized, with an apical complex marking the front and constituting the nucleation point for the glideosome, but also chiral: When placed on a glass slide, the cells circle due to their curved shapes, but the majority will circle counterclockwise (seen from above).

Chirality is defined as the property of being different from its own mirror image. Prime examples of this are helices, which are either left- or right-handed. In biology, chirality is omnipresent at the nanoscale, for example with nearly all biologically relevant amino acids being L-chiral, while DNA is (usually) a right-handed double helix. Easier to grasp is the left-right symmetry breaking of our bodies, propagated from more microscopic chirality during embryonic development. For the roundworm *C. elegans*, the left-right symmetry breaking is known to arise from the fixed chirality of actin filaments [12]. Another everyday example is the pair of aromas—spearmint and caraway—both produced by a molecule identical except for chirality, called carvone. In the case of malaria parasites, we not only find counterclockwise vs. clockwise circling in 2D, but also strong right-handed chirality of helical trajectories traveled by the parasites in 3D.

In this thesis, we analyze the properties of these helical trajectories, rationalize how they result from the glideosome motor machinery, find the advantages that helices offer for migration, and finally uncover how their chirality is encoded in the layout of the cell. Taking the malaria parasite as a model organism and motivation, the theoretical models developed offer insight into the principles governing gliding motility of many microbes, from medically relevant parasites to bacteria and even algae.

Outline

Chapter 1 sets the stage by introducing the biological and theoretical foundations. We explain the biology of malaria parasites, in particular their motor machinery, in more detail, and introduce other gliding stages of the malaria life cycle, and the parasite *Toxoplasma gondii*, a close relative to *Plasmodium* that serves as an important reference and model system. After the biological introduction, we review some relevant biophysical theories on cell motility in general and specifically important previous models for the gliding motility of *Plasmodium* and *Toxoplasma*.

Chapter 2 is dedicated to the experiments of our close collaborators at the parasitology department, the analysis methods we developed, and the obtained results. We track the sporozoites in a 3D gel assay to find the aforementioned right-handed chirality, and further quantify the trajectories and also the shapes of individual sporozoites. With that, the foundation for the modeling in the following chapters is set.

The following three chapters introduce different theoretical models, starting from the most coarse-grained, and subsequently incorporating more biological detail.

Chapter 3 focuses on the stochastic properties of helical trajectories in general, reducing the parasite to an active particle. Importantly, we abstract main characteristics that apply to the parasite's force-generation mechanism and migration: moving through a gel, classical Brownian noise is less relevant, as stochasticity is mainly introduced by the motor machinery itself, a paradigm also valid for larger microswimmers. This drive-based noise is generated in the frame of the particle and is time-correlated, motivating us to introduce a general model for helical motion of microorganisms in 3D based on an Ornstein-Uhlenbeck process to describe the noisy state of the internal force generation apparatus. In this model, we find advantages for helical trajectories, which can integrate out part of the noise to become more persistent than straight trajectories, leading to helices being "straighter than a straight line". These findings were published as Lettermann et al., *Physical Review Letters*, 2025, see 2 in the List of Publications.

Chapter 4 moves on to include more details about the force generation and transmission of a general glider. We introduce a model that describes how the surface flow on a fixed geometric shape results in motion of that shape. Importantly, we assume that the surface flow is actively generated, and responds

to the motion it itself creates. This sets up a subtle self-organization problem, where the geometry of the glider dictates stationary and stable configurations of the surface flow. Our analytical solutions predict an axisymmetric body will have a strong tendency to rotate around its symmetry axis, providing an explanation for why *Plasmodium*, *Toxoplasma*, and many of its relatives are curved, thereby breaking axial symmetry. These results were published as Lettermann et al., *Proceedings of the National Academy of Sciences of the U.S.A.*, 2024, see 1 in the List of Publications.

Chapter 5 finally comes back to a more detailed, quantitative comparison with the experimental data from Chapter 2. We extend the general glider model from the previous Chapter 4 to a more complex model of the surface flow and include some degree of shape deformability. This allows us to accurately reproduce the measured trajectories, using either of two competing models for the origin of chirality. By comparison with the experiments described in Chapter 2, but also specifically designed two-sided traction force microscopy assays and STED super-resolution microscopy experiments, we are able to show that the most likely mechanism generating chirality in sporozoites is an asymmetric distribution of adhesins, generated by a tilt in the apical organelle responsible for releasing the adhesins in the outer parasite membrane. The experimental results presented in Chapter 2 and the results from this chapter were jointly submitted and accepted for publication as Lettermann, Singer, et al., *Nature Physics*, in press, see 3 in the List of Publications.

The **Summary & Outlook** distills the findings into a coherent picture of gliding motility in malaria parasites and its consequences for parasite architecture. Furthermore, some currently pursued or possible future research avenues and yet open questions are presented.

1

Chapter 1

Active motility of malaria parasites

This chapter outlines the physical and biological foundations relevant to this thesis. We begin with a brief overview of relevant physical models of microscale motility, then introduce the biology of gliding malaria parasites, and conclude by revisiting prior modeling specific to these parasites.

1.1 Modeling of microbial motility

Evolution has created a vast zoo of different motility mechanisms, which inspired a similar manifold collection of models focusing on different systems and aspects of motility, ranging from detailed models of individual molecular motors [13] to understanding large-scale collective motion of bacteria, cells, or even flocks of birds [14, 15].

1.1.1 Cell crawling and active gel theory

A significant part of the literature is concerned with the internal dynamics behind the crawling of mammalian cells [16]. While this is not directly relevant to modeling gliding, we will see that the underlying theory describing the actomyosin machinery is. The theory of active gels [17] combines the polarity of the actin network with the out-of-equilibrium energy turnover of myosin motors into a consistent, hydrodynamic theory of intracellular force generation [18]. While the gliding of apicomplexans utilizes short actin filaments and fixed myosin motors in the quasi two-dimensional space defined by the glider's surface, and is hence very distinct from classical branched actin networks, we will rely on the general ideas to introduce a continuum description for such a system popularized by active gel theory.

1.1.2 Swimming and active particle models

A second aspect of microbial motility that has been explored from a more physical viewpoint is swimming. While models concerned with the specifics of propulsion of different microbes, including bacterial and eukaryotic flagella [19], are far from our work, the distributed force generation of ciliated swimmers bears some resemblance to gliding [20]. Furthermore, we will see that swimming and gliding can be modeled similarly if abstracted sufficiently, in which case the mode of force generation is no longer of primary importance. This leads to the large class of models called active particles. The most prominent representative, the active Brownian particle (ABP, [21]), asks the question of how the active propulsion of a microscopic agent interacts with thermal fluctuations, leading to diffusion in both position and orientation, a well-known challenge famously raised by H.C. Berg and E.M. Purcell [1, 2, 22] for bacteria. The simple 2D ABP model assumes a particle with an orientation given by an angle θ that actively travels with a velocity v_0, and is subject to translational and rotational diffusion given by D_x and D_r:

$$\mathrm{d}\mathbf{x} = v_0\,\hat{\mathbf{e}}(\theta)\,\mathrm{d}t + \sqrt{2D_x}\,\mathrm{d}\mathbf{\Lambda}_x(t) \tag{1.1}$$

$$\mathrm{d}\theta = \sqrt{2D_r}\,\mathrm{d}\Lambda_r(t), \tag{1.2}$$

where $\mathrm{d}\mathbf{\Lambda}_x(t)$ and $\mathrm{d}\Lambda_r(t)$ are the Wiener noise processes generating translational and rotational Brownian motion, respectively, and $\hat{\mathbf{e}}(\theta)$ is the unit vector in direction given by θ. For suitable parameter values, this system shows different motility behaviors for three different time scales. On very short time scales, if the translational diffusion is stronger than the actively traveled distance, the particle moves diffusively. On intermediate time scales, if active travel overtakes diffusion, but rotational diffusion does not yet deflect the particle's orientation, the particle travels ballistically on a nearly straight line. For long times, the rotational diffusion leads to random changes in orientation, such that the trajectory wanders like a random walk, yielding diffusive behavior once more, but now with a large diffusion constant determined by v_0 and D_r.

The simplicity of active particle models, by prescribing some rules of propulsion and interaction with the environment, has made them a widely used tool for modeling individual microbes, but also collective motion [23–26]. From the many applications and extensions concerning single active particles [21, 27–31], the ones most interesting to us are those considering not only a force or propulsion velocity, but adding a torque or angular velocity to obtain a so-called circle

swimmer [32–38]. This angular velocity (which is simply adding a constant in Eq. 1.2) adds a sense of chirality to the particle, which (as most such models are two-dimensional) leads to circling. The stochastic fluctuations, however, make these circles imperfect, such that a circle swimmer will perform a random walk over time. That means adding angular velocity typically reduces the diffusion of the particle; it can only be partially offset by introducing noise, as without noise the particle is stuck on its deterministic circle. A second important extension to the original ABP is to replace the uncorrelated white noise with time-correlated noise [39–44].

In Chapter 3, we will see how the combination of an angular velocity and time-correlated noise in case of 3D motility can have the opposite effect compared to circle swimmers: adding the rotation can stabilize trajectories, enhancing persistence and therefore enlarging the effective diffusion constant, because the rotation integrates out part of the noise.

1.2 Plasmodium biology and life cycle

Malaria is caused by unicellular protozoan parasites of the genus *Plasmodium*, which belong to the phylum Apicomplexa. Apicomplexa are the only large taxonomic group that overwhelmingly consists of parasitic organisms, but still encompasses a very diverse spectrum of species [45]. They share the name-giving apical complex, an organelle used for secretions related to invasion and motility [46–48]. Many apicomplexan parasites feature complicated life cycles, where different stages occupy different host animals or tissues, and reproduction can happen in a sexual or asexual manner at different stages [49]. Examples include *Toxoplasma*, which can infect all warm-blooded animals but requires felids (i.e., cats) for sexual reproduction [50], whereas gregarines infect invertebrates [51].

The life cycle of *Plasmodium* alternates between a mosquito vector and a vertebrate host. In the mosquito, sexual reproduction and development of sporozoites occurs, culminating in the formation of thousands of sporozoites inside oocysts attached to the insect's midgut wall. Once mature, sporozoites egress from oocysts and invade the salivary glands of the mosquito [4]. During a blood meal, an infected *Anopheles* mosquito injects a small inoculum of sporozoites into the skin of the host (Fig. 1.1a, [52]). The sporozoites are motile, slender crescent-shaped cells about 10–15 µm in length, with their diameter constrained to be smaller than 1 µm as they need to fit through the

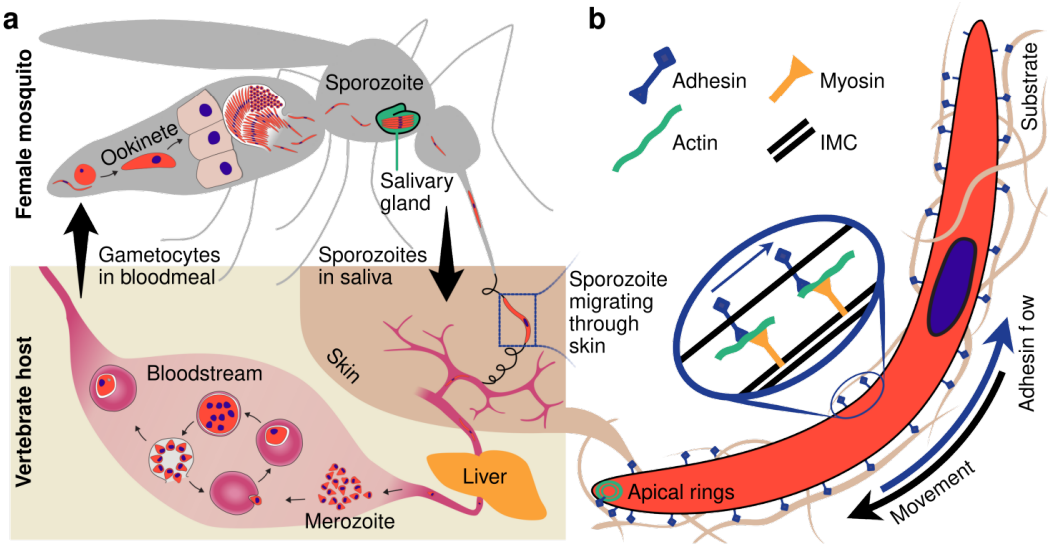

Figure 1.1: **a:** Life cycle of malaria parasites. The sporozoite is the slender and crescent form of the parasite that is injected by female *Anopheles* mosquitoes into the skin of the vertebrate host. In the skin, sporozoites migrate at high speed, up to $3\,\mu m\,s^{-1}$, until they enter a blood vessel. **b:** Sporozoites move by gliding motility. Myosin motors are located on the inner membrane complex (IMC), a flattened organelle subtending the plasma membrane. Short actin filaments are polymerized at the apical rings and are pushed to the basal end of the parasite by the myosin motors. The actin filaments in turn connect to adhesins spanning the plasma membrane, which are released at the front. The surface flow of adhesins leads to productive parasite movement once the adhesins couple to the extracellular environment. From publication 3.

tiny salivary ducts of the mosquito. After transmission, they rapidly glide through the dermis of the host at speeds around 1–3 $\mu m\,s^{-1}$ [53]. This active migration in the skin is crucial: sporozoites must find and enter blood capillaries to be carried to the liver, where they infect hepatocytes and develop into liver-stage forms. Successful infection of the liver by even a few sporozoites is a prerequisite for the subsequent pathogenic blood stage of malaria. If sporozoites fail to reach a blood vessel, they remain in the skin and the infection is aborted. This makes the sporozoite stage a critical bottleneck in the parasite's life cycle and an important target for prophylactic interventions such as vaccines [5–11]. Indeed, the only licensed malaria vaccine (RTS,S) targets the sporozoite's major surface protein (circumsporozoite protein, CSP), aiming to neutralize sporozoites before they establish infection in the liver [54].

In the liver, each sporozoite invades a hepatocyte and transforms into an intermediary liver stage, producing tens of thousands of merozoites (see Fig. 1.1a, [55]). Merozoites are then released into the bloodstream, where they

initiate the asexual blood cycle by invading red blood cells (RBCs), causing the symptomatic phase of malaria. Each infected RBC releases between six and more than 30 new merozoites after species-specific times. The number of merozoites can vary and depends on an asynchronous replication scheme [56]. The release time is well coordinated and varies even among the human-infecting species: *P. knowlesi* taking 24 hours, *P. malariae* 72 hours, and the medically most relevant *P. falciparum* and *P. vivax* 48 hours [57, 58], similar to the rodent-infecting *P. berghei* [59]. Notably, all the clinical symptoms of malaria are caused by the exponential replication of parasites in blood, whereas the preceding sporozoite and liver stages are clinically silent. Nonetheless, these stages are essential to expand the handful of sporozoites to thousands of merozoites starting the blood stage infection. Finally, some blood-stage parasites differentiate into sexual forms (gametocytes), which are taken up by the next mosquito during its blood meal, thereby perpetuating the transmission cycle (Fig. 1.1a, [60]).

This chapter focuses on the biology of the sporozoite stage, with particular emphasis on its abilities for rapid locomotion ("gliding motility") and active host-cell invasion. As parasites, apicomplexans are subject to high evolutionary pressure to co-evolve with their hosts' defense mechanisms, leading to a highly specialized biochemical apparatus. We will first describe the unique gliding motility machinery of apicomplexan parasites and then discuss how sporozoites utilize this machinery to achieve their remarkable journey from the mosquito to the liver. Throughout, we will highlight current knowledge of the molecular components (especially the actin–myosin motor system) and recent insights into the regulation and biophysics of sporozoite motility.

1.3 Gliding motility of apicomplexan parasites

Gliding motility in general describes a substrate-based (i.e. different from swimming) locomotion of microorganisms that does not require major shape changes or internal remodeling (i.e. different from crawling). Furthermore, the force generation is distributed over the surface, not concentrated at a few large organelles as in the type IV pili-based motility of some bacteria, which is called twitching. Tab. 1.1 gives an overview of example organisms for the different types.

Sporozoites, like other invasive stages of Apicomplexa (e.g. *Toxoplasma gondii* tachyzoites), have evolved a sophisticated and well-conserved gliding

Mode of motility	Description and examples
Gliding	Smooth, continuous, substrate-dependent locomotion without substantial cell-shape changes. Force generation is distributed across the cell surface, typically involving surface adhesins linked to an internal motor (actin–myosin or bacterial gliding machinery).
Apicomplexa	*Plasmodium* sporozoites: 1–3 µm s^{-1} [61], *Toxoplasma gondii* tachyzoites: 1.5 µm s^{-1} [62],
Bacteria	*Mycoplasma mobile*: up to 4.5 µm s^{-1} [63], *Flavobacterium johnsoniae*: gliding with 1–3 µm s^{-1} [64] *Myxococcus xanthus*: gliding with ≈2 µm min^{-1} [65]
Diatoms	*Nitzschia ovalis*: circular gliding, ≈1–2 µm min^{-1} [66] *Craspedostauros australis*: straight and circular gliding, ≈1–3 µm min^{-1} [67]
Crawling	Locomotion involving substantial shape changes and internal cytoskeletal remodeling (e.g., amoeboid movement). Typically driven by actin polymerization and depolymerization cycles. *Fish epidermal keratocytes*: 0.2–0.5 µm s^{-1} [68, 69] *Dictyostelium discoideum (amoeba)*: 7 µm min^{-1} [70] *Human neutrophils*: approximately 20 µm min^{-1} [71].
Swimming	Propulsion through a fluid environment without substrate interaction, typically driven by flagella or cilia. *Escherichia coli (flagellated bacteria)*: about 10–20 µm s^{-1} [72], *Chlamydomonas reinhardtii (algae)*: 20–40 µm s^{-1} [73], *Trypanosoma brucei (protozoan parasite)*: around 5–10 µm s^{-1} [74].
Twitching	Surface-associated bacterial locomotion driven by extension, attachment, and retraction of type IV pili, causing intermittent, jerky movements. *Pseudomonas aeruginosa*: approximately 1 µm min^{-1} [75], *Neisseria gonorrhoeae*: around 1–2 µm s^{-1} [76].

Table 1.1: Overview of microorganism locomotion modes with representative organisms, measured speeds, and references.

machinery, called the glideosome. Gliding allows the parasite to traverse biological barriers (such as the dermis or blood vessel walls), migrate through tissues, and actively invade host cells without destroying them in the process. Maintaining a constant shape allows sporozoites to migrate much faster (1–3 µm s^{-1}) compared to the immune cells they need to outrun, which crawl at about 0.1–0.3 µm s^{-1}.

1.3.1 The actomyosin motor and glideosome architecture

The engine powering apicomplexan motility is an actin–myosin motor complex localized at the interface of the parasite plasma membrane (PM) and the inner membrane complex (IMC). This machinery, often called the *glideosome*, is highly conserved in apicomplexans and is responsible for gliding locomotion as well as supporting active host cell invasion [48,77–79]. Figure 1.1b schematically illustrates the core components of the glideosome in a sporozoite [80,81]. The central force-producing element is class XIV myosin, specifically Myosin A (MyoA), a small single-headed motor (92 kDa) that is tethered into the IMC by a group of anchoring proteins [82,83]. These anchoring proteins form a complex that immobilizes MyoA with respect to the IMC, and also maintains a controlled spacing to the outer plasma membrane [48,81].

While one end of the motor complex is anchored to the IMC, the other end must interact with the filamentous actin (F-actin) that connects to the parasite's external adhesins. Apicomplexan parasites express a divergent form of actin (Actin I, or Act1) that polymerizes into unusually short, dynamic filaments [84]. In the classic model, first proposed two decades ago [85], the parasite's transmembrane adhesins (such as TRAP in sporozoites [86,87], MIC2 in tachyzoites [88], etc.) form a bridge between the substrate and actin filaments inside the parasite: their cytoplasmic tails bind to actin either directly or indirectly via connector proteins (e.g. aldolase or others), and their ectodomains engage ligands in the environment.

MyoA, anchored to the IMC, then walks along the short actin filaments, carrying the attached adhesins rearwards in the frame of the parasites [85,89]. As MyoA motors repeatedly powerstroke, they drive a continuous *retrograde flow* of actin filaments and adhesins from the anterior (front) end of the cell, where adhesins are released from micronemes through the apical polar rings (APR), toward the posterior end [90]. Because the adhesins are temporarily adhesive to the substrate, their rearward movement imparts forward thrust to the parasite, much like someone pulling themselves along a rope. Upon reaching the parasite's posterior, the adhesin molecules are cleaved or released, completing the cycle. This model of gliding motility is often likened to a tank tread: the parasite's surface proteins engage the substrate at the front and disengage at the back, with actin filaments acting as the conveyor belt and myosin as the (stationary) motor.

This general picture holds for many apicomplexan motile life cycle stages, while deviations in the adapter proteins [48] or different myosin motors [91]

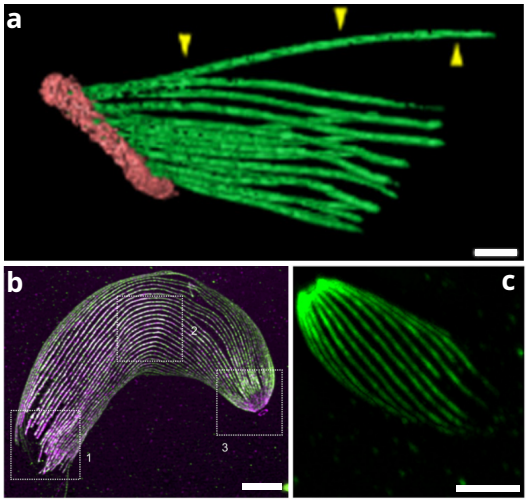

Figure 1.2: **a:** Volume rendering of an electron tomogram of a sporozoite, displaying reconstructed apical ring (pink) and microtubules (green), with the single microtubule clearly distinct (yellow arrows) (from Fig. 4F in [104]). Scale bar is 100 nm **b:** Confocal expansion microscopy image of a *Plasmodium* ookinete, showing the dense corset of MTs (from Fig. 4A in [106]). Scale bar is 5 µm, note this is enlarged due to expansion. **c:** *Toxoplasma* tachyzoite in confocal expansion microscopy (from Fig. 7A). Scale bar is 5 µm, again sample enlarged due to expansion.

are mostly specific adaptations that leave the general working mechanism unchanged. As throughout this thesis we mostly rely on abstract representations of this general glideosome, we will not dive into the extensive knowledge of apicomplexans'—and even species'—detailed molecular glideosome architecture.

One exception we make is to briefly explore the mechanical skeletons of *Plasmodium* and *Toxoplasma*. As they produce forces distributed over their whole surface, gliders need rigid elements to maintain a prescribed shape. In the absence of branched actin networks that usually support the membranes of eukaryotic cells [92], they utilize a combination of two elements to achieve mechanical rigidity. The first are subpellicular microtubules (SPMTs), which lie directly underneath the IMC and run parallel to the parasite's body axis [93]. These microtubules grow from and are organized by the apical ring complex (APR, pink in Fig. 1.2a) [94, 95], ranging back over the whole shape in *Plasmodium* ookinetes and *Toxoplasma* tachyzoites [96–98], while sporozoite MTs only cover the first half to two-thirds of the cell, ending at the nucleus, but are essential to the formation and function of the cell [99–103]. Importantly, the MTs of *Toxoplasma* tachyzoites and *Plasmodium* ookinetes are distributed around the full circumference of the cell evenly, but form helices rotating around the cell as followed from apical to polar end. In the case of sporozoites, the microtubules are unevenly distributed, forming a 15 + 1 distribution around the circumference in *P. berghei* sporozoites, but following the axis of the cell without twisting around (see Fig. 1.2 for some examples from the literature) [102, 104–107].

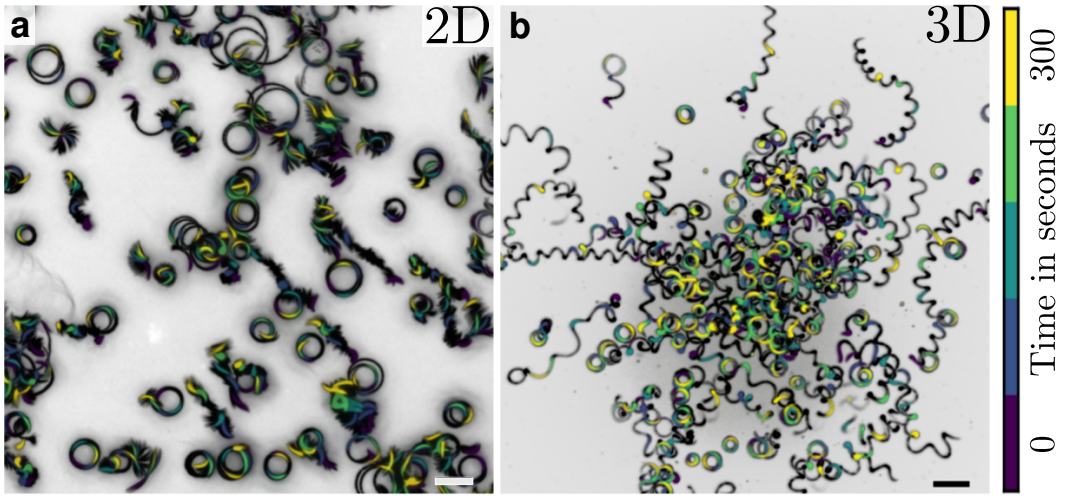

Figure 1.3: Trajectories of malaria parasites on a 2D glass substrate (**a**) and in a 3D hydrogel (**b**). Scale bars 20 µm. From publication 1.

1.3.2 Experimental observations of gliding motility

Analyzing the motility of apicomplexans under different conditions has been employed as a way to assess their reaction to environmental conditions [108] and later genetic mutations [61] for more than half a century. It offers important insights into whether the cell is functioning correctly, because lowered motility often correlates with reduced infectivity [109]. Mostly, these experiments use 2D assays, where the parasites move on glass slides or gel substrates [61, 62, 110–112]. To more closely approximate the physiological environments, 3D environments have been introduced for *Toxoplasma* tachyzoites [113, 114], *Plasmodium* ookinetes [115], and sporozoites [116]. Given their curved shapes, these parasites tend to circle on 2D substrates, and move along helical trajectories in 3D substrates, as illustrated for sporozoites in Fig. 1.3.

Central to this thesis is the observation that the motion of these apicomplexan parasites comes with a very specific set of chiralities. While *Toxoplasma* tachyzoites and *Plasmodium* ookinetes do not circle as regularly as the much more slender sporozoites, they still possess a preferred orientation (i.e. clockwise [CW] vs. counterclockwise [CCW]) when circling on 2D. In 3D, the helices of all three of these examples show a 3D chirality, i.e. the helical trajectories are preferably left- or right-handed, see Tab. 1.2. Investigating and understanding this chirality and its origin in the surface flow machinery, particularly for sporozoites, is one main focus of this thesis.

Cell	Toxoplasma tachyzoite	Plasmodium ookinete	Plasmodium sporozoite
2D chirality	counterclockwise	counterclockwise	counterclockwise
3D chirality	left-handed	left-handed	right-handed
Aspect ratio	3.3	5.7	12.5
Reference	[113, 117]	[115, 118]	[61, 119]

Table 1.2: Chirality behavior and aspect ratio of different apicomplexan gliders.

Detailed observations of the surface flow

While the observations above are concerned with the motility of the cell as a whole, it is much harder to experimentally access how this motility is actually generated by the glideosome. As the machinery is small, it cannot be directly imaged as for example flagella. One possible approach is to put tracer beads on the surface, which can be bound by the surface adhesins and are subsequently transported with the flow, as has been done for sporozoites [120, 121] and tachyzoites [111]. This allowed quantification of the forces exerted on such a bead by optical tweezers measurements, resulting in 100 to nearly 200 pN for sporozoites [121].

An alternative approach is to label the participating molecules, e.g. the adhesins. This is difficult because the majority of these molecules are stored inside the cell, drowning out the signal from those actively engaged in motility generation at the surface machinery. Advanced imaging techniques are necessary to overcome these challenges, and it was only recently that single-molecule observations of sparsely tagged actin allowed some direct insight into the surface flow of *Toxoplasma* [117], see Section 1.4.3.

Traction force microscopy

A further inroad into understanding gliding motility from a more mechanistic perspective is to directly measure the produced forces. In the microbial realm, this is mostly accomplished by traction force microscopy [122–124], even though more recently the introduction of molecular force sensors offers an alternative [125, 126]. The classical traction force assay observes cells on an elastic gel substrate, which incorporates fluorescent tracer particles. As the cell attaches to the substrate and pulls it by establishing focal adhesions, the substrate gets deformed, which can be quantified by observing the tracer particles. Subsequently, a deformation field can be obtained, and afterwards the

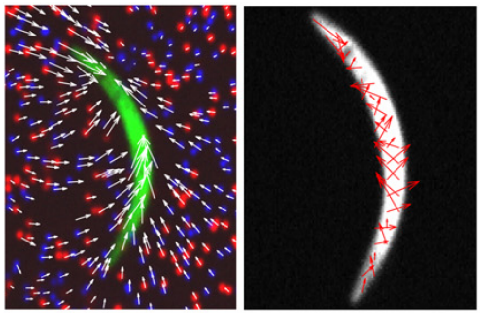

Figure 1.4: Observations of traction force microscopy of sporozoites circling on soft elastic gels (from Fig. 4 in [61]). Left: Sporozoite on top of tracer particles in two different fluorescent channels. Right: Reconstructed tractions obtained from the displacements of the tracer particles.

inverse problem of predicting the stress (or traction) applied on the substrate producing the observed deformation can be solved [124]. For sporozoites, or also apicomplexan gliders in general, this technique has been successfully applied in the past, though the low magnitude of the applied forces combined with the fast movement of the cells make it challenging to do so. In [61], the forces generated by a sporozoite gliding in 2D were resolved over time (see Fig. 1.4). This revealed that the produced tractions corresponded to the buildup of adhesion sites, a stretching of the sporozoite, and an eventual decline as the adhesion at the sporozoite's posterior end is released.

More recently, Ref. [127] studied in more detail how the behavior of sporozoites and the observed forces depend, for example, on the elastic properties of the gel used as substrate. Similar assays have also been performed for *Toxoplasma* tachyzoites [105], even though their more irregular shape and discontinuous gliding on 2D substrates makes for a more complicated multistep migration process.

Alternatively, traction force microscopy can also be performed in 3D, by a multitude of different approaches, including measuring the deformation of oil droplets or elastic beads as sensors [128–130], tracing the movement of beads or other fluorescently labeled tracers to obtain deformation fields as for the 2D method [131, 132], or inferring forces from geometric features, for example the angles between cell membranes in organoids [133]. Using fluorescent collagen fibers and tracer beads, traction force microscopy was performed on *Toxoplasma* tachyzoites moving through a 3D environment [114]. There, strong inward forces toward the parasite were observed, similar to what was seen in [61] in 2D (cf. Fig. 1.4). Interestingly, the tachyzoites seem to move by turnover of discrete circular attachment zones, formed at the front and stationary in space as the parasite squeezes through. The forces measured in [114] suggest that the constriction is created by the parasite itself, rather than being the effect of an existing pore in the gel as previously suggested [134].

Motility and invasion

There is plentiful evidence that the glideosome is not simply a motility machinery, but that it doubles up as a mechanical assistance system for host cell invasion. The final target of the sporozoite's journey is to invade specific liver cells, hepatocytes, where the life cycle continues. *Toxoplasma* tachyzoites, on the other hand, are known to invade a large number of different cells, including fibroblasts and epithelial cells [135, 136]. These invasions typically have a large biochemical component, including the release of an invasion-specific cocktail of molecules stored in specialized organelles, rhoptries, but have been shown to be dependent on a functioning glideosome for both *Toxoplasma* tachyzoites [137] and *Plasmodium* sporozoites [79, 138].

1.4 Existing physical models of gliding motility

The fascinating apparatus of gliding motility in apicomplexan parasites has already seen some attention from biophysics. Here, the most relevant previous works specific to apicomplexan gliding will be introduced.

1.4.1 Geometric resolution of sporozoite movement in obstacle arrays

In Battista et al. [139], the motion of sporozoites on a 2D assay extended by pillars rising from the glass slide was investigated, finding that the sporozoites prefer to circle around pillars with a radius corresponding to the roughly 5 µm radius of curvature usually observed for *P. berghei* sporozoites. In a more detailed analysis, a model for sporozoite motility was introduced treating them as self-propelled rods following the shape of a circular arc, with varying radius allowing them to elastically deform. Combined with rules for the resolution of collisions with the pillar obstacles, including deforming or flipping to their other side (see Fig. 1.5), this model was able to reproduce observed motion patterns of sporozoites in obstacle arrays with varying geometry.

1.4.2 Self-sorting of sporozoites during collective motion in vortices

Focusing on the collective motion of sporozoites from the salivary gland, in Patra et al. [140], the authors observed the behavior of squished infected salivary

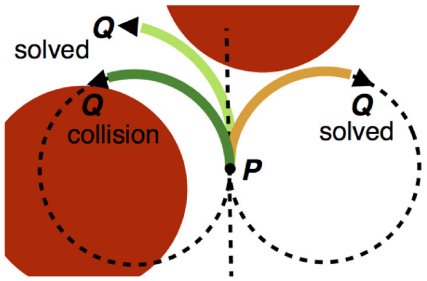

Figure 1.5: Modeling sporozoites and their interactions with pillar arrays in 2D using active rods with the shape of circular arcs (from Fig. 5 in [139]).

glands, finding that this procedure leads to the sporozoites in the gland starting to form active vortices (Fig. 1.6a). Tracking individual sporozoites in these vortices, a puzzling relation between velocity and radial distance was discovered, neither agreeing with a constant propulsion speed of the sporozoites, nor with the proportionality expected from a solid rotating disc. To understand this behavior, a more detailed sporozoite model was introduced, where the sporozoite consists of around 15 elastically coupled beads, each of which contributes a constant propulsion force along the sporozoite axis (Fig. 1.6b+c). Based on this model, collisions between sporozoites could be simulated, and hence their full collective dynamics resolved. With these simulations, the authors eventually uncovered that the biological variance in sporozoite properties, leading to a distribution of speeds and curvatures, coupled with a self-sorting of the different sporozoites within the vortices could explain the observed velocity-radius relation.

This study used advanced image analysis and modeling, but focused on 2D and collective motion, meaning that the model of the individual sporozoite was relatively simple, and the force generated at every bead is a prescribed constant. In this thesis, we will explore more detailed models representing the biological force generation mechanism and its physical implications.

1.4.3 Actin self-organization in the glideosome of *Toxoplasma*

The most influential study to this thesis was put forward by Christina Hueschen et al. in [117]. This study is concerned with the dynamics of actin in the glideosome of *Toxoplasma* tachyzoites, combining advanced modeling with challenging single-molecule experiments. Sparsely tagging actin, and stabilizing it with the drug jasplakinolide, produced a small number of long, fluorescent actin filaments that were moved around by the motors of the glideosome machinery and could be observed in TIRF microscopy (total internal reflection fluorescence, essentially using an exponentially decaying evanescent wave to

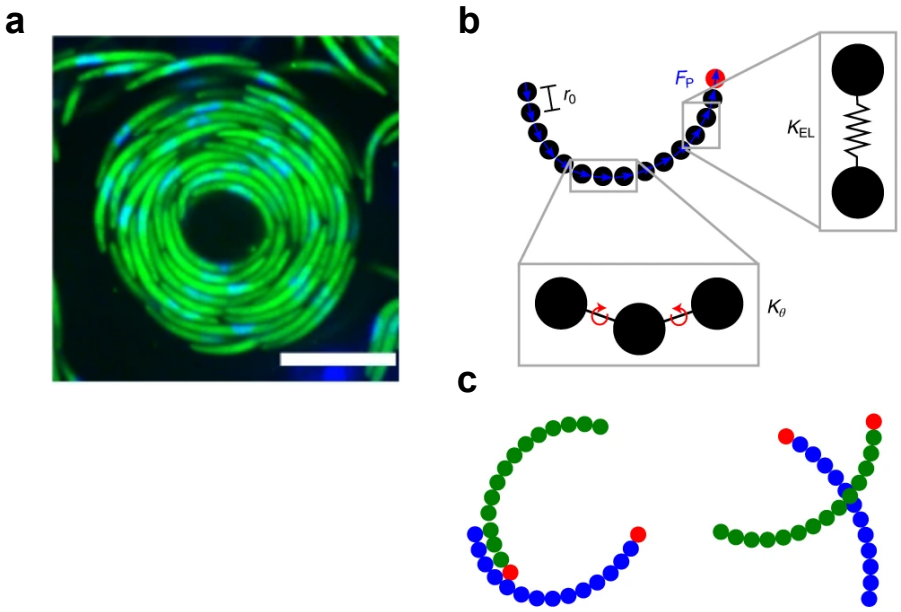

Figure 1.6: **a:** Collective motion of sporozoites in a gently squeezed salivary gland, forming vortices (from Fig. 1 in [140]). **b+c:** Modeling sporozoites as chains of elastically coupled beads (b), with a focus on their collective migration in constrained spaces, where they either align or pass over each other in the event of a collision (c) (from Fig. 3 in [140]).

only excite fluorophores close to the glass slide, Fig. 1.7a). This presents one of the most direct observations of the surface flow (though at the level of actin, not adhesins), and strongly confirms the idea that the direction and flow pattern of the surface flow is not locked in, but can dynamically change and self-organize, as the actin filaments observed in [117] moved around widely over the whole cell. Importantly, the focus of this study was the actin motility of its own, and the cells were not coupled to a substrate and productively gliding while these observations were made. Later in this thesis we will introduce the importance of the coupling to the environment, not only for the resulting motion of the cell, but also for the organization of the surface flow.

Here, the authors focused on the self-organization of the free, i.e. uncoupled actin in the glideosome. To model the collective dynamics of many small actin filaments, they turn to a continuum description, more specifically a Toner-Tu type flocking model [141]. These models are originally developed for the collective motion of swarming animals, but adapted by Hueschen et al. for flocks on curved geometries [142] or the dynamics of actin on the irregular geometry of the *Toxoplasma* tachyzoite.

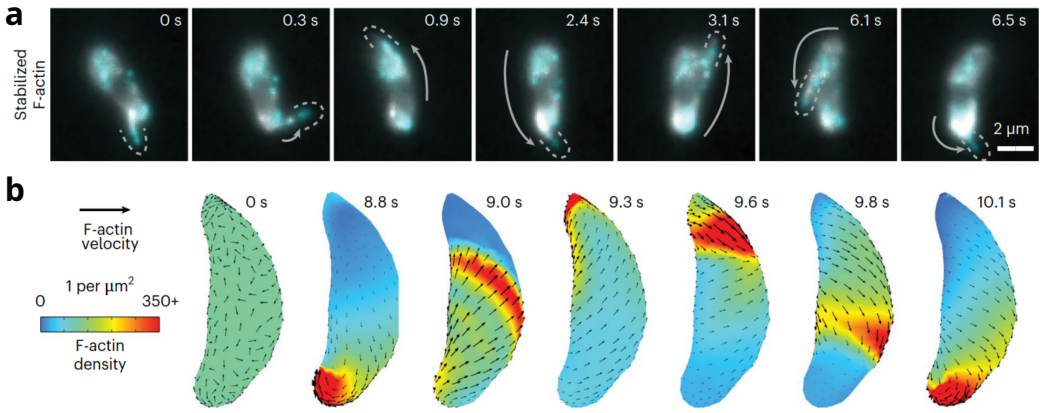

Figure 1.7: Modeling the surface dynamics of the actomyosin machinery in the glideosome of *Toxoplasma gondii* (from Fig. 3 in [117]). **a:** Actin filaments stabilized with jasplakinolide can be seen moving around by the glideosome motors, observed in TIRF microscopy. **b:** Simulation of dynamic actin motion by self-organized flocking on *Toxoplasma* shapes experimentally measured by soft X-ray tomograms.

Minimal Toner–Tu model.

The coarse-graining of the many-agent dynamics into continuum fields on space and time yields a filament number density $\rho(\mathbf{r}, t)$ and a mean velocity $\mathbf{v}(\mathbf{r}, t)$. In the present context these fields are effectively two-dimensional (confined to the local tangent plane of the surface), and their evolution is governed by coupled PDEs, explored in detail in [142].

Mass conservation. In the absence of sources/sinks, density obeys the continuity equation

$$\partial_t \rho + \nabla \cdot (\rho\, \mathbf{v}) = 0 \ , \tag{1.3}$$

where possible decay proportional to the density or constant source terms can be added on the right side of the equation to reflect filament turnover.

Velocity dynamics (minimal Toner–Tu). The coarse-grained velocity follows

$$\partial_t \mathbf{v} = \Big[\alpha\big(\rho - \rho_c\big) - \beta\,|\mathbf{v}|^2\Big]\mathbf{v} \ + \ D\,\nabla^2\mathbf{v} \ - \ \sigma\,\nabla\rho \ - \ \lambda\,(\mathbf{v}\cdot\nabla)\mathbf{v} \ , \tag{1.4}$$

where

- α and β are Landau-type coefficients controlling spontaneous polar order. Below a critical density ρ_c the stable state is disordered ($\mathbf{v} = \mathbf{0}$); for $\rho > \rho_c$ a finite-speed state emerges with a characteristic magnitude $|\mathbf{v}| \sim \sqrt{\alpha(\rho - \rho_c)/\beta}$.

- $D\,\nabla^2\mathbf{v}$ promotes local alignment/smoothing of the velocity field.
- $-\sigma\,\nabla\rho$ is a pressure-like term coupling density gradients to the flow, helping to keep ρ within a physical range and enabling propagating modes.
- $-\lambda\,(\mathbf{v}\cdot\nabla)\mathbf{v}$ is a self-advection nonlinearity characteristic of polar active matter and responsible for convective transport of orientation and speed. Usual advection as observed in fluid flow corresponds to $\lambda = 1$, whereas for example spatially stationary components that encode the velocity field can reduce it.

Together, Eq. 1.3–1.4 constitute the minimal hydrodynamic description of a polar active flock. They capture the order–disorder transition at ρ_c and the ensuing spatiotemporal patterns (e.g. density waves and flocking streams) arising from the interplay of alignment (D), pressure-like coupling (σ), and advection (λ).

The main complication for the application of this theory to the case of *Toxoplasma* is the curved geometry. Just solving these equations while correctly constraining them to the irregular shape is difficult, and only feasible numerically, using a combination of 3D and 2D descriptions paired with appropriate projections onto the tangent space [142]. For this study, the authors used appropriate functions in COMSOL Multiphysics, a powerful finite element software. Furthermore, the authors estimated that the curvature might exert a torque on actin filaments. If the two principal curvatures of the surface differ, the actin prefers to be aligned with the direction of lower curvature, to minimize its own curvature energy. This yields an additional, geometry-dependent reorientation term in Eq. 1.4. The resulting actin surface flow can organize in different modes, which can be associated to different observed gliding behavior, e.g. oscillatory modes that might correspond to back-and-forth gliding (cf. Fig. 1.7b).

2

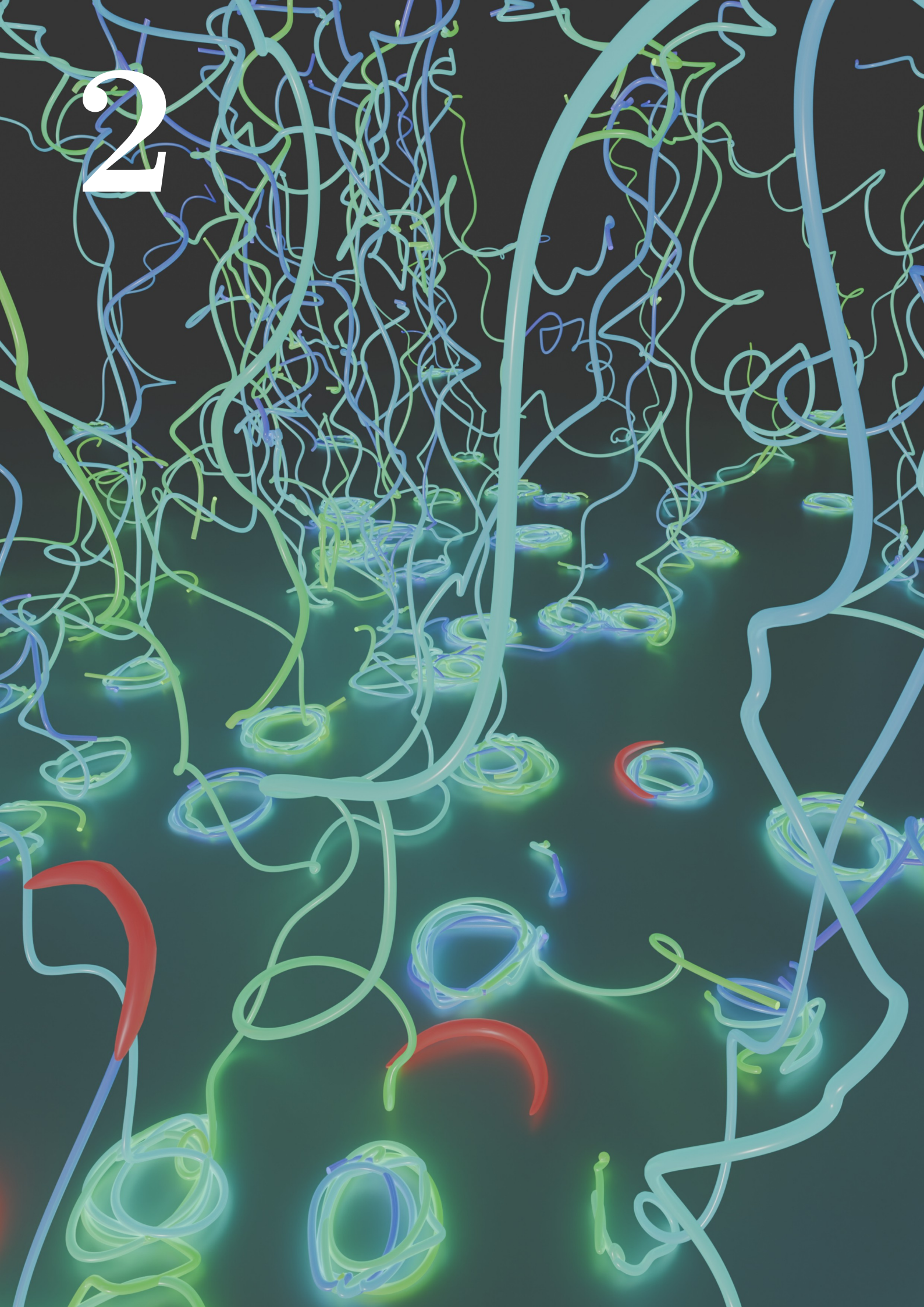

Chapter 2

Experimental results and data analysis

This chapter is based on parts of publication 3,
Lettermann, Singer et al., Nature Physics, in press.

Starting point of the understanding of the force generation underlying malaria parasites' gliding motility, and in particular their chirality, is a robust, quantitative analysis of their motion. While the movement on 2D assays, i.e. on a glass slide, is well established, 3D assays are newer, and only little data existed. Therefore, in cooperation with the group of Freddy Frischknecht at the Center for Integrative Infectious Disease Research at Heidelberg University, and in particular Mirko Singer, who conducted most experiments discussed in this thesis, we acquired fast 3D imaging of sporozoites moving through 3D hydrogels. I then implemented an automated analysis workflow, enabling the analysis of thousands of sporozoite trajectories imaged and extracting the sporozoite migration patterns. In this chapter, I will present the experimental setup, explain the image analysis pipeline, and discuss the results.

2.1 Experimental setup

Sporozoites move by gliding motility (see Chapter 1), which allows them to maintain a constant shape and therefore move more rapidly than crawling immune cells they want to outrun, at speeds reaching 1–3 µm s^{-1}. Coupled with their small diameter of about 1 µm, time-resolved imaging of their motility is challenging, as it requires sufficient 3D resolution, but simultaneously relatively high frame rates. This can be achieved by spinning-disk confocal microscopy, which offers a compromise of speed and resolution [143]. By combining many confocal light paths, created by pinholes and microlenses arranged on two rotating disks, samples can be scanned much quicker than with traditional single-focus confocal microscopy. This comes at the cost of reduced resolution, particularly in z direction, and requires deconvolution of the images.

The sporozoites should be imaged in a 3D environment, because this is closer to the physiological tissue they migrate through than the 2D assays. While it is possible to directly image sporozoites in living host tissue [53], the complexity of the real physiological environment makes it difficult to draw general conclusions about gliding motility. Therefore, we used a recently established polyacrylamide hydrogel assay [116]. The experimental setup is illustrated in Fig. 2.1: The salivary gland is dissected from an infected mosquito, and afterwards placed on top of the hydrogel, which is incubated on a glass slide and imaged from below by spinning-disk microscopy. The sporozoites can then egress the salivary gland and invade the hydrogel, such that imaging the gel underneath the salivary gland allows observation of large numbers of migrating sporozoites. We mainly focus on a rodent-infecting species, *P. berghei*, but also investigate the medically most relevant human-infecting species, *P. falciparum*. We use parasite lines that express a fluorescent protein in their cytoplasm, allowing visualization via spinning-disk confocal microscopy. Details of the experimental procedures are given in Appendix A.2.

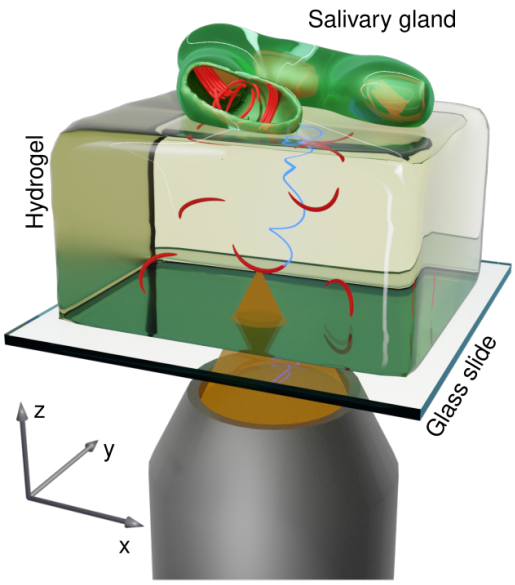

Figure 2.1: Schematics of the experimental setup. A soft polyacrylamide hydrogel is prepared on a glass slide. A salivary gland from an infected mosquito is placed on top and covered with a second glass slide (not shown). Sporozoites (red) invade the hydrogel beneath the salivary gland. The fluorescent parasites can then be observed migrating in 3D with a spinning-disk confocal microscope (tracks in blue).

In Fig. 2.2a, we show a representative experiment in which the sporozoites' trajectories are projected over time and color-coded by their z-position. As can be readily seen, in the relatively homogeneous 3D environment, the motion of the sporozoites is very regular. Three main classes of motion can be distinguished: (1) helical motion within the 3D gel, (2) circular motion at the bottom gel-glass interface, and (3) transitions where sporozoites come down from the gel but then start circling once obstructed by the glass substrate (Fig. 2.2b).

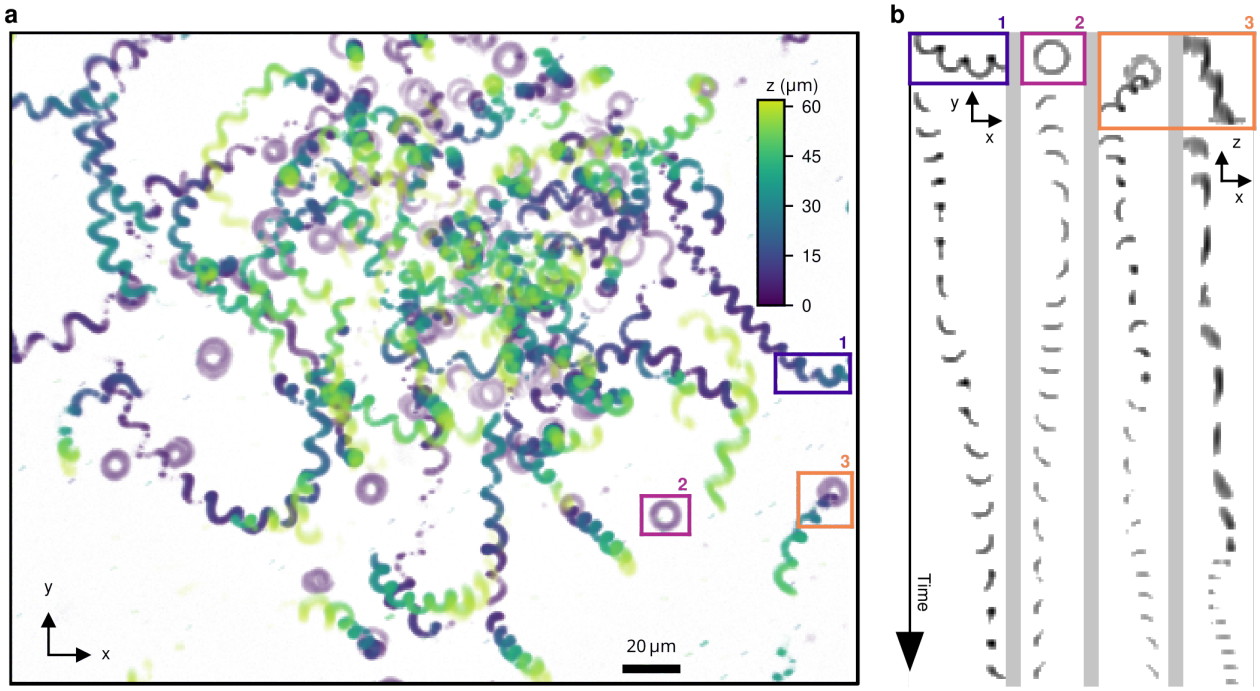

Figure 2.2: **a:** Sporozoite migration through the hydrogel reveals corkscrew patterns in the gel and circular movement at the glass below the gel. Experimentally recorded images projected over time and color-coded by z-position. The boxes mark examples highlighted in b. **b:** Representative events from a for the following classes: helical motion (1), circular motion at bottom (2), transition from helical to circular motion (3). For the example from the transition class, a side view is shown in addition to the z-projection.

2.2 Image analysis pipeline

To systematically analyze sporozoite motility in 3D, we developed a dedicated image analysis pipeline (Fig. 2.3). First, the fluorescence images are background-subtracted, then deconvolved using a special blind deconvolution approach. This is necessary because the salivary gland, located just above the imaged volume, emits out-of-focus light and complicates standard deconvolution. After deconvolution, the images are thresholded, and we apply tracking with a collision resolution step to handle overlapping sporozoites in highly dense areas.

2.2.1 Automatic sporozoite tracking

The tracking of sporozoites in 3D spinning-disk microscopy data of our assay faces a number of challenges:

1. The large z-extension of the point spread function (PSF) of the spinning-

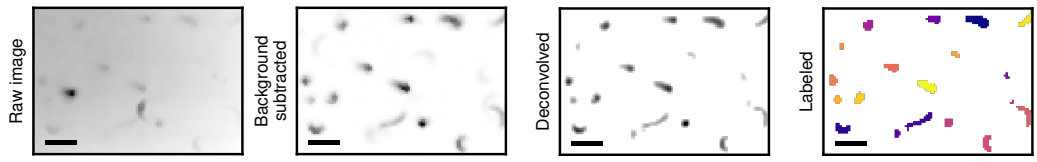

Figure 2.3: The image processing pipeline including background subtraction, automatic blind deconvolution, thresholding and labeling lead to the tracking of hundreds of sporozoites within a single experiment. Scale bars: 10 µm

disk microscope has to be compensated by deconvolution. However, the salivary gland on top of the gels gives off a strong signal into the imaging domain, even though it is just not inside the imaged volume itself. This is problematic for standard deconvolution techniques.

2. Many tracking algorithms (e.g. [144]) are primarily used to track roughly circular/spherical objects such as beads, whereas the sporozoites have a very distinct, high aspect ratio and curved shape. This cannot only impede such tracking algorithms, but also make the center of mass (which is often outside of the shape itself) an ill-posed point to use as a tracer for trajectories.

3. Especially underneath the salivary gland and at the bottom glass slide, the sporozoites can reach higher densities leading to frequent collisions or overlaps. This complicates distinguishing them for the purpose of tracking individual sporozoites.

To address these challenges, we custom-built an image analysis pipeline in Python, consisting of a deconvolution and tracking part. The code is available in the git repository `github.com/LeonLettermann/hei-sporo-code-tracking`.

Automatic blind deconvolution with out-of-volume reconstruction

We require deconvolution primarily to reduce the extent of recovered sporozoite labels, particularly in the z direction, to facilitate precise localization and discrimination of close-by sporozoites.

Before deconvolution, we normalize intensities across the stack, and subtract a smoothed background estimate. The background arises primarily from signal bleed-through from the salivary gland, which is not imaged directly but contributes a diffuse signal due to the limited axial confinement of the spinning disk PSF. To address this, we estimate a background image by averaging low-intensity regions across time and space, and then apply spatial smoothing.

Following background subtraction, intensity outliers are suppressed using a combination of Gaussian and median filtering.

Since a directly measured PSF cannot be easily applied after the background subtraction, we implemented a blind PSF estimation procedure. The PSF is initialized based on the observed data by selecting bright subvolumes and statistically aggregating their profiles. The size of the PSF is limited to a fixed kernel (typically 35×25×25 pixels) and symmetrized to enforce physical plausibility.

We apply an iterative blind deconvolution algorithm that simultaneously refines both the reconstructed image estimate and the PSF using a custom optimization loop over a user-specified number of epochs (typically 500). The loss function combines two main criteria: the reconstructed image convolved with the current PSF estimate should resemble the measured image, and the intensity within the reconstructed image should be concentrated in small volumes. With additional normalization constraints, this loss function works well to obtain sharpened sporozoite shapes for more precise tracking.

3D tracking of sporozoites with iterative collision resolution

The deconvolved stack is first rescaled to 8-bit and binarized in two steps: (i) an adaptive Gaussian threshold is applied independently to every z-slice to capture local contrast; and (ii) the result is intersected with a global intensity mask to suppress dim background voxels. Small gaps are filled by morphological closing, and an optional dilation can be added when a more generous outline is desired. Connected-component labeling is then performed in three dimensions (i.e., independently for each frame). Components outside user-defined size limits are discarded, yielding an initial label field $L(t, z, x, y)$ in which each voxel belongs either to exactly one sporozoite or to the background.

Tracking is now the problem of pairing labels in subsequent frames. We iterate six times over the movie, alternating forward and backward temporal directions. In each step the label map of frame t is compared with that of frame $t-1$:

1. **One-to-one assignments.** If a child label in t overlaps a single parent in $t-1$, the child is reassigned to that parent.

2. **Collision or split events.** If a child overlaps *multiple* parents, collision resolution is triggered.

When two tracked objects touch or overlap, they may momentarily merge into a single connected component. To separate them, we

1. identify the two best parent candidates by voxel overlap with the merged region;

2. compute a smooth *decision image*

$$D \;=\; G_\sigma * (M_1 - M_2),$$

   where $M_{1,2}$ are binary masks of the two parents and G_σ is a separable Gaussian ($\sigma \approx 2$ px in z,x and y); pixels of the child with $D \geq 0$ are reassigned to parent 1, the remainder to parent 2;

3. suppress fragments smaller than a minimum size; otherwise they become new tracks with fresh labels.

Because the split is based on a blurred difference image, the resulting decision surface follows the curved interface between two sporozoites and preserves thin tips that would be lost with straight-line Voronoi splits. After the forward/backward relabelling, every track is examined in four dimensions. If a label consists of multiple disconnected sub-components, the largest is kept and each remaining component is moved to a new label, guaranteeing that every track is a single connected object in space–time. Tracks that disappear temporarily (e.g. due to transient dimming or occlusion) are reconnected if easily possible: for every gap of one frame, we pair end points and new beginnings whose 3D centers of mass are closer than a maximum reconnect distance.

Because of the sporozoites' characteristic crescent shape, a simple center of mass can lie outside of the shape itself, and hence does not provide a good tracer for generating trajectories. Instead, we trace the middle point of the middle cross-section, which we refer to as *biocenter*. This point can be found algorithmically by the following steps:

1. Perform a principal component analysis on the voxelated shape.

2. Take all points close to the center of mass in the leading principal component direction. This generates a section from the center of the sporozoite.

3. Take the center of mass of this section, which is short enough not to be significantly curved.

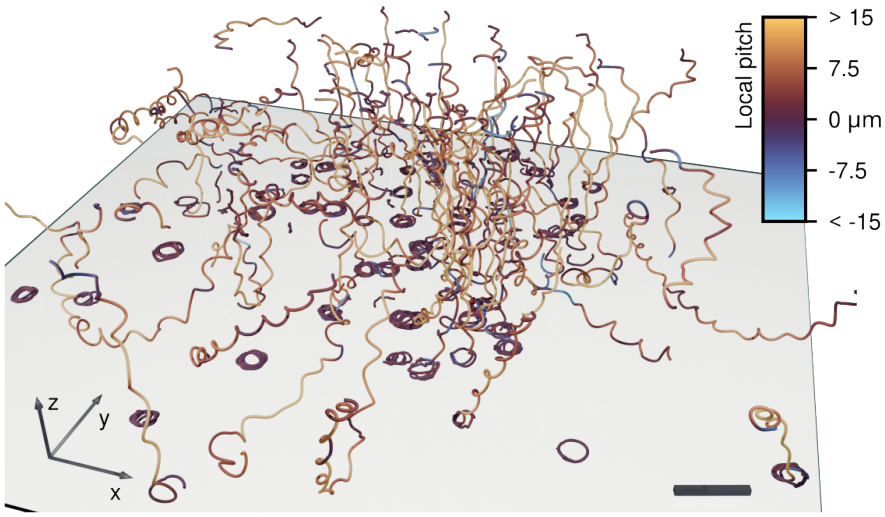

Figure 2.4: Tracks of migrating sporozoites in a single experiment. Color map displays the local pitch, computed from curvature and torsion obtained from fitting the trajectories with a Fourier series. Positive pitches correspond to right-handed, negative to left-handed chirality. Scale bar: 20 µm

The resulting trajectories are shown in Fig. 2.4, color-coded by local pitch (obtained from the curvature and torsion of the trajectories, fitted via a Fourier expansion similar to the approach of Ref. [113]). The pitch of a helix is the distance advanced along the helical axis per full turn. We assign positive pitch to right-handed helices and negative pitch to left-handed helices. At the bottom interface, where motion is circular, the pitch is effectively zero. We find that the vast majority of 3D sporozoite trajectories are well-defined, right-handed helices with a positive pitch, manifesting strong chirality.

2.2.2 Helical fit for trajectory segments

In order to quantify more thoroughly the helical geometry of the trajectories, we want to fit overlapping trajectory snippets with an analytical helix model. This model is defined as

$$\mathbf{r}(t) = \mathbf{r}_0 + \underbrace{\big(s\,t\big)\,\mathbf{a}}_{\text{axial advance}} + r\Big[\cos\Big(\big(1-2\,\iota\big)\,t\Big)\,\mathbf{R}_1 - \sin\Big(\big(1-2\,\iota\big)\,t\Big)\,\mathbf{R}_2\Big],$$

with parameters screwness s yielding pitch $2\pi s$, radius r, center $\mathbf{r}_0$, unit axis vector $\mathbf{a}$, orthonormal radial basis vectors $\mathbf{R}_{1,2}$ and a binary flag $\iota \in \{0, 1\}$ that allows to account for both right- and left-handed chirality. An additional 3-parameter Euler rotation $R(\alpha, \beta, \gamma)$ lets the basis $(\mathbf{a}, \mathbf{R}_1, \mathbf{R}_2)$ deviate from

the principal axes initially estimated from the data.

For every time point of every track we form a window of an adjustable number of frames centered on that time point. A fast principal-component analysis (PCA) of the window provides $\lambda_1 \leq \lambda_2 \leq \lambda_3$ and eigenvectors $\mathbf{e}_{1,2,3}$. Three cases are distinguished:

1. **Helical segment:** $\lambda_1 > 0.05\,\mu\text{m}^2$ and $\lambda_3 \geq 10\,\mu\text{m}^2 \Rightarrow \mathbf{a} = \mathbf{e}_3$.
2. **Flat circle:** $\lambda_1 < 0.05\,\mu\text{m}^2 \Rightarrow \mathbf{a} = \mathbf{e}_1$ (normal to the disk).
3. **Undetermined:** otherwise $\Rightarrow$ $\mathbf{a}$ is simply the end-to-end vector of the snippet.

The center $\mathbf{r}_0$ is the mean position, the initial radius is twice the minimal radial distance, and the initial screwness is a small constant ($s \simeq 2\,\mu\text{m}$ for helices, $s = 0$ for circles). Let τ_i be the phase assigned to frame i. Given a segment from a trajectory with coordinates $\mathbf{x}_i$, the loss function

$$\mathcal{L} \;=\; \sum_i \Big\|\mathbf{r}(\tau_i) - \mathbf{x}_i\Big\|^2 \;+\; 20 \sum_i \mathrm{ReLU}(-\Delta\tau_i)\,, \qquad \mathrm{ReLU}(x) = \max(0, x)\,,$$

penalizes the squared distance between predicted and observed coordinates and enforces strictly increasing phases ($\Delta\tau_i = \tau_{i+1} - \tau_i$). Parameters $\Big(s, r, \mathbf{r}_0, \alpha, \beta, \gamma, \{\tau_i\}\Big)$ are refined by 100–500 steps of gradient descent, using JAX for just-in-time compilation and automatic differentiation. To remove the handedness ambiguity the optimization is executed twice, with $\iota = 0$ and $\iota = 1$; the solution of lower loss is retained. This segment fit is vectorized twice using JAX, so it can be executed efficiently for each of the overlapping segments of a given trajectory and all trajectories in a dataset, performing $\sim$100 000 fits in total.

2.2.3 Trajectory geometry for different species and temperatures

Applying the pipeline introduced above to the *P. berghei* trajectories yields for each sporozoite median velocities, pitch, and radius, the radius being that of the local cylindrical hull of the helices (Fig. 2.5a–c). Across 21 experiments and in accordance with a recent report [119], we find an overwhelmingly positive pitch distribution centered around 12 µm (Fig. 2.5a), indicating that virtually all sporozoites follow right-handed trajectories. A small fraction with negative pitch arises from irregular or collision-affected tracks. The typical radius is

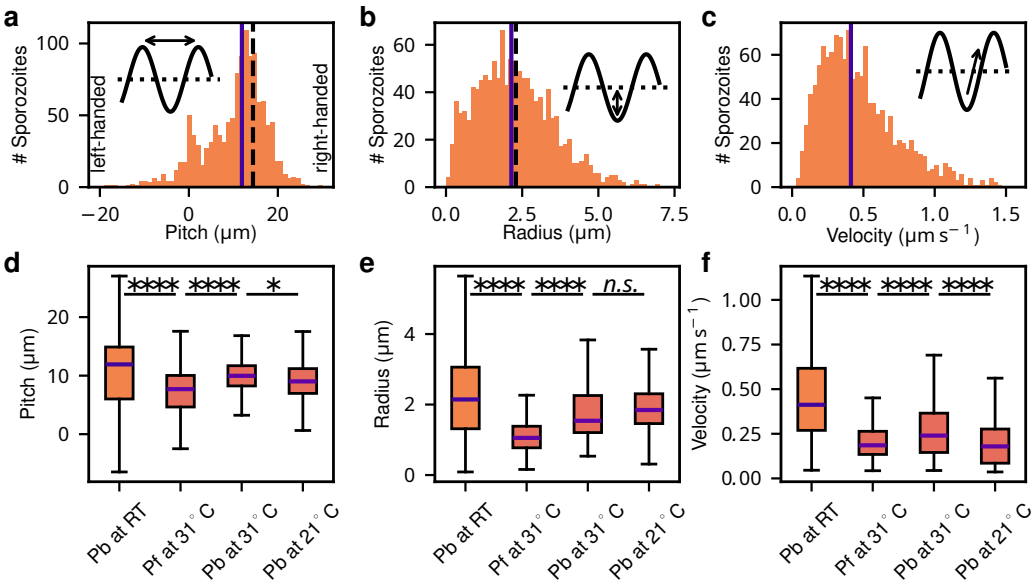

Figure 2.5: Automated image analysis quantifies geometrical features of sporozoite trajectories in 3D hydrogels. **a:** To obtain averaged pitch and radius values, helical segments are fitted to every 10 frame segment taken from the trajectories away from the top/bottom borders within the hydrogel, and the median of the segments computed for each sporozoite. The distribution of the resulting pitches reveals a preferred pitch of the helical trajectories of around 12 µm (violet line, median). Dashed lines are theoretical predictions from Eq. 2.2. **b:** Radii of the fitted helices, with a median of 2.4 µm. **c:** Velocity values observed along trajectories, with median velocity of 0.42 µm s^{-1}. **d:** Measured pitches compared between experiments with *P. berghei* at room temperature (RT) (Pb at RT, same data as c) and with *P. falciparum* at 31 °C (Pf at 31 °C) and *P. berghei* at 31 °C and 21 °C. Significances are reported as n.s. for p>0.05, ∗ for p<0.05 and ∗∗∗∗ for p<0.0001. **e,f:** Measured radii (e) and velocities (f) from the experiments in d. Statistical comparisons of trajectory properties were performed using two-sided independent-sample t-tests without assuming equal variances (Welch's t-test). Box plots display the median (central line), the interquartile range (box from the first to third quartile), and whiskers extending to the most extreme data points within 1.5 times the interquartile range from the box. The number of individual sporozoites in Fig. 2.5 and following were 1222, Pb at RT; 304, Pf at 31 °C; 319, Pb at 31 °C; 2190, Pb at 21 °C.

2.4 µm (Fig. 2.5b), and the median velocity is 0.42 µm s^{-1} (Fig. 2.5c). This value is somewhat smaller than in medium or collagen gels, possibly due to the small pore size of the polyacrylamide gels. Its stiffness was measured via indentation, obtaining an approximate Young's modulus of about 150 Pa (in four independent gels). The gel stiffness was measured by Zeynab Tavasolyzadeh from the group of Prof. Christine Selhuber-Unkel in the Biomechanics Core Facility of the Institute for Molecular Systems Engineering and Advanced

Materials (IMSEAM) at Heidelberg University.

We next compared *P. berghei* with the human pathogen *P. falciparum*. As *P. falciparum* sporozoites are more sensitive to environmental conditions, requiring 31 °C for motility, we also performed *P. berghei* runs at 31 °C and 21 °C to allow direct comparisons (Fig. 2.5d–f). We found that *P. falciparum* also glides in a right-handed fashion (Fig. 2.5d), but with significantly smaller pitch, radius, and velocity compared to *P. berghei* (Fig. 2.5e,f). Furthermore, changing temperature for *P. berghei* had little influence on pitch or radius, but strongly affected velocity (Fig. 2.5f), suggesting that macroscopic geometry remains robust while the microscopic rates of the force-generating processes (in particular for the myosin motors) scale with temperature, as seen also in 2D [110]. The experiments for *P. falciparum* were performed by Smilla Steinbrück and Sachie Kanatani in the group of Prof. Photini Sinnis at Johns Hopkins University, Baltimore.

2.2.4 Pitch vs. radius relation suggests torsion more flexible than curvature

Mathematically, the macroscopic pitch p and radius R of a helix can be related to the microscopic parameters curvature κ and torsion τ, if those are assumed to be constant:

$$p = \frac{2\pi\tau}{(\kappa^2+\tau^2)}, \quad R = \frac{\kappa}{(\kappa^2+\tau^2)}. \tag{2.1}$$

Hence, changing torsion at a fixed curvature results in different pitches and radii (Fig. 2.6a). Increasing torsion initially raises the pitch, then lowers it again (Fig. 2.6b). A scatter plot of radius versus pitch (Fig. 2.6c, for *P. berghei*) suggests that the trajectories in hydrogels exhibit varying torsion with a relatively constant curvature around $\kappa = 0.22\,\mu\text{m}^{-1}$. This value corresponds to a flat, untwisted radius of 4.5 µm, close to previously measured data [139, 140], but now with less variability (Fig. 2.7).

Interestingly, if torsion increases at fixed curvature, there is a point of maximal pitch and a corresponding radius:

$$p_{\max} = \frac{\pi}{\kappa}, \qquad R_{\max} = \frac{1}{2\kappa}, \qquad \tau_{\max} = \kappa\ . \tag{2.2}$$

Indeed, for the fitted curvature this pitch and radius closely match observations (dashed line in Fig. 2.5a,b). The *P. falciparum* data (Fig. 2.6d) are somewhat

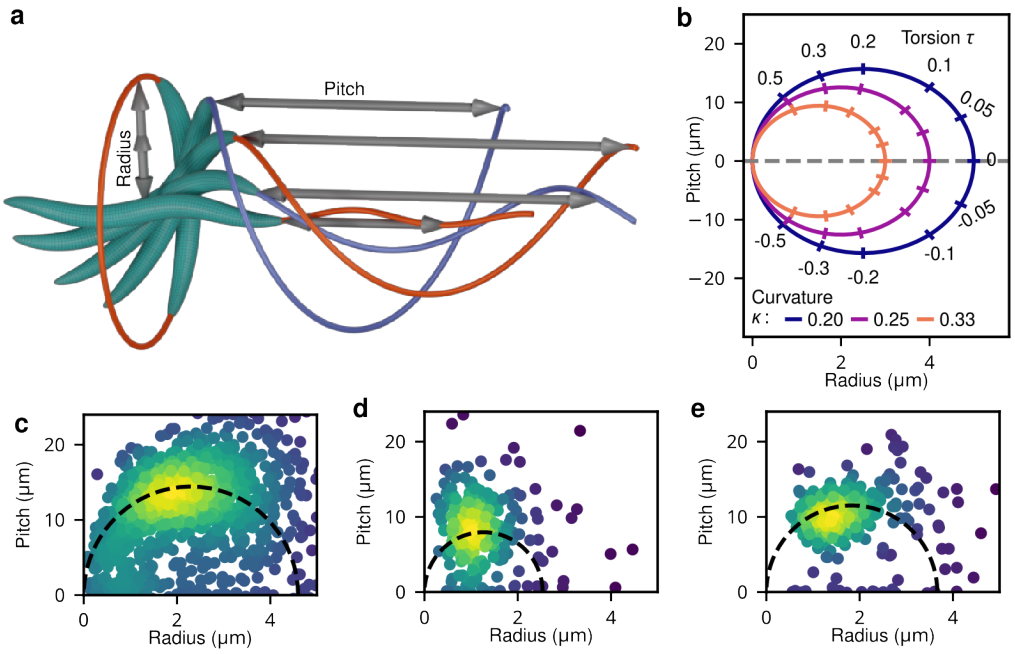

Figure 2.6: **a:** At fixed curvature, increasing torsion progressively reduces the radius of the shape and its extended centerline, but the pitch is first increased and later decreased again. **b:** For a given curvature κ, the theoretically possible pitch and radius values are shown. Each point on the lines corresponds to a certain torsion. **c:** Scatterplot of pitch vs. radius for Pb at RT, with dashed line illustrating allowed values if a fixed curvature is assumed, fitted to $\kappa = 0.22\,\mu m^{-1}$. **d:** Same as c for the *P. falciparum* measurement, resulting fit $\kappa = 0.36\,\mu m^{-1}$. **e:** Same as c for the *P. berghei* at 31 °C measurement, resulting fit $\kappa = 0.27\,\mu m^{-1}$.

more limited, but suggest a larger curvature ($\kappa = 0.36\,\mu m^{-1}$) that agrees with that species' smaller pitch/radius, and is also larger than the curvature measured for *P. berghei* at 31 °C (Fig. 2.6e).

2.2.5 3D chirality determines 2D – 3D transitions

As shown in Fig. 2.2b, sporozoites reaching the substrate at the bottom of the gel continue to circle at the interface. Strikingly, they do so in clockwise direction (Fig. 2.8a), whereas in the classical 2D motility assay (glass with medium on top), they circle counterclockwise (Fig. 2.8b) [108, 110]. The clockwise circling under gel is the consequence of the right-handed helix hitting the glass slide at the bottom of the gel from above (Fig. 2.8c). The experimentally observed counterclockwise circling of sporozoites on glass in medium therefore means that they do not aim to invade the substrate, as commonly assumed, but rather the medium above (Fig. 2.8d).

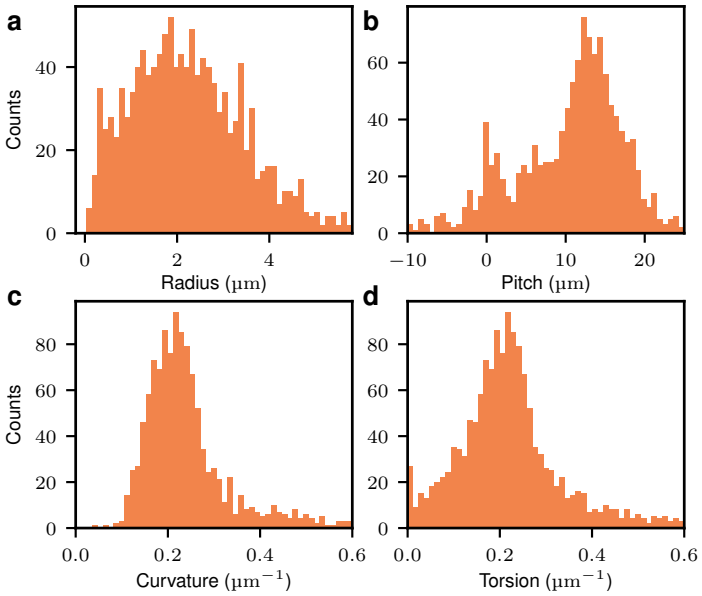

Figure 2.7: Histograms of median per sporozoite of radius (**a**), pitch (**b**), curvature (**c**) and torsion (**d**) for the *Plasmodium berghei* measurements. Radius and Pitch are one full set to describe the helical geometry, as are curvature and torsion. Comparing the four histograms, the curvature one is the one most concentrated.

To quantify these observations, we introduce a **Clockwise score.** Let $\mathbf{x}(t)$ be a 2D (x,y) trajectory and $\tilde{\mathbf{x}}(t) = \mathbf{x}(t) - \langle \mathbf{x} \rangle$, with $\langle \cdot \rangle$ the time average. Then the clockwise score of this trajectory is computed from the direction of movement and direction from the average position,

$$\mathbf{d}_k = \frac{\tilde{\mathbf{x}}_{k+1} - \tilde{\mathbf{x}}_k}{\|\tilde{\mathbf{x}}_{k+1} - \tilde{\mathbf{x}}_k\|} \qquad \hat{\mathbf{x}}_k = \frac{(\tilde{\mathbf{x}}_{k+1} + \tilde{\mathbf{x}}_k)}{\|(\tilde{\mathbf{x}}_{k+1} + \tilde{\mathbf{x}}_k)\|} \,. \tag{2.3}$$

by taking a cross-product with padded zeroes in the third component, $C = \langle (\mathbf{d}_k \times \hat{\mathbf{x}}_k)_z \rangle_k$. This quantification, displayed in Fig. 2.9a, finds that almost all sporozoites follow the previous observation, i.e. sporozoite underneath the gel circle the other way round compared to those on a glass slide in medium. Besides those sporozoites circling, there also exists a significant fraction of sporozoites that performs unclear (non-circular) motility (see arrows in Fig. 2.8a,b), in agreement with early observations for sporozoites on flat substrates in medium, which apart from circling also show back-and-forth motion (patch gliding) and waving motion (where one end is attached and the other moves) [110]. The velocities of those that do circle are comparable between both cases (Fig. 2.9b,c) and also similar to the velocity observed in 3D (Fig. 2.5c).

Having established that the 3D chirality of sporozoites determines their motion patterns at 2D interfaces, we next asked if chirality also determined how they switch from 2D interfaces to 3D environments. To this end, we devised a novel sandwich invasion assay in which purified sporozoites are first pipetted onto a hydrogel, then immediately covered with a second hydrogel, and

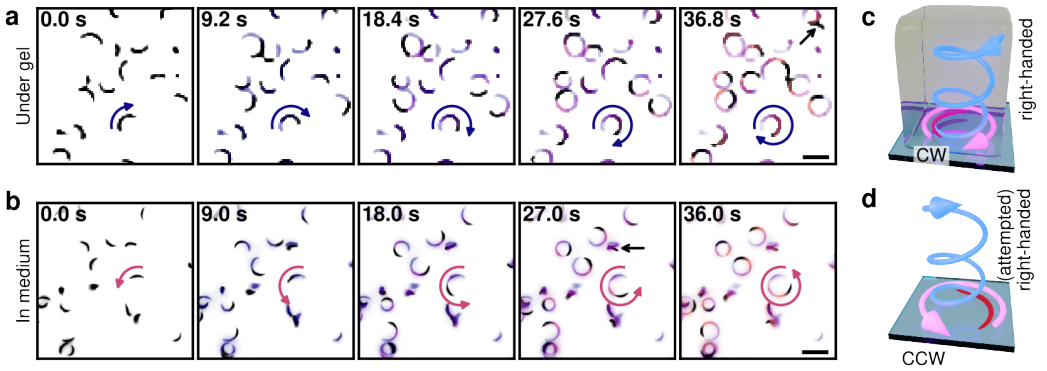

Figure 2.8: **a:** Sequential frames from the bottom layer showing migrating sporozoites at the glass slide underneath a gel. Colored overlay shows previous frames. Note that almost all sporozoites move in a clockwise fashion. Scale bar 10 µm. **b:** Sporozoites gliding on a glass slide in medium. Note that almost all sporozoites move in a counterclockwise fashion. Scale bar 10 µm. **c:** Right-handed helices predict clockwise rotation for sporozoites reaching the glass bottom. **d:** Counterclockwise motion on a glass slide with medium would correspond to a right handed helix leading upwards (blue arrow) into the medium.

subsequently imaged as they migrated into the gels (Fig. 2.10a, Appendix A.3 for details). The side view of sporozoite tracks in Fig. 2.10b shows that sporozoites can invade both up and down, probably depending on their initial orientation. Defining the turning direction at the top vs. bottom planes (Fig. 2.11) indicates that top-plane sporozoites predominantly turn counterclockwise (seen from above), while bottom-plane sporozoites turn clockwise—all consistent with right-handed helices that either ascend (CCW) or descend (CW) into the gels. Note that the majority of sporozoites that do not enter any hydrogel have unclear rotation, likely because most sporozoites moving CW or CCW have entered the hydrogel. Together, these results establish that 3D chirality

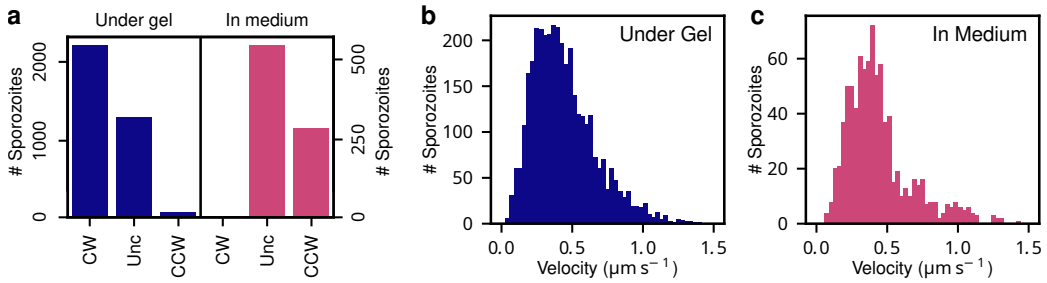

Figure 2.9: **a:** Number of sporozoites with observed direction (counterclockwise [CCW, $C < -0.33$], clockwise [CW, $C > 0.33$] or unclear [Unc]), compared for under gel or in medium. **b:** Median velocities of sporozoites circling under gel. **c:** Median velocities of sporozoites circling on glass in medium.

determines the transitions between motions in 2D and 3D, both of which occur during the initiation of a malaria infection.

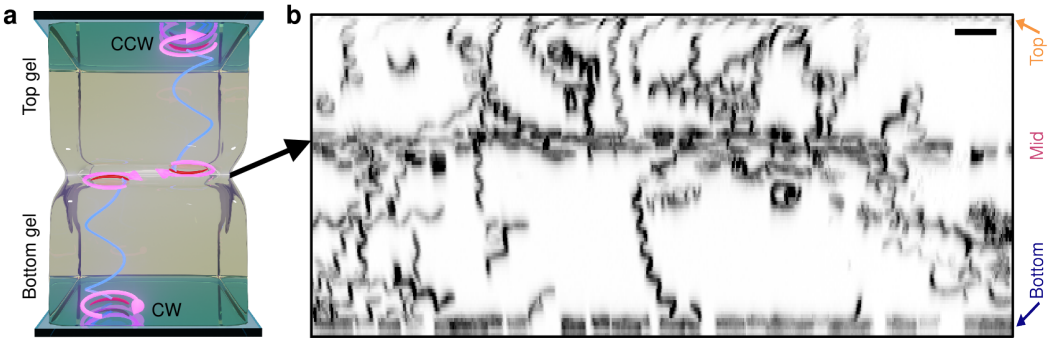

Figure 2.10: **a:** Experimental setup of the sandwich invasion assay: two gels are prepared, purified sporozoites pipetted on top of the bottom gel. Afterwards, the top gel is added, such that sporozoites are trapped in the small gap between the gels. **b:** Trajectories of migrating sporozoites in a hydrogel sandwich experiment projected in time and viewed from the side. Arrow indicates layer between the gels, where sporozoites were initially added. Scale bar 20 µm.

2.3 Analysis of sporozoite shapes

Complementing our analysis of the trajectories, we also reconstructed the shapes of individual sporozoites. Even in the deconvolved images, the segmentation is often still blurred in z direction, because our deconvolution is limited by the missing information at top and bottom of the imaged volume and the relatively low sampling in z direction, limited by time resolution. Therefore, we tried to directly infer the shapes of individual sporozoites from 3D frames by a direct approach, utilizing the knowledge of the sporozoite shape to improve compared to a standard deconvolution.

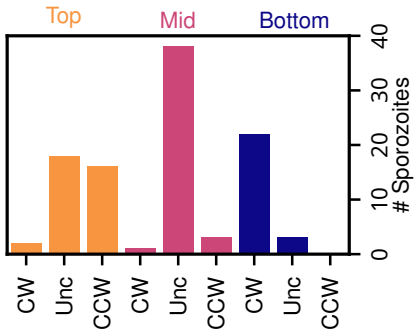

Figure 2.11: Number of sporozoites turning clockwise (CW), in an unclear fashion (Unc) or counterclockwise (CCW) for the top, mid and bottom planes.

2.3.1 3D shape reconstruction

To extract the central axis of each sporozoite, we implemented a 3D "skinning" algorithm that reduces the thickness of segmented objects to better define their original shape, which at roughly 1 µm diameter is filling about one voxel.

The skinning procedure operates on deconvolved intensity data and binary threshold masks for each tracked sporozoite. For each 3D frame, we identify ridge-like structures by detecting voxels that are local maxima along each spatial axis. Specifically, for each dimension (x, y, and z), we find voxels where the intensity is greater than both adjacent neighbours in that direction, creating binary ridge maps.

These binary ridge maps are then convolved with a 1D kernel [1, 2, 3, 2, 1] along each respective axis, creating weighted ridge responses that emphasize continuous ridge structures, still counting voxels next to a local maximum, though with a lower weight. The algorithm sums the weighted responses from all three spatial directions. Voxels with combined scores exceeding 6 are classified as belonging to the sporozoite's central structure, ensuring that only voxels that form ridge-like structures in multiple directions are selected. The resulting binary mask is then refined by intersection with a dilated version of the original threshold mask to maintain spatial constraint within the segmented object, followed by morphological closing with 2 iterations to ensure connectivity and remove small artifacts.

This skinning approach successfully reduces the effective thickness of sporozoites in x, y and especially z direction. The visual impression suggests that the reconstructed geometries of the sporozoites and their trajectories conform to each other (Fig. 2.12a).

2.3.2 Helical fitting of sporozoite shapes

In order to compare the geometries of sporozoite shapes to the extracted parameters of their helical trajectories, we employ a similar fitting pipeline as before. Instead of the trajectory, we want to fit a helical segment to the collection of voxel coordinates found for the segmentation of a sporozoite in the previous step. This is complicated by

1. the fact that the segmented voxels have no natural time order along the helical segment, differing from the previously used trajectories.

2. the shape resembling only very short helical segments, often less than

half a helical turn.

The combination of both makes the fit largely ill-conditioned, and prone to finding local minima quite far from a visually good agreement between helical segment and shape. To overcome this issue we employed a multiple shooting

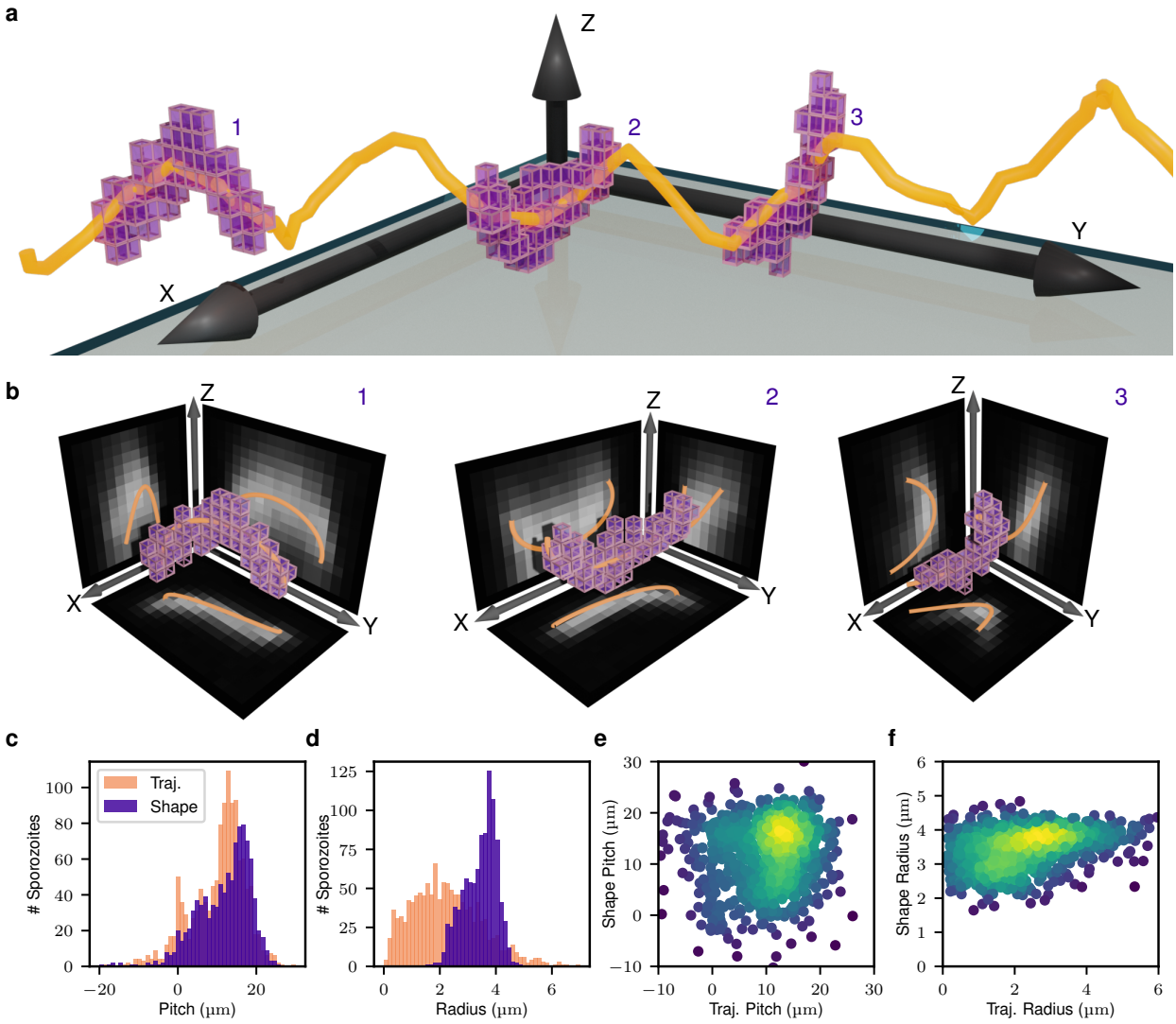

Figure 2.12: Shapes of individual sporozoites conform to the helical trajectories. **a:** Example trajectory with the shapes reconstructed from the 3D spinning-disk images inserted at 3 time points. **b:** Details of the 3D reconstruction of individual sporozoite shapes from a in voxels, with voxel sizes 0.66 µm in x,y and 1.0 µm in z. The orthogonal planes show projections of the imaging data. The dotted line shows a short helical segment fitted to the reconstructed shape to obtain pitch and radius. **c:** Pitches extracted from the shapes in comparison to the previously shown data from the trajectories, medians per sporozoite. **d:** Same as c for radius. **e:** Correlation of pitch of trajectory and shape, Pearson correlation of r=0.13 (p=3.8e-05). **f:** Correlation of radii of trajectory and shape, Pearson correlation of r=0.32 (p=3.9e-24).

method. For each sporozoite shape, we started with 200 randomly initialized parameters for the helical segment (bound to some reasonable ranges), 100 each for left- and right-handed helices. Each parameter set was optimized for 1500 iterations using gradient descent, and finally the lowest loss over all parameter sets accepted. This produced visually stable results.

However, the fitted values for pitch and curvature still showed very wide distributions. This is plausible, because for the still not perfectly slim segmentations both are only weakly constrained if the shape only contains notably less than half a helical turn. To make this analysis more robust, we added a second fitting step, in which the results are additionally constrained to follow the previously observed maintained curvature (cf. Fig. 2.6a). While this is an additional assumption, it reduces the degrees of freedom and thereby ensures that the fitting is reproducible and more robust against noise, and produces accurate helical center lines (Fig. 2.12b).

The resulting values of pitch and radius for the shapes can be compared to the parameters measured from the trajectories. Given the resolution limit, especially for small shape radii, shapes and trajectories show similar geometrical features (cf. Fig. 2.12c-f). Because variabilities are largest in sporozoite pitch and trajectory radius, we conclude that sporozoites in 3D tend to twist rather than to bend. In general, these results support the notion that the observed trajectories result from the combination of sporozoite flexibility and their physical interactions with the environment.

2.3.3 Sporozoite shapes show kink at 3D to 2D transition

Moving from the 3D helical migration within the gel, we investigated how the shape reacts to the rapid change in environmental stiffness presented by the glass slide at the bottom of the gel, where 3D helical trajectories are blunted to perform 2D circling motility. Reconstruction of sporozoite shape at this transition revealed that sporozoites tend to kink as they hit the bottom glass slide (Fig. 2.13), in agreement with earlier observations that extreme deformations can occur in mechanically challenging environments [140].

2.4 Conclusion

The results presented in this chapter represent the most thorough study of the 3D motility of *Plasmodium* parasites to date. The polyacrylamide hydrogel assay allows large numbers of sporozoites to invade, which can be simultaneously

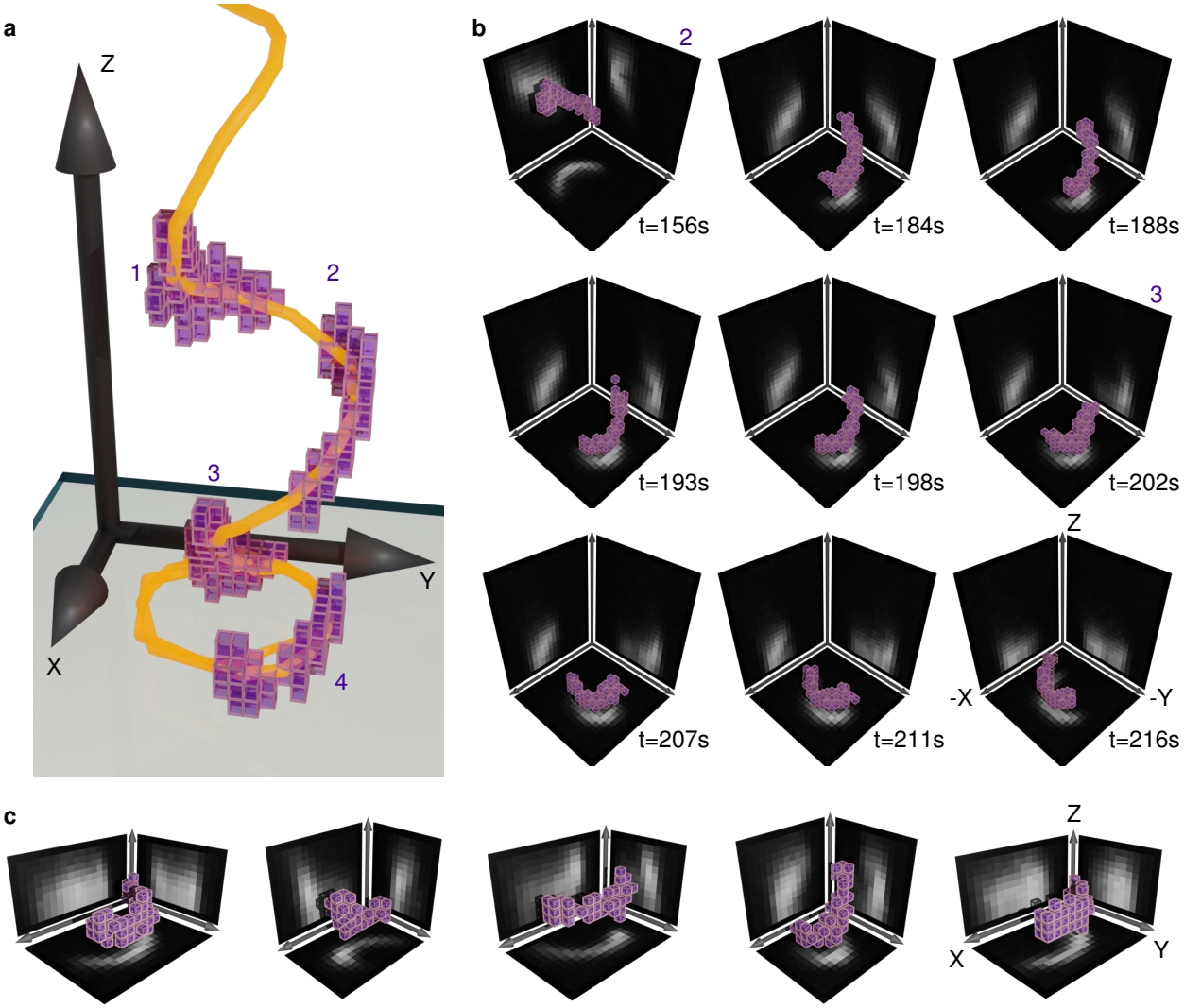

Figure 2.13: Shape reconstruction suggests kinking in sporozoites during transition from 3D to 2D. **a:** Example trajectory transitioning from 3D helical motility to 2D circling motility upon reaching the glass slide at the bottom of the gel. **b:** Time series of 3D reconstructions of the sporozoite shapes from a, with voxel sizes 0.66 µm in x,y and 1.0 µm in z. The orthogonal planes show projections of the imaging data. The section of the time evolution around the kink shown here includes shapes 2 and 3 from panel a. **c:** Five other different sporozoites during respective transitions from 3D to 2D motility.

observed in 3D with spinning-disk microscopy. The automated image analysis pipeline enables automated tracking and analysis of these large numbers of sporozoites. Key components are the specific blind deconvolution, built to be more stable against light sources just outside the imaged volume, and the collision resolution tracking that allows us to maintain 3D tracks under more crowded conditions. The combination of these methodological advances allows

to observe hundreds of sporozoites in 3D, improving compared to previous studies in collagen gels, where individual sporozoites were observed [119], or studies that relied on 2D imaging only considering the projection of the 3D trajectories [116]. These large sample sizes, combined with the complex study including the model system *P. berghei* and the medically most relevant *P. falciparum*, and the advanced analysis significantly advance our knowledge of parasite migration in 3D.

Firstly, we confirm the right-handed chirality of *P. berghei*, previously reported in [119], and extend this observation to *P. falciparum*. We find that radius and pitch of helical trajectories are smaller for *P. falciparum* than for *P. berghei*. Additionally, temperature variations impacted primarily the velocity, while the geometric quantities of the trajectories remained mostly unchanged. The right-handed helices in 3D lead to clockwise circling at the bottom glass slide, which we observed to be similarly stable to the usual 2D glass slide assay. However, in these assays the parasites circle mostly counterclockwise. This realization implies a major shift in understanding the 2D assay: instead of trying to invade the glass slide, sporozoites are actually moving on their back, trying to move upward, as we were able to confirm in our sandwich invasion assay. An important conclusion is that the (unphysiological) 2D circling might be unfavorable to invasion, which could contribute to low infectivity in hepatocyte invasion assays, where sporozoites circle on hepatocyte monolayers [145, 146].

The large amount of observed sporozoites and our automatic image processing allowed us to investigate in more detail the quantitative properties of the trajectories. The comparison of pitch and radius suggests that sporozoite trajectories roughly keep a constant curvature, while their torsion varies more widely. Intriguingly, we saw that for given curvature, the trajectories seem to maximize pitch. But more than just trajectories, we could also reconstruct individual sporozoite shapes. While this reconstruction is limited in resolution, we could support the idea that sporozoites have sufficient mechanical flexibility to twist in order to align with their helical trajectories, providing important input for models. Even more striking, we were able to reliably visualize a characteristic kink in the sporozoite as it transitions from 3D to 2D motility at the gel-glass interface, demonstrating how the sporozoite might be reacting to tissue barriers or other sudden changes in environmental stiffness in the skin.

The data presented here were taken with an (up to fluorescence) wild-type parasite strain. The established procedure of dissecting the molecular mechanisms and players within these parasites heavily relies on genetically

modified parasite lines, e.g., knock-outs of certain proteins. The assays, analysis, and results we presented here form an important baseline for comparison. For example, some mutant lines that are non-motile in 2D assays show some degree of motility in the 3D gel assay. Therefore, the 3D assay can serve as a more sensitive and more physiological tool to assess sporozoites' migration capabilities.

By focusing on capturing many parasites simultaneously we necessarily sacrificed resolution, both in space and, more importantly, in time. Due to frame rates on the order of seconds, we were not able to analyze whether the stop-and-go motion observed in 2D [61] exists to the same degree for 3D motility in the gel, or if movement in the gel is more continuous, with stopping a consequence of the less physiological 2D assay. Higher spatial resolution would, in particular, be interesting to study deformations of the parasite itself, e.g., as it collides with the bottom glass slide or other obstacles, in more detail. The experimental data presented in this chapter form the basis for several models introduced in the following chapters.

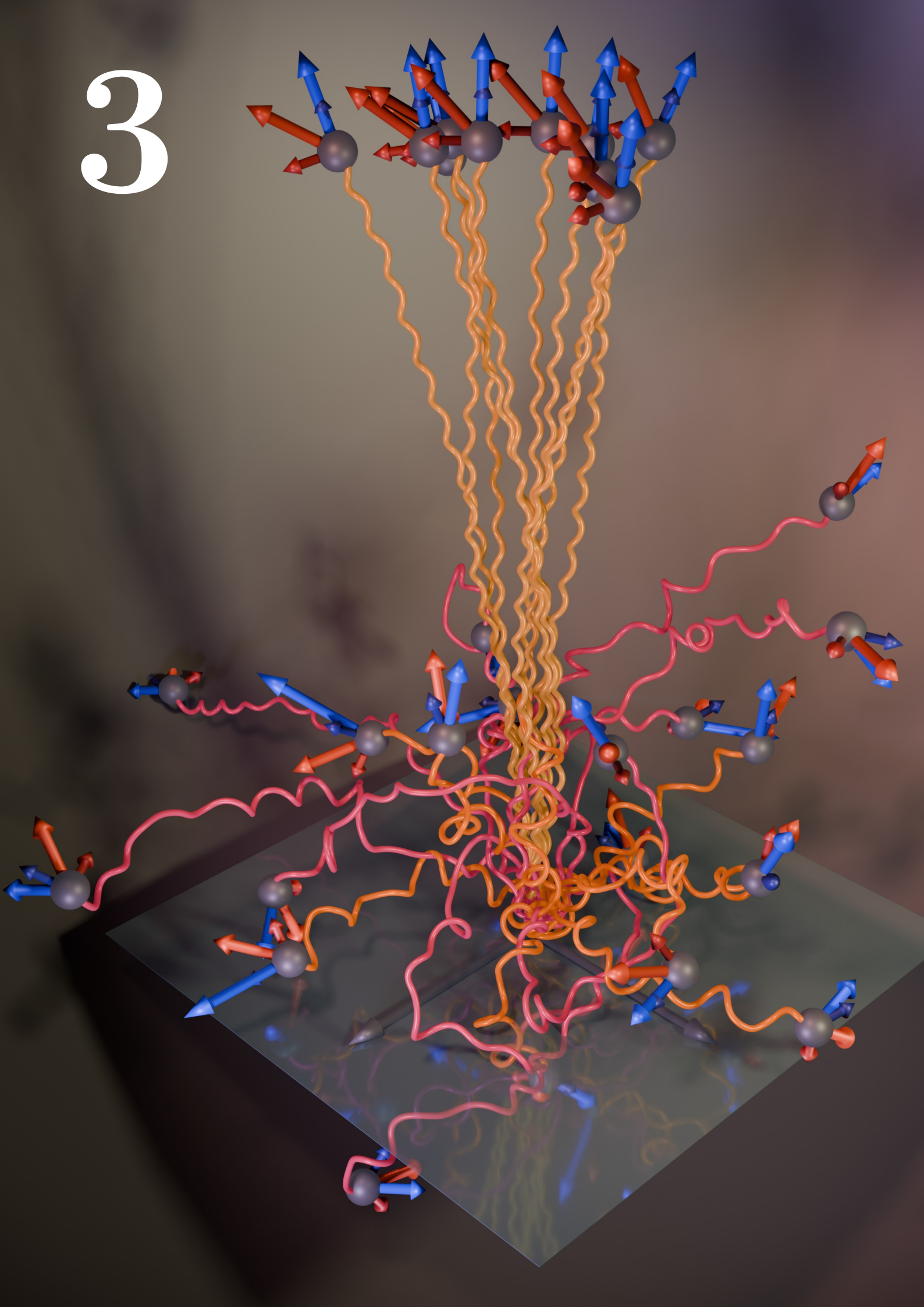
3

Chapter 3

Stochastic particle model for helical trajectories

This chapter is based on publication 2,
Lettermann et al., Physical Review Letters, 2025.

3.1 Context

The helical trajectories observed in the previous chapter are by no means a unique characteristic of malaria sporozoites. Quite the opposite, it is a common feature among motile microbes [147,148]. The survival of microbes like bacteria or algae is tightly connected to their ability to actively move, which is essential to seek out more favorable conditions, e.g., places which offer more nutrients or sunlight for photosynthesis [149, 150]. Although sometimes movement is collective, e.g., in biofilms or during swarming, at the heart of all migration processes is always the capability of single microbes to internally generate forces and torques [151–153]. The motion resulting from these forces often leads to helical trajectories. This includes not only the parasites discussed before, but also species of swimming bacteria [154, 155] and swimming algae [156–158]. In this chapter, we will introduce an active particle model that relates the persistence of helical trajectories, important for how efficiently a microbe explores its environment, to the internal stochastic properties of its motion machinery.

As described in Chapter 1, active particle models have been extensively used to describe in particular swimming microbes. However, most of these studies considered 2D cases, whereas helical motion of chiral active particles occurs in 3D [29]. If chiral active motion in 3D was analyzed theoretically, then mostly in the context of swimming. An early work on asymmetric swimmers in 3D considered the analogy to polymer models to extract new power laws for effective diffusion [159]; in general, the statistics of fluctuating helices is also an important aspect of helical biopolymers like DNA [160]. Previous work on

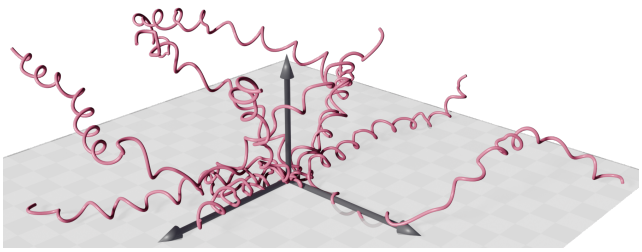

Figure 3.1: Trajectories of malaria parasites gliding through synthetic hydrogels, interpolated using a Fourier series fit.

sperm swimming considered stochasticity on the level of curvature and torsion and showed that helical trajectories are useful search strategies for chemotaxis in noisy environments [161, 162]. This line of work also considered colored noise in the form of a power spectrum [162]. One study of chiral motion in 3D started from the full mobility tensor for an arbitrarily shaped particle and showed that helical trajectories are the most likely outcome [163]. Similarly, a chiral active Brownian particle model has been used to describe the helical motion of colonial choanoflagellates and to show that purely stochastic propulsion can result in effective dispersion [164]. Very recently, it has been shown in a deterministic model for sperm swimming that an asymmetric beat of the flagellum leads to helical trajectories with high persistence [165]. Collectively, this body of work demonstrates that helical trajectories can have evolutionary advantages for microorganisms whose movement is subject to external noise.

Noise does not only arise from the interaction of the microorganisms with their environment, but also from the internal force generating processes, which might have a correlation time on the same scale as the movement that they generate [40]. To address this aspect of the system, Ornstein-Uhlenbeck (OU) processes have been used, usually replacing the body-fixed constant velocity with a noisy velocity performing an OU-process around a body-fixed average [166]. This naturally introduces a time scale to the noise and in the context of 2D swimmers in recent years has attracted substantial attention [167–174]. However, the approach of using an OU-process has not yet been explicitly extended to chiral particles in 3D, although the earlier work with the power spectrum also allows to address the effect of internal correlation times [162] (see below).

Here, we introduce a three-dimensional model which represents the noise in the generation of torque as an OU-process, similarly as suggested previously for 2D [40]. This introduces a finite correlation time, reflecting transient but slower additional processes in the torque-generation mechanism, in contrast to uncorrelated (white) Brownian noise.

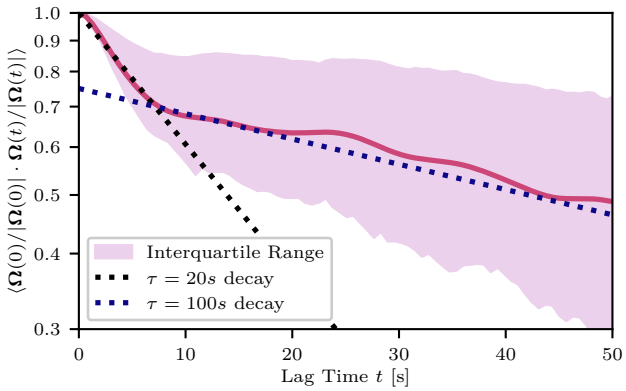

Figure 3.2: The autocorrelation of the normalized Darboux vector, $\langle \mathbf{\Omega}(0)/|\mathbf{\Omega}(0)| \cdot \mathbf{\Omega}(t)/|\mathbf{\Omega}(t)| \rangle$, as estimated from experimental trajectories, displays a decay of autocorrelation with a fast ($\tau = 20$ s) and a slow ($\tau = 100$ s) regime. The shaded area displays the 25-75% interquartile range and the solid line is the average.

3.2 Obtaining correlation times from measured trajectories

Utilizing our tracked motion of the malaria parasites through hydrogels (cf. Chapter 2), we can try to extract the persistence time not only of the trajectory itself, but also of the motor machinery. The experimentally observed sporozoites do not move at a constant speed, and even their average speed can vary between different parasites by a factor of 3. For the analysis in this chapter, we resampled the trajectories by fitting a Fourier series (similar to [113]) and assuming a constant speed of $1\,\mu\mathrm{m\,s}^{-1}$. In Fig. 3.1, 10 of these interpolated trajectories are shown. The motor machinery produces a forward force, but also a torque, yielding an angular velocity. Fluctuations in the force generation machinery will produce deviations of this torque, and hence changes in the angular velocity $\mathbf{\Omega}_{(t)}$ and its direction, which would be constant for a regular helix. To estimate the correlation time scale of the angular velocity, we can obtain the estimated vector $\mathbf{\Omega}_{(t)}$ from the trajectories as the Darboux vector of the Frenet frame, which can be derived from the fitted Fourier series. While the modulus shows a relatively noisy behavior, the direction decays on two clearly separated time scales as shown in Fig. 3.2. The large time scale of $\tau \approx 100$ s describes the decorrelation of the helical axis. Additionally, a second, shorter time scale is visible, as expected from the Ornstein-Uhlenbeck process (Gaussian white noise would lead to decay with only a single time scale). This short time scale of $\tau = 20$ s represents the time scale on which the axis of rotation of the internal force-generating apparatus fluctuates during motion.

We conclude that this case is best described by an OU-process. The internal

correlation time likely results from reorientation in the self-organized flow field of the adhesins on the parasite surface, which will be more closely analyzed in Chapter 4 and Chapter 5. But also for other systems, the internal motor machinery can become the most important source of noise, notably, for example, if systems get larger, like choanoflagellate colonies [164], or more powerful, as in sperm [165].

As we will demonstrate in the following, our 3D OU-model for chiral active particles can be treated analytically by suitably truncating a hierarchy of equations. We derive equations for the effective correlation time, the mean position and the mean squared displacement (MSD). Our main finding is that, in 3D, chirality and hence rotation can lead to enhanced effective persistence compared to non-rotating particles by an integrative effect of stochastic noise; a stabilization that can even lead to helical trajectories becoming "straighter than a straight line", i.e. allowing for larger long-time MSD compared to a particle moving with the same speed on a straight trajectory without rotation. A similar conclusion has been drawn before from computer simulations of swimming sperm [165]. This suggests that helical trajectories are favored for microorganisms that have to quickly move large distances through their environment. Finally we compare our model to experimental data from malaria parasites, demonstrating that it can describe the experimentally observed large MSD.

3.3 Model

Swimming and gliding microorganisms move in an overdamped fashion and therefore all internally generated forces and torques are immediately counterbalanced by drag, such that forces and torques can be replaced by translational and angular velocities, respectively. To model the intrinsic rotational noise, we consider an active particle that is moving with a body-fixed constant translational velocity $\mathbf{V}_0^{\text{body}}$. Its rotational velocity performs an OU-process around the body-fixed average, $\mathbf{\Omega}_0^{\text{body}}$. In the lab frame we use two vectors to track the orientation of the particle. $\mathbf{n}_1$ is the direction of the mean angular velocity $\mathbf{\Omega}_0$ and $\mathbf{n}_2 \perp \mathbf{n}_1$ is defined with the angle α between $\mathbf{\Omega}_0$ and $\mathbf{V}_0$ (see Fig. 3.3):

$$\mathbf{\Omega}_0 = \Omega_0 \mathbf{n}_1 \ , \qquad \mathbf{V}_0 = |\mathbf{V}_0| \left(\mathbf{n}_1 \cos\alpha + \mathbf{n}_2 \sin\alpha\right) \ . \tag{3.1}$$

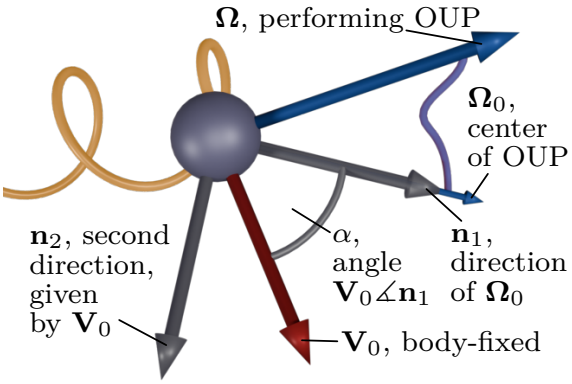

Figure 3.3: Model schematics. The translational velocity $\mathbf{V}_0$ is fixed in the body frame, but the angular velocity $\mathbf{\Omega}$ performs an Ornstein-Uhlenbeck process (OUP) centered around the body fixed $\mathbf{\Omega}_0$. The body coordinates are given by the vectors $\mathbf{n}_1$, the direction of the average angular velocity $\mathbf{\Omega}_0$, and $\mathbf{n}_2$, chosen such that $\mathbf{V}_0$ is in the plane spanned by $\mathbf{n}_1$,$\mathbf{n}_2$, with an angle of α between $\mathbf{V}_0$ and $\mathbf{n}_1$.

For simplicity, we set $|\mathbf{V}_0| = 1$ in the following. In the lab frame, the equations of motion are

$$\mathrm{d}\mathbf{\Omega} = -k\,(\mathbf{\Omega} - \Omega_0 \mathbf{n}_1)\,\mathrm{d}t + h\mathrm{d}\mathbf{\Lambda} \tag{3.2}$$

$$\mathrm{d}\mathbf{n}_1 = (\mathbf{\Omega} \times \mathbf{n}_1)\mathrm{d}t \tag{3.3}$$

$$\mathrm{d}\mathbf{n}_2 = (\mathbf{\Omega} \times \mathbf{n}_2)\mathrm{d}t \tag{3.4}$$

$$\mathrm{d}\mathbf{r} = (\cos(\alpha)\mathbf{n}_1 + \sin(\alpha)\mathbf{n}_2)\,\mathrm{d}t\,. \tag{3.5}$$

Here, k is the potential strength and h the noise amplitude of the OU-process. $\mathrm{d}\mathbf{\Lambda}$ is a 3D standard Wiener process. Note that noise is not multiplicative in the lab frame. Focusing on the intrinsic noise for simplicity, we disregard external noise (such as Brownian translational noise) or intrinsic noise in the translational velocity.

3.3.1 Rotation

The rotational part described by Eq. 3.2-3.3 is decoupled from the rest and can be solved first. The dynamical equations for the expectation values $\langle\mathbf{\Omega}\rangle$ and $\langle\mathbf{n}_1\rangle$ constitute an infinite hierarchy of expectation values of cross products of these two quantities, the first four being $\langle\mathbf{\Omega}\rangle$, $\langle\mathbf{n}_1\rangle$, $\langle\mathbf{\Omega} \times \mathbf{n}_1\rangle$ and $\langle\mathbf{\Omega} \times (\mathbf{\Omega} \times \mathbf{n}_1)\rangle$. We can apply moment closure to the higher order terms in the dynamic equation for $\langle\mathbf{\Omega} \times (\mathbf{\Omega} \times \mathbf{n}_1)\rangle$ to truncate this hierarchy.

The dynamic equations for the first four moments expanding the rotational

problem (Eq. 3.2-3.3) are

$$\mathrm{d}\langle\boldsymbol{\Omega}\rangle = -k\left(\langle\boldsymbol{\Omega}\rangle - \Omega_0\langle\mathbf{n}_1\rangle\right)\mathrm{d}t \tag{3.6}$$

$$\mathrm{d}\langle\mathbf{n}_1\rangle = \langle\boldsymbol{\Omega}\times\mathbf{n}_1\rangle\,\mathrm{d}t \tag{3.7}$$

$$\mathrm{d}\langle\boldsymbol{\Omega}\times\mathbf{n}_1\rangle = -k\langle\boldsymbol{\Omega}\times\mathbf{n}_1\rangle\,\mathrm{d}t + \langle\boldsymbol{\Omega}\times(\boldsymbol{\Omega}\times\mathbf{n}_1)\rangle\,\mathrm{d}t \tag{3.8}$$

and

$$\begin{aligned}\mathrm{d}\langle\boldsymbol{\Omega}\times(\boldsymbol{\Omega}\times\mathbf{n}_1)\rangle = &-2k\langle\boldsymbol{\Omega}\times(\boldsymbol{\Omega}\times\mathbf{n}_1)\rangle\,\mathrm{d}t\\ &+\langle\boldsymbol{\Omega}\times(\boldsymbol{\Omega}\times(\boldsymbol{\Omega}\times\mathbf{n}_1))\rangle\,\mathrm{d}t\\ &+k\Omega_0\langle\mathbf{n}_1\times(\boldsymbol{\Omega}\times\mathbf{n}_1)\rangle\,\mathrm{d}t\\ &+h^2\langle\mathrm{d}\boldsymbol{\Lambda}\times(\mathrm{d}\boldsymbol{\Lambda}\times\mathbf{n}_1)\rangle\ .\end{aligned}$$

To obtain an analytical solution, we apply moment closure by approximating the second and third term in this equation. The truncation cannot be performed earlier due to the necessity of retaining terms up to second order in Ω to properly account for the effect of noise. First, assuming $\langle\boldsymbol{\Omega}^2 A\rangle \approx \Omega_0^2\langle A\rangle$, we get for the second term $\langle\boldsymbol{\Omega}\times(\boldsymbol{\Omega}\times(\boldsymbol{\Omega}\times\mathbf{n}_1))\rangle \approx -\Omega_0^2\langle\boldsymbol{\Omega}\times\mathbf{n}_1\rangle$. For the third term, upon replacing $\boldsymbol{\Omega}$ with $\boldsymbol{\Omega}^\perp$, its component perpendicular to $\mathbf{n}_1$, the relevant contribution for the cross product, and applying similar logic as before but with $|\mathbf{n}_1| = 1$, we get $\langle\mathbf{n}_1\times(\boldsymbol{\Omega}\times\mathbf{n}_1)\rangle = \left\langle\boldsymbol{\Omega}^\perp\right\rangle = \langle\boldsymbol{\Omega} - (\boldsymbol{\Omega}\cdot\mathbf{n}_1)\mathbf{n}_1\rangle \approx \langle\boldsymbol{\Omega}\rangle - \Omega_0\langle\mathbf{n}_1\rangle$. For the last approximation, we assumed that the variance of the OU-process is small, such that $\boldsymbol{\Omega}$ stays close to its average $\Omega_0\mathbf{n}_1$. The noise term can be explicitly computed, and we can close the hierarchy by rewriting its fourth equation as

$$\begin{aligned}\mathrm{d}\langle\boldsymbol{\Omega}\times(\boldsymbol{\Omega}\times\mathbf{n}_1)\rangle = &-2k\langle\boldsymbol{\Omega}\times(\boldsymbol{\Omega}\times\mathbf{n}_1)\rangle\,\mathrm{d}t\\ &-\Omega_0^2\langle\boldsymbol{\Omega}\times\mathbf{n}_1\rangle\,\mathrm{d}t + k\Omega_0\left(\langle\boldsymbol{\Omega}\rangle - \Omega_0\langle\mathbf{n}_1\rangle\right)\mathrm{d}t - 2h^2\langle\mathbf{n}_1\rangle\,\mathrm{d}t.\end{aligned} \tag{3.9}$$

In numerical simulations, we can verify that our truncation works quite well, as shown in Fig. 3.4

By rotational symmetry, only the component singled out by the initially parallel $\boldsymbol{\Omega}$ and $\mathbf{n}_1$ axes is relevant (as the rotational problem is independent of $\mathbf{n}_2$), and the other two components of each vector vanish upon averaging (we choose this direction to be z). Hence, the truncated system defines a four-dimensional, linear, homogeneous ordinary differential equation problem, which we can analyze by its eigenvalues.

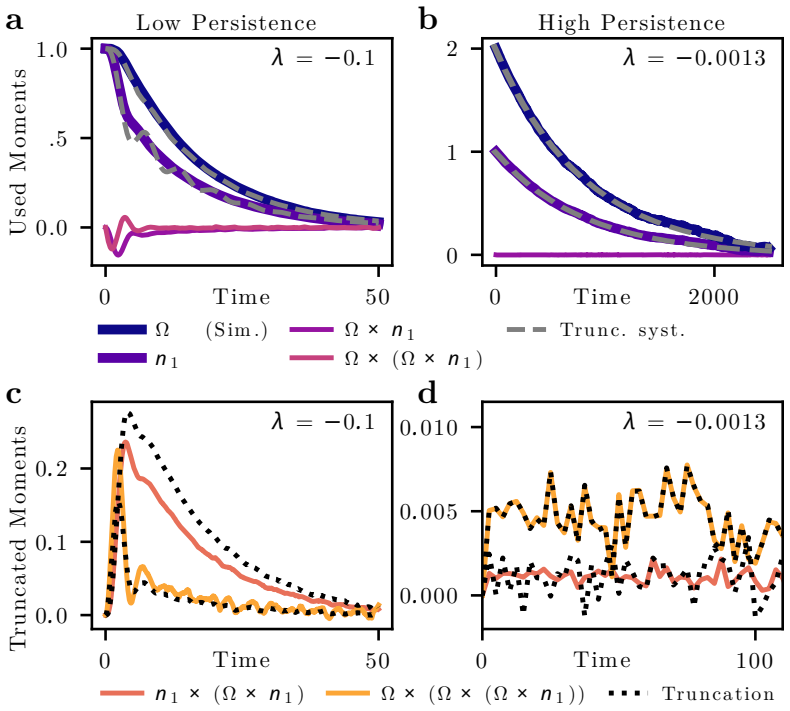

Figure 3.4: **a**: Time course of different moments obtained by averaging numerical simulation (Eq. 3.2-3.5) in comparison with numerical solution of the truncated system (Eq. 3.6-3.9, gray dashed lines) Parameter values: potential strength $k = 0.2$, noise amplitude $h = 0.3$, angular speed $\Omega_0 = 1$, angle $\alpha = \pi/6$. **b**: Same as a, but now for $k = 2$, $h = 0.1$ and $\Omega_0 = 2$, i.e. much reduced noise and faster turning. Here, the agreement between simulations and theory is even better. **c**: The truncated moments and the approximation used for truncation in Eq. 3.9. **d**: Same as c at parameters from b. Here, the truncated moments are already very small, and even at 20000 simulations the averages have not yet completely converged. Nonetheless, it is apparent that the approximations used for truncation work well.

The mode relevant for the long-time behavior can be identified as the unique mode with real eigenvalue and parallel $\langle \mathbf{\Omega} \rangle$ and $\langle \mathbf{n}_1 \rangle$, which describes the decorrelation of $\langle \mathbf{\Omega} \rangle$ from its initial orientation. The other eigenvalues describe the unstable state where $\mathbf{\Omega}$, $\mathbf{n}_1$ are antiparallel, and oscillatory states, all of which decay more quickly. The relevant eigenvalue can be computed exactly, but is cumbersome as a solution of a fourth-order polynomial. Expanding for small k/Ω_0, i.e., assuming the rotation is faster than the time scale on which the OUP returns to its average, we get the approximation

$$\lambda = -\frac{h^2 + \Omega_0^2 k + k^3 - \sqrt{k^2 \left(\Omega_0^2 + k^2\right)^2 - h^4}}{\Omega_0^2 + k^2} \tag{3.10}$$

which describes the decay as $\langle \mathbf{\Omega} \rangle = (0, 0, \Omega_0) \exp(\lambda t)$ and $\langle \mathbf{n}_1 \rangle = (0, 0, 1) \exp(\lambda t)$. The more negative λ, the faster $\mathbf{\Omega}$ and $\mathbf{n}_1$ decorrelate from their initial orientation. For fixed noise amplitude h, both decreasing the strength k of the OUP potential and decreasing angular speed Ω_0 lead to faster decorrelation, suggesting that the rotation has a stabilizing effect. In the limits of vanishing noise, diverging potential strength or diverging angular speed, the time scale of decorrelation diverges. In the limit of small noise amplitude, λ converges to the power spectrum of the OU-process evaluated at the angular speed, consistent with a derivation starting from power spectra ([162], Section 3.5).

The truncation presented above breaks down for $\Omega_0 = 0$, because the equation for $\mathbf{\Omega}$ decouples from the rest, and $\langle \mathbf{\Omega} \rangle$ is dominated by the mean squared displacement (MSD) of the OUP instead of Ω_0. However, in the limit of small noise ($h^2 \ll k^3$), the previously derived eigenvalue (Eq. 3.10) has a well-defined limit

$$\lambda\Big|_{\Omega_0=0} \approx -\frac{h^2}{k^2} \,. \tag{3.11}$$

Following through the previous derivation of Eq. 3.9 for the case of $\Omega_0 = 0$, and truncating $\langle \mathbf{\Omega} \times (\mathbf{\Omega} \times (\mathbf{\Omega} \times \mathbf{n}_1)) \rangle \approx -h^2/(2k) \langle \mathbf{\Omega} \times \mathbf{n}_1 \rangle$, using the MSD of the OUP instead of Ω_0^2, we find the same result. Therefore, even if the original derivation is not valid, the eigenvalue as written correctly includes the $\Omega_0 \to 0$ limiting case. This is also confirmed by the numerical simulations for the $\Omega_0 = 0$ case in Fig. 3.6.

To validate our approximations, we compared the solutions against numerical simulations of the initial model, i.e. Eq. 3.2-3.5, implemented in JAX [175] using standard solvers for stochastic differential equations, set up in diffrax [176], code available at `https://github.com/LeonLettermann/3D-Chiral-OUP`. In Fig. 3.5, different expectation values obtained from averaging 20000 numerical simulations are compared with (i) the numerically solved truncated ODE system (Eq. 3.6-3.9, dashed gray) and (ii) the analytical exponential decay given by the dominant eigenvalue λ. As shown in Fig. 3.5a, larger noise yielding faster decorrelation produces larger values of the higher order expectation values. We find that the truncations are qualitatively correct (Fig. 3.4), while quantitative differences are visible – the numerical solution of the truncated system shows some additional oscillations. The exponential decay by λ is too fast here, which signifies that during the relatively rapid decay, additional modes are relevant. For lower noise, in Fig. 3.5b we see excellent agreement between numerical simulation, numerical solution of the truncated system, and the exponential decay given by λ from Eq. 3.10. The latter decay completely dictates the

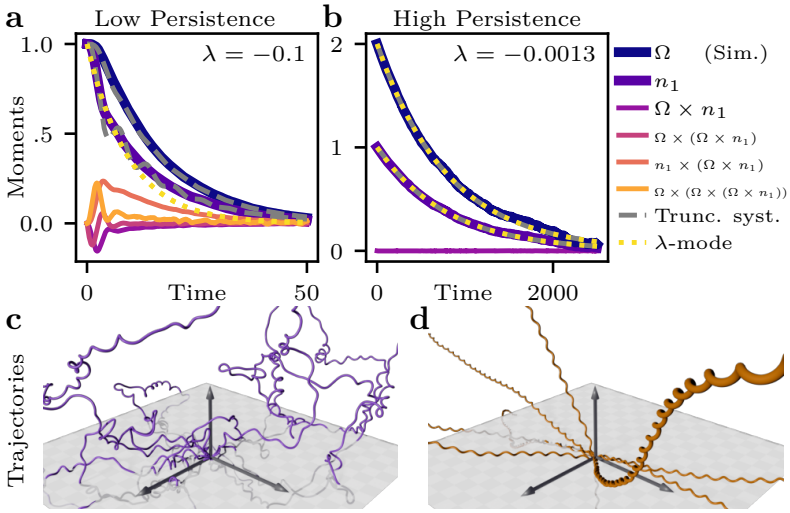

Figure 3.5: **a**: Same as Fig. 3.4, with analytical approximation predicting exponential decay with eigenvalue λ (Eq. 3.10, yellow dotted lines). Parameter values: potential strength $k = 0.2$, noise amplitude $h = 0.3$, angular speed $\Omega_0 = 1$, angle $\alpha = \pi/6$. **b**: Same as a, but now for $k = 2$, $h = 0.1$ and $\Omega_0 = 2$, i.e. much reduced noise and faster turning. Here, the agreement between simulations and theory is even better. **c**: Simulated trajectories at parameters from a. **d**: Simulated trajectories at parameters from b. The reduced noise leads to more regular trajectories.

persistence in the resulting motion, as also apparent in the resulting trajectories illustrated in Fig. 3.5c+d. Generally, lower decorrelation can be reached by lower noise amplitude h, stronger Ornstein-Uhlenbeck potential k, or higher angular speed Ω_0.

3.3.2 Translation

For the analytical treatment of the translational part, we assume that initially $\mathbf{\Omega} = \Omega_0 \mathbf{n}_1$ is in z direction. The solution of the rotational part then allows to solve Eq. 3.5 for the motion in z, $\mathrm{d}\langle z \rangle = \cos(\alpha)\langle \mathbf{n}_1 \rangle$. To obtain the MSD and the remaining coordinate, we need an expression for $\langle \mathbf{n}_2 \rangle$. By construction, $\mathbf{n}_2 \perp \mathbf{n}_1$, so $\mathbf{n}_2$ is rotating in the plane perpendicular to $\mathbf{n}_1$ with angular frequency Ω_0, which is on average the x-y-plane. We assume that $\mathbf{n}_2$ initially points in x-direction. The decorrelation of $\mathbf{n}_1$ is also decorrelating the plane in which $\mathbf{n}_2$ rotates, but the latter additionally decorrelates within the plane by variations of the magnitude of the rotational velocity. Both effects are caused by $\mathbf{\Omega}$ deviating from $\mathbf{\Omega}_0$, the tilting of the plane by deviations perpendicular to $\mathbf{\Omega}_0$, and in-plane deviations by parallel components. Because of this additional

effect, we obtain a twofold faster decorrelation of $\langle \mathbf{n}_2 \rangle$ compared to $\langle \mathbf{n}_1 \rangle$ (see Appendix A.6),

$$\langle \mathbf{n}_2 \rangle = \Big(\cos \Omega_0 t, \sin \Omega_0 t, 0 \Big) \, e^{2\lambda t} \ . \tag{3.12}$$

The MSD can now be obtained by first computing it from the formal solution and inserting the solutions obtained for $\langle \mathbf{n}_1 \rangle$ and $\langle \mathbf{n}_2 \rangle$. Starting with the formal solution

$$\mathbf{r}_{(t)} = \int_0^t \mathrm{d}t \left(\cos(\alpha) \mathbf{n}_1 + \sin(\alpha) \mathbf{n}_2 \right) \ , \tag{3.13}$$

this yields

$$\begin{aligned} \left\langle \mathbf{r}_{(t)}^2 \right\rangle = \int_0^t \mathrm{d}s_1 \int_0^t \mathrm{d}s_2 \Big(& \cos^2(\alpha) \left\langle \mathbf{n}_1(s_1) \cdot \mathbf{n}_1(s_2) \right\rangle \\ & + \sin^2(\alpha) \left\langle \mathbf{n}_2(s_1) \cdot \mathbf{n}_2(s_2) \right\rangle \Big) \ , \end{aligned} \tag{3.14}$$

where the mixed terms vanish, as due to their perpendicularity and the rotational symmetry the expectation value of their scalar products has to be zero even if evaluated at different times. The remaining correlation functions can be directly obtained from the solutions obtained for $\langle \mathbf{n}_1 \rangle$ and $\langle \mathbf{n}_2 \rangle$ as

$$\langle \mathbf{n}_1(s_1) \cdot \mathbf{n}_1(s_2) \rangle = e^{\lambda |s_1 - s_2|} \ , \tag{3.15}$$

$$\langle \mathbf{n}_2(s_1) \cdot \mathbf{n}_2(s_2) \rangle = \cos(\Omega_0 |s_1 - s_2|) e^{2\lambda |s_1 - s_2|} \ , \tag{3.16}$$

such that we finally compute the MSD by simple integration, resulting in (except for the degenerate case $\Omega_0 = 0$ and $\alpha > 0$):

$$\begin{aligned} \left\langle \mathbf{r}_{(t)}^2 \right\rangle = & \frac{2\cos^2(\alpha) \left(-\lambda t + e^{\lambda t} - 1 \right)}{\lambda^2} \\ & + \frac{2\sin^2(\alpha)}{\left(4\lambda^2 + \Omega_0^2\right)^2} \Big[-4\lambda^2 + \Omega_0^2 - 2\lambda \left(4\lambda^2 + \Omega_0^2 \right) t \\ & + \left(4\lambda^2 - \Omega_0^2 \right) e^{2\lambda t} \cos(\Omega_0 t) + 4\lambda \Omega_0 e^{2\lambda t} \sin(\Omega_0 t) \Big] \ . \end{aligned} \tag{3.17}$$

Let us consider two limiting cases. First, for $\alpha = 0$, corresponding to a particle rotating while traveling in average on a straight line, we obtain

$$\left\langle \mathbf{r}_{(t)}^2 \right\rangle = -\frac{2}{\lambda} t - \frac{2}{\lambda^2} \left(1 - e^{\lambda t} \right) \ , \tag{3.18}$$

which recovers the case of an active Brownian particle (see Section 3.5, note $\lambda < 0$). Second, for general α in the limit of large t, we can approximate $\left\langle \mathbf{r}_{(t)}^2 \right\rangle \approx 6 D_\infty t$, where we obtain the effective diffusion constant describing the

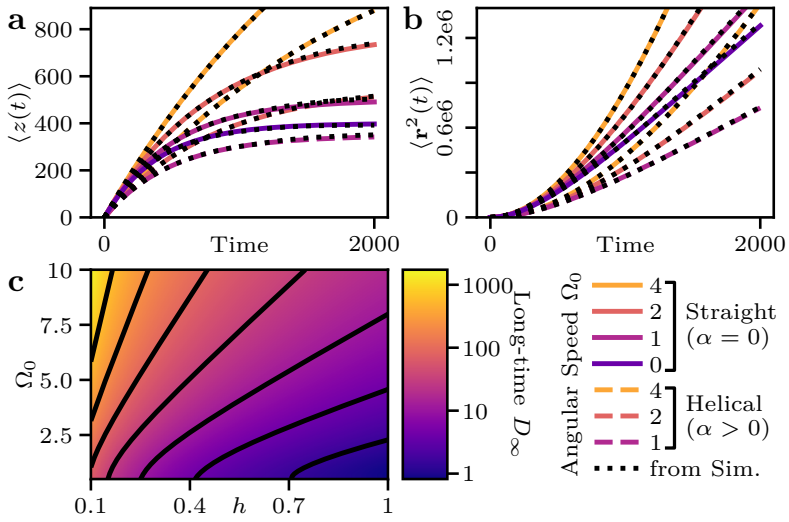

Figure 3.6: **a**: Mean distance traveled in z-direction (the initial orientation of the helical axis) for different Ω_0 at $k = 2$, $h = 0.1$. Full lines show particles moving straight while turning (α=0), dashed lines particles on helical trajectories (α=$\pi/4$), which can be seen overtaking slower turning straight particles. Colored and black lines are theoretical and numerical, respectively, and in very good agreement. **b**: Mean squared displacement for the same parameters as shown in a, theoretical results from Eq. 3.17 in color. **c**: Effective long-time diffusion constant D_∞, cf. Eq. 3.19, as a function of noise amplitude h and angular speed Ω_0. Black lines mark contours of constant D_∞.

long time behavior as

$$D_\infty = -\frac{\lambda}{3}\left(\frac{\cos^2(\alpha)}{\lambda^2} + \frac{2\sin^2(\alpha)}{(4\lambda^2+\Omega_0^2)}\right) . \tag{3.19}$$

In the case $\lambda^2 \ll \Omega_0^2$, meaning small noise leading to a decay time much longer than the rotation period, and $\alpha < \pi/2$, i.e. the particle not just circling, but having some average net movement, this reduces to $D_\infty \approx -\cos^2(\alpha)/(3\lambda)$.

Lastly, with Eq. 3.12 we compute $\langle x\rangle$ and $\langle y\rangle$ by integrating $\mathrm{d}\langle x\rangle = \sin(\alpha)\langle \mathbf{n}_2\rangle_x \,\mathrm{d}t$, allowing to obtain the expectation value of the trajectory,

$$\left\langle \mathbf{r}_{(t)} \right\rangle = \begin{pmatrix} \sin(\alpha)\frac{e^{2\lambda t}(2\lambda\cos(\Omega_0 t)+\Omega_0\sin(\Omega_0 t))-2\lambda}{4\lambda^2+\Omega_0^2} \\ \sin(\alpha)\frac{e^{2\lambda t}(2\lambda\sin(\Omega_0 t)-\Omega_0\cos(\Omega_0 t))+\Omega_0}{4\lambda^2+\Omega_0^2} \\ \frac{\cos(\alpha)}{\lambda}\left(e^{\lambda t}-1\right) \end{pmatrix} , \tag{3.20}$$

which is a logarithmic spiral on a radical surface, i.e. $z \propto \sqrt{r}$.

3.4 Results

The derived solutions show that increasing rotation Ω_0 stabilizes the particle against its intrinsic noise. In Fig. 3.6a and b we plot the mean z-position and the MSD, respectively, which both increase with increasing angular speed. In both cases we find that the numerical simulations agree well with the analytical results, cf. the third component of Eq. 3.20 and Eq. 3.17. The plots show that if the particle travels on a helix (case $\alpha = \pi/4$, cf. dashed lines in Fig. 3.6a,b) with the same speed as a non-rotating particle traveling in a straight fashion, if it turns sufficiently fast (i.e. if the helix is sufficiently tightly wound) it travels further from the origin on average at large time scales. Therefore a helical trajectory can be "straighter than a straight line".

The long time behavior is described by the effective diffusion constant Eq. 3.19, which has a complicated dependence on Ω_0, k and h through λ. In Fig. 3.6c we see that at constant OU potential strength k, D_∞ increases with higher angular speed Ω_0, as this suppresses deviations of the helical axis, different from what was found for chiral active Brownian particles without the OU-process [164] (see Section 3.5). This effect becomes more pronounced for higher noise amplitude h, i.e. at higher noise, the stabilizing effect of rotation is more pronounced. Increasing effective diffusion by introducing rotation or equivalently chirality is strikingly different from known examples. In 2D, chirality reduces long-time diffusion by enforcing circular turning [36, 177]. Similarly, a 3D active Brownian particle with external torque exhibits reduced long-time diffusion [29].

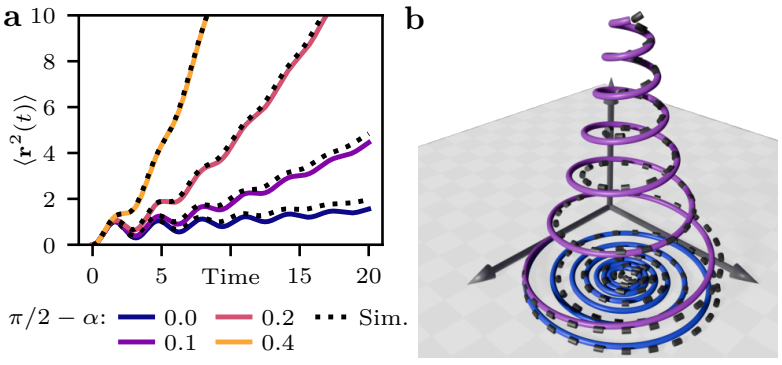

Figure 3.7: **a**: Mean squared displacement for α close to $\pi/2$, such that the particles are close to describing circles, with $k = 1$, $h = 0.5$, $\Omega_0 = 2$. Black dotted lines are averages from numerical simulations. **b**: Theoretical expectation value of trajectories (Eq. 3.20) for the two lower values of $\pi/2 - \alpha$.

We can also study the short time behavior. Fig. 3.7a shows that at short

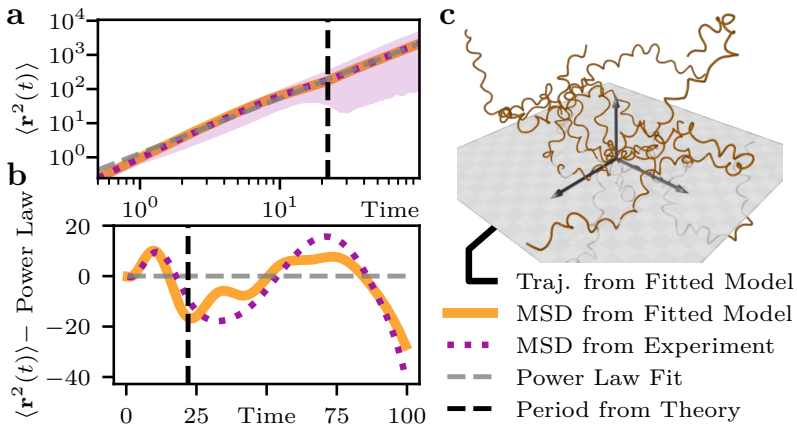

Figure 3.8: **a**: Log-log plot of the mean squared displacement extracted from observed malaria parasite trajectories as shown in Fig. 3.1 (purple, dotted), with 5th and 95th percentiles (purple, shaded) and the fitted model (orange). The gray dashed line is a fitted power law. **b**: Deviation from fitted power law. The vertical dashed line marks one period of rotation as extracted from the fitted model. **c**: Trajectories simulated with parameters obtained from MSD fit resembling Fig. 3.1.

times, the MSD of a helix grows slower, because it is curving back onto itself, depending on the pitch of the helix defined by the angle α. For $\alpha = \pi/2$, the MSD shows strong oscillations, as the mean position, see Fig. 3.7b, describes a planar inward spiral due to the influence of noise that diverts it from the circle of a noise-free particle. For smaller α, the spiral gets the 3D structure of a logarithmic spiral on a radical surface as found in Eq. 3.20, with both cases showing good agreement between the numerical and analytical results (a similar spiral was found numerically in [163] for active Brownian particles with torque, see Section 3.5).

Finally, we can use our measured trajectories for malaria parasites in hydrogels to extract their MSD (Fig. 3.8a, averaged from 140 trajectories) and fit it with our model prediction of Eq. 3.17, similar to what has been done before in 2D-projections for choanoflagellate colonies [164]. In general, we find good agreement. Our theory successfully describes the first two extrema in the deviation of the MSD from a power law (Fig. 3.8b), corresponding to the first turn of the helix. Our theory also predicts some effects of second and third turns visible in the MSD deviation, which are not observable in the experimental data, most likely because the biological population has a distribution of helical pitches and radii such that the later turns cannot be resolved in the average. From the fitted model parameters (Tab. 3.1), we can derive estimates for pitch and radius of the helical trajectories as 13.2 µm and 2.8 µm, respectively, well

Parameter	Ω_0	α	k	h
Fit Result	0.285 1/s	0.926	1.078 1/s	0.154 $1/s^{3/2}$

Table 3.1: Results for fitting the model to the MSD computed from experimentally observed and resampled trajectories of malaria parasites.

within the observed range [116]. We note in passing that a phenomenological fit of the period as the period in the MSD-deviation would yield incorrect results for the oscillation period. Trajectories simulated with the fitted parameters (Fig. 3.8c) visually resemble the observed trajectories from Fig. 3.1.

It is notably smaller than the time scale $1/k$ as extracted from the MSD fit, which would give the time scale of decay for the full $\mathbf{\Omega}$ in the OUP if $\mathbf{n}_1$ would be fixed. Note, however, that the direction of angular velocity $\mathbf{\Omega}/|\mathbf{\Omega}|$ relative to the moving center of the OUP follows a more complicated decay law. Additionally, it is likely that for the malaria parasite the assumed isotropy of the OUP is not exactly true, and the magnitude of the angular velocity fluctuates faster then the direction.

3.5 Comparison with related models

To better understand the properties of the model we introduce here, in the following we will define some related models and compare them to the chiral OUP.

Active Brownian particles (ABPs) are the most common active particle model, and are usually written down with a translational and rotational noise, the latter given by a rotational diffusion D_Ω [21, 29]. Disregarding the translational noise (to compare to our approach), the MSD in 3D reads

$$\left\langle \mathbf{r}^2_{(t)} \right\rangle = \frac{V_0^2}{D_\Omega} t - \frac{V_0^2}{2D_\Omega^2} \left(1 - e^{-2D_\Omega t}\right) \tag{3.21}$$

which reproduces the $\alpha = 0$ limit from Eq. 3.18 with $\lambda = -2D_\Omega$.

Worm-like chain (WLC) models [178, 179] describe the configuration of a fixed-length polymer with a given persistence length. Replacing the total length with the traveled distance (using a velocity V_0), and writing a persistence time $\tau = P/V_0$ instead of the persistence length P we recover the MSD of the ABP above, where $\tau = -1/\lambda = 2/D_\Omega$.

The ABP or WLC model can describe the MSD of our theory for $\alpha = 0$, but deviate for the true helical case ($\alpha > 0$). This is apparent for the long

time limit, where Eq. 3.21 yields (scaling V_0 with $\cos\alpha$) $D_\infty^{\mathrm{ABP}} = \cos^2(\alpha) D_\Omega$, i.e. these theories do not include the translation generated by the imperfect circular motion in the plane perpendicular to the helix, which is relevant for larger α as seen from Fig. 3.9a.

Chiral active Brownian particles as discussed in [164] include this effect. Rewriting the long-time diffusion from their work by replacing the velocities $v_p = \cos\alpha$ and $v_\omega = \sin\alpha$ it reads (Eq. 4 in [164])

$$D_\infty^{\mathrm{cABP}} = \frac{\cos^2(\alpha)}{4D_\Omega} + \frac{\sin^2(\alpha) D_\Omega}{4} \left(\frac{1}{9D_\Omega^2 + \Omega_0^2} + \frac{2}{4D_\Omega^2 + \Omega_0^2} \right), \tag{3.22}$$

which has a similar form as our Eq. 3.19, but considers a 2D projection of the 3D problem because their experiments imaged 2D projections. However, it decreases monotonically with increasing Ω_0. Hence, importantly, the stabilizing influence of rotation as observed in our model is not present, as expected because their rotational noise is classical rotational diffusion (external, white noise); thus, the rotation cannot act to integrate out part of the noise.

Arbitrarily shaped active Brownian particles were studied in 3D in [163] by starting from the full 6x6 diffusion tensor and subsequently analyzing its symmetry properties dependent on the shape's symmetry. For an orthotropic particle (i.e., possessing three pairwise orthogonal planes of symmetry) and in the absence of noise they analytically solved the resulting helical trajectory as a function of active force, torque, and shape-dependent drag of the particle.

By numerical simulations including noise they found the expectation value of many stochastic helical trajectories as an exponentially damped helix, or a concho-spiral, as found here analytically in Eq. 3.20. They fitted two exponential decay scales, $\gamma_1 = 0.04$ and $\gamma_2 = 0.06$ describing the decay of radius and decay in axial direction respectively. Interestingly, identifying these for the Ornstein-Uhlenbeck particle presented here, we find $\gamma_1 = -2\lambda$ and $\gamma_2 = -\lambda$, and in particular $\gamma_1 > \gamma_2$, meaning faster radial than axial decay. This might be caused by the difference of Brownian to Ornstein-Uhlenbeck particle, or by the particular diffusion tensor used to obtain this result in [163].

In a related manner to the shape dependence one could study direction-dependent internal noise in the OUP, by exchanging h and k with 3x3 tensors, describing different noise strengths in different directions in the body frame and necessarily being appropriately rotated to the lab frame. This would allow, for example, different behavior in the magnitude and orientation of the angular velocity, as discussed for the experimental data above. Because this would

introduce multiplicative noise, similarly to [163] an analytical solution would be challenging and likely only possible in certain special cases.

Stochastic trajectory models have been proposed in [161,162] to describe helical swimming and chemotaxis of sperm cells. There, the curvature $\kappa_{(t)}$ and torsion $\tau_{(t)}$ are the main properties of interest, and modeled including stochastic influences of arbitrary, possibly correlated noise. Although in these references Gaussian white noise is used in their explicit solutions, it is possible to approximately solve our OU model in their framework. Rewriting our model with (in the body-frame) fixed, unit-length velocity $\mathbf{V}_0$ and dynamic angular velocity $\mathbf{\Omega}_{(t)} = \Omega_0 \mathbf{n}_1 + \omega_{(t)}$, with ω a 3D Ornstein-Uhlenbeck process centered around 0, curvature and torsion at time t are given as

$$\kappa_{(t)} = \left\| \mathbf{\Omega}_{(t)} \times \mathbf{V}_0 \right\| = \left\| \Omega_0 \sin\alpha \mathbf{n}_3 + \omega_{(t)} \times \mathbf{V}_0 \right\| \tag{3.23}$$

$$\tau_{(t)} = \mathbf{\Omega}_{(t)} \cdot \mathbf{V}_0 = \Omega_0 \sin\alpha + \omega_{(t)} \cdot \mathbf{V}_0 \tag{3.24}$$

We can then decompose the 3D OUP $\omega_{(t)}$ into two independent 1D processes, $\omega^{\parallel}_{(t)}$ parallel to $\mathbf{V}_0$, and $\omega^{\perp}_{(t)}$ perpendicular to both $\mathbf{V}_0$ and $\mathbf{n}_3$. The latter is one of two directions relevant for the curvature, but the leading-order contribution. Expanding the norm we find

$$\kappa_{(t)} = \Omega_0 \sin\alpha + \omega^{\perp}_{(t)} \ , \qquad \tau_{(t)} = \Omega_0 \cos\alpha + \omega^{\parallel}_{(t)} \ . \tag{3.25}$$

Hence, in leading order we find both the curvature and the torsion being subject to independent Ornstein-Uhlenbeck noises. Using the power spectrum of the OUP [180], we can evaluate the combined power spectrum of curvature and torsion noise ($\tilde{S}_2(\omega)$ in [162]), as its value at Ω_0 is proportional to the rotational diffusion of the helical centerline (Eq. (4) in [162]):

$$\tilde{S}_2(\Omega_0) = \frac{h^2}{k^2 + \Omega_0^2} \tag{3.26}$$

Therefore, we recover the power spectrum of an Ornstein-Uhlenbeck process. Furthermore, this result is (up to sign) identical to a low noise expansion $h \ll 1$

of the eigenvalue λ found in Eq. 3.10:

$$\begin{aligned}\lim_{h\to 0}\lambda &= \lim_{h\to 0} -\frac{h^2+\Omega_0^2 k+k^3-\sqrt{k^2\left(\Omega_0^2+k^2\right)^2-h^4}}{\Omega_0^2+k^2}\\ &= -\frac{h^2+\Omega_0^2 k+k^3-k\left(\Omega_0^2+k^2\right)-\mathcal{O}\left(h^4\right)}{\Omega_0^2+k^2}\\ &= -\frac{h^2}{\Omega_0^2+k^2}+\mathcal{O}\left(h^4\right)\end{aligned}$$

Thus, we can (to leading order) recover our results for the orientation decorrelation (or equivalently the persistence of the helix center line) from the moment closure procedure by solving our model with the approach from [162].

Limit of OUP as Gaussian White Noise and direct comparison. For a direct comparison of the long time diffusion dependency on the angular speed Ω_0 between the different models, we first look at the Brownian-like limit of the OUP, that is taking $k\to\infty$ and $h\to\infty$ simultaneously, while keeping the variance $\sigma^2=\frac{h^2}{2k}$ constant. This leads to vanishing correlation time $1/k$ of the Ornstein-Uhlenbeck process, and subsequently $\mathbf{\Omega}$ as a random variable becomes Gaussian white noise, around its center $\Omega_0\mathbf{n}_1$ with fixed variance and delta-peak time correlation (see [181]),

$$\begin{aligned}\mathbf{\Omega}_{(t)} &\sim \mathcal{N}\left(\Omega_0\mathbf{n}_1(t),\sigma^2\right)\\ \left\langle\left(\mathbf{\Omega}_{(t)}-\Omega_0\mathbf{n}_1(t)\right)_i\left(\mathbf{\Omega}_{(s)}-\Omega_0\mathbf{n}_1(s)\right)_j\right\rangle &= \delta_{ij}\delta_{(t-s)}\ .\end{aligned}$$

This means $\mathbf{\Omega}$ becomes a non-continuous process, which can be understood as a derivative of Brownian motion as its rescaled integral

$$\mathbf{\Theta}_{(t)}=\frac{1}{\sqrt{k}}\int_0^{kt}\mathbf{\Omega}_{(t)}=\sigma_*\mathcal{B}_t,\quad \sigma_*^2=2\sigma^2$$

recovers Brownian motion $\mathcal{B}_t$ [182], where the rescaling is necessary, as otherwise the variance of the integral vanishes for $k\to\infty$. The resulting system is hence different from a Brownian particle where the angle/orientation performs Brownian motion, but using the rescaling we can identify it with Brownian motion of the orientation with variance $2\sigma^2$.

Utilizing this identification, we can derive the effective long time diffusion D_∞ equivalent to Eq. 3.19 for the different models discussed above. For the

classic ABP, we obtain

$$D_\infty^{\mathrm{ABP}} = \frac{V_0^2}{6D_\Omega} \quad \text{with} \quad D_\Omega = \sigma^2 = \frac{h^2}{2k} \,,$$

where V_0 is either 1, the particle velocity, or $V_{\mathrm{CL}} = \cos\alpha$, the effective velocity along the centerline.

For the chiral ABP from [164] we take D_∞^{cABP} given in Eq. 3.22, rescaled by $\frac{4}{6}$ to get effective 3D instead of 2D diffusion and also utilizing the same estimated D_Ω as above.

Lastly, for the stochastic trajectory model from [162] with the decorrelation time for the OUP obtained from the power spectrum in Eq. 3.26, we take the ABP again but estimate D_Ω based on the persistence time obtained from the power spectrum as

$$D_\infty^{\mathrm{St.Traj.}} = \frac{V_0^2}{6D_\Omega} \quad \text{with} \quad D_\Omega = 2\frac{\tilde{S}_2(\Omega_0)}{4} = \frac{h^2}{2(k^2+\Omega_0^2)} \,.$$

Fig. 3.9b displays these different results compared to D_∞ for the chiral OUP (Eq. 3.19). The solution for the chiral OUP has a minimum at low (but non-zero) angular speed, which agrees with the estimated behavior of the ABP based on the effective velocity of the helix center line. If the angular speed is approaching zero, both the chiral OUP and the chiral ABP capture that the effective long-time diffusion increases: the chirality is hindering the diffusivity, and reducing it makes both solutions approach the ABP solution with the particle velocity V_0. Towards higher angular speeds, the chiral OUP as well as the stochastic trajectory model for the OUP capture the increase in persistence due to the rotation, and agree well for these parameters. The stochastic trajectory model describes only the center line, and hence misses the increase of persistence with low angular speed, as this description breaks down. Additionally, if the helix is at low pitch, i.e., α close to $\pi/2$, inaccurate circling contributes to the MSD in addition to the motion of the helix center line, such that the stochastic trajectory model underestimates the MSD for those cases (Dotted lines in Fig. 3.9a), while still more accurate than the straightforward ABP estimate.

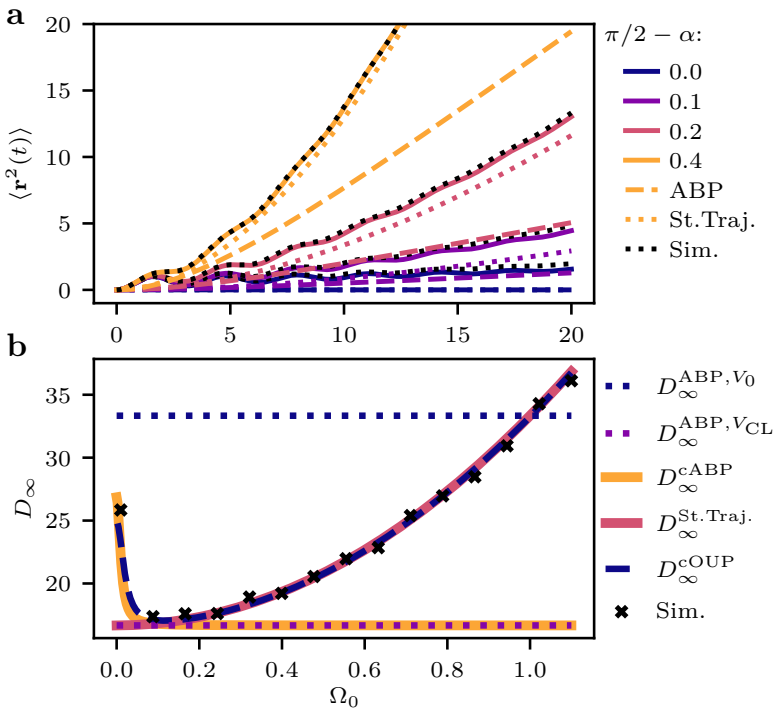

Figure 3.9: **a**: Mean squared displacement for α close to $\pi/2$, such that the particles are close to describing circles, with $k = 1$, $h = 0.5$, $\Omega_0 = 2$. Black dotted lines are averages from numerical simulations. Dashed colored lines are the MSD as estimated for the active Brownian particle (ABP) with rotational diffusion derived from the variance of the Ornstein-Uhlenbeck process. Dotted lines are the MSD for the helical centerline with the persistence derived from stochastic trajectory models. **b**: Long-time effective diffusion D_∞ for different models, compared to the result found in Eq. 3.19 for the chiral OUP. Parameter values: potential strength $k = 1$, noise amplitude $h = 0.1$, angular speed $\Omega_0 = 1$, angle $\alpha = \pi/4$.

3.6 Conclusion

In this chapter we introduced a novel 3D active particle model that includes stochastic influences due to fluctuations in the driving mechanism of the particle. This is distinct from the more commonly used Brownian noise in two regards: Firstly, the motor machinery is not necessarily subject to white noise, but more likely has a characteristic time scale which is also represented in the noise. Secondly, this noise is generated in the body frame of the particle, i.e., rotated with the particle. Both points raise complications for the mathematical implementation of such a model, and in particular its solution. The active Ornstein-Uhlenbeck model proposed here retains these characteristics, while being simple in its composition, allowing for powerful analytical solutions.

From these solutions, we concluded that helical trajectories provide an

advantage for swimming or gliding microorganisms with noisy force generation to effectively cover distance more quickly than when going straight. This result from a general stochastic theory for microorganisms with colored noise in their internal torque generation complements earlier insights about the potential evolutionary advantages of helical motion for swimming [161, 164, 165].

Because of its simple structure still allowing analytical solutions, the model we propose here can serve as a baseline model for 3D chiral motility. It can be extended to study the behavior of such particles in confined environments, or the collective motion of many identical chiral particles.

The underlying assumption of the model is relatively simple: The internally generated noise of the motor machinery dominates external noise from the environment. This can be expected for many systems, in nature as well as artificially created ones. Systems that are sufficiently large or fast, as multicellular motile colonies, will likely fall in this category, but also synthetic microswimmers. In the future, our model could guide the design of micro- and nanobots [183, 184], for example in medical applications where enhanced persistence of motion is required [185].

4

Chapter 4

Analytical theory for geometric gliders

This chapter is based on publication 1,
Lettermann, Ziebert, Schwarz, PNAS, 2024.

4.1 Context

In the previous chapter, we discussed helical motility as a pattern repeatedly observed over many different species. From the more macroscopic perspective in Chapter 3, investigating the trajectories produced by total forces, torques, and their stochasticity, we now move to modeling directly the force generation mechanism of the sporozoite. This will also require including the geometry of the cell, instead of treating it as a particle.

The physical mechanisms used by cells and microbes to achieve motility vary vastly [152]. In a fluid environment, motility is often achieved by swimming with rotating or beating flagella. For animal cells, the most common form of motility is crawling, when the front is pushed forward by a lamellipodium and the back is pulled forward by actomyosin contractility [186]. While swimming is typically as fast as 100 µm/s, crawling is much slower, with a typical speed of 1 µm/min. Besides swimming and crawling, other major modes of cell motility are twitching and gliding, which both do not require major shape changes. While twitching uses pili that extend and retract, here we focus on gliding, usually based on surface flow of adhesion molecules as introduced in Chapter 1. Because the internal structure of gliders does not need to change, high speeds are possible, typically in the range of 1 µm/s. Gliding motility has evolved mainly for organisms that have to quickly move in a solid environment that provides substrates to which they can adhere. The model presented here is motivated by the well-conserved gliding machinery of apicomplexan parasites [48, 187, 188], but has applications to other gliding microbes, including bacteria [64, 189] and diatoms [66].

We briefly recap the main elements in gliding motility of *Plasmodium* sporozoites (Chapter 1). Sporozoites have the shape of a 10 µm long, thin, curved rod and move with high speeds up to 3 µm/s to cross tissue barriers and escape the immune system of the host. Adhesins like the thrombospondin-related anonymous protein (TRAP, [190]) are released at the front and effectively pulled towards the rear by an actomyosin system located below the membrane. On a flat (2D) substrate sporozoites primarily run on circular trajectories [61], while in a more physiological 3D environment they move on helical tracks [116] (cf. Fig. 1.3). The ookinetes of *Plasmodium* and invasive stages of other apicomplexan parasites, such as *Toxoplasma* tachyzoites and sporozoites, perform similar gliding motility and also tend to have helical trajectories [191, 192]. Although the helical trajectories of microgliders resemble the ones predicted for microswimmers (Chapter 3, [163]), the underlying physical mechanisms are fundamentally different, namely substrate- and not fluid-based. Recently, the self-organized surface flow has been investigated for experimentally measured shapes of *Toxoplasma gondii* tachyzoites ([117], Section 1.4.3) and their motility patterns in structured environments have been characterized by different biophysical methods [112], but the exact relation between cell shape, surface flows and motility patterns has not been addressed yet, which we aim to do in this chapter.

In addition, gliding motility is not only prominent for apicomplexa, but also for many bacteria [64, 189]. Gliding motility of bacteria is based on a larger range of mechanisms than for the apicomplexa, but here we focus on the ones similar to apicomplexa in that their gliding is based on a surface flow adhesively coupled to the substrate, like the adventurous mode of *Myxococcus xanthus* or the gliding motility of *Flavobacterium johnsoniae* [65, 193–202]. Both bacteria have the shape of cylindrical rods of 5 to 10 µm length and 1 µm diameter, and rotate around their long axis while gliding along their body axis, with *Flavobacterium johnsoniae* being roughly 50 times faster at 2 µm/s. While the machineries generating gliding motility in these bacteria are not yet fully understood, it is known that *Myxococcus xanthus* elastically couples to the substrate [197]. Moreover, its motor units are rotary and not stationary [203] and move MreB-filaments along helical tracks inside the cells [204]. In *Flavobacterium johnsoniae*, the motor units are also rotary, but stationary [195]. While the molecular basis of gliding motility in bacteria is diverse and still unclear, the general concept seems to be similar to the case of apicomplexa, namely that spatially distributed force generators effectively

move adhesins over the cell surface. Our treatment will not cover twitching motility of bacteria like the social mode of *Myxococcus xanthus* or motility of *Neisseria gonorrhoeae*, which are based on pilus retraction rather than surface flow and therefore are also more jerky than the gliding motility discussed here.

Given the importance of surface flow for gliding, it is clear that cell shape plays a central role in determining the resulting motility patterns. However, a unifying theory relating cell shape, surface flow and motility patterns is missing. In this chapter, we introduce such a theory to describe how the shape of a microglider determines its motility. Importantly, our approach is geometrical in nature and does not depend on the details of the gliding motility apparatus. Motivated by the case of the apicomplexa, we start with the assumptions that gliding motility is driven by independent motor units, which are uniformly distributed below the glider's surface, and that they self-organize to generate motion through adhesive coupling to a solid substrate. From these assumptions we derive the complete phase behavior of possible motility patterns of microgliders.

We then extend the model to also address gliding bacteria, which in contrast to the apicomplexa predominantly move on surfaces and use internal tracks to control surface flow. Again our theory can be used to predict cell trajectories from microscopic rules.

In general, our theory reveals that the surface flows powering gliding always have a strong tendency to rotate the glider in place, and that additional elements are required to avoid pure rotation without productive translocation. We show that curved shape for apicomplexa and pre-patterned flow for bacteria would both serve such a function and lead to circular and helical trajectories, exactly as observed for gliding apicomplexa and bacteria. Finally, we also introduce diatoms, hard-shelled algae, as a particularly interesting and simple special case to which the developed theory can be applied.

4.2 Geometrical theory of gliding

While the majority of experimental work investigating gliding motility is performed with 2D substrates, the more physiological environment for apicomplexan parasites is 3D. Motivated mainly by this case, we first formulate our theory for 3D environments and later specify it also for 2D. We consider gliding motility that is based on adhesion distributed over the complete surface and thus take a continuum approach. We make the following assumptions, as

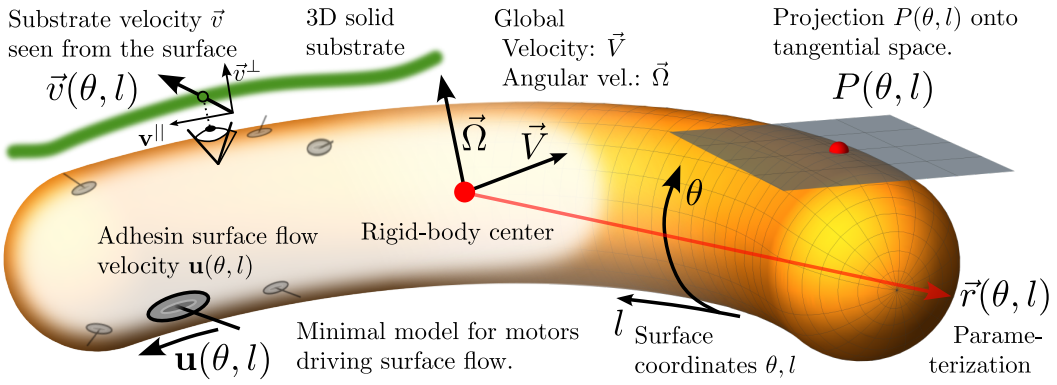

Figure 4.1: Schematic representation of a microglider and its mathematical description. Gliding motility is generated by independent motor units, distributed below the surface of the fixed-shape microglider. The geometry of the glider is described by its surface shape $\vec{r}_{(\theta,l)}$ and its global movement with translational and rotational velocities $\vec{V}$ and $\vec{\Omega}$, respectively. The motors generate a surface flow of adhesins, $\mathbf{u}_{(\theta,l)}$, which generates friction through the difference to the local relative velocity of the environment, $\vec{v}_{(\theta,l)}$. This friction determines the global motion and also reorganizes the surface flow.

visualized in Fig. 4.1:

1. The glider is a rigid body of fixed geometry, which leads to its surface parameterization $\vec{r}_{(\theta,l)}$, and it performs global motion with translational and angular velocities $\vec{V}$ and $\vec{\Omega}$, respectively. Thus we do not consider any deformations of the cell body.

2. Gliding motility is caused by the surface flow $\mathbf{u}_{(\theta,l)}$ of adhesins, actively driven by a distributed motor machinery.

3. The driving motor system has a fixed target flow speed, which by choice of units is set to 1. Because experimental evidence does not suggest otherwise, we assume that the driving is isotropic, that is individual motors do not have any preferred direction.

4. The surface motors tend to align their direction with the relative movement direction of the environment. This means that the mismatch between the motor target velocity and the actual environment velocity does not only create forces, but also feeds back into the motor configuration, establishing a mechanism for adaptive self-organization.

The existence of the surface flow field $\mathbf{u}_{(\theta,l)}$ is not only the simplest assumption to explain gliding motility, it also has been directly measured by particle tracking [112, 121, 193] or indirectly by fluorescence microscopy of moving parts

of the motor machinery [117, 194]. Due to the small density of adhesins in the membrane, this flow is assumed to be infinitely compressible (or, equivalently, pressure free). Moreover, the density of the adhesins is assumed to be constant, resulting in a constant coupling strength between surface flow and environment over the whole surface.

In order to describe the coupling between cell and environment, we first consider how movement determines surface flow; then we consider how the surface flow determines movement. The surface flow has to be compared with the relative velocity of the environment to a surface element, $\vec{v}_{(\theta,l)}$, which depends on the total translational and angular velocities through

$$\vec{v}_{(\theta,l)} = -\left(\vec{V} + \vec{\Omega} \times \vec{r}_{(\theta,l)}\right) . \tag{4.1}$$

The relative velocity can be further decomposed into tangential and normal parts by means of the local projection into the surface:

$$\mathbf{v}^{\parallel}_{(\theta,l)} = P_{(\theta,l)}\vec{v}_{(\theta,l)}, \; \vec{v}^{\perp} = \left(1 - P^{T}_{(\theta,l)}P_{(\theta,l)}\right)\vec{v} . \tag{4.2}$$

Here bold symbols, like $\mathbf{u}_{(\theta,l)}$ and $\mathbf{v}^{\parallel}_{(\theta,l)}$, denote 2-component vector fields in the tangent bundle of the surface, while usual vector arrows mark 3-component vectors. A tangential 2-component vector at coordinates (θ, l) can be embedded into the lab-frame by $P^{T}_{(\theta,l)}$. This can be defined via the tangent vectors

$$\vec{t}_{\theta}(\theta,l) = \frac{\partial \vec{r}_{(\theta,l)}}{\partial \theta} , \qquad \vec{t}_{l}(\theta,l) = \frac{\partial \vec{r}_{(\theta,l)}}{\partial l} \tag{4.3}$$

as the 2×3 matrix given by the transposed and normalized version of these tangents:

$$P_{(\theta,l)} = \begin{pmatrix} \hat{\vec{t}}_{\theta}{}^{T}(\theta,l) \\ \hat{\vec{t}}_{l}{}^{T}(\theta,l) \end{pmatrix} . \tag{4.4}$$

It projects a 3-component lab-frame vector $\vec{a}$ into a 2-component surface vector $\mathbf{a}$. Its transpose, P^{T}, embeds a 2-component surface vector in the lab-frame.

Assuming linear feedback of friction from the difference between surface flow $\mathbf{u}_{(\theta,l)}$ and tangential environmental velocity $\mathbf{v}^{\parallel}_{(\theta,l)}$ into the motor machinery with a coupling constant Γ, as well as a third order active driving term with driving strength η as known from Vicsek or other flocking models [117, 141, 205], the following is the simplest generic evolution equation for the surface flow:

$$\partial_t \mathbf{u}_{(\theta,l)} = -\Gamma\left(\mathbf{u}_{(\theta,l)} - \mathbf{v}^{\parallel}_{(\theta,l)}\right) + \eta \mathbf{u}_{(\theta,l)}\left(1 - |\mathbf{u}_{(\theta,l)}|^2\right) . \tag{4.5}$$

Through $\mathbf{v}^{\parallel}$, this equation depends on the global motion, described by $\vec{V}$ and $\vec{\Omega}$. There are numerous additional contributions that could be included, as advection of the polarised component of the motor machinery (and hence the velocity), or local ordering. While relevant to the dynamics in the absence of coupling to the environment [117], we omit them here in our analytical theory. If the coupling with the environment is strong, as assumed in the following, these additional local contributions will be negligible compared to the global geometric constraints. In the numerical simulations, however, we can introduce these terms, and later verify that their influence on the stationary solutions is small (see Section 4.3.8).

We next consider how the surface flow leads to movement, thus closing the equations of our gliding model. The mismatch between surface flow and environment velocity in the tangent space creates frictional forces with a friction constant γ, leading to a driving force resulting from integration over the surface:

$$\vec{F}^{\parallel} = -\gamma \int dA \; P^T_{(\theta,l)} \left[\mathbf{u}_{(\theta,l)} - \mathbf{v}^{\parallel}_{(\theta,l)} \right] \; . \tag{4.6}$$

The environmental velocity normal to the surface also creates friction, for which we introduce a dimensionless factor ζ to allow for different friction behavior between tangential and normal velocity:

$$\vec{F}^{\perp} = \zeta\gamma \int dA \; \vec{v}^{\perp}_{(\theta,l)} \; . \tag{4.7}$$

In the context of adhesive friction in a complex solid environment, it is an unknown parameter that we assume to be of order unity. An estimate for the related friction anisotropy in *Myxococcus xanthus* is also in this range [206]. For microswimmers, the global analog ζ has the typical value of 2 [22]. Assuming overdamped dynamics, for a given surface flow $\mathbf{u}$ the rigid body dynamics will immediately adapt and $\vec{V}$ and $\vec{\Omega}$ are determined according to the force balance

$$\vec{F}^{\parallel}(\mathbf{u}_{(\theta,l)}, \vec{V}, \vec{\Omega}) + \vec{F}^{\perp}(\mathbf{u}_{(\theta,l)}, \vec{V}, \vec{\Omega}) = 0 \; . \tag{4.8}$$

In this overdamped description, $\vec{V}$ and $\vec{\Omega}$ are not dynamical quantities, but are instantaneously determined by the surface flow field $\mathbf{u}_{(\theta,l,t)}$, which is the only dynamical field of the theory. The global motion is determined by an integral of the surface flow, making this an integro-differential equation. For the torques, we have a similar balance equation as for the forces, by locally

introducing $\vec{r}_{(\theta,l)}\times$ factors,

$$\vec{M}^{||}(\mathbf{u}_{(\theta,l)},\vec{V},\vec{\Omega})+\vec{M}^{\perp}(\mathbf{u}_{(\theta,l)},\vec{V},\vec{\Omega})=0\ , \tag{4.9}$$

thus completing our model definition.

4.2.1 Stationary solutions

We start our discussion of the solutions of our gliding model with the stationary solutions of the dynamical equation Eq. 4.5. We immediately see that these solutions require a parallel orientation of the surface flow to the environmental velocity, that is $\mathbf{u}_{(\theta,l)}||\mathbf{v}^{\parallel}_{(\theta,l)}$ everywhere. This reduces it to a scalar equation, which as a third order polynomial can be solved analytically. We now make the assumption of strong coupling to the environment, $g=\Gamma/\eta\gg 1$, which means that an adhesin, bound on one side to the environment and on the other side subject to the motor machinery of the glider, will mostly be stationary with respect to the environment, as indeed observed for clusters of adhesins in apicomplexan parasites as well as in gliding bacteria [61, 65, 194]. Under this assumption, the only physically relevant, positive, real solution is

$$\mathbf{u}(\mathbf{v}^{\parallel})=\mathbf{v}^{\parallel}+\frac{1-|\mathbf{v}^{\parallel}|^2}{g}\mathbf{v}^{\parallel}\ . \tag{4.10}$$

We conclude that the surface flow generally follows the environment, but will be slightly faster and driving the system if the tangential environmental speed $\mathbf{v}^{\parallel}$ is smaller than the motors target speed 1. Otherwise it will be slower and reduce the motion. Overall, this defines a stable stationary solution of the system.

With Eq. 4.10, we can now eliminate the surface flow $\mathbf{u}$ from the force balance, Eq. 4.8. We introduce the generalized 6-component velocity $\vec{W}=(\vec{V},\vec{\Omega})$ and find

$$\begin{aligned}\vec{F}^{||}=&-\gamma\int dA\ P^TP\left[\frac{1-|\mathbf{v}^{\parallel}|^2}{g}\vec{v}\right]\\ =&\frac{\gamma}{g}\int dA\left(1-\vec{W}^TG_{(\theta,l)}\vec{W}\right)\\ &\times P^TP\left[\vec{V}+\vec{\Omega}\times\vec{r}_{(\theta,l)}\right]\ .\end{aligned} \tag{4.11}$$

Here the 6×6 geometrical kernel $G_{(\theta,l)}$ arising from $|\mathbf{v}^{\parallel}|^2$ is defined as

$$G_{(\theta,l)} = \begin{pmatrix} P^T_{(\theta,l)}P_{(\theta,l)} & P^T_{(\theta,l)}P_{(\theta,l)}[\vec{r}_{(\theta,l)}]^T_\times \\ [\vec{r}_{(\theta,l)}]_\times P^T_{(\theta,l)}P_{(\theta,l)} & [\vec{r}_{(\theta,l)}]_\times P^T_{(\theta,l)}P_{(\theta,l)}[\vec{r}_{(\theta,l)}]^T_\times \end{pmatrix} \tag{4.12}$$

and combines the surface orientation information $P_{(\theta,l)}$ relevant to determine the tangential part with the position information $\vec{r}_{(\theta,l)}$ in form of the matrix representation of the cross product $[\vec{r}]_\times \vec{a} = \vec{r} \times \vec{a}$, necessary to compute the effect of rotation.

4.2.2 Introducing geometry tensors

The geometric part of the problem can now be condensed into the geometry tensors

$$\mathcal{G}^{ij} = \int dA\ G^{ij}_{(\theta,l)}\ , \tag{4.13}$$

$$\mathcal{G}_2^{klij} = \int dA\ G^{kl}_{(\theta,l)} G^{ij}_{(\theta,l)}\ . \tag{4.14}$$

The substructure of three velocity and three angular velocity components of $\vec{W}$ gives $\mathcal{G}$ a block matrix structure. The upper left sub-matrix can be understood as the mean projection of a vector given in the lab frame onto the surface, while the other block matrices are weighted with the distance vector to the origin. As one can see from Eq. 4.12, $\mathcal{G}$ is symmetric. Under an affine transformation of the parameterization with rotation R and translation $\vec{d}$

$$\vec{r}_{(\theta,l)} \to \tilde{\vec{r}}_{(\theta,l)} = R\vec{r}_{(\theta,l)} + \vec{d}\,, \tag{4.15}$$

projection and cross product matrix change as

$$\tilde{P}_{(\theta,l)} = P_{(\theta,l)}R^T\ , \qquad \left[\tilde{\vec{r}}_{(\theta,l)}\right]_\times = R[\vec{r}_{(\theta,l)}]_\times R^T + \left[\vec{d}\right]_\times , \tag{4.16}$$

which can be used to see that the geometric kernel G changes as

$$\tilde{G}_{(\theta,l)} = \mathcal{T} G_{(\theta,l)} \mathcal{T}^T\ , \qquad \mathcal{T} = \begin{pmatrix} R & 0 \\ 0 & R\ \left(\mathbb{I} + \left[\vec{d}\right]_\times\right) \end{pmatrix}. \tag{4.17}$$

The same transformation $\mathcal{T}$ applies to the integrated tensor quantities $\mathcal{G}^{ij}$, $\mathcal{G}_2^{klij}$, i.e.

$$\tilde{\mathcal{G}}_2^{klij} = \mathcal{T}^{ka}\mathcal{T}^{lb}\mathcal{T}^{ic}\mathcal{T}^{jd}\mathcal{G}_2^{abcd} \tag{4.18}$$

where summation over repeated indices is implied. These transformation laws are reminiscent of the ones for the hydrodynamic resistance tensor [207, 208].

Identifying the remaining geometry dependent part of Eq. 4.11 as the top row of $G_{(\theta,l)}\vec{W}$, and the bottom row as the similar term that would arise in the respective expression for $\vec{M}^{||}$, we find for the forces and torques:

$$\begin{aligned}\begin{pmatrix}\vec{F}^{||}\\ \vec{M}^{||}\end{pmatrix}_i &= \frac{\gamma}{g}\int dA\left(1-\vec{W}^T G_{(\theta,l)}\vec{W}\right)G^{ij}_{(\theta,l)}\vec{W}_j\\ &= \frac{\gamma}{g}\left(\mathcal{G}^{ij}-\mathcal{G}_2^{ijkl}W_kW_l\right)W_j\ .\end{aligned} \tag{4.19}$$

Repeating the same line of argument for the normal component (Eq. 4.7), a third geometry tensor $\mathcal{R}^{ij}$ emerges, similar to $\mathcal{G}^{ij}$, but replacing the projections P in Eq. 4.12 with identity operators, taking the full space instead of the projection to the tangent space into account,

$$G^{\text{Full}}_{(\theta,l)} = \begin{pmatrix}\mathbb{I} & [\vec{r}_{(\theta,l)}]^T_\times\\ [\vec{r}_{(\theta,l)}]_\times & [\vec{r}_{(\theta,l)}]_\times[\vec{r}_{(\theta,l)}]^T_\times\end{pmatrix} \tag{4.20}$$

and therefore

$$\mathcal{R}^{ij} = \int dA\ G^{\text{Full},ij}_{(\theta,l)}\ . \tag{4.21}$$

Using this, the normal space can be expressed by the difference of $\mathcal{R}$ and $\mathcal{G}$:

$$\begin{pmatrix}\vec{F}^{\perp}\\ \vec{M}^{\perp}\end{pmatrix}_i = -\zeta\gamma\left(\mathcal{R}^{ij}-\mathcal{G}^{ij}\right)W_j\ . \tag{4.22}$$

Finally, we can rewrite the force and momentum balance Eq. 4.8 and 4.9 as a condition on the global motion $\vec{W}$,

$$\left(\mathcal{G}^{ij}-\mathcal{G}_2^{klij}W_kW_l\right)W_j - \zeta g\left(\mathcal{R}^{ij}-\mathcal{G}^{ij}\right)W_j = 0\ , \tag{4.23}$$

which effectively is a third order polynomial in $\vec{V}$ and $\vec{\Omega}$. Its coefficients encode the geometric shape of the glider and its solutions determine the full stationary field configuration of the surface flow via Eq. 4.2 and Eq. 4.10. Furthermore, these solutions depend only on one effective parameter, $c = \zeta g = \zeta\Gamma/\eta$. This c is small for strong driving, weak coupling and weaker normal than tangential friction, and large for weak driving, strong coupling and stronger normal than tangential friction. Our theory as discussed here is an approximation for the large coupling case. The geometry tensors can be calculated analytically for

many shapes of interest (for the simplest case of an open cylinder, the results are shown in detail in Section 4.2.4).

4.2.3 Stability analysis

A linear stability analysis in regard to the surface flow $\mathbf{u}_{(\theta,l)}$ based on Eq. 4.5 shows that the stationary solutions are stable as long as the global motion $\vec{W}$ is not affected. This makes sense because we already have seen from Eq. 4.10 that mechanisms exist to stabilize the surface flow. Therefore it is a better question to ask about an effective, more global view on stability: if by an external influence (e.g. a collision with an obstacle) the surface flow is globally changed with a resulting deviation in $\vec{W}$, will the surface flow afterwards relax back towards the previous configuration, necessarily also reverting $\vec{W}$ to its previous value, or not?

To answer this question, we start with a perturbation $\delta\vec{W}$ around a solution $\vec{W}$ with corresponding surface flow $\mathbf{u}_{(\theta,l)}$ and look for the change

$$\delta\mathbf{u}_{(\theta,l,t)} = -P_{(\theta,l)}\left(\delta\vec{V} + \delta\vec{\Omega}\times\vec{r}_{(\theta,l)}\right). \tag{4.24}$$

As a measure for the effect of the perturbation, we will investigate the dynamics of

$$\Delta(t) = \int dA \ \left|\delta\mathbf{u}_{(\theta,l,t)}\right|^2, \tag{4.25}$$

which is the surface integrated change in surface flow induced by the perturbation. Upon expanding expanding in small perturbations and large coupling c, it is found to be

$$\partial_t\Delta(t) \approx \ 2\mathcal{J}^{ij}\delta\vec{W}_i\delta\vec{W}_j \tag{4.26}$$

$$\mathcal{J}^{ij}(\vec{W}) = \Big[g\left(\mathcal{G}\left(\zeta\mathcal{R}+(1-\zeta)\mathcal{G}\right)^{-1}\mathcal{G}\right)^{ij} + (1-g)\mathcal{G}^{ij} - \mathcal{G}_2^{ijkl}W_kW_l - 2\mathcal{G}_2^{ikjl}W_kW_l\Big]. \tag{4.27}$$

A stationary solution of global movement $\vec{W}$ is hence predicted to be stable in the above-defined sense if the matrix $\mathcal{J}(\vec{W})$ is negative definite. As this procedure probes only a subspace of possible perturbations and only uses the surface integrated perturbation $\Delta(t)$ to decide about growth or decay of a particular perturbation, our stability analysis is not complete. We therefore complement it by numerical simulations that directly solve Eq. 4.5-4.9 with

appropriate discretizations (details in Section 4.3.2). In general, we find excellent agreement with the predictions of our stability analysis. In contrast to the analysis of the stationary solutions, we find that the stability depends directly on the individual values of g and ζ, and not only on their product (in the following, we will use $\zeta = 1/2$, cf. also Fig. 4.6). This results from the fact that while the stationary problem could be reduced to the finite space of the rigid-body motion described by Eq. 4.10, the underlying dynamical problem is still that of the infinite dimensional surface flow field $\mathbf{u}_{(\theta,l)}$.

4.2.4 Detailed derivation for the open cylinder

Geometry tensors

As one of the simplest possible examples, we calculate the quantities defined above for an open cylinder, that is omitting the spherical caps that will later on be included to arrive at the closed spherocylindrical cell shape we will use as a model for rod shaped bacteria below. First, we parameterize the cylinder of length 1 and radius R as

$$\vec{r}_{(\theta,l)} = \begin{pmatrix} R\cos\theta \\ R\sin\theta \\ l \end{pmatrix}, \qquad \theta \in [0, 2\pi),\ l \in [-1/2, 1/2]. \tag{4.28}$$

This gives the normalized tangents and the projection P as

$$\hat{\vec{t}}_\theta(\theta, l) = \begin{pmatrix} -\sin\theta \\ \cos\theta \\ 0 \end{pmatrix}, \quad \hat{\vec{t}}_l(\theta, l) = \begin{pmatrix} 0 \\ 0 \\ 1 \end{pmatrix}, \quad P_{(\theta,l)} = \begin{pmatrix} -\sin\theta & \cos\theta & 0 \\ 0 & 0 & 1 \end{pmatrix}. \tag{4.29}$$

Next, we write the 3x3-matrices

$$P^T_{(\theta,l)} P_{(\theta,l)} = \begin{pmatrix} \sin^2(\theta) & -\sin(\theta)\cos(\theta) & 0 \\ -\sin(\theta)\cos(\theta) & \cos^2(\theta) & 0 \\ 0 & 0 & 1 \end{pmatrix}, \tag{4.30}$$

$$[\vec{r}_{(\theta,l)}]_\times = \begin{pmatrix} 0 & -l & R\sin\theta \\ l & 0 & -R\cos\theta \\ -R\sin\theta & R\cos\theta & 0 \end{pmatrix}. \tag{4.31}$$

which can be combined to give $G_{(\theta,l)}$ (cf. Eq. 4.12):

$$G_{(\theta,l)} = \begin{pmatrix} \sin^2(\theta) & -\sin(\theta)\cos(\theta) & 0 & l\sin(\theta)\cos(\theta) & l\sin^2(\theta) & -R\sin(\theta) \\ -\sin(\theta)\cos(\theta) & \cos^2(\theta) & 0 & -l\cos^2(\theta) & -l\sin(\theta)\cos(\theta) & R\cos(\theta) \\ 0 & 0 & 1 & R\sin(\theta) & -R\cos(\theta) & 0 \\ l\sin(\theta)\cos(\theta) & -l\cos^2(\theta) & R\sin(\theta) & l^2\cos^2(\theta)+R^2\sin^2(\theta) & \sin(\theta)\cos(\theta)(l-R)(l+R) & -lR\cos(\theta) \\ l\sin^2(\theta) & -l\sin(\theta)\cos(\theta) & -R\cos(\theta) & \sin(\theta)\cos(\theta)(l-R)(l+R) & l^2\sin^2(\theta)+R^2\cos^2(\theta) & -lR\sin(\theta) \\ -R\sin(\theta) & R\cos(\theta) & 0 & -lR\cos(\theta) & -lR\sin(\theta) & R^2 \end{pmatrix} \tag{4.32}$$

Upon integrating to obtain the geometry tensors, many of these terms vanish and we obtain

$$\mathcal{G} = \begin{pmatrix} \pi R & 0 & 0 & 0 & 0 & 0 \\ 0 & \pi R & 0 & 0 & 0 & 0 \\ 0 & 0 & 2\pi R & 0 & 0 & 0 \\ 0 & 0 & 0 & \pi\left(R^3+\frac{R}{12}\right) & 0 & 0 \\ 0 & 0 & 0 & 0 & \pi\left(R^3+\frac{R}{12}\right) & 0 \\ 0 & 0 & 0 & 0 & 0 & 2\pi R^3 \end{pmatrix}. \tag{4.33}$$

Note that the $3,3$-entry is the surface area of the cylinder (length has been set to 1). A velocity in z-direction is tangential everywhere on the surface. An x- or y-velocity is tangential only half of the time, hence the $1,1$- and $2,2$-entries are half as large. The $6,6$-entry can be explained similarly: rotation around the z-axis generates tangential velocity everywhere, weighted here by the square of the distance to the axis of rotation (via two factors $[\vec{r}_{(\theta,l)}]_\times$ in Eq. 4.12).

Finally we give a single 6×6 submatrix of the 4th order tensor $\mathcal{G}_2$, to exemplify that it captures more complicated aspects of the geometry and can have non-diagonal entries even for this simple example, and the third geometry tensor $\mathcal{R}$:

$$\mathcal{G}_2^{12ij} = \begin{pmatrix} 0 & \frac{\pi R}{4} & 0 & 0 & 0 & 0 \\ \frac{\pi R}{4} & 0 & 0 & 0 & 0 & 0 \\ 0 & 0 & 0 & 0 & 0 & 0 \\ 0 & 0 & 0 & 0 & \frac{1}{48}\pi R\left(12R^2-1\right) & 0 \\ 0 & 0 & 0 & \frac{1}{48}\pi R\left(12R^2-1\right) & 0 & 0 \\ 0 & 0 & 0 & 0 & 0 & 0 \end{pmatrix}. \tag{4.34}$$

$$\mathcal{R} = \begin{pmatrix} 2\pi R & 0 & 0 & 0 & 0 & 0 \\ 0 & 2\pi R & 0 & 0 & 0 & 0 \\ 0 & 0 & 2\pi R & 0 & 0 & 0 \\ 0 & 0 & 0 & \frac{1}{6}\pi\left(6R^3+R\right) & 0 & 0 \\ 0 & 0 & 0 & 0 & \frac{1}{6}\pi\left(6R^3+R\right) & 0 \\ 0 & 0 & 0 & 0 & 0 & 2\pi R^3 \end{pmatrix}. \tag{4.35}$$

Polynomial for stationary solutions

The polynomial from Eq. 4.23 leads to 6 equations for the components of V and Omega. They determine the stationary global solutions for the cylinder. Given the geometry tensors computed above, it turns out as

$$V_x\left(16c+12V_y^2+\left(12R^2+1\right)\Omega_x^2+\left(4R^2+3\right)\Omega_y^2+48R^2\Omega_z^2-16\right)+12V_x^3+16V_xV_z^2+8R^2V_y\Omega_x\Omega_y-32R^2V_z\Omega_x\Omega_z=2V_y\Omega_x\Omega_y$$

$$V_y\left(16c+\left(4R^2+3\right)\Omega_x^2+\left(12R^2+1\right)\Omega_y^2+48R^2\Omega_z^2-16\right)+12V_x^2V_y+8R^2V_x\Omega_x\Omega_y+12V_y^3+16V_yV_z^2-32R^2V_z\Omega_y\Omega_z=2V_x\Omega_x\Omega_y$$

$$V_z\left(12V_x^2+12V_y^2+\left(36R^2+1\right)\Omega_x^2+\left(36R^2+1\right)\Omega_y^2+24R^2\Omega_z^2-24\right)+24V_z^3=24R^2V_x\Omega_x\Omega_z+24R^2V_y\Omega_y\Omega_z$$

$$\Omega_x\left(-960R^2+80c+\left(720R^4+40R^2+9\right)\Omega_y^2-80\right)+\left(720R^2+60\right)V_x^2\Omega_x+\left(240R^2+180\right)V_y^2\Omega_x$$
$$+\left(2880R^2+80\right)V_z^2\Omega_x+\left(720R^4+40R^2+9\right)\Omega_x^3+\left(960R^4+240R^2\right)\Omega_x\Omega_z^2=120\left(1-4R^2\right)V_xV_y\Omega_y+1920R^2V_xV_z\Omega_z$$

$$\Omega_y\left(-960R^2+80c-80\right)+60\left(4R^2+3\right)V_x^2\Omega_y+120\left(4R^2-1\right)V_xV_y\Omega_x+\left(720R^2+60\right)V_y^2\Omega_y+\left(2880R^2+80\right)V_z^2\Omega_y$$
$$+\left(720R^4+40R^2+9\right)\Omega_x^2\Omega_y+\left(720R^4+40R^2+9\right)\Omega_y^3+\left(960R^4+240R^2\right)\Omega_y\Omega_z^2=1920R^2V_yV_z\Omega_z$$

$$\Omega_z\left(12V_x^2+12V_y^2+8V_z^2+\left(\left(4R^2+1\right)\Omega_x^2+\left(4R^2+1\right)\Omega_y^2-8\right)+8R^2\Omega_z^2\right)=V_z(8V_x\Omega_x+8V_y\Omega_y)$$

To simplify, we can ask what the possible solutions are if we consider only $V_z, \Omega_z \neq 0$ and all others vanishing, that is only translation along the cylinder axis and rotation around it. Only two of the six equations above remain, giving

$$V_z\left(V_z^2+R^2\Omega_z^2\right)=V_z\ , \qquad \Omega_z\left(V_z^2+R^2\Omega_z^2\right)=\Omega_z \tag{4.36}$$

with solutions

$$V_z^2+R^2\Omega_z^2=1 \Rightarrow V_z=\pm\sqrt{1-R^2\Omega_z^2}, \quad \Omega_z\in[-1/R,1/R]. \tag{4.37}$$

This result is shaped by the very regular geometry of the cylinder: if it turns and translates in this way, every point on its surface has precisely the same relative velocity. If this velocity matches unity, the surface flow is completely force free. Obviously, this does not reflect the full, real situation, as the

cylinder is open on both ends here, and the spherical caps included later would generate drag dependent only on the translational part, leading to a collapse of the continuous space of solutions onto the discrete solutions appearing in the bifurcation diagrams shown in Section 4.3.3.

Stability matrix

Finally, we document the stability matrix $\mathcal{J}$ for this reduced cylindrical case, i.e. we assume $\vec{W} = (0, 0, V_z, 0, 0, \Omega_z)$, leading to

$$\mathcal{J}(\vec{W}) = \begin{pmatrix} C_1 & 0 & 0 & 2\pi R^3 V_z \Omega_z & 0 & 0 \\ 0 & C_1 & 0 & 0 & 2\pi R^3 V_z \Omega_z & 0 \\ 0 & 0 & C_2 & 0 & 0 & -4\pi R^3 V_z \Omega_z \\ 2\pi R^3 V_z \Omega_z & 0 & 0 & C_3 & 0 & 0 \\ 0 & 2\pi R^3 V_z \Omega_z & 0 & 0 & C_3 & 0 \\ 0 & 0 & -4\pi R^3 V_z \Omega_z & 0 & 0 & C_4 \end{pmatrix}, \tag{4.38}$$

$$\begin{aligned} C_1 &= -\frac{\pi R\left(c + (\zeta+1)\left(3R^2\Omega_z^2 + V_z^2 - 1\right)\right)}{\zeta+1}, \\ C_2 &= -2\pi R\left(R^2\Omega_z^2 + 3V_z^2 - 1\right), \\ C_3 &= -\frac{\pi R\left(12cR^2 + c + \left(\zeta + 12R^2 + 1\right)\left(12R^4\Omega_z^2 + 3R^2\left(12V_z^2 + \Omega_z^2 - 4\right) + V_z^2 - 1\right)\right)}{12(\zeta + 12R^2 + 1)}, \\ C_4 &= -2\pi R^3\left(3R^2\Omega_z^2 + V_z^2 - 1\right). \end{aligned}$$

The eigenvalues determining the stability are rather cumbersome in general, but can be computed easily for a specific solution.

Extension to spherocylindrical shape

The degeneracy of the solutions in Eq. 4.37 is due to the open shape of the cylinder, offering no resistance to translation in z-direction. However, as the geometry tensors are defined as surface integrals, they are additive under constructing the geometry tensors for a more complicated surface from simpler components of that surface. Therefore, we can complete the cylinder with two spherical caps by solving separately for the geometry tensors of spherical caps, either parameterizing them at the right spatial position to be aligned with the cylinder, or transforming the spherical cap into the right position by means of Eq. 4.17. For the open cylinder, this leads to the axisymmetric (straight) spherocylinder as discussed in Section 4.3.3. As shown there, the continuous solution space of the open cylinder then collapses on the rotational and translational solutions, with the first and second being stable and unstable, respectively.

4.2.5 Breaking local isotropy by introducing bias

Our theory assumes that the surface flow is self-organized, with individual motors being completely isotropic. This is a strong assumption, and a possible point of attack for evolution to engineer additional control of the surface flow and the subsequent dynamics. We can extend our framework to include a directional bias of the surface flow, which we will later find necessary to describe certain situations. Assume we want to achieve global motion in direction of the unit vector $\hat{e}_V$, then we assume that we locally want to add a bias term in equation Eq. 4.5 so it becomes

$$\partial_t \mathbf{u}_{(\theta,l)} = -\Gamma\left(\mathbf{u}_{(\theta,l)} - \mathbf{v}^{\parallel}_{(\theta,l)}\right) + \eta\mathbf{u}_{(\theta,l)}\left(1 - |\mathbf{u}_{(\theta,l)}|^2\right) - \eta B P_{(\theta,l)}\hat{e}_V \ , \tag{4.39}$$

where B measures the bias strength in units of the isotropic drive strength η. For small bias B, in the strong coupling limit this shifts the stationary solution found in Eq. 4.10,

$$\mathbf{u}(\mathbf{v}^{\parallel}) = \mathbf{v}^{\parallel} + \frac{1 - |\mathbf{v}^{\parallel}|^2}{g}\mathbf{v}^{\parallel} - \frac{B}{g}P_{(\theta,l)}\hat{e}_V \ . \tag{4.40}$$

Tracing the additional term through the force balance, we eventually find the new force balance equation replacing Eq. 4.23,

$$\left(\mathcal{G}^{ij} - \mathcal{G}_2^{klij}W_kW_l\right)W_j - \zeta g\left(\mathcal{R}^{ij} - \mathcal{G}^{ij}\right)W_j = B\mathcal{G}^{ij}\begin{pmatrix}\hat{e}_V\\ \hat{e}_\Omega\end{pmatrix} \ . \tag{4.41}$$

Here, for full generality we included a vector $\hat{e}_\Omega$ giving the lab-frame orientation for a desired angular speed that should be generated by the bias. With this equation we find again that we can reduce the problem of surface flow and motility to a third order polynomial in the global motion, where the bias introduces a zero order term.

In the first order expansion for the bias B, it is shifting the positions of stationary solutions, but the stability theory around this stationary solutions remains as before. Hence we can analytically obtain stability of the biased stationary solutions by the eigenvalues of the previously described matrix $\mathcal{J}(\vec{W})$.

4.3 Results

4.3.1 Overview

In the following, we apply our geometrical theory of gliding motility to a range of different cell shapes, starting with rods and ellipsoids and continuing with curved rods. Afterwards we investigate the motion on a 2D substrate, with particular attention to gliding bacteria. In general, all our results are analytical solutions to the central equation Eq. 4.23, as demonstrated for the example of the open cylinder above in Section 4.2.4. For each case of interest, the geometry tensors $\mathcal{G}^{ij}$, $\mathcal{G}_2^{ijkl}$ and $\mathcal{R}^{ij}$ are calculated analytically with the computer algebra software Mathematica. Once a solution is obtained in terms of the global movement $\vec{W}$, we can find the corresponding surface flow field $\mathbf{u}_{(\theta,l)}$. Stability of the solutions is decided according to the matrix $\mathcal{J}(\vec{W})$ from Eq. 4.26. Very importantly, all our analytical results are verified by numerical solutions.

4.3.2 Numerical solution

The goal of the numerical solution is to solve the dynamical system posed by Eq. 4.5-4.9, in order to verify the analytical treatment. To this end, we briefly introduce here a simplified version of the more complex numerical framework developed in Chapter 5. To do so, the shape is discretized by a grid, e.g. 20 gridpoints around and 61 along the axis of the shapes. Each of these points carries a distance vector $\vec{r}$ to the origin of the parameterization, an assigned surface area, the local projection P, and a value for the current surface flow $\mathbf{u}$. With this information, at a timestep the force and momentum balance condition,

$$\vec{F}^{\parallel}(\mathbf{u}_{(\theta,l)},\vec{V},\vec{\Omega}) + \vec{F}^{\perp}(\mathbf{u}_{(\theta,l)},\vec{V},\vec{\Omega}) = 0 \,, \tag{4.42}$$

$$\vec{M}^{\parallel}(\mathbf{u}_{(\theta,l)},\vec{V},\vec{\Omega}) + \vec{M}^{\perp}(\mathbf{u}_{(\theta,l)},\vec{V},\vec{\Omega}) = 0 \,, \tag{4.43}$$

$$\vec{F}^{\parallel}(\mathbf{u}_{(\theta,l)},\vec{V},\vec{\Omega}) = -\gamma \int dA\; P^T_{(\theta,l)} \left[\mathbf{u}_{(\theta,l)} - \mathbf{v}^{\parallel}_{(\theta,l)}\right] \,, \tag{4.44}$$

$$\mathbf{v}^{\parallel}_{(\theta,l)} = -P_{(\theta,l)} \left(\vec{V} + \vec{\Omega} \times \vec{r}_{(\theta,l)}\right) \,, \tag{4.45}$$

$$\vec{F}^{\perp}(\mathbf{u}_{(\theta,l)},\vec{V},\vec{\Omega}) = \zeta\gamma \int dA\; \vec{v}^{\perp}_{(\theta,l)} \tag{4.46}$$

define a linear problem in $\vec{W} = (\vec{V},\vec{\Omega})^T$, where the integrals are converted to sums over the grid points, weighted by their area. The resulting linear problem can be solved dependent on the current surface flow configuration to obtain the

instantaneous velocity and angular velocity by explicitly computing the linear problem and inverting the relevant matrix.

With the global motion $\vec{W}$ determined, the surface flow evolution can be computed by its evolution equation Eq. 4.5 which can be evaluated separately for every grid point.

The procedure outlined above was implemented in Python using JAX [175] for higher performance, and solved using a Dopri5 (Mixed 4th/5th order Runge-Kutta ODE solver with Dormand-Prince adaptive step sizing, [209]) provided by the JAX odeint routine. The intermediately computed instantaneous translational and rotational velocities were integrated in order to obtain trajectories.

4.3.3 Spherocylindrical cell shape

The spherocylinder is the open-ended cylinder discussed before, but closed by two spherical caps, and can be readily treated by our theory. Due to the three symmetry planes, the geometry tensor $\mathcal{G}$ has to be diagonal. With the radius set to 1, aspect ratio α and the axis of symmetry in z-direction, it can be written as

$$\mathrm{Diag}(\mathcal{G}) = \frac{2\pi}{3}\begin{pmatrix} 3\alpha+1 \\ 3\alpha+1 \\ 6\alpha-2 \\ \alpha^3+\alpha^2+4\alpha-2 \\ \alpha^3+\alpha^2+4\alpha-2 \\ 6\alpha-2 \end{pmatrix}. \tag{4.47}$$

We find only two non-trivial solutions, namely pure rotation (only Ω_z nonzero) and pure translation (only V_z nonzero):

$$\Omega_z^{\mathrm{rot.}} = \sqrt{\frac{15\alpha-5}{15\alpha-7}}\,, \qquad V_z^{\mathrm{trans.}} = \sqrt{5}\sqrt{\frac{3\alpha-c-1}{15\alpha-7}}\,. \tag{4.48}$$

The respective surface flows generating these motions are displayed in Fig. 4.2a. For large aspect ratio α, both values approach unity, because for very elongated shapes the driving force created at the tangential part of the surface dominates over the drag created at the ends (note that both velocity and radius are normalized to 1, thus also normalizing angular velocity). For aspect ratio approaching 1 (the case of a sphere), the angular velocity actually becomes larger than 1, because now a larger portion of the surface drives the rotation from positions close to the axis of rotation.

We next investigated the stability of the two stationary solutions and found

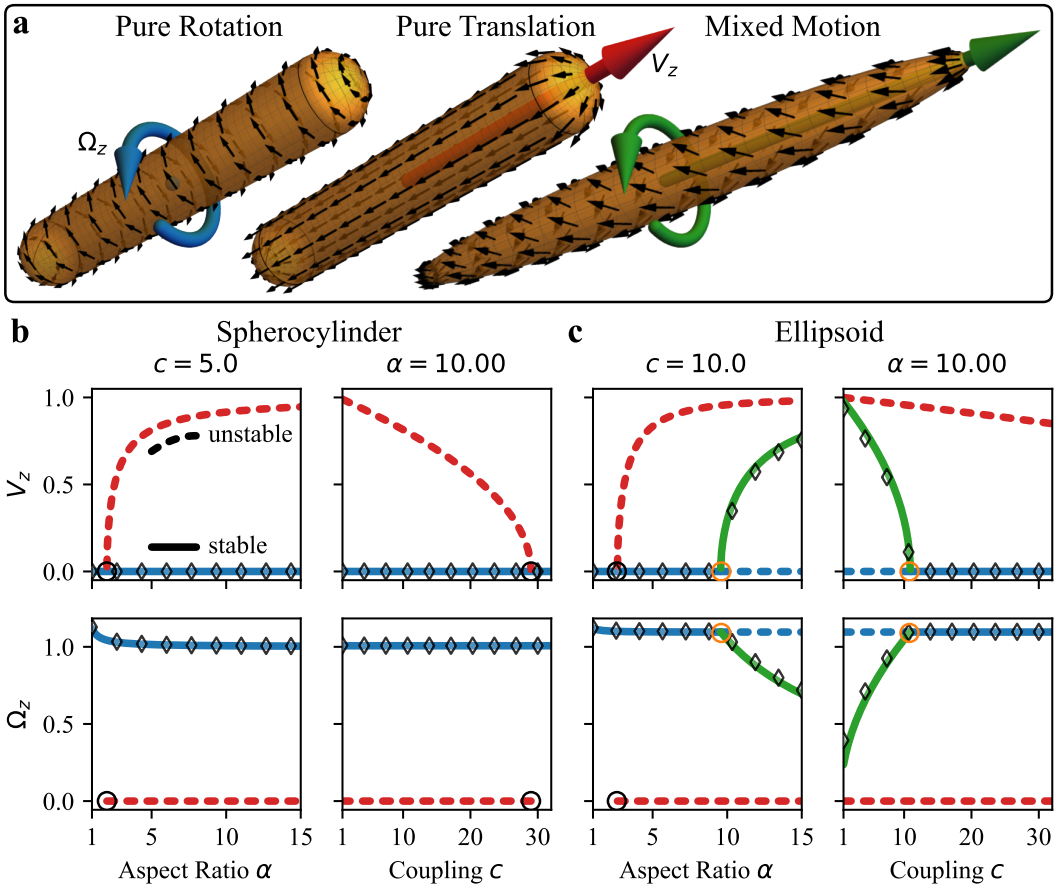

Figure 4.2: Steady-state solutions for rotationally symmetric shapes, namely a spherocylinder and an ellipsoid, in a 3D environment. **a:** The surface flows for the three types of solutions identified by the theory: pure rotation (blue), pure translation (red), and mixed motion (green). **b,c:** Bifurcation diagram for the spherocylinder (b) and for the ellipsoid (c). Top row shows velocity in direction of the long axis and bottom row angular velocity around that axis. The three fundamental solutions are distinguished by the same colors used in (a). Dashed and solid lines are unstable and stable solutions, respectively. Both the aspect ratio α and the coupling c of the surface flow to the environment are varied as bifurcation parameters. The bifurcation diagrams are symmetric under sign change and only the positive branches are shown. Black circles denote pitchfork bifurcations from the trivial solution, which is not shown. Orange circles denote pitchfork bifurcations. Diamonds are steady-states found by numerical simulation and are in excellent agreement with the analytical results.

that pure rotation is always stable, while pure translation is always unstable. The corresponding bifurcation diagrams are shown in Fig. 4.2b, with solid and dashed lines for stable and unstable solutions, respectively. The translational solution bifurcates from the trivial solution with increasing aspect ratio, i.e. it does not exist for a near spherical shape, where the surface area parallel to the

motion used for driving is comparable to the perpendicular area, generating friction. The translating solution also bifurcates into the trivial solution for higher coupling, i.e. weaker driving. The trivial solution (vanishing surface flow and hence no motion) remains unstable before and after both these bifurcation points, as it is still unstable to perturbations in the direction of the rotational solution. Other solutions, such as rotations around another axis, arise only at $c < 1$, outside the range in which our theory is valid, or at aspect ratios $\alpha \approx 1$, where the solutions become degenerate as the geometry approaches a sphere.

The fact that the spherocylindrical glider in 3D prefers the rotating solution can be understood from an energy perspective: for the rotating cylinder, the surface is fixed in space, as the surface flow compensates the underlying rotation, hence minimizing drag and dissipation. For a biological system, which invests energy to drive the surface flow in order to move, the global stability of the solution with pure rotation is a fundamental problem. In the following we will investigate which different shapes can help to mitigate the tendency of surface flow motors to rotate the glider in place.

4.3.4 Ellipsoidal cell shape

The ellipsoid, more specifically a prolate spheroid with short semi-axis 1 and long semi-axis α, shows similar rotational and translational solutions as the spherocylindrical glider. Strikingly, however, now a third mode becomes possible, namely a mixed solution with a tilted flow field, as shown in Fig. 4.2a on the right.

In Fig. 4.2c we show the corresponding bifurcation diagrams. The rotational and translational solutions in Fig. 4.2c look similar to the previous case of the spherocylinder. The translational solution only deviates by the bifurcation into the trivial solution being shifted to even higher coupling, caused by the smaller proportion of perpendicular surface area for the ellipsoid compared to the spherocylinder. The rotating solution bifurcates into the new mixed solution for increasing aspect ratio or decreasing coupling, made possible by the varying radius of the ellipsoid: while for the spherocylindrical glider the radius is constant and the surface flow can be at its target speed everywhere except at the caps, for the ellipsoidal glider the varying distance from the axis of rotation creates a mismatch. To compensate, additional flow in z-direction is created where the radius and hence the velocity due to rotation is smaller, causing translation. As all bifurcations in our theory are symmetric under velocity reversal, this solution spontaneously breaks symmetry to decide in

which direction the glider starts to move.

4.3.5 Curved cell shape

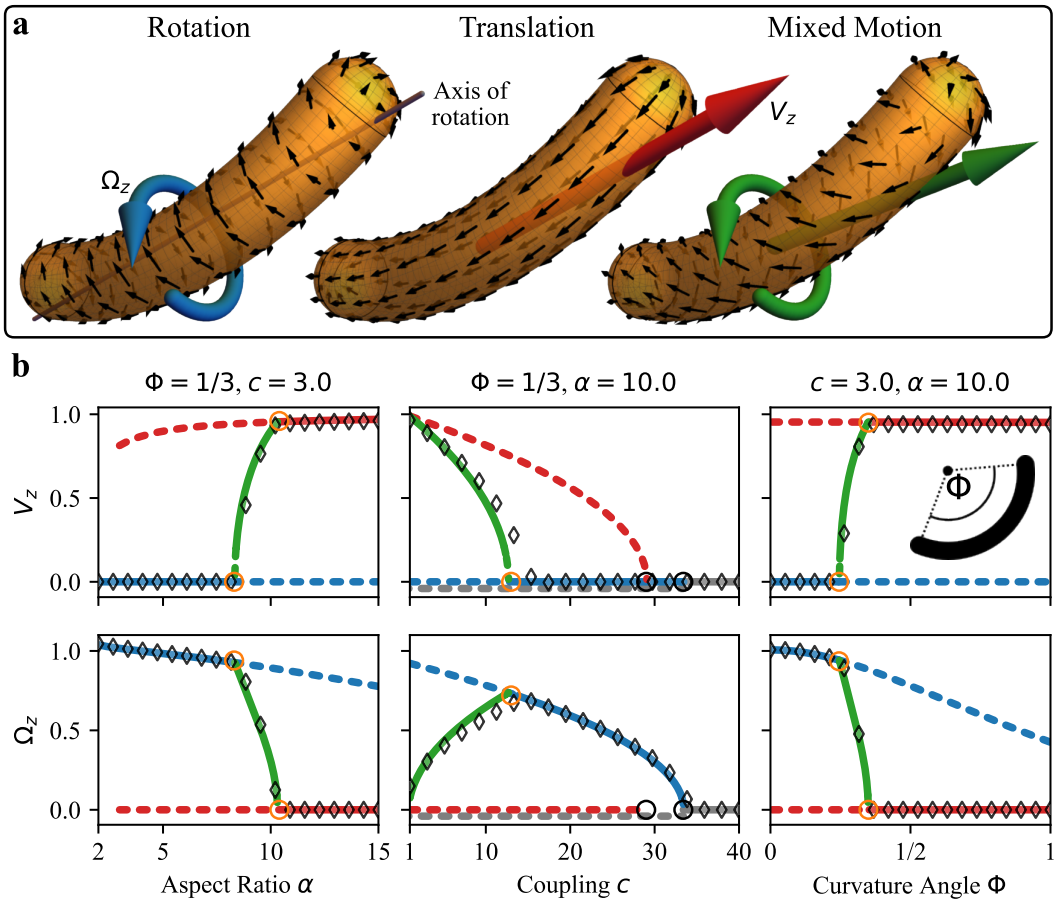

Figure 4.3: Steady-state solutions for a curved spherocylinder (segment of a torus with spherical caps), which breaks rotational symmetry, gliding in a 3D environment. **a:** The surface flows for the three types of solutions identified by the theory. **b:** Bifurcation diagrams. Top row shows velocity in direction of the long axis and bottom row angular velocity around that axis. Colors again as in a. The trivial solution is plotted in gray, but only in the middle column where it is displaced below 0 for better visibility where necessary, otherwise it remains unstable and is omitted. Dashed and solid lines are unstable and stable solutions, respectively. The bifurcation parameters are the aspect ratio α, the coupling c of the surface flow to the environment and the curvature angle Φ as described in the inset. The bifurcation diagrams are symmetric under sign change, only the positive branches are shown. Black circles mark pitchfork bifurcations from the trivial solution, orange circles pitchfork bifurcations between the displayed solutions. Diamonds are steady-states found by numerical simulation and are in excellent agreement with the analytical results.

The most obvious solution to overcome the pure rotation solution is to

break rotational symmetry of the shape, which is achieved e.g. by a curved rod. This immediately suggests that *Plasmodium* sporozoites have evolved curvature in order to avoid the stability of the rotational solution.

We define the geometry of the curved rod as a torus segment of curvature angle Φ, closed by spherical caps like the straight spherocylinder. The surface flow for this shape allows in principle the same three solutions as previously discussed and now shown in Fig. 4.3a. However, due to the curved shape, the rotational solution becomes coupled to a V_y contribution, offsetting the axis of rotation, while the translational solution becomes coupled to an Ω_y rotation, leading to circular trajectories. The mixed motion here has non-zero V_y, V_z, Ω_y and Ω_z, and because the coefficients are very complex combinations in the free parameters, the aspect ratio α, curvature angle Φ and coupling c, the solutions for the mixed state here were obtained as numerical roots of the polynomial Eq. 4.23.

To keep the bifurcation diagrams simpler, we only present the z-quantities in Fig. 4.3b. The dependent y-quantities are shown in Fig. 4.4. In general, we find that the mixed solution bifurcates from the rotational solution as before, but now leads into a stable translational solution with increasing aspect ratio or curvature, or decreasing coupling. Taking a closer look at the coupling in Fig. 4.3b, we notice that high coupling leads to another bifurcation of the rotational solution into the trivial solution. Opposed to the rotationally symmetric shapes, here the trivial state becomes stable at sufficiently high coupling, as the asymmetry prevents friction free rotation.

To represent the complete solution space of our theory, in Fig. 4.5 we have assembled phase diagrams. In Fig. 4.5a we show as a reference the phase diagram for the previously discussed ellipsoid, which has stability regions for both rotating (blue) and mixed (green) solutions. From the analytical solutions, the critical value of coupling $c_{\text{Crit.}}$ separating rotational and mixed solution can be approximated as

$$c_{\text{Crit.}}(\alpha) \approx \frac{8(\alpha-1)}{35} + \frac{596(\alpha-1)^2}{3675} + \mathcal{O}\left((\alpha-1)^3\right) , \tag{4.49}$$

which is shown in orange in Fig. 4.5a. From the phase diagrams for the curved spherocylinder, Fig. 4.5b-d, we see that now the solution with translation (red regions), which leads to circular trajectories, is very prominent. As before, there are also parameters for which only rotation can occur (blue regions). The mixed state (green region), which leads to helical trajectories, usually occurs

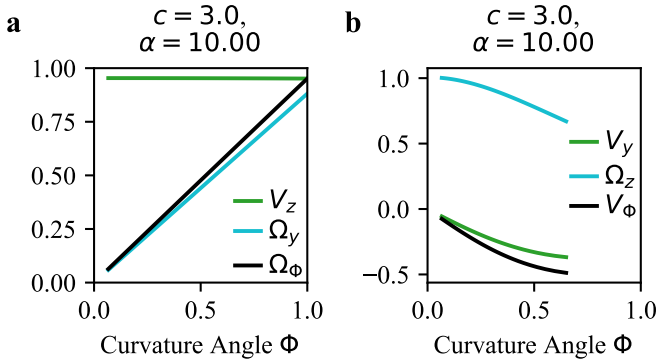

Figure 4.4: Dependencies of Ω_y, V_y (in Fig. 4.3, only V_z, Ω_z were shown) on curvature angle Φ. **a:** In the pure translating solution, the rotation around the y axis based on the V_z speed and the curvature angle Φ, where Ω_Φ is the rotation speed corresponding to circular trajectory of the identical radius as the underlying torus (cf. Fig. 4.3). The rotation around the y axis is only slightly below what is expected based on the V_z speed and the curvature angle Φ, i.e. the circular trajectory has slightly larger radius than the underlying torus. **b:** In the pure rotation solution, the Ω_z rotation causes a V_y velocity, where V_Φ is an estimate based on an assumed displacement of the origin from the axis of rotation of half the projected distance to the center of the spherical caps. The movement of the origin in y direction is at low curvatures well captured by assuming the axis of rotation is placed halfway between the origin and the centers of the spherical caps, putting the origin at distance $\propto \sin(\Phi/4)$. At higher curvatures, where the rotating solution is already unstable, the V_y speed becomes larger than predicted by this simple argument, indicating that the solution here resembles a translation in V_y direction.

as a transitional state between rotation and translation, with the transition taking place at higher curvatures for lower aspect ratios (Fig. 4.5c). This can be understood as the influence of curvature being more pronounced in a more slender shape. At high coupling and fixed curvature, Fig. 4.5b additionally reveals that the transition in aspect ratio can also have an intermediate regime where the trivial state is stable, i.e. a thick rod rotates, at an intermediate thickness the rod is motionless, and a thin rod translates. For fixed aspect ratio, the coupling determines if with increasing curvature the rotational solution transitions into the translational (low coupling) or trivial solution (high coupling). At the bifurcation points and boundaries more complicated solutions arise, including e.g. a rotation around an additional axis, which we omitted above as the stable solutions we discuss cover the vast majority of the phase space. In Fig. 4.5e we show one of the helical trajectories occurring in the mixed state (the blue and red lines track the center and an off-axis point on the surface, respectively). Such helical trajectories are precisely what we

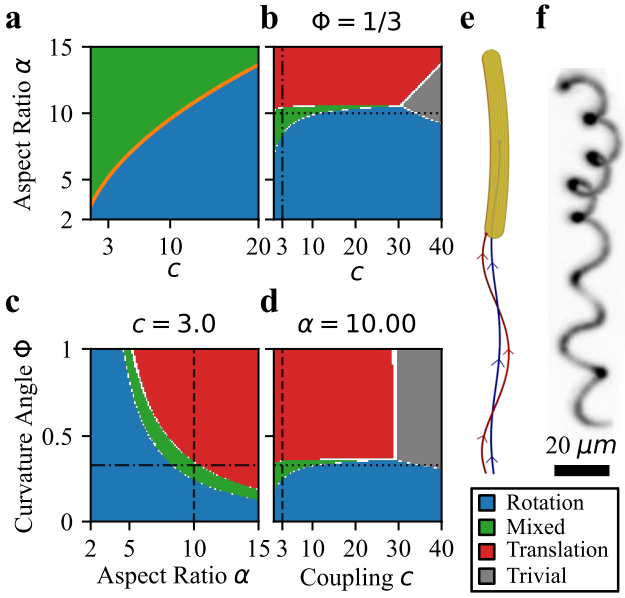

Figure 4.5: **a:** Phase diagram for the ellipsoid as a function of aspect ratio α and coupling c ($\zeta = 1/2$), showing the transition from stable rotating solution (blue) to stable mixed solution (green), with the analytical critical value Eq. 4.49 (orange). Compare Fig. 4.6 for different values of ζ. **b-d:** Cross sections of the parameter space of stable solutions for the curved spherocylinder, at fixed curvature angle Φ (b), coupling c (c) or aspect ratio α (d). Dash-dotted, dotted and dashed lines correspond to the planes intersecting each other and the conditions shown in the first, second and third column of Fig. 4.3, respectively. **e:** Helical trajectory of the mixed state at $\Phi = 1/3$, $c = 3$ and $\alpha = 10$, in blue the trajectory of the center, in red that of an off-axis point at the rear of the shape. **f:** Maximum intensity projection in z and time for fluorescence microscopy images of a *Plasmodium* sporozoite moving through a 3D hydrogel, exhibiting a helical trajectory. Data courtesy of Mirko Singer and Friedrich Frischknecht.

found in the 3D experiments in Chapter 2, and a close-up for an experimental example is shown in Fig. 4.5f.

4.3.6 2D gliding of apicomplexa

Many experiments on apicomplexa are performed on 2D substrates rather than in their natural 3D environments. Therefore we now consider the 2D case as a limit of our 3D theory (see Fig. 4.7a for schematics). To this end we have to make two changes: First, the geometry tensors $\mathcal{G}^{ij}$, $\mathcal{G}_2^{ijkl}$ and $\mathcal{R}^{ij}$, previously obtained by integration over the whole surface, are now computed only for the part of the glider's surface that is sufficiently close to the substrate to interact adhesively, described by a contact angle δ_S (cf. Fig. 4.7b). Second, assuming

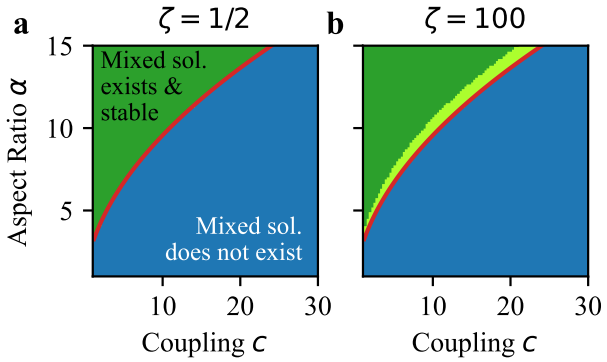

Figure 4.6: **a:** Phase diagram as Fig. 4.5 as a function of aspect ratio α and coupling c for the ellipsoid and low ζ, showing the transition from stable rotating solution (blue) to stable mixed solution (dark green). **b:** At high ζ an unstable mixed solution regime appears. While the existence of solutions does only depend on the combined parameter c, the stability can change by ζ. At high ζ values the mixed solution becomes stable only at even weaker couplings.

the body keeps maximal contact with the substrate, the degrees of freedom of the rigid body movement are restricted as explained below.

The curved spherocylinder on a substrate (Fig. 4.7a) resembles the well established 2D gliding assay as introduced for *Plasmodium* sporozoites in Chapter 2. We assume the body is oriented and stays oriented maximizing contact area, hence allowing only rotation perpendicular to the substrate. We find stable translation on shape dependent circular trajectories and analyze these by comparing the trajectory radius R_T to the glider's radius of curvature R_C. We find that generally R_T is larger than R_C. This effect is partly due to the friction at the caps generating torque against turning, hence increases with larger contact angle δ_S (Fig. 4.7c). Secondly, the flow on the inner side of the contact area has a slightly smaller effective radius, but the same target speed, resulting in an increasing trajectory radius for low coupling (Fig. 4.7d). The analytical prediction is once again confirmed by the simulation, showing that our theory can include subtle effects as the distribution of the force generation over different radii (i.e. inside vs outside of contact area) and the torque generated by friction at the spherical caps, all as a function of contact angle δ_S.

4.3.7 2D gliding of bacteria

Finally, we investigate the straight spherocylinder on a substrate, a situation resembling the geometry of gliding bacteria, which often move on 2D surfaces. *Flavobacterium johnsoniae* and *Myxococcus xanthus* are both known to rotate

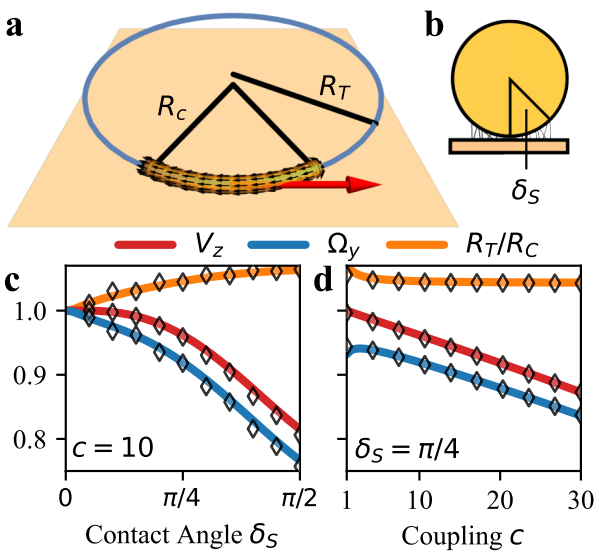

Figure 4.7: Gliding of a curved rod on a substrate at aspect ratio $\alpha = 10$ and curvature angle $\Phi = 1$. **a:** Schematics and definition of the trajectory radius R_T and radius of curvature R_C. **b:** Definition of the contact angle δ_S. **c,d:** Solutions and radius mismatch as function of contact angle δ_S (c) and coupling c (d).

while gliding on a substrate [194, 198, 203]. An ad hoc application of our theory finds again that the only stable solution is rotation in place (Fig. 4.8), without productive gliding. Because these microgliders are not curved and axisymmetric, other mechanisms must be at play to avoid the stability of the rotating solution.

From the assumptions made for the general 3D theory motivated by the apicomplexa, the most obvious aspect that does not fit to bacteria is the assumption that the motor-driven movement of the adhesins is isotropic. In fact it is well known that the propulsion of the adhesins in bacteria is more directed, often along internal tracks of a helical geometry as shown in Fig. 4.9a. We therefore start by introducing a small directional bias B to the motors, which is dimensionless and measured relative to the driving strength η, as introduced in Section 4.2.5.

In contact with the substrate, there is an additional effect on the bias to be accounted for. For a given surface contact angle δ_S (see Fig. 4.7), a certain location on the substrate only spends a fraction of δ_S/π in contact with the substrate, as the rod rotates. The analytical theory only models the part of the surface in contact with the substrate. If B is small, the bias will persistently act on the surface flow while it is not in contact with the substrate. As only the bias during contact is modeled, we have to account for the non-contact action of the bias by introducing an additional π/δ_S factor scaling the bias strength. This correction is no longer needed if the solution we look at is not rotating.

We can analytically solve the resulting dynamic equation for its stable states, depending on aspect ratio α, coupling strength c, contact angle δ_S and

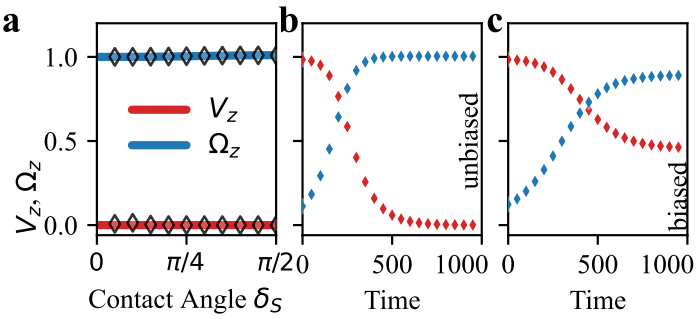

Figure 4.8: Spherocylinder gliding on a 2D substrate without bias. **a:** Bifurcation diagram for the analytical model coupled to the 2D substrate shows that only the rotating solution is stable without bias. Symbols are numerical simulations. **b:** Time evolution of V_z and Ω_z in a simulation, initialized close to a purely translating solution. **c:** Same as b, but now with a surface flow evolution biased in direction of the long axis, favoring the translational solution, resulting in a helical surface flow pattern with one way flow lines as displayed in Fig. 4.9.

bias strength B. For suitable parameters, a stable mixed solution as shown in Fig. 4.9b (compare Fig. 4.8) emerges. This demonstrates that anisotropic flow stabilizes forward motion. Furthermore, the flow field of the mixed state produce flow lines (green in Fig. 4.9b) that follow the observed helical track in bacterial surface flows in one direction.

Investigating the parameter dependence in more detail, the bifurcation diagram Fig. 4.9c demonstrates that effective motility can be obtained with small bias values of around 0.01, suggesting a small anisotropy is sufficient to shift the stable solution to mixed translation and rotation. At a finite bias, a pitchfork bifurcation occurs and the rotation vanishes completely. As discussed in Section 4.2.5, the stability theory introduced before remains valid for small B, but we can observe that the stability change of the pure translation branch after the pitchfork bifurcation at higher bias is not captured anymore, and corrections for the bias in the stability theory are necessary. The bifurcation as function of contact angle δ_S in Fig. 4.9d is largely the inverse, at large contact angle the higher friction at the caps favors rotation. This suggests a more rigid shape, which in reality reduces contact area due to reduced flattening, makes it easier to glide productively. The relation between coupling c and bias B in Fig. 4.9e shows that the higher the coupling the stronger the anisotropy has to be in order to obtain the same translational velocity. This is similar to a recently found trade-off in twitching motility of *Pseudomonas aeruginosa*, which need to balance their adhesion in order to avoid being ripped off the

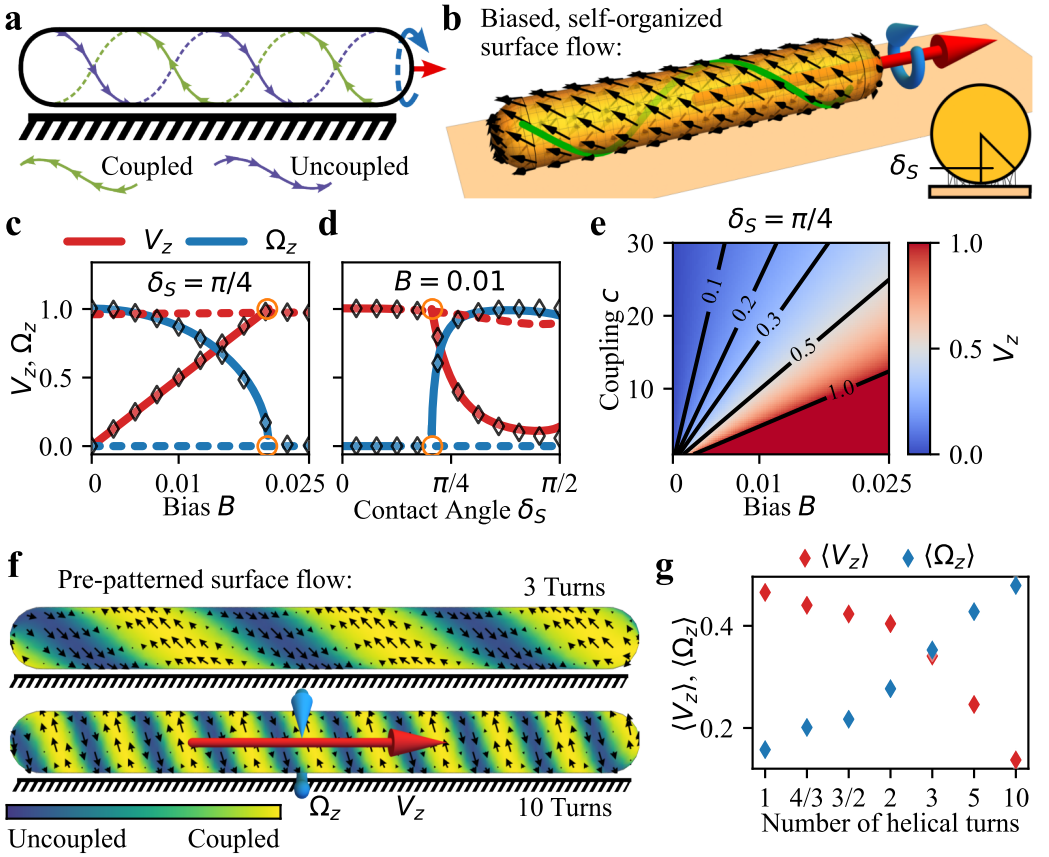

Figure 4.9: Bacterial gliding on surfaces. **a:** Schematic of the gliding of bacteria, gliding forward while simultaneously rotating. Experiments suggest *Flavobacterium johnsoniae* and *Myxococcus xanthus* organize the flow along opposing helical tracks, possibly with only one track coupled for productive motility. **b:** With a small bias along the long axis, we obtain self-organized surface flow patterns resulting in simultaneous rotation and translation. This generates the one-way helical flow lines along the surface (green) shown in a. Inset shows a cross section and the definition of the contact angle δ_S. **c:** Bifurcation diagram displaying the solutions for the translational velocity along (red) and rotational velocity around (blue) the long axis of the cylinder, as function of bias B with fixed $\delta_S{=}\pi/4$ and $\alpha{=}c{=}10$. Orange circles mark pitchfork bifurcations, and diamond symbols results of numerical simulations. **d:** Same as c, but now bifurcation diagram as function of contact angle δ_S at fixed bias $B{=}0.01$ **e:** Translational velocity in the coupling c vs. bias B phase space. **f:** Pre-patterned surface flow with helical pattern turning around the cell body in opposite directions as illustrated in a, with color map showing coupling strength. **g:** Resulting mean translational (red) and angular (blue) velocities for prescribed helical surface flows as shown in f.

surface, but still be able to migrate [210].

The helical surface flow lines used by this model are not closed, they only move from the front to the back. We can also consider a pre-patterning in the

model, replacing the self-organization with a detailed patterning of the surface flow consisting of intertwined bidirectional helical trajectories (Fig. 4.9f). The opposing tracks would generate forces canceling each other. We additionally assume that only one of the two directions is coupled to the substrate (Fig. 4.9a), a mechanism that was proposed and investigated for gliding bacteria in a simplified 1D model in [211]. Varying the number of helical turns along the cell length, the model can predict the corresponding motility patterns (Fig. 4.9g). The more helical turns are included, the more dominant rotational motion becomes compared to translation. The absolute pre-patterning is neglecting the dynamic component of the surface flow, but demonstrates that these surface flows, once established, are mechanistically consistent with the observed global motion.

4.3.8 Influence of additional terms in surface flow evolution

Within the numerical simulation, it is possible to investigate the influence of additional terms, which are omitted in the analytical treatment but suggested by Toner-Tu-like models for collective self-propelled objects (see Section 1.4.3). The first such term is a velocity advection term, as expected when a large part of the polarization is due to a mobile component, i.e. actin filaments. The second term is a neighbor alignment, which can be written as an effective diffusion of velocity. The equation for the surface flow evolution then becomes

$$\begin{aligned}\partial_t \mathbf{u}_{(\theta,l)} = & -\Gamma\left(\mathbf{u}_{(\theta,l)} - \mathbf{v}^{\parallel}_{(\theta,l)}\right) + \eta \mathbf{u}_{(\theta,l)}\left(1 - |\mathbf{u}_{(\theta,l)}|^2\right) \\ & - \lambda(\mathbf{u}_{(\theta,l)} \cdot \nabla)\mathbf{u}_{(\theta,l)} + D\nabla^2 \mathbf{u}_{(\theta,l)},\end{aligned} \tag{4.50}$$

where λ measures the strength of the advective term, and D is the diffusion constant of the velocity. For comparison, we define a rescaled, dimensionless D^*, rescaled by the timescale given due to coupling to the environment Γ, and estimated length scale of neighbor interactions $\alpha/10$ based on the shape radius α (for sporozoites, this corresponds to the length of actin filaments), such that $D^* = D/(\Gamma(\alpha/10)^2)$. We run simulations corresponding to the middle column of Fig. 4.3 to compare for the influence of these effects. We find no qualitative changes, only some quantitative derivation for larger diffusion constants (cf. Fig. 4.10).

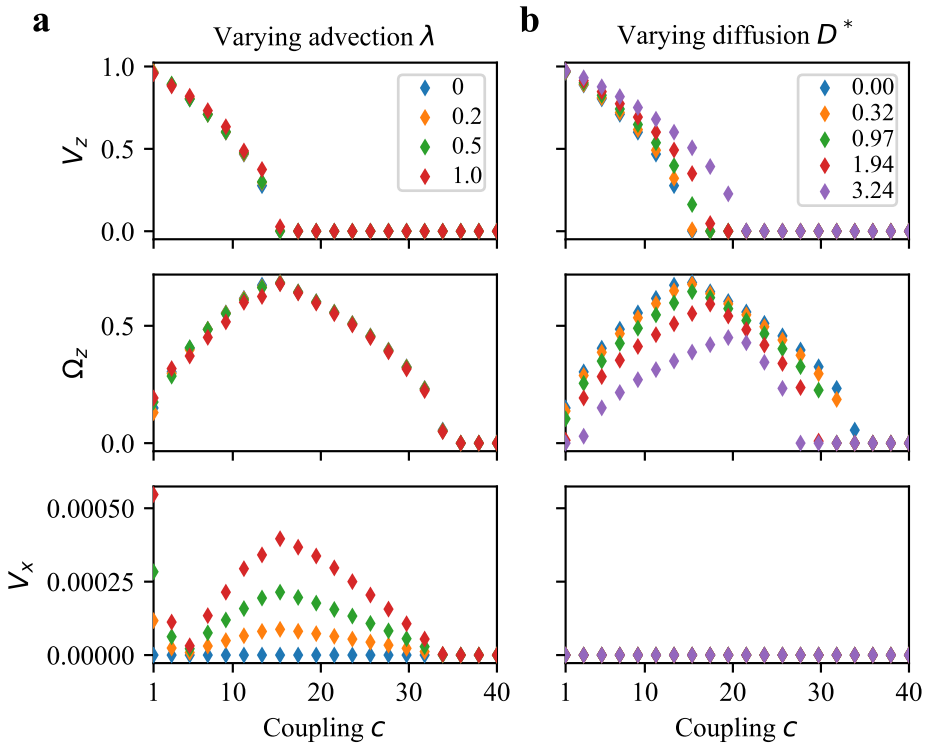

Figure 4.10: Steady-state solutions for a curved spherocylinder (segment of a torus with spherical caps), as Fig. 4.3, but obtained by numerical simulation of the extended surface flow evolution including velocity advection (**a**) and diffusion (**b**). Different velocity components V_z, Ω_z, and V_x are shown in different rows. Right column varies the advection strength λ from 0 (no advection) to 1 (full advection). Right column varies the diffusion constant D^*, which is the diffusion divided by the timescale set by the coupling to the environment Γ and the expected neighbor interaction length scale $\alpha/10$, where α is the shape's radius, $D^* = D/(\Gamma(\alpha/10)^2)$.

4.4 A simple special case: Diatoms

Diatoms are a large group of microalgae, encompassing around 200 000 species [212], living mostly in the oceans. They contribute a major part of the total biomass on earth and are estimated to perform 20 % of all photosynthesis on the planet [213, 214]. They protect their regularly 20–200 µm large bodies by a hard silicate shell, which can have a number of slits called raphes. It is through these raphes, which can vary widely in shape, that diatoms perform gliding motility, resulting in equally varying motility patterns [66].

The force generation within the cell is believed to be based on two fixed bundles of actin, on which mobile myosin motors run [215, 216]. In some sense this is inverted compared to the case of apicomplexan gliding, which utilizes

fixed myosins moving short actin filaments. How these forces are transduced to the substrate is not completely understood, but thought to use a combination of secreted mucus and adhesive strands that the diatom also uses to stick to the substrate [217, 218]. The raphe therefore defines a quasi 1D line of force generation, producing a 2D path as the diatoms glide on a glass slide. We can apply the mechanistic understanding of how local forces lead to whole cell motion developed in this chapter to explicitly compute this raphe to path geometry relationship.

4.4.1 Assumptions

1. The raphe is assumed to be a 1D feature, described by a line parameterized in 2D as $\vec{r}(s)$ (see Fig. 4.11). Here, s is parameterizing the position along the raphe. This can parameterize the whole raphe, or subsections of it that are regarded as in active contact with the substrate. The parameterization $\vec{r}(s)$ is relative to a reference point $\vec{r}_{\text{ref.}}$, i.e. the cell center. Later inferred trajectory information describes the trajectories of this point.

2. We assume that the active section of the raphe is producing a constant motion of the mucus layer in a single tangential direction. This velocity is in direction of the tangent $\vec{t}(s)$, with speed $\bar{v}$.

3. The whole cell moves as a rigid body with a translational velocity $\vec{V}$ and angular velocity (rotating around the reference point) Ω. As we are moving in 2D now, and assume the diatom is rotating only perpendicular to the plane, not around itself, Ω is a scalar. As before in Eq. 4.1, a point on the raphe at s is moved over the substrate due to the global motion of the cell as $\vec{V} + \vec{\Omega} \times \vec{r}(s)$ (where the 3D cross product is used by extension).

4. We assume a local force is produced at position s due to the friction of the mucus/adhesive strand motion relative to the substrate. That means the force is proportional (with a constant that we set to 1 here) to the resulting relative velocity, obtained by adding the velocity due to cell motion and the velocity of tangential motion of the motors in the raphe. If both velocities add up to zero, the adhesion point is stationary on the substrate, and no force is produced. Hence, we get the force density

$$\vec{f}(s) = \bar{v}\vec{t}(s) + \vec{V} + \vec{\Omega} \times \vec{r}(s) \ . \tag{4.51}$$

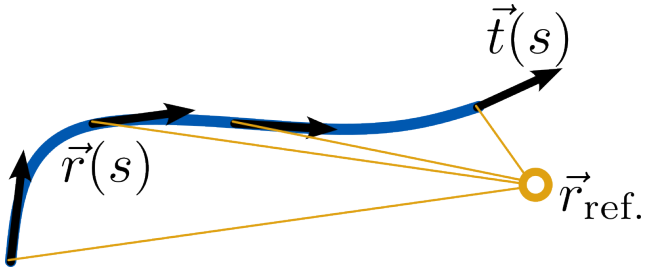

Figure 4.11: Schematics of an assumed active raphe segment (blue), described by parameterization $\vec{r}(s)$ relative to reference point $\vec{r}_{\text{ref.}}$, and with tangent vectors $\vec{t}(s)$

Based on this setup, we get the motion of the cell described by $\vec{V}$ and Ω, by enforcing global force balance,

$$\vec{F} = \int \vec{f}(s)\sqrt{g}ds = \int \left(\bar{v}\vec{t}(s) + \vec{V} + \vec{\Omega} \times \vec{r}(s)\right)\sqrt{g}ds = 0, \tag{4.52}$$

where $\sqrt{g}$ is the Jacobian determinant necessary if $\vec{r}(s)$ is not an arc-length parameterization. Because we assume a constant force per length, and not an adapting self-organization of the force generation machinery, this equation directly delivers a condition for $\vec{V}$ and Ω. Paired with an analogous condition for torque balance, we get three equations (as the force equation has two components, but we only have one relevant torque perpendicular to the plane), for three unknowns V_x, V_y, and Ω. The problem can be formulated as a 3×3 inhomogeneous linear matrix problem, where the matrix coefficients are dependent on the raphe geometry and can easily be computed by numerical integration. This problem (usually) has a unique solution, which gives us the velocity $\vec{V}$ and rotation around the reference point Ω that fulfill global force and torque balance. As both are constants, the resulting trajectory will be a circle (with the exception of either $\vec{V}$ or Ω vanishing, yielding a point or a line, respectively). The radius of the resulting circle is given as $R = |\vec{V}|/\Omega$.

4.4.2 Example results

Fig. 4.12 displays results for example shapes. Fig. 4.12a is modeled to agree with the experimentally observed end segment of the raphe of *Craspedostauros australis* [67]. In other, more academic examples we can see that if the raphe is a perfect circular segment (Fig. 4.12b), the trajectory will follow that arc. For more complex shapes, the precise radius of the resulting circle becomes harder to predict by eye (Fig. 4.12c). A publication using this model in combination with experimental results from collaborators in Dresden is in preparation as

publication 13.

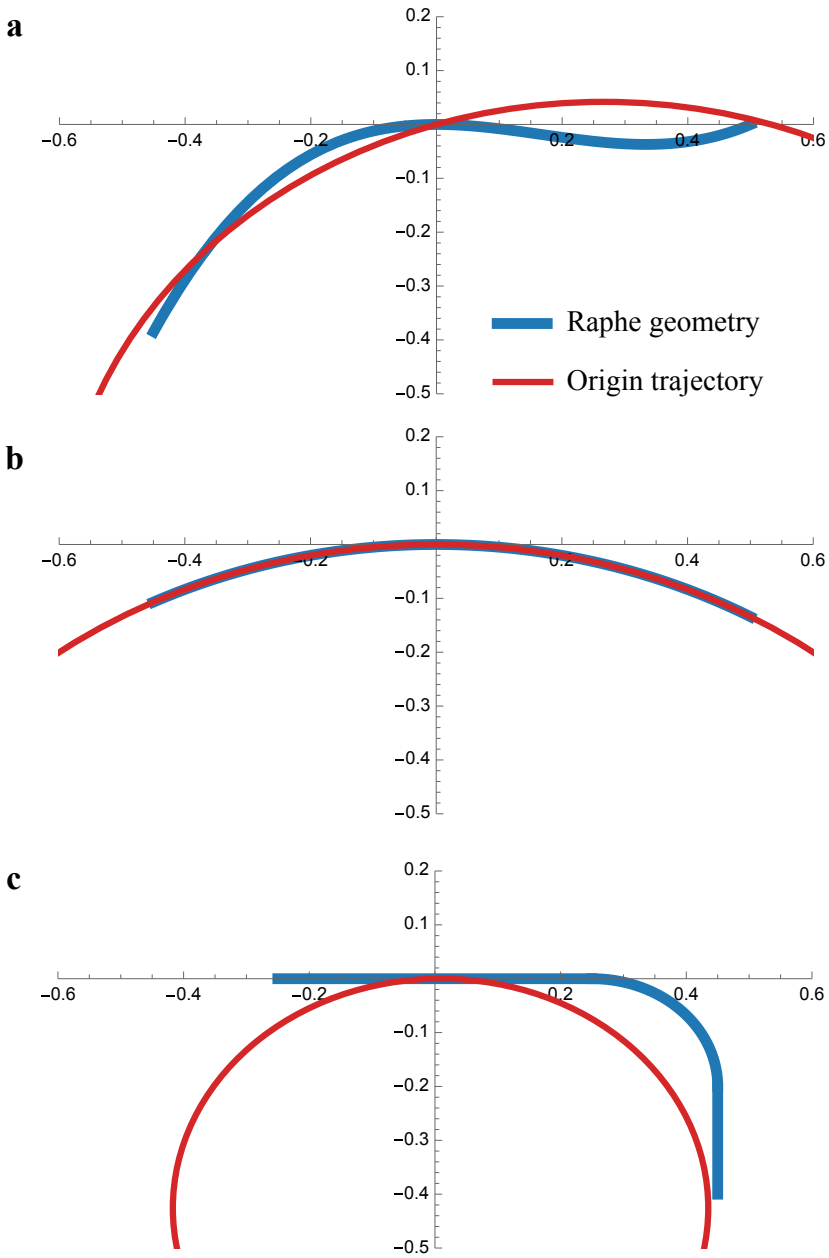

Figure 4.12: Examples of 3 shapes for the active raphe (blue) and the resulting trajectory of the reference point (here (0,0)) in red, in arbitrary units. **a:** Analytical shape roughly approximating the raphe towards the end. **b:** A circle segment of radius 1, where the trajectory aligns with the raphe shape. **c:** A straight leg meeting a circular segment.

4.5 Conclusion

In this chapter we have presented a universal and geometrical theory of how active surface flow leads to the motility patterns of microgliders. The overall thrust of this theory is similar to the question how the local movements of microswimmers lead to their large-scale motility patterns. We found that the central concept required to answer this question is the definition of geometrical quantities (the three geometry tensors $\mathcal{G}^{ij}$, $\mathcal{G}_2^{ijkl}$ and $\mathcal{R}^{ij}$), which capture the important influence of cell shape, and which have similar transformation properties like the resistance tensors for microswimmers. Otherwise, however, the underlying physics is very different and therefore we also find unique answers that have not been described before.

As we show here, the three geometry tensors can be calculated analytically for all shapes of interest, namely spherocylinders modeling rod-like bacteria, ellipsoids modeling bulky shapes like *Plasmodium* ookinetes and curved spherocylinders modeling *Plasmodium* sporozoites and *Toxoplasma* tachyzoites. Inserting them into the force balance, Eq. 4.23, we succeeded in analytically deriving stationary solutions and their stability, in excellent agreement with the results from numerical simulations.

Our theory reveals a tight interaction between rotation and translation for gliding microorganisms. In a simple axisymmetric shape, the rotational solution is dominant, and has to be suppressed for productive forward motion. This might be achieved by curved shapes, like for *Plasmodium* sporozoites. The curved shape of sporozoites leads to circular and helical trajectories. Helical trajectories allow for productive motility, but exist only in 3D environments, hence curved shapes might not be as favorable for organisms that require motility on 2D substrates. The helical trajectories of the mixed state of the curved spherocylinders resemble the experimentally observed motility patterns of *Plasmodium* sporozoites and *Toxoplasma* tachyzoites [114, 116]. Although other reasons exist that might have favored the evolution of such helical trajectories, like circling around blood vessels or efficient search strategies in complicated 3D environments [139, 219], or the heightened persistence discovered in Chapter 3, our universal theory makes a strong case for the need to avoid rotation by shape control. A notable exception seems to be the case of certain gregarines, which have been observed to glide on straight paths on 2D substrates [220]. However, at several hundred µm in length, these parasites are one to two orders of magnitude larger compared to gliding *Plasmodium* or *Toxoplasma* gliders,

thus several additional effects might come into play, most prominently the effects of cell deformability. Our theory assumes a rigid shape that leads to instantaneous information transfer across the whole cell body; in practice, even *Plasmodium* sporozoites are known to be rather flexible [140].

Another limitation of our theory is that helical trajectories emerge only for the mixed state of curved spherocylinders, while the phase diagrams from Fig. 4.5b-d show larger stability regions for rotating and circular solutions. This might be in part due to the assumption of a rigid shape. Allowing the shape to twist and adapt to the helical trajectory could widen the parameter region where the mixed solution is stable. We will explore this to some degree in Chapter 5. Generally, deformation is another layer of complexity to the motility situation, as many of the organisms described here are observed to deform, at times strongly, e.g. kink, during motility. However, they usually return to their prescribed shape rather quickly. Hence, we believe that our theory is a valid reference case, upon which deformability acts as an additional degree of freedom. The (in)stability behavior of deformability might open interesting insights into interactions with obstacles and path finding in constrained environments, but has to be studied by more complex numerical models.

We further note that our theory predicts bifurcations that are invariant under velocity reversal and therefore symmetric in regard to the direction of motion, while many biological systems of interest are polarized and favor one direction of motion (including a preference for a certain chirality). Yet our theory provides an interesting reference against which one now can discuss potential mechanisms to break this symmetry. An obvious one would be to abandon the isotropic activity of the motors and to give them a preferred direction; however, for sporozoites there is no experimental evidence in this direction. This suggests that the self-organized nature of the surface flow has other advantages; in particular, it might be needed to quickly switch motility patterns if the glider runs into a mechanically difficult situation. Another and possibly more likely way to control the direction of surface flow is the secretion of the adhesins, which is known to be strongly polarized in apicomplexa (secreted at the apical ring at the front and severed by enzymes at the back). This will also be investigated in the more detailed model in Chapter 5.

Extending the theory, developed for apicomplexa, to bacteria, which typically move on external surfaces, we find that also on 2D substrates the rotating solution is stable. For motility on a substrate, curvature as in sporozoites leads to circular trajectories, hence bacteria necessarily have to find another

solution to this fundamental constraint. We show that locally biasing the direction of the surface flow, which leads to helical surface flow fields, can accomplish this. Experimental observations suggest that the organization of the flow field enforced by bacteria might be more complex, featuring opposing helical tracks, which might be needed to ensure material transport in both directions. Pre-patterning such surface flows yields comparable resulting global motion within our theory. In both cases, the initial stability of the rotational solution is mirrored by the mixed nature of the resulting motion.

The general set-up of our theory allows to derive corollaries for related biological situations, for example the gliding of diatoms. Due to their fixed shell, with gliding forces only generated along the quasi-1D raphe, they present an excellent simplified example. An important difference from apicomplexans they share with bacteria is the missing cell polarity along the direction of movement, which leads to the frequent observation of reversals. This points to a stochastic component of the gliding machinery, which might assume bistable states moving in one direction for some time, but eventually flip direction. The simplified system of the diatom promises an excellent starting point of stochastic generalizations of the deterministic model we introduced here, including stochastic binding dynamics [221], and tug-of-war type direction determination [211, 222].

Due to its general nature, our theory should also be useful to design synthetic microgliders. Moving microorganisms are a great inspiration for the design of autonomous nano- and microrobots, and many different designs have already been suggested [223]. Gliding motility driven by surface flow of adhesins, like discussed here, has not been realized yet in this context, but the gliding motility of *Mycoplasma mobile* ghosts suggests that such designs might be possible [224]. One interesting avenue in this context might be the use of DNA-origami, which has strongly advanced over the recent decade as an extremely versatile approach to engineer molecular machines [225]. In particular, a synthetic DNA-glider has been engineered, in which DNA-nanotubes with different binding tracks, similar to the internal bacterial tracks discussed above, are propelled over a field of beating molecular motors [226]. It has been noted before that shape design of such DNA-origami will determine its gliding motility [227], but for more autonomous control of these microgliders, the motors should be placed on the surface of the object itself, similar to the case of *Mycoplasma mobile*.

In summary, our universal theory of gliding motility does not only explain many experimental observations, it also provides a useful reference to explain

deviations from our predictions and to identify the ways in which microorganisms have managed to avoid the fundamental physical constraints geometry imposes on gliding motility. Moreover, it might be helpful for the design of synthetic microgliders.

5

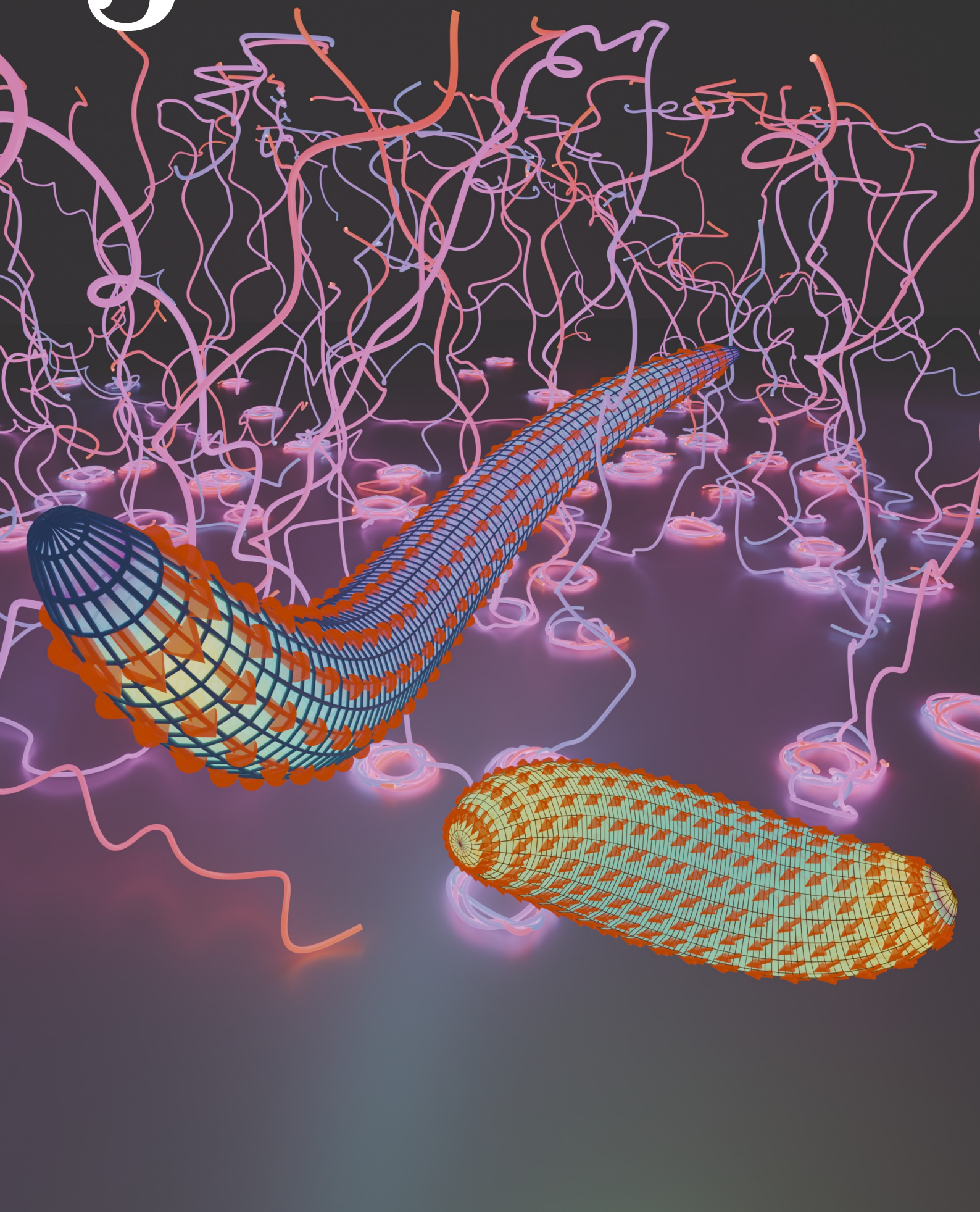

Chapter 5

Unraveling chirality with simulations, traction force and STED

This chapter is based on parts of publication 3, Lettermann, Singer et al., Nature Physics, in press.

5.1 Context

In this thesis, we have so far explored the motility of malaria parasites from different experimental and theoretical perspectives. In the experiments introduced in Chapter 2, we found regular, helical trajectories. These were the motivation for the two theoretical frameworks introduced thus far: In the active particle model in Chapter 3, we found that the stochastic nature of the force generation machinery can give rise to an advantage of persistence of helical compared to straight trajectories. Taking more detail into account, in Chapter 4 we saw that the curved shape can assist the self-organization of the surface flow to produce productive motility, also suggesting helical trajectories as a natural consequence of the needed curvature. In this chapter, we finally increase the level of detail in our modeling to the extent that we can directly compare it to the experimental data. Where the previous models suggested reasons for why helical trajectories were developed, here we shift to how these trajectories are achieved by the cell, and in particular where in the architecture of the parasite the observed chirality is encoded.

Revisiting the experimental results from Chapter 2, the most important observation is the overwhelming right-handed chirality of the 3D trajectories (Fig. 2.5). However, we will see that particularly the combination of 3D with 2D chirality is a powerful guide to finding the origin of chirality. We saw that while sporozoites turn counterclockwise on 2D glass assays, underneath the 3D gel they turn clockwise, as dictated by the right-handed 3D chirality (Fig. 2.8).

This, in particular, meant that sporozoites on glass are on their back, trying to invade the medium above.

Next to chirality, a second important experimental observation was the dependence of pitch and radius on each other, suggesting a relatively fixed curvature in contrast to varying torsion (Fig. 2.6). We will use this result, because we need to incorporate some degree of deformability to accurately represent the experiments, as we saw significant deformation of sporozoites. This is challenging, and to use torsion as the single deformable degree of freedom is an important simplification we can make based on these observations.

In this chapter, we will focus primarily on the specific chirality of *Plasmodium* sporozoites, only occasionally comparing it to ookinetes or *Toxoplasma* tachyzoites. Leaving the more general scope of the previous models, as well as choosing numerical over analytical approaches, allows us to construct a model that can be directly compared to the behavior of sporozoites in different environments. In the first part of this chapter, we will use this framework to investigate two different models for the origin of chirality, one based on a directional bias of the surface flow, the other on an asymmetric distribution of adhesins. Finding only the latter in agreement with all chirality observations listed above, we use this hypothesis to design two follow-up experiments. First, a two-sided traction force microscopy assay allowed us to distinguish forces on different sides of the sporozoite, finding a difference confirming the asymmetric distribution model. Secondly, STED super-resolution microscopy revealed that the apical ring complex, where the adhesins are released, is actually tilted toward the expected higher adhesin concentration, making this tilt a prime candidate for the architectural encoding of chirality.

5.2 Detailed numerical model of sporozoite motility

We first devised a theoretical model (Fig. 5.1) that allows us to test different possible scenarios. For that, we extend the mathematical model introduced in Chapter 4, that predicts how cell shape and actively generated surface flow determine the motion pattern of a gliding cell. We add several elements that become relevant in this context. First, in order to address the question of how adhesion molecules are distributed across the surface, we added a corresponding concentration field that couples to the flow field. Second, motivated by the observed variability in torsion, we added deformability to our model framework.

Since we focus on steady-state solutions, we do not explicitly model rapid shape changes, but use an iterative scheme: we first fix a shape and equilibrate the surface flow, then relax the shape given the new flow, and repeat until stable.

5.2.1 Theoretical framework to describe gliding motility based on shape, surface flow, and adhesion

We extend the analytical model from Chapter 4 with an adhesion field $b_{(\theta,l)}$, that describes the concentration of bound adhesins. This includes the assumption that there is no highly relevant binding/unbinding kinetics, and that adhesins are binding while at the front, and being cleaved in the posterior section by rhomboid proteases. This assumption is in agreement with previous observations of discrete adhesion sites [61].

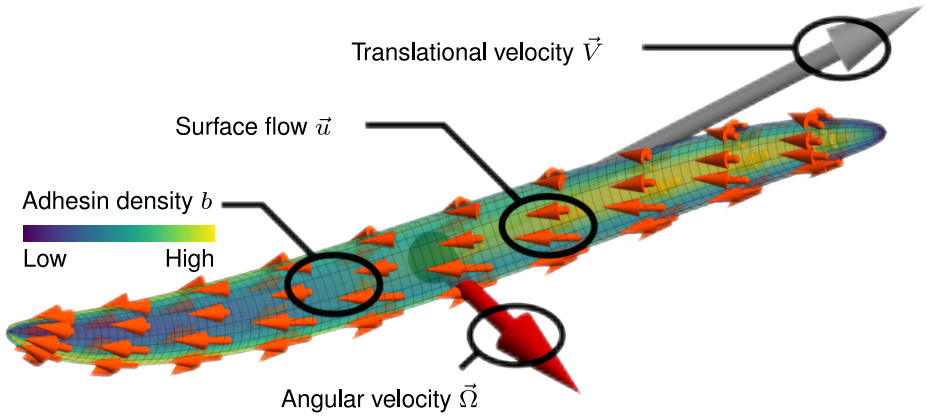

Figure 5.1: Theoretical model: vectorial surface flow field $\vec{u}$ (orange arrows) and the scalar adhesion density field b (colormap) together determine the global motion of the sporozoite described by translational and angular velocities, $\vec{V}$ and $\vec{\Omega}$.

In the following we present the detailed mathematical description of our model. Throughout this section, we use bold letters to describe two component vectors in the tangent bundle of the glider's surface (e.g. $\mathbf{u}_{(\theta,l)}$), and vector arrows to denote three component 3D vectors as the parameterization, $\vec{r}_{(\theta,l)}$. At every point on the surface a projection $P_{(\theta,l)}$ maps a 3D vector into the local tangent space. Describing the shape as a rigid body that moves with translational speed $\vec{V}$ and angular speed $\vec{\Omega}$, we can also use this projection to write down the relative speed of the substrate as seen from a surface element

on the sporozoite and its tangential and normal components as

$$\vec{v}_{(\theta,l)} = -\left(\vec{V} + \vec{\Omega} \times \vec{r}_{(\theta,l)}\right) \ , \quad \mathbf{v}^{\parallel}_{(\theta,l)} = P_{(\theta,l)}\vec{v}_{(\theta,l)} \ , \quad \vec{v}^{\perp} = \left(1 - P^{T}_{(\theta,l)}P_{(\theta,l)}\right)\vec{v} \ , \tag{5.1}$$

identical to Eq. 4.1 and 4.2 introduced in the previous chapter.

Surface dynamics

The two dynamical fields in our theory are the surface flow $\mathbf{u}_{(\theta,l)}$, which represents how adhesins move relative to the parasite surface under the action of myosin motors and the adhesion concentration $b_{(\theta,l)}$. The evolution of $\mathbf{u}_{(\theta,l)}$ is an extension of Eq. 4.5:

$$\begin{aligned}\partial_t \mathbf{u}_{(\theta,l)} + \lambda\nabla\cdot\left(\mathbf{u}_{(\theta,l)} \otimes \mathbf{u}_{(\theta,l)}\right) = \\ -\Gamma b_{(\theta,l)}\left(\mathbf{u}_{(\theta,l)} - \mathbf{v}^{\parallel}_{(\theta,l)}\right) + \eta\mathbf{u}_{(\theta,l)}\left(1 - |\mathbf{u}_{(\theta,l)}|^2\right) + D_{\mathbf{u}}\Delta\mathbf{u}_{(\theta,l)} - \chi_p\nabla b_{(\theta,l)} \ .\end{aligned} \tag{5.2}$$

Here, $\mathbf{u}$ tries to align with the local relative speed of the substrate $\mathbf{v}^{\parallel}$, with coupling proportional to b and a constant Γ, while the internal motor machinery sets a preferred magnitude of $\mathbf{u}$ with a strength η. The diffusion $D_{\mathbf{u}}$ is aligning nearby motors with each other. As the motors are fixed on the surface, there is no usual advection which would correspond to $\lambda = 1$, though there might be some transport of orientation in direction of the surface flow by the actin filaments, which can be modeled by choosing a small, non-zero λ.

The adhesion field is moved by the surface flow according to

$$\partial_t b_{(\theta,l)} + \ \nabla\cdot\left(b_{(\theta,l)}\ \mathbf{u}_{(\theta,l)}\right) = D_b\Delta b_{(\theta,l)} + b^{+}_{(t,\theta,l)} - c_{(\theta,l)}b_{(\theta,l)} \ . \tag{5.3}$$

The adhesion concentration b is generated near the apical region (where the adhesins are released and bind to substrate and actin), as modeled by a source field $b^{+}_{(t,\theta,l)}$, and then transported rearward by the surface flow $\mathbf{u}$. As adhesins are also cleaved more strongly at the posterior end (where rhomboid proteases act), the adhesin concentration obeys a spatially variable decay c proportional to its local concentration. Importantly, adhesins are transported with the flow, hence they are subject to a regular advection term. The diffusion of adhesins parameterized by D_b and the pressure gradient prefactor χ_p in Eq. 5.2 are chosen to be very small, as we consider b to describe bound adhesins, and mostly used for numerical stability.

Forces and global motion

At each surface element, the mismatch $(\mathbf{u}-\mathbf{v}^{\parallel})$ weighted by b produces frictional forces, with a friction coefficient γ, which reduces to the case from Eq. 4.6 for constant uniform adhesion. The shape of the glider is prescribed by a parameterization $\vec{r}_{(\theta,l)}$. With $P_{(\theta,l)}$ the projection into the tangent space, P^T, embeds a two-component tangent vector into 3D space, necessary to compare the local forces generated at different points. We then get the force generated by the tangential mismatch between substrate velocity and surface flow as

$$\vec{F}^{\parallel} = -\gamma \int dA\; b_{(\theta,l)} P^T_{(\theta,l)} \left[\mathbf{u}_{(\theta,l)} - \mathbf{v}^{\parallel}_{(\theta,l)}\right] \; . \tag{5.4}$$

The analogous normal component is independent of the surface flow, and we allow an additional scaling ζ (set to 1/2, see Section 4.2.3), to allow for differences in normal vs. tangential frictional behavior,

$$\vec{F}^{\perp} = \zeta\gamma \int dA\; b_{(\theta,l)} \vec{v}^{\perp}_{(\theta,l)} \; . \tag{5.5}$$

Including an additional $\vec{r}_{(\theta,l)}\times$ in these integrals allows to define the corresponding torques $\vec{M}^{\parallel}$ and $\vec{M}^{\perp}$. Assuming that we are in the typical overdamped regime, these force and torques prescribe the global motion $\vec{V}$, $\vec{\Omega}$, for a given surface flow configuration by demanding force and torque balance,

$$\vec{F}^{\parallel}(\mathbf{u}_{(\theta,l)}, b_{(\theta,l)}, \vec{V}, \vec{\Omega}) + \vec{F}^{\perp}(\mathbf{u}_{(\theta,l)}, b_{(\theta,l)}, \vec{V}, \vec{\Omega}) = 0 \tag{5.6}$$

$$\vec{M}^{\parallel}(\mathbf{u}_{(\theta,l)}, b_{(\theta,l)}, \vec{V}, \vec{\Omega}) + \vec{M}^{\perp}(\mathbf{u}_{(\theta,l)}, b_{(\theta,l)}, \vec{V}, \vec{\Omega}) = 0 \; . \tag{5.7}$$

Because adding an adhesion field greatly increases the complexity compared to the analytically solvable cases previously investigated in Chapter 4, here we perform a numerical solution. The code is written in JAX [175] as an extension of our earlier code that confirmed analytical results in simpler (non-adhesive) models (see 5.2.2).

Parameterizing the sporozoite shape

In our previous, analytical model, we used simple shapes like curved spherocylinders. Here, as we perform a numerical treatment and also want to encompass torsion as a second deformation next to curving, we are aiming for a more accurate and consequently more complex shape. In order to model apicomplexan gliders, in particular sporozoites, we use a curved, twisted ellipsoid.

Let the center line $c_{(l)}$ of this ellipsoid be given as a helix with radius R and screw parameter s (related to pitch p as $p = 2\pi s$), and the shape around this line have cross-sectional radius r_{CS} given as

$$c_{(l)} = \begin{pmatrix} R(1-\cos(l\phi_0)) \\ l\phi_0 s \\ R\sin(l\phi_0) \end{pmatrix}, \quad \phi_0 = \frac{1}{\sqrt{R^2+s^2}}, \quad r_{CS(l)} = \alpha\sqrt{1-4l^2}\ . \tag{5.8}$$

Here, l is the coordinate along the axis, normalized to $l \in [-1/2, 1/2]$, ϕ_0 is the angular extent of the shape along the helix, and α is the radius of the cross-section at its thickest position, in the center. Then, constructing tangential and normal vectors to $c_{(l)}$, a parameterization of the desired shape (where the rotation of the normal vectors is chosen such that the resulting coordinate system is orthogonal) is obtained with azimuthal coordinate θ:

$$\vec{r}_{(\theta,l)} = \begin{pmatrix} \alpha s\sqrt{\frac{1-4l^2}{R^2+s^2}}\sin\left(\frac{l}{\sqrt{R^2+s^2}}\right)\sin\left(\frac{ls}{R^2+s^2}-\theta\right) + \cos\left(\frac{l}{\sqrt{R^2+s^2}}\right)\left(\alpha\sqrt{1-4l^2}\cos\left(\frac{ls}{R^2+s^2}-\theta\right)-R\right)+R \\ \frac{ls-\alpha\sqrt{1-4l^2}R\sin\left(\frac{ls}{R^2+s^2}-\theta\right)}{\sqrt{R^2+s^2}} \\ \sin\left(\frac{l}{\sqrt{R^2+s^2}}\right)\left(R-\alpha\sqrt{1-4l^2}\cos\left(\frac{ls}{R^2+s^2}-\theta\right)\right)+\alpha s\sqrt{\frac{1-4l^2}{R^2+s^2}}\cos\left(\frac{l}{\sqrt{R^2+s^2}}\right)\sin\left(\frac{ls}{R^2+s^2}-\theta\right) \end{pmatrix} \tag{5.9}$$

From this parameterization (Fig. 5.1 shows one realization), other quantities like the local metric tensor or its partial derivatives $\frac{\mathrm{d}\vec{r}_{(\theta,l)}}{\mathrm{d}R}$ and $\frac{\mathrm{d}\vec{r}_{(\theta,l)}}{\mathrm{d}s}$ can be obtained by Mathematica. The notebook including these is provided in the simulation git repository (see Section 5.2.2).

Iterative scheme to equilibrate the geometry of gliders

The interaction between surface flow, geometry and the resulting forces is especially challenging if the sporozoite can deform, since its total movement and its shape changes are coupled degrees of freedom, both reacting to the forces created by the surface flow. Rather than looking for the fully dynamical shape evolution, which is very challenging [228, 229], we seek equilibrium solutions by alternating two steps:

1. Equilibrate the surface flow $\mathbf{u}(\cdot)$ and adhesion $b(\cdot)$ on a fixed shape.
2. Relax the shape based on the computed forces, and update its shape accordingly.

We model the sporozoite as a curved, twisted ellipsoid described by a curvature κ and a variable torsion τ, or equivalently radius and screw parameter as used in Eq. 5.8. Motivated by the findings in Fig. 2.6, we assume that the sporozoite

keeps a fixed curvature, such that we can reduce the deformation problem to a single degree of freedom, the torsion. The shape has a torsional elastic energy with modulus K_τ:

$$E_{\text{Torsion}} = \tfrac{1}{2} K_\tau \tau^2. \tag{5.10}$$

In each iteration step, we project local forces onto the torsional degree of freedom to see whether they favor increased or decreased torsion, iterating until an overall equilibrium is found. This yields a self-consistent shape, flow field, and adhesion distribution that can be used to predict the parasite's helical path.

5.2.2 Numerical solution and implementation

With the addition of adhesion and the more complex shapes including deformability a numerical simulation framework has to be used to solve the equations. It was custom implemented in JAX [175], which allows for just-in-time compilation of code and hence performant execution. The sporozoite shapes were discretized with 20 points around their circumference and 91 points along their axis, and subsequently finite difference schemes were used to implement the dynamics of the dynamical fields $\mathbf{u}_{(\theta,l)}$ and $b_{(\theta,l)}$ on the 2D geometry defined by the parameterization. Laplace-Beltrami operators with 5-point stencils were used for diffusion terms, at the poles, coordinates where continued using methods from [230]. The advection terms were implemented using a first-order upwind scheme in curvilinear coordinates. As we are only investigating equilibrium behavior here, the finite difference scheme is sufficient, especially as it makes implementation of the global constraints and deformation easier and faster compared to finite element approaches that were used for similar (but not including substrate interactions and deformability) dynamical theories of actin flocking on curved surfaces in *Toxoplasma* [117, 142]. The code for the simulations, visualizations, as well as the implementation of the iterative deformation equilibration scheme, is available on GitHub at `https://github.com/LeonLettermann/hei-sporo-code-simulation`.

5.2.3 Two different mechanisms to explain 3D chirality

The described motion patterns of *Plasmodium* sporozoites differ from the ones known from other apicomplexan forms like *Plasmodium* ookinetes and *Toxoplasma* tachyzoites. Both parasite forms have been reported to run on left-handed helices in 3D gels [113, 115], implying they circle CCW when contacting

a rigid boundary from above. In 2D and in medium, both prefer CCW motion if they circle, signifying a distinctly different chirality behavior than *Plasmodium* sporozoites. To better understand why this case differs so strongly from the others, we set out to identify its origin. Our comprehensive model framework now allows us to define two fundamentally different models that are informed by experimental observations and can explain chirality in the gliding motility of apicomplexa. We start defining the models and presenting their conclusions, with estimated simulation parameters and details on the deformation procedure used given at the end of this section.

In model I (chiral flow), we assume that surface flow is not isotropic, but has a chiral bias (Fig. 5.2a). Structurally, this model requires the motors to exert forces in certain directions, e.g. because their orientation is biased by the underlying microtubule system. In fact this seems to be likely for the cases of *Plasmodium* ookinetes and *Toxoplasma* tachyzoites, which have a twisted corset of microtubules. Similar mechanisms also seem to be at work for some types of gliding bacteria, which seem to have fixed internal helical tracks [194, 203].

In model II (asymmetric distribution), we assume that chirality arises from an asymmetric distribution of adhesion molecules (Fig. 5.2b). This asymmetry could arise from the known tilt of the apical ring [104], which might lead to an asymmetry in the secretion of adhesins at the apical ring. This case might specifically apply to *Plasmodium* sporozoites, because their microtubule corset is straight and because they are the only apicomplexan parasite form with a tilted ring.

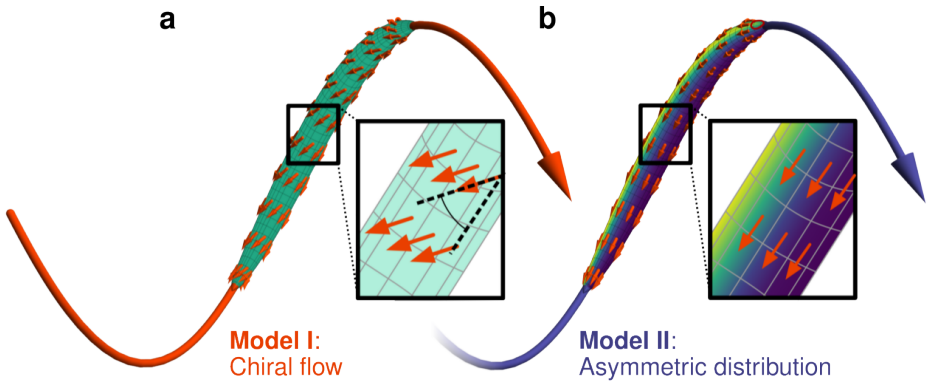

Figure 5.2: **a:** Chiral flow model (model I): directional bias in the surface flow of adhesins can produce chiral helical trajectories. **b:** Asymmetric distribution model (model II): asymmetric adhesin release or binding creates a biased distribution of force generation which can result in chiral helical trajectories.

For model I (chiral flow), the bias to the direction of the surface flow **u**

was included as a preferred direction, conferred by an angle ϕ_{Bias}, and a bias strength B_{Bias}. These were included in Eq. 5.2 as an additional term of the form

$$\partial_t \mathbf{u}_{(\theta,l)} = \ldots - \left| B_{\text{Bias}} \mathbf{u}_{(\theta,l)} \times \hat{\mathbf{e}}(\phi_{\text{Bias}}) \right| \frac{\mathbf{u}_{(\theta,l)} \times \hat{e}_n}{|\mathbf{u}_{(\theta,l)}|} , \tag{5.11}$$

where we use the cross product with the two-component vector $\hat{\mathbf{e}}(\phi_{\text{Bias}})$ by appending zeros to specify an angle, and the cross-product of the two-component vector $\mathbf{u}$ with the orthogonal three-component vector $\hat{e}_n$ to rotate by $\pi/2$. For the chiral flow model, we used an angle of $\phi_{\text{Bias}} = \pi/6$, i.e. a 30° angle offset from the straight backwards direction.

For model II (asymmetric distribution), the asymmetry of the release of adhesins at the tip of the parasite is controlled by an asymmetry parameter A_{Release}, such that the profile of release (up to normalization) in the θ coordinate is given as

$$b^{+}_{(t,\theta,l)}(\theta) = A_{\text{Release}} \exp\left[-\left(1 - \cos\left(-\pi/2 + \theta\right)\right)/2 \right] + \left(1 - A_{\text{Release}}\right) , \tag{5.12}$$

interpolating between a strongly one-sided ($A_{\text{Release}} = 1$) and uniform ($A_{\text{Release}} = 0$) angular distribution.

Simulation results for 3D chirality

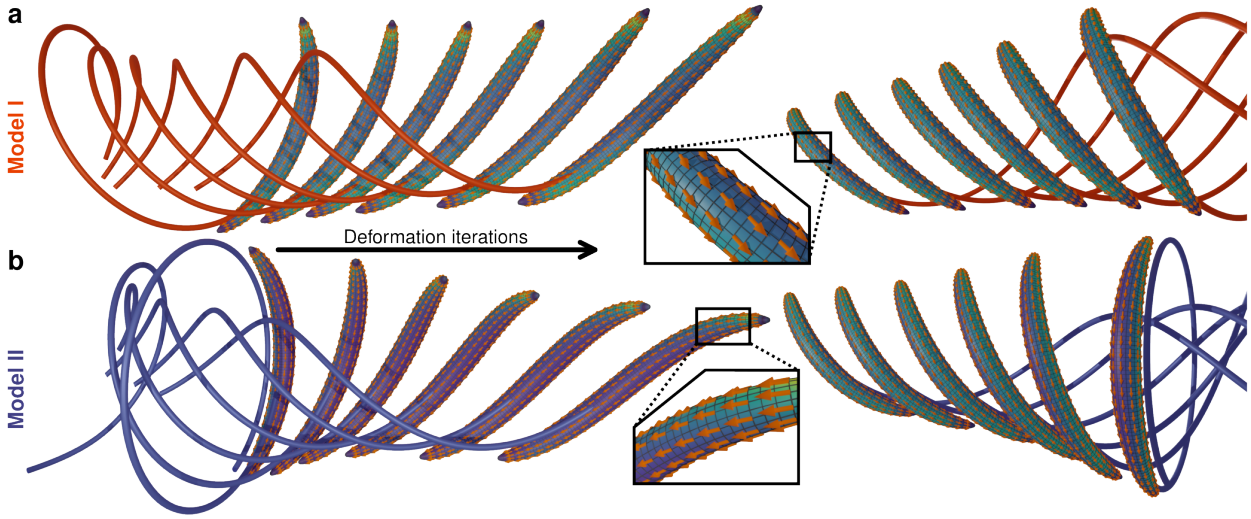

Figure 5.3: Results of numerical simulations alternately equilibrating surface flow configuration and parasite shape, shown are the first five and the final iterations for model I (**a:**; chiral flow) and model II (**b:**; asymmetric distribution). Left and right are two views on the same configurations.

Using our computer simulations, we first checked that both models can

reproduce the experimentally measured trajectories for reasonable parameter values (Fig. 5.3). In model I (chiral flow), the sporozoite can achieve the target pitch of the trajectory with comparatively less torsion of the shape, because the flow itself already induces twisting. In Fig. 5.3a, an untwisted shape still follows a significantly helical path. By contrast, in model II (asymmetric distribution), the untwisted shape circles with almost zero pitch ($p \approx 0$) (Fig. 5.3b), so the sporozoite shape must twist more to match the measured trajectory pitch. Here, we find the more adhesive side on the back (dorsal side) of the sporozoite, which predicts that the apical ring faces backwards.

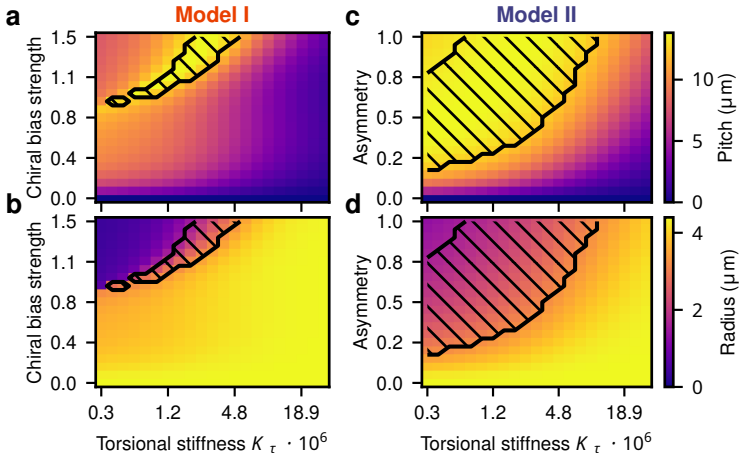

Figure 5.4: Resulting pitch (**a:**,**c:**) and radius (**b:**,**d:**) (color coded, color map given to the right) of the shape after equilibrating for different torsion stiffness K_τ (relative to the adhesion strength) and chiral flow bias (a,b; model I) or adhesin release asymmetry (c,d; model II). Shaded areas are within 33 % of experimentally found values.

We next examined how each model responds to changes in parameters. Model I exhibits a strong variation of pitch (Fig. 5.4a) and radius (Fig. 5.4b) with torsion stiffness and chiral flow bias, achieving the high pitches observed experimentally only in a narrow parameter subset. Model II is smoother (Fig. 5.4c,d) and has a larger parameter regime consistent with the experimental data. Because the sporozoite is quite slender, it has only a short lever arm for any lateral force. Thus, in a chiral flow scenario, the flow bias must be precisely tuned to avoid high torsion regimes where pitch/radius are too small (upper-left region of Fig. 5.4a,b). This sensitivity is also visible in Fig. 5.5a,b, which compares pitch/radius of the shape itself to that of the resulting trajectory, revealing a mismatch for the chiral flow as discussed before. Lastly, the coupling parameter c, determining the ratio of environment coupling to motor driving in the model, mostly affects velocity (Fig. 5.5c), without strongly altering

geometry, unless it becomes so large to stall gliding (Fig. 5.7).

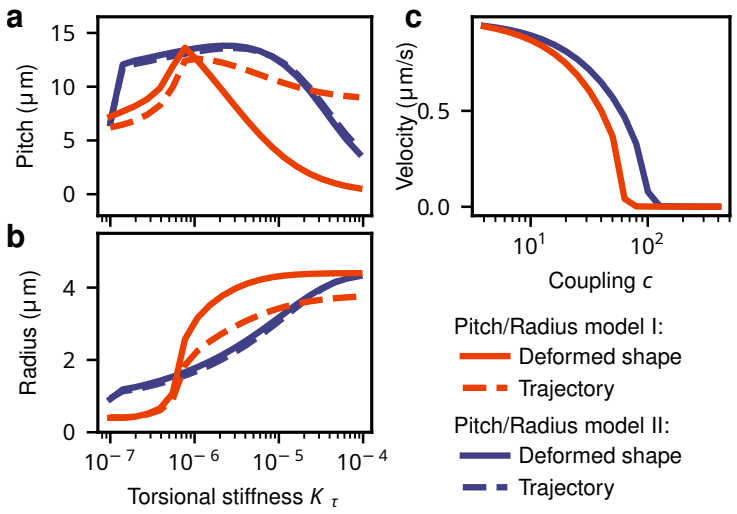

Figure 5.5: **a,b:** Resulting pitch (a) and radius (b) as in Fig. 5.4, but at fixed chiral flow bias (model I) or adhesin release asymmetry (model II). Dashed lines show similarly the pitch and radius of the resulting trajectory, which can deviate from those of the shape. **c:** Velocity as function of the coupling parameter c, which is the quotient of coupling to the environment and driving strength of the motor machinery.

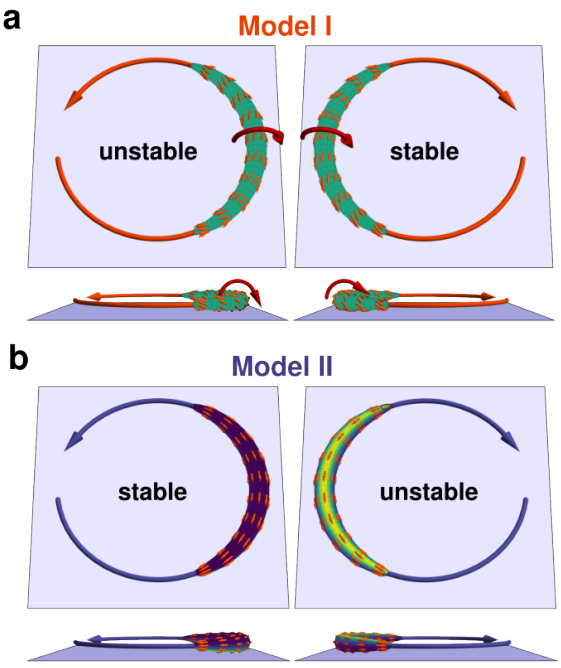

Figure 5.6: Models for right-handed 3D chirality make opposite predictions for 2D chirality on a substrate covered in medium only. The chiral flow model (**a**) produces a torque rendering CCW motion unstable. The asymmetric distribution model (**b**) is stable if the more adhesive/active side is facing towards the substrate, rendering CW motion unstable as observed experimentally.

Chirality models suggest opposite 2D chirality

Having established our models in 3D, we next used them to predict motion patterns in 2D. We found that model I predicts a torque that renders CCW motion on a 2D substrate unstable (Fig. 5.6a), while CW motion would be stable. In contrast, model II stably supports CCW rotation, where the more adhesive side is against the substrate (Fig. 5.6b), as experimentally observed. Model II also explains the unintuitive result that sporozoites attempt to move upwards from the glass in 2D: in 3D, the back side of the parasite has more adhesins, generating right-handed helices. In medium, the parasite circles on its back, which is more adhesive and in direct contact with the glass.

Estimating parameter values for chirality models

The undeformed reference geometries for both the sporozoite and toxoplasma/ookinete case were constructed with the same parameterization Eq. 5.9, but different sets of parameters as specified in Tab. 5.1. Note that for use with the non-dimensionalized versions of the equations, these parameters were converted to units rescaled by the length of a parasite of around 10 µm.

Model	R	s	α
Sporozoite	4.4 µm	0 µm	0.4 µm
Toxoplasma/Ookinete	4.7 µm	0 µm	1.5 µm

Table 5.1: Parameters specifying the geometry of gliders, with data for sporozoites estimated from [61, 139], and for Toxoplasma from [117].

The parameters for the surface dynamics, in the dimensionless formulation of the equations based on L=10 µm, the shape length, and T=10 s, such that the target speed of the surface flow is 1), are given in Tab. 5.2. For the steady-state, only the coupling parameter $c = \zeta\Gamma/\eta$ (with $\zeta = 1/2$) is relevant, not their individual values as found in Section 4.2.3. The relative values of Γ and η are chosen to get the correct resulting movement velocity (Fig. 5.7), while absolute magnitudes control the timescale of the dynamics, chosen suitable for our numerical simulations as we are only interested in the equilibrium configurations. Here, we chose $\Gamma = 10$ such that the timescale of the surface flow adapting to the environment is T_Γ =0.1 T.

The diffusion coefficient $D_{\mathbf{u}}$ describes the alignment of nearby motors, which primarily happens if they are coupled to the same actin filament. The actin filaments are around 100 nm=0.01 L in length, and if motors are bound to the

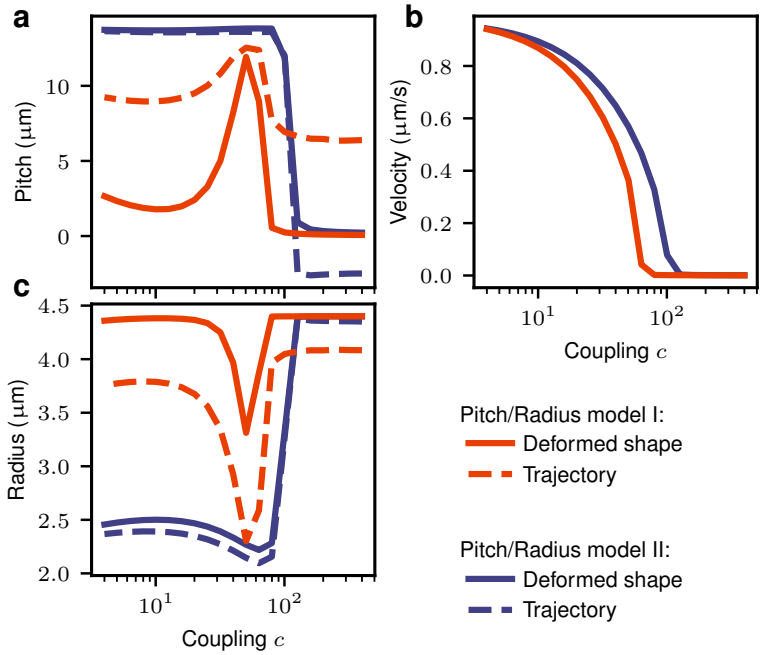

Figure 5.7: The resulting pitch (a), velocity (b) and radius (c) of the shape and the trajectory as obtained from numerical simulations after equilibration and as function of varying coupling strength c.

same actin filament alignment should happen on a similar timescale as alignment via the environment (as given by T_Γ), hence we estimate $D_{\mathbf{u}} = (0.01\,\mathrm{L})^2/0.1\,\mathrm{T} = 0.001\,\mathrm{L}^2/\mathrm{T}$. The advection parameter λ controlling the orientation transport with the flow was set at $\lambda = 0.1$, to include some transport, but the simulation for alternatively $\lambda = 0; 1$ did not show a strong influence of this choice (Fig. 5.8).

For the adhesion, diffusion constants (D_b) and pressure response (χ_p) are believed to play a minor role, as our adhesin field explicitly models adhesins bound to the environment, which are mostly fixed. Therefore, the small values used were chosen for numerical stability. Changing the different parameters for comparing the simulations inevitably changes the surface flow configuration, and, at fixed $b^+_{(t,\theta,l)}$ and c, thereby the overall abundance of adhesins. That in turn has a similar effect as changing Γ, and can heavily alter the behavior, for example increasing the effective Γ to a level where the motion arrests (Fig. 5.7). To avoid this, we regulated the adhesin release $b^+_{(t,\theta,l)}$, such that the average density of adhesins on the surface was always 1.0.

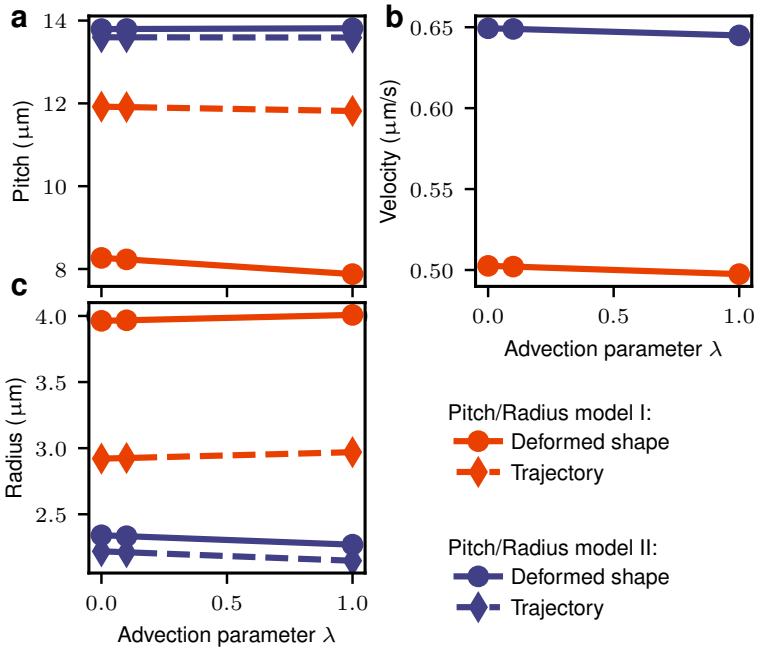

Figure 5.8: The resulting pitch (a), velocity (b) and radius (c) of the shape and the trajectory as obtained from numerical simulations after equilibration and as function of varying surface flow advection λ.

Parameter	Γ	η	$D_{\mathbf{u}}$	λ	D_b	χ_p
Value	10	0.125	0.001	0.1	1×10^{-6}	1×10^{-5}

Table 5.2: Parameters of the surface dynamics, in dimension-free units based on L=10 µm and T=10 s.

Estimating deformation forces in iterative equilibration

At this point, we review the technical details of the procedure to iteratively equilibrate of the deformation used to obtain the results above. We aim for a simplified description, which allows us to estimate equilibrium shapes, i.e. we look for configurations where the shape naturally follows the motion prescribed by the surface flow. Trying to naively decouple global motion and deformability, we compare two approaches: First, computing the deformation force before any reaction of the global motion, i.e. we assume a local force is created at each surface element by the surface flow while the shape is kept at rest,

$$\vec{f}^{\,\text{rest}}_{(\theta,l)} = -P^T_{(\theta,l)}\mathbf{u}_{(\theta,l)} \ . \tag{5.13}$$

This is a very rough estimate, because usually most of the forces created by the surface flow should result in motion instead of deformation. Alternatively, we

can take first the global motion ($\vec{V}$,$\vec{W}$) computed by global force balance of the rigid shape as before, and afterwards compute the local force as the mismatch of the surface flow with the resulting tangential velocity,

$$\vec{f}^{\,\text{moving}}_{(\theta,l)} = P^T_{(\theta,l)} \left(\mathbf{u}_{(\theta,l)} - \mathbf{v}^{\parallel}_{(\theta,l)} \right) \ . \tag{5.14}$$

This includes the global motion, but needs to encompass an additional minus to agree qualitatively with the previous estimate as shown below and allow equilibration, most likely because the a priori equilibration of the global motion for the rigid shape overestimates the reduction of the forces for deformation.

To compare these two approaches, we first map the field of local forces to a single effective force on the sporozoite's torsion. Given our parameterization Eq. 5.9, we can project either of the local forces defined above to a local contribution of force affecting the shape radius R and screwness s using the partial derivatives of the parameterization. Integrating yields effective forces on R and s,

$$F_R = \int dA\, \vec{f}_{(\theta,l)} \cdot \frac{\mathrm{d}\vec{r}_{(\theta,l)}}{\mathrm{d}R} \qquad\qquad F_s = \int dA\, \vec{f}_{(\theta,l)} \cdot \frac{\mathrm{d}\vec{r}_{(\theta,l)}}{\mathrm{d}s} \tag{5.15}$$

As we want fixed curvature and varying torsion, we project these forces onto an effective force that changes the torsion, and combine it with the contribution given by the torsional energy $E_\tau = \frac{1}{2} K_\tau \tau^2$ to obtain

$$F_\tau = \frac{\mathrm{d}R}{\mathrm{d}\tau} F_R + \frac{\mathrm{d}s}{\mathrm{d}\tau} F_s - K_\tau \tau \,, \tag{5.16}$$

where the last term models the elastic relaxation towards the untwisted ($\tau = 0$) state.

To compare the two different schemes of estimating the effective local deformation force above, in Fig. 5.9 we analyze F_τ for $K_\tau = 0$. As expected, we find the force if computed with respect to the shape at rest around two orders of magnitude larger than if we take the forces including the global motion of the rigid body. Moreover, we generally see a decrease for both forces and both models with increased torsion. However, this decrease is much more notable for model II, the asymmetric distribution model, compared to model I, the chiral flow model. As this difference between the models is also similarly observed for both introduced schemes for estimating the local force, we conclude that our observation above that model I requires more finely tuned relation between bias strength and elastic constant K_τ holds for both schemes. In order to include

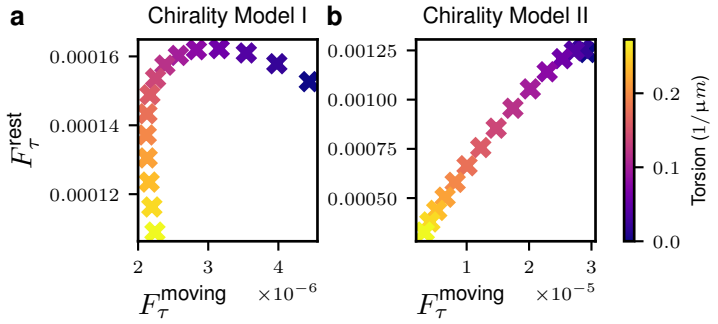

Figure 5.9: Effective torsion deformation force F_τ computed without taking global motion into account (F_τ^{rest}) and (sign-flipped) force computed from the velocity mismatch $\mathbf{u} - \mathbf{v}^{\parallel}$, that is with the shape performing rigid body motion (F_τ^{moving}), for the chiral flow (a) and asymmetric distribution (b) model for different torsions of the shape in color (untwisted, blue; twisted, yellow).

the global motion, we used the local force $\vec{f}_{(\theta,l)}^{\text{moving}}$ for our equilibration scheme. If one would instead use the other scheme based on $\vec{f}_{(\theta,l)}^{\text{rest}}$, similar results would be obtained, except the torsional stiffness K_τ would be about two orders of magnitude larger.

With this choice, we can use this force F_τ to alternately update the torsion of the shape, and the surface flow and adhesin configuration on the deformed shape. Once this scheme converges, we have obtained an estimate for the equilibrium shape and flow configuration. Note that the absolute values of K_τ as shown in Fig. 5.4 depend on the local force scheme chosen, and it is only used as an effective elastic torsional stiffness to compare the behavior of different surface dynamics and cannot be easily related to the actual stiffness of the parasite.

5.2.4 Comparison to other apicomplexan gliders

Figure 5.10: **a:** Schematics of predicted *Toxoplasma* or ookinete movement under gel (cf. Fig. 5.11). **b:** Schematics of predicted motion of *Toxoplasma* or ookinete in medium.

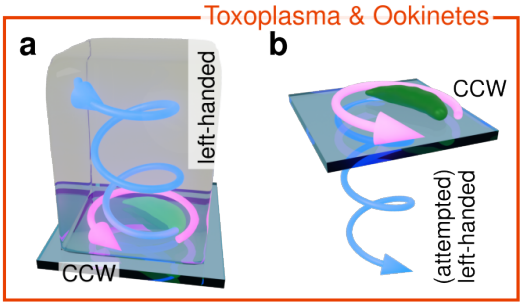

The results above strongly indicate that indeed model II seems to apply to *Plasmodium* sporozoites. However, remembering the different chirality for

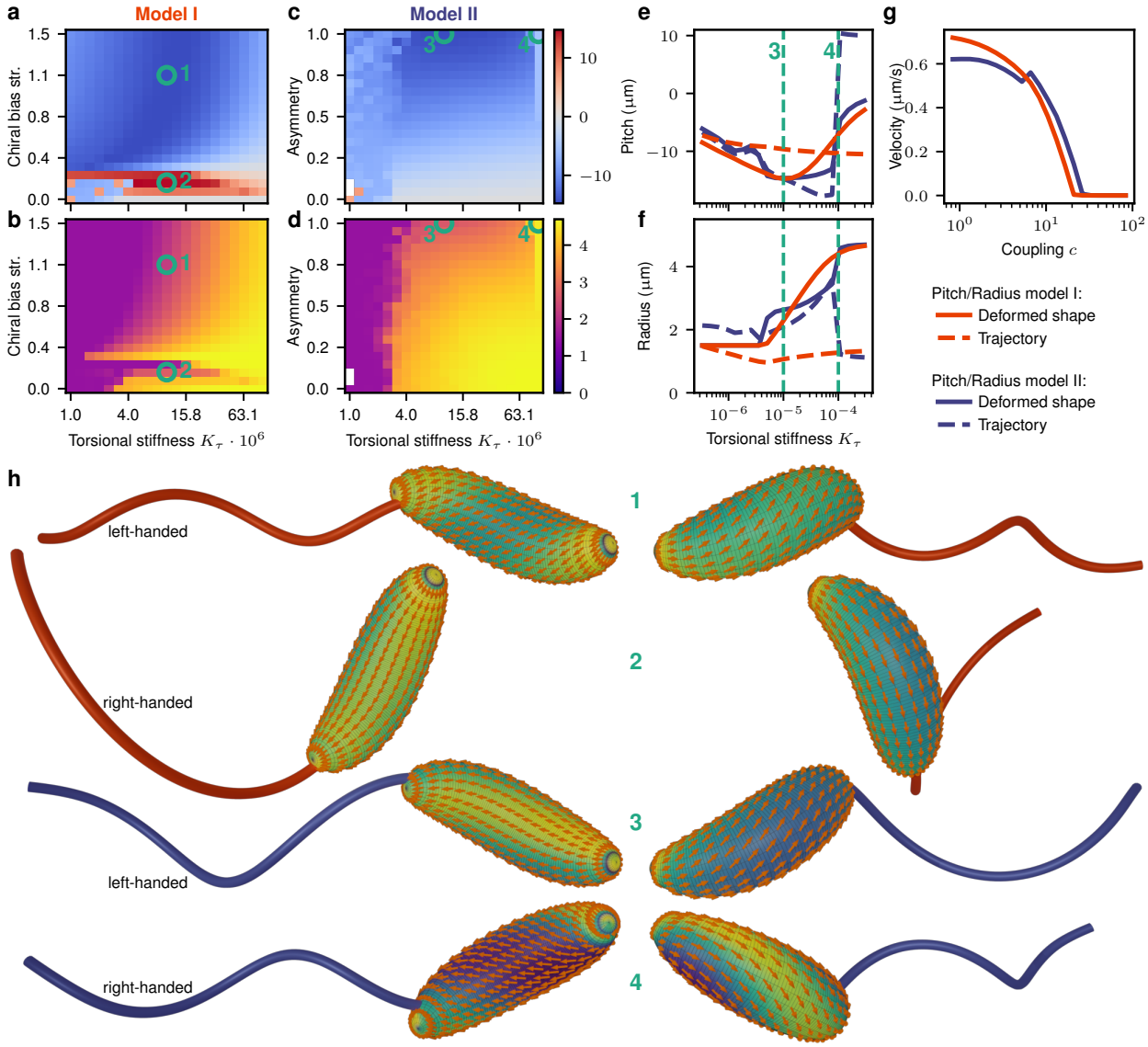

Figure 5.11: Deformation analysis for shapes thicker than sporozoites (aspect ratio of 3.33 instead of 12.5). **a-d:** Resulting pitch (a,c) and radius (b,d) after equilibrating in simulations performed for different torsional stiffness K_τ (relative to the adhesion strength) and chiral flow bias (a,b; Model I) or adhesin release asymmetry (c,d; Model II). **e,f:** Resulting pitch (e) and radius (f) after equilibrating in simulations performed for different torsion stiffness K_τ at fixed chiral flow bias (l; Model I) or adhesin release asymmetry (m; Model II). Dashed lines show the pitch and radius of the resulting trajectory. **g:** Velocity as function of the coupling parameter c. **h:** Results of numerical simulations including deformability. Final configurations for four sets of parameters marked in the previous panels are shown, a higher (1) and reduced (2) bias of the chiral flow model (Model I), as well as an intermediate (3) and higher (4) torsional stiffness in the asymmetric adhesion model (Model II). Left and right are two views on the same configurations.

ookinetes and *Toxoplasma*, the predictions of model I seem to fit better to these other apicomplexan forms, as they do not exhibit the observed inversion associated to moving on their back for sporozoites. Their left-handed helices imply CCW circles when contacting a rigid boundary from above (Fig. 5.10a), but they also prefer CCW circles in medium, suggesting they try to invade the glass slide (Fig. 5.10b).

We note that they are thicker (aspect ratio smaller) and have denser and chiral microtubule corsets, thus might more easily establish a rotationally biased actin flow. Indeed, simulations of model I with thicker shapes (see Fig. 5.11) show a less sensitive response to the chiral bias strength, expected due to the larger radius of the shape. However, more complicated flow patterns can emerge with small parameter changes, supporting the earlier suggestion that more accurate models of the actual shape are required to predict the motion of these forms [112, 117].

5.3 Two-sided traction force microscopy supports the asymmetric distribution model

To directly test the predictions of model II (asymmetric distribution) that different physical forces should appear at the ventral and dorsal side of the sporozoite, we developed a two-sided traction force microscopy assay. Purified sporozoites in a small amount of medium are pipetted on one traction force gel, then immediately covered with another. The amount of medium is controlled to yield a roughly 1 µm gap, allowing the sporozoites to move in between both gels while being in contact with both (See Appendix A.4 for experimental details).

Unlike the invasion sandwich, here the gels are stiffer and contain fluorescent beads, which can be imaged in two distinct planes above and below the sporozoite (Fig. 5.12a). Fig. 5.12b shows an example of the top plane with tracked beads; Fig. 5.12d zooms in. Fig. 5.12c,e show the bottom plane. This assay is more challenging than for mammalian cells [231, 232] for several reasons: sporozoites move quickly (leaving limited time to capture images), the forces are small and localized in very small regions, and the two planes are just $1-2\,\mu m$ apart, so many beads appear in both planes. Because the top and bottom gels closely approach each other and are coupled by the sporozoite, the usual assumption of force balance in a single gel is not valid. Additionally, all bead displacements are imaged from below in an inverted microscope, resulting in an optical distortion of the beads directly above the sporozoite by the sporozoite

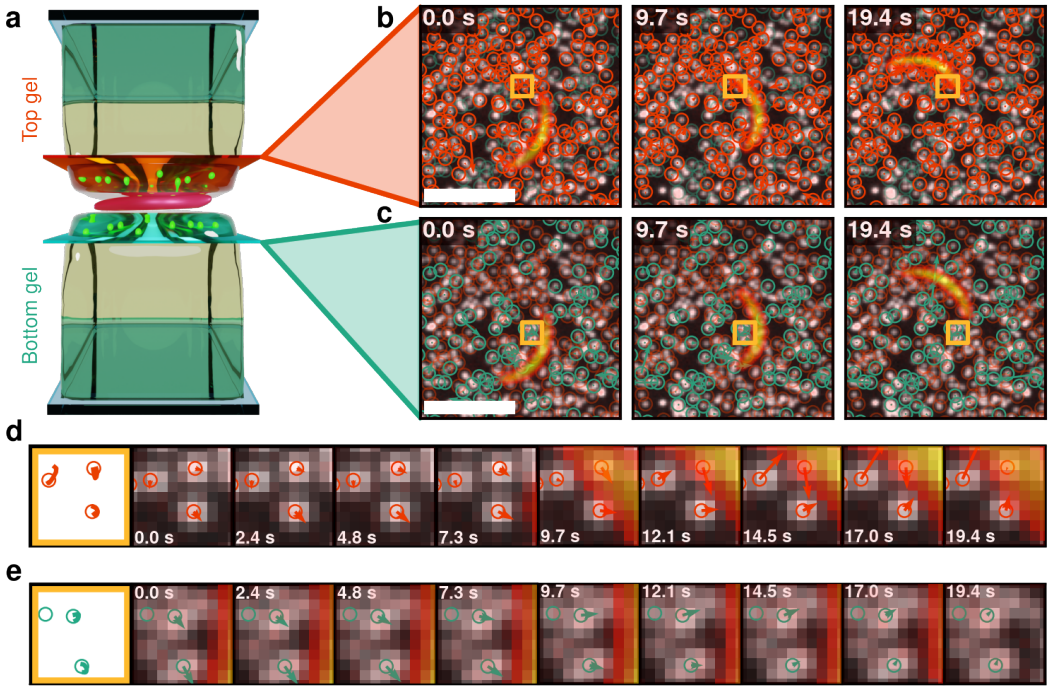

Figure 5.12: Two-sided traction force assay reveals asymmetry in force generation. **a:** Schematics of a gel sandwich traction force assay. Sporozoites (red) are sandwiched between two gels, which are too stiff to be invaded, but contain fluorescent beads imaged in two planes, above (orange) and below (cyan) the sporozoite. **b:** Top gel imaging plane with tracked beads that were localized in the top gel (orange) and computed displacements for three frames. Scale bar 10 µm. **c:** Same as b for bottom gel. **d:** Zoom-in view: The first panel shows enlarged bead trajectories; subsequent panels display consecutive frames showing the individual positions and displacements. **e:** Zoom-in as c for bottom gel.

itself.

We address these challenges in two ways. First, the assay provides an intrinsic control: we can compare clockwise and counterclockwise sporozoites under identical conditions. Second, we exploit the regular circular motion of sporozoites to compile bead displacements from multiple frames into a single aggregate displacement field, registering each displacement by the relative position of the sporozoite (Fig. 5.13a, see Section 5.3.1).

We then use a model-based approach to infer forces from these displacement fields. The model allows for a force plus a contractile dipole on top and bottom gels at 20 points along the sporozoite's length, details given below. We fit this model to the displacement field around the sporozoite, excluding points directly under and above it (to avoid optical lensing artifacts) and points too far away (where gel-gel coupling might overshadow local differences). Crucially,

global force balance is imposed, so we simultaneously reconstruct forces on both gels (Fig. 5.13b,c). From the resulting forces, we compute the total tangential component (along the parasite axis). A positive tangential force drives motion, while a negative one is dragging the sporozoite. Plotting the difference in tangential force between top and bottom gels for 13 sporozoites (Fig. 5.13d) reveals that CCW sporozoites show a negative difference, meaning they drive more strongly on the bottom gel and drag on the top, whereas CW sporozoites

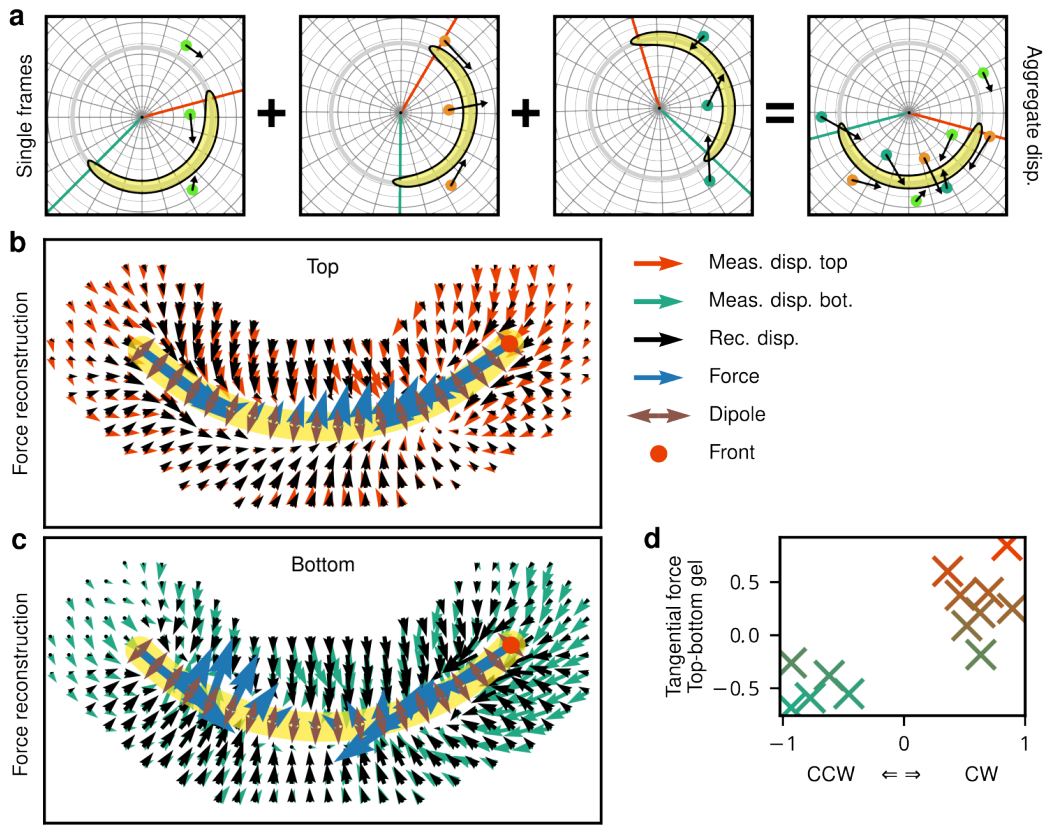

Figure 5.13: **a:** Schematics of generating an aggregate displacement field by overlaying displacements from multiple single frames, using their position in a polar coordinate system aligned to the current sporozoite position, in order to obtain a single displacement field from the observed motion of the sporozoite. **b:** Displacement field of the top gel averaged from multiple frames where the sporozoite was stopping (red), which is now generated by forces (blue) and force dipoles (brown), predicting the black displacement field. This sporozoite moves counterclockwise, i.e. it faces to the right. **c:** Same as b for bottom gel. **d:** Difference of the total tangential force produced by the sporozoite on the top vs. the bottom gel, where positive tangential force is defined as driving the sporozoite forward, and negative tangential force is dragging it. Hence, a positive difference means the sporozoite is exerting more driving force on the top gel, and more dragging on the bottom gel, and vice versa for a negative difference.

do the opposite. This strongly supports the asymmetric distribution model, in which the side with more adhesins (which convey the active driving force) faces downward for CCW motion and upward for CW motion, while the less-adhesive side creates drag by friction due to non-specific interactions. The question remains as to how a difference in adhesion strength can be established in the first place.

5.3.1 Details of traction force analysis

Here we describe the analysis used to obtain the traction force results described above in more detail. The analysis is divided in two parts. First, a displacement field is derived from the imaging data, and in a second step the forces creating these displacements are estimated.

Construction of the experimental displacement field

1. The time-lapse stack contains two channels with two z-slices each: top-gel beads ($z = +\Delta$), bottom-gel beads ($z = -\Delta$) and the sporozoite fluorescence in both slices.

2. Because most beads are visualized in both z-slices, we cannot construct the deformation field by standard PIV or optical flow techniques, correlating small windows of the image [124], because beads from both layers would be mixed. Instead, we want to track individual beads, and then assign every bead to one of the z-slices. Bead centers are detected in every frame (using the python package TrackPy [144]) and linked into trajectories with a nearest-neighbor linker (search radius 1.5 px, memory 3). Each top-plane trajectory is paired to its counterpart in the bottom plane by joint linking through an interleaved frame series and by majority voting of overlapping detections.

3. Within our experimental protocol, we cannot take reference images without the sporozoites. For every bead i the frame-averaged position $\langle \mathbf{b}_i \rangle$ weighted by its distance to the sporozoite (such that positions far from the sporozoite, which have lesser expected displacement, are weighted more strongly) is taken as reference and the raw displacement $\tilde{\mathbf{u}}_i(t) = \mathbf{b}_i(t) - \langle \mathbf{b}_i \rangle$ is smoothed with a 2-frame Gaussian kernel. Global stage drift is removed by subtracting the running mean of all bead displacements.

4. The sporozoite is segmented independently in both focal planes, yielding a label field and coordinates of center, tip and tail, which are used to define the sporozoite arc as a circular segment connecting all three points.

5. By fitting a circular arc to the sporozoite, a polar coordinate system was defined in each frame (with origin at the circle center, and angles and radius defined relatively from radius and front/end position of the sporozoite). Aggregating these displacements from all frames where the sporozoite briefly stopped (i.e. got stuck and hence created larger forces) in a single coordinate system and averaging nearby displacements produced more reliable displacement maps.

Force inference with a bi-layer elastic model

To obtain forces, we used a simple model to describe the force generation along the sporozoite: at 20 points along its length (such that the distance between the points is comparable to the thickness of the contact surface and we can use circular contacts at each point as approximation), we positioned a force and a contractile dipole, each for both the top and bottom gel. The dipole was necessary as we observed strong inward forces, similar to what was previously observed for classical traction force microscopy of sporozoites [61] or 3D traction force of Toxoplasma [114]. Using a Green's-functions approach, from a prescribed set of forces and dipoles we computed the displacements independently for top and bottom gel and compared them with the aggregate. Combining this with the constraint of vanishing total force (i.e. sum of top and bottom forces), which we also demanded in the summed tangential component, a loss function was formulated, which was implemented in JAX and subsequently minimized, thereby simultaneously optimizing top and bottom forces.

Force representation. The cell is discretised into N centers $\mathbf{r}_i$ equally spaced along the sporozoite arc, each with a tangential point force $\mathbf{F}_i$ and co-located contractile dipole D_i (scalar, direction $\hat{\mathbf{e}}_D$ orthogonal to the sporozoite arc) on both the top (superscript 1) and bottom (superscript 2) gels.

Elastic kernel. Each substrate is treated as an infinite-thickness, linear, isotropic layer (Young modulus E, Poisson ratio ν). The in-plane displacement generated by a single force is obtained from a modified Boussinesq/Hertz Green function $\mathbf{G}(\mathbf{x}; E, \nu, a)$ [233]. A dipole enters via the

spatial derivative $\nabla\mathbf{G}$ [234]. The predicted displacement at bead location $\mathbf{x}_k$ in the top plane therefore reads

$$\mathbf{u}_k^{\text{pred}} = \sum_{i=1}^{N}\Big[\mathbf{G}(\mathbf{x}_k-\mathbf{r}_i)\,\mathbf{F}_i^{(1)} + \nabla\mathbf{G}(\mathbf{x}_k-\mathbf{r}_i) : \big(D_i^{(1)}\hat{\mathbf{e}}_D\otimes\hat{\mathbf{e}}_D\big)\Big],$$

and analogously for the bottom plane.

Joint optimisation. Forces and dipoles of the two gels are obtained by minimising the cost functional (with $\mathbf{u}_k^{\text{meas}}$ the displacement previously obtained from the bead measurements)

$$\begin{aligned}\mathcal{J} = {}& \frac{1}{2}\sum_{k\in\text{top}}\big\|\mathbf{u}_k^{\text{pred}}-\mathbf{u}_k^{\text{meas}}\big\|^2 + \frac{1}{2}\sum_{k\in\text{bot}}\big\|\mathbf{u}_k^{\text{pred}}-\mathbf{u}_k^{\text{meas}}\big\|^2\\ &+\lambda_1\sum_i\Big(\|\mathbf{F}_i^{(1)}\|^2+\|\mathbf{F}_i^{(2)}\|^2+|D_i^{(1)}|^2+|D_i^{(2)}|^2\Big)\\ &+\lambda_2\sum_i\Big(\|\nabla\mathbf{F}_i^{(1)}\|^2+\|\nabla\mathbf{F}_i^{(2)}\|^2+|\nabla D_i^{(1)}|^2+|\nabla D_i^{(2)}|^2\Big)\\ &+\lambda_3\Big(\Big\|\sum_i\mathbf{F}_i^{(1)}+\mathbf{F}_i^{(2)}\Big\|^2+\Big\|\sum_i\mathbf{r}_i\times(\mathbf{F}_i^{(1)}+\mathbf{F}_i^{(2)})\Big\|^2\Big),\end{aligned} \tag{5.17}$$

where λ_1 controls usual regularization, λ_2 regularizes spatial variation of the forces, and the last line enforces global force and torque balance. Automatic differentiation (JAX) supplies gradients and the exact Hessian for a trust-region Newton solver.

These routines are available in the git repository https://github.com/LeonLettermann/hei-sporo-code-tracking.

5.4 STED microscopy reveals a consistent chiral orientation of the apical complex relative to sporozoite curvature

Previous work using cryo-electron tomography of sporozoites showed two types of asymmetries at the apical end. The APR of sporozoites is tilted and the subpellicular microtubules originating from the APR are arranged in a peculiar 15+1 fashion relative to the tilt such that the single microtubule reaches the most apical position (Fig. 5.14a, [104]). However, with cryo-electron tomography, we were not able to reveal the orientation of the APR relative to the substrate during gliding as sporozoites detach during sample preparation [235]. Clearly,

the asymmetric distribution model could be explained by one-sided secretion of adhesins through the tilted APR. Thus, we aimed to measure the tilt of the APR relative to the gliding orientation by live-cell microscopy.

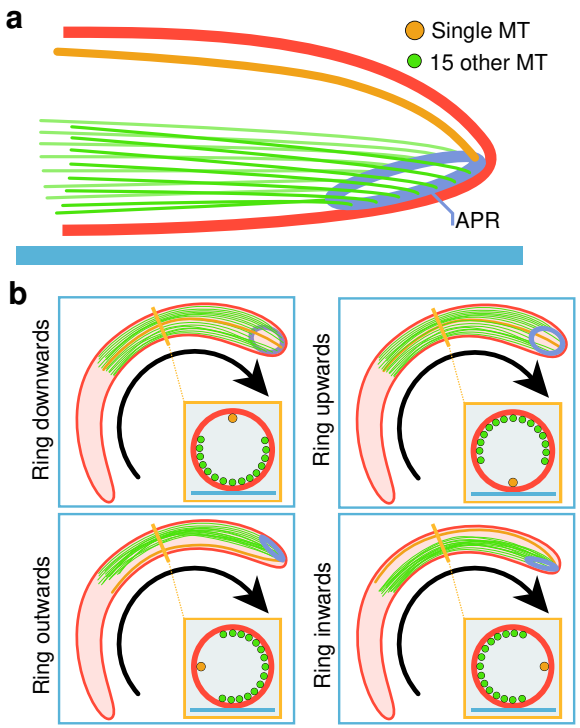

Figure 5.14: **a:** Cartoon (with enlarged apical region) showing the position of the apical polar ring APR (blue) with respect to the single (orange) and all other 15 microtubules (green) as observed by electron tomography [104]. **b:** Top view of different possible positions of the apical ring and microtubules, inset showing a cross-section.

However, the APR is small and challenging to visualize by live cell microscopy [104, 236]. We thus performed STED super-resolution microscopy of microtubules labeled with SiR-tubulin in live sporozoites that had reached the bottom of the gel and were circling with the aim of visualizing the position of the single microtubule, indicating the ring tilt (Fig. 5.14b). Sporozoites that were still motile at the bottom of the hydrogel were imaged continuously in confocal mode, and a volume of the first half of the sporozoite was acquired immediately if a sporozoite paused in 3D STED mode. If a sporozoite moved or died (resulting in a strong increase of background signal) during volume acquisition, the dataset was discarded (see Appendix A.5 for details on the sample preparation). After several hours, the sporozoites were trapped inside the hydrogel and regularly stopped moving for a few seconds. This allowed us to capture 3D image stacks of parasites at the bottom of the gel. In the top-down view (Fig. 5.15a+c), we aligned a circular arc with the sporozoite, and subsequently defined cross-sections perpendicular to this arc every 120 nm. These cross-sections revealed an isolated signal that likely corresponds to the single microtubule (Fig. 5.15b+d). By averaging the angular intensity profile of multiple cross-sections along a sporozoite, we consistently observe a small

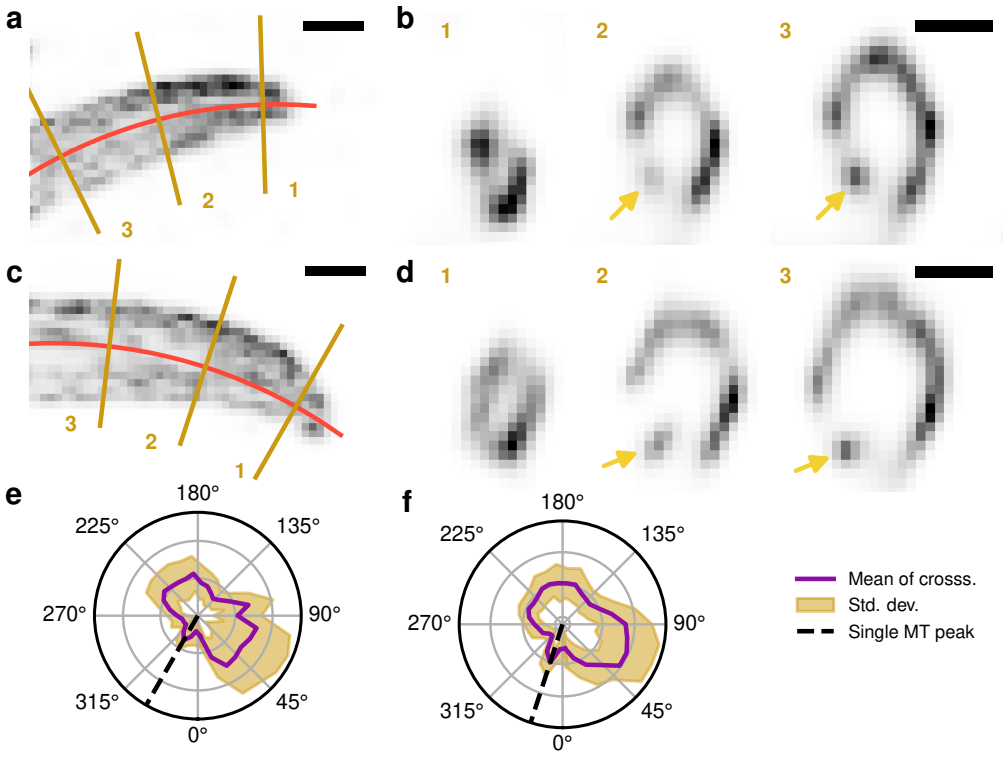

Figure 5.15: **a:** An example of 3D STED imaging of living sporozoites labeled with SiR-tubulin and moving clockwise at the bottom of the hydrogel. Three optical sections at different positions are indicated in this top view. Scale bar 500 nm. **b:** Cross-sections marked in d. Note the single microtubule in images 2 and 3 (bottom left). Scale bar 500 nm. **c,d:** Same as a,b for a second sporozoite. **e:** Angular intensity profile from a single sporozoite (a) averaged over different cross sections along the imaged part of the sporozoite (Std. dev. over cross sections in yellow). A single, isolated peak (dashed line) marks the peak corresponding to the single MT. **f:** Same as e for sporozoite from c.

isolated peak feature corresponding to that single microtubule (Fig. 5.15e+f, see Section 5.4.1).

Figure 5.16: Cross sections from six different sporozoites, illustrating that the orientation of the single microtubule is highly reproducible. Scale bars 500 nm.

In 20 out of 30 imaged sporozoites a single microtubule was distinctly visible. It was invariably located at the bottom side, i.e. toward the glass slide (Fig. 5.16).

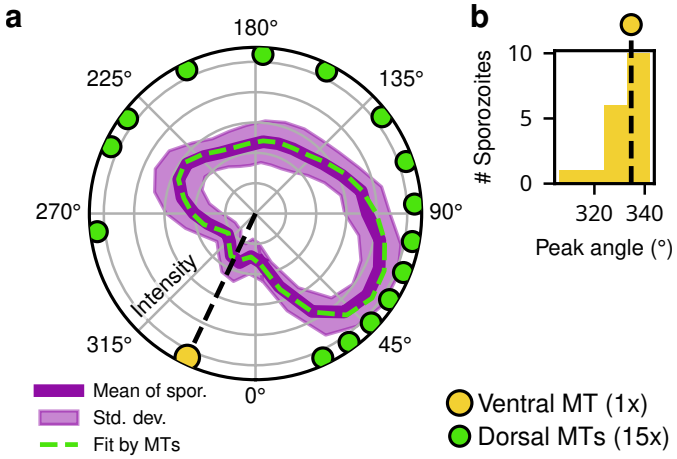

Figure 5.17: **a:** Results aggregated from STED microscopy of sporozoites reaching the glass underneath the gel (see d and following for details), showing the angular dependence of the intensity averaged over sporozoites. Fitting the intensity profile by angular positions of 16 microtubules reveals the single microtubule at the bottom as predicted, but slightly offset. **b:** Distribution of angles at which the peak in the angular intensity distribution corresponding to the single MT could be clearly identified (18 sporozoites). Dashed line marks the position of the single MT fitted to the average of all sporozoites.

Aggregating the average angular profiles from all sporozoites yields the distribution in Fig. 5.17a. As this intensity is generated by 16 microtubules, we were able to reconstruct their positions (details given below), placing the single microtubule at 335°. This agrees with the single microtubule peak location from individual sporozoite measurements in Fig. 5.17b. From this, we conclude that the single microtubule faces the glass and hence that the APR is tilted upward, away from the glass slide confining the hydrogel. This suggests that adhesins are released on the dorsal surface of the parasite, consistent with the asymmetric distribution model for 3D chirality.

5.4.1 STED cross-sections and azimuthal mapping of the 16 subpellicular microtubules

Computation of angular profile

STED stacks were resliced perpendicular to the longitudinal axis of the sporozoite; therefore, each slice shows an approximately circular cross section of the

cell cortex. For a given slice image $I(\mathbf{x})$ the position of the center $\mathbf{c}$ is selected at that pixel position that maximizes

$$\mathcal{C}(\Delta\mathbf{c}) = \Big[\textstyle\sum_r \tilde{I}_r^2\Big] \times \Big[\textstyle\sum_\theta \tilde{A}_\theta^{1/2}\Big],$$

where $\tilde{I}_r$ is the sum of intensities around the tentative center at radius r and $\tilde{A}_\theta$ is the maximal intensity along the corresponding angular sector (30 bins). This optimization selects the center such that it is surrounded on all sides equally ($\tilde{A}_\theta$ term to power $\frac{1}{2}$), but the radial intensity is concentrated at one radius ($\tilde{I}_r^2$ term). The cross sectional radius is estimated as the first maximum of $\tilde{I}_r$. Slices are discarded when they contain excessive background or an angular profile with $> 50\,\%$ values below half the slice mean. The angular profiles $A^{(k)}(\theta)$ of valid slices counted by k are normalized, and, assuming the distribution is similar over the cross sections in the sporozoite region we observe, averaged,

$$\bar{A}(\theta) = \frac{1}{K}\sum_{k=1}^{K} \frac{A^{(k)}(\theta)}{\int_0^{2\pi} A^{(k)}(\theta)\,d\theta}.$$

Inference of microtubule positions

For inferring the distribution of microtubules, we can use that the angular profile above is generated by exactly 16 microtubules. Assuming each microtubule contributes an identical Gaussian line source at azimuth ϕ_i with amplitude A, offset B and standard deviation σ:

$$S_i(\theta) = A\,e^{-(\Delta\theta_i)^2/2\sigma^2} + B, \qquad \Delta\theta_i = \min_{n\in\mathbb{Z}} |\theta - \phi_i - 2\pi n|.$$

With $N = 16$ microtubules the predicted profile is $S(\theta) = N^{-1}\sum_{i=1}^{N} S_i(\theta)$.

The unknown parameters are the 16 angles ϕ_i and the common parameters σ, A, B controlling the intensity profile of a single microtubule. They are obtained by minimizing

$$\mathcal{L}(\boldsymbol{\phi}, \sigma, A, B) = \sum_\theta \frac{\big[S(\theta) - \bar{A}(\theta)\big]^2}{\bar{A}(\theta)^2} + \sum_{i<j} \exp\Big[-\frac{\Delta\phi_{ij}^2}{2\delta^2}\Big],$$

where the second term ($\delta = 0.05\,\mathrm{rad}$) penalizes unrealistically close microtubules. Gradients and the Hessian are supplied by JAX; a simultaneous gradient descent on $\boldsymbol{\phi}$ and (σ, A, B) converges within $\sim 10^6$ iterations (git repository https://github.com/LeonLettermann/hei-sporo-code-sted).

5.5 Conclusion

Here, we analyzed how 3D chirality determines the motion patterns of *Plasmodium* sporozoites, the transmission form of malaria-causing parasites. We found that in homogeneous 3D environments, they move in a right-handed fashion, in contrast to the left-handed migration of *Plasmodium* ookinetes [115] and *Toxoplasma* tachyzoites [113]. Our data suggest that sporozoites generate macroscopic chirality via an asymmetrically tilted apical complex, resulting in an asymmetric force distribution stabilizing counterclockwise motility in 2D and right-handed motility in 3D (schematic summary in Fig. 5.18). In contrast, ookinetes and tachyzoites appear to use a chiral surface flow to generate chirality.

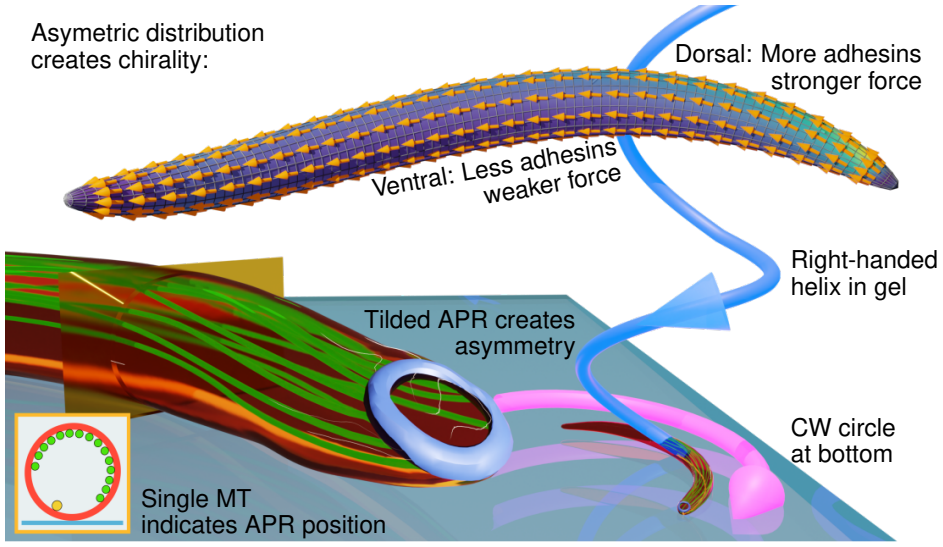

Figure 5.18: Schematics of the suggested model for sporozoite chirality.

Our data provide the first explanation why the sporozoite is the only form with a tilted apical end and features microtubules that show an uneven distribution pattern (15+1 in *P. berghei*) but run straight along the parasite's longitudinal axis. A key implication of our finding is that sporozoites generate forces as they glide that are different on their dorsal and ventral sides. While previous experiments on sporozoites addressed forces on either the substrate-facing side by traction force microscopy [61, 116] or on the substrate-opposing side by optical tweezers trapping beads [120, 121, 237], our sandwich traction force microscopy setup allowed us to determine force generation on both sides. Remarkably, this showed that sporozoites moving CCW produce more force on the bottom gel and those moving CW produce more force on the upper gel.

Together with our finding that CCW-moving sporozoites move upward and those moving CW move downward in a soft sandwich gel assay, this suggests that sporozoites placed on liver cells are geared to move away (upward) from them, rather than into them. This suggests a reason why liver cell invasion assays produce very low rates of infection [145, 146] and opens the prospect of improved liver invasion assays, which are crucial to identify the involved molecules and potential inhibitors.

In conclusion, our combination of theoretical and conceptual analysis with novel experimental setups allowed us not only to better understand the chirality encoded in the cellular architecture of sporozoites, but also how it might fundamentally differ from gliding machinery of related systems that are similar in many molecular aspects. Our work provides new physical understanding of how to realize chirality in microscopic agents, and has medically relevant implications for the invasion behavior of *Plasmodium* sporozoites.

Summary & Outlook

In this thesis, we explored the gliding motility of apicomplexans, in particular *Plasmodium* sporozoites. Focusing on 3D, we started with experimental results, derived by advanced image analysis from microscopy data of a hydrogel assay, finding helical tracks with right-handed chirality. Introducing an active particle model, we saw that noise in the internal motor machinery can be partly compensated by the rotation of a helical trajectory, yielding higher persistence. Moving into more detail, we developed a theoretical and numerical framework to treat the self-organization problem of the actively generated surface flow on the gliders, coupled to the motion this surface flow produces. This proved to be a powerful tool, allowing insights into why these parasites might be curved, and how they generate their chirality.

Malaria parasites are a fascinating biophysical system. As we introduced in **Chapter 1**, they can assume different shapes during their mosquito–vertebrate alternating life cycle. Our main focus was on sporozoites, the long, slender, highly polarized form of the parasite transmitted from the mosquito, migrating through the host skin to find a blood vessel. Their motility is powered by the glideosome, a highly evolved machinery allowing them to outrun the immune system. The distributed force generation of this glideosome, posing a self-organization problem and the possibility of approaching it using mean-field descriptions, makes it a prime target for the methodology of theoretical biophysics. Understanding sporozoite migration is of direct medical relevance, as stopping the relatively small number of sporozoites from reaching blood vessels offers an early block to infection, as attempted by current vaccine efforts.

The basis of this thesis is the experiments and the biological understanding of Mirko Singer and Freddy Frischknecht from the parasitology department. The gel assay previously developed in the group [116] and refined for this study allowed us to simultaneously observe many sporozoites migrating in a 3D hydrogel. This environment was closer to physiological conditions than the simple 2D assay, while still being much simpler and more homogeneous than true *in vivo* assays. This offered the perfect setup for a physical understanding of their 3D migration, as presented in **Chapter 2**. Mirko and I optimized the experiments for the best compromise of spatial and temporal resolution, with the requirements of automatic image analysis necessitated by the large number of sporozoites as a baseline. I developed the full image and data analysis pipeline,

which allowed us to track hundreds of sporozoites and quantify their trajectories. Core achievements of this analysis pipeline are the blind deconvolution, more stable against diffuse scattering from outside the imaged volume, and the collision resolution, which, in combination, allowed reliable tracking of many sporozoites in dense scenarios. Main results obtained from this include the right-handed chirality of both the rodent-infecting *Plasmodium berghei*, and the human pathogen *Plasmodium falciparum*. Furthermore, we discovered a radius-to-pitch relationship pointing toward a maintained, constant curvature of the parasites. Within this relationship, we find that the maximum possible pitch and associated radius are very close to the median values observed; while we did not deeply investigate the possible reasons for this, it seems plausible that this optimizes the explored volume. How precisely this works remains an open question, partly because the extent to which sporozoites are directed by chemical, mechanical, or temperature gradients toward blood vessels is the subject of current research [238].

The regularity of the helical trajectories (sometimes neatly following a helix for 10 or more turns) motivated the most general of the models in this thesis, the chiral active Ornstein-Uhlenbeck particle introduced in **Chapter 3**. The underlying assumption is that for sporozoites moving through a gel, Brownian motion induced by the environment is less relevant, and the stochasticity of their motion is mostly introduced by fluctuations in the forces and torques the parasite actively generates. However, this certainly is also relevant for microorganisms that are sufficiently large or fast (i.e. strongly driven) such that the external fluctuations become less important by comparison. We introduced a novel active particle model, reminiscent of famous models, such as the active Brownian particle [21] and the circle swimmer [32]. In our model, we propose an inclusion of stochastic effects by the motor machinery through an Ornstein-Uhlenbeck process in the dynamics of the angular velocity. This captures two main properties of noise introduced by a microbe's motor machinery: it is internally generated, i.e. moves with the microbe, and will usually have a characteristic time scale depending on the propulsion mechanism. Both are distinct from an active Brownian particle, where the white noise is attributed to the environment and has vanishing internal correlation time. The model we propose includes these effects, but at the same time is sufficiently simple to still allow analytical solutions, which we derived for the expected trajectory and the mean squared displacement. These revealed a strong stabilizing influence of rotation and hence chirality: because the noise is time-correlated, and fixed to

the particle, a rotating particle can integrate out part of the noise if the time scale of rotation is similar to or smaller than the time scale of the noise. This effect proved to be so strong that a particle traveling on a helix can on average even travel farther from the initial position than a particle running straight. Even if, after the time of one helical turn has passed, a straight-traveling particle will on average be farther, the helix maintains the direction of its center line more persistently, such that the helix ends up "straighter than a straight line". Extracting the MSD from the experimentally measured trajectories, we were able to show that we can fit our active Ornstein-Uhlenbeck particle to the trajectories of sporozoites in a 3D gel and obtain correct predictions for pitch and radius. Because the trajectory segments we observe are limited by the extent of the imaged volume, we obtained these results from fitting the beginning of the MSD curve. To more clearly quantify whether sporozoite helices make use of the stabilization effect we discovered here, experimental data of even more sporozoites, traveling unconstrained for even longer distances, would be necessary, posing an experimental challenge.

From the abstract description of the active particle we moved to a more detailed description of the force generation during gliding motility in **Chapter 4**. Assuming a rigid cell shape, two main parts to the physics can be distinguished: First, the actively generated surface flow is evolving as a result of its internal driving and the friction it receives. This friction, on the other hand, depends on the global motion of the rigid body, which is a result of the current overall configuration of the surface flow and the cell geometry. We formulated a closed system of integro-differential equations describing this intricate coupling, and found that the introduction of geometry tensors, condensing the static influence of geometry and removing it from the dynamical problem, was key. Computing these geometry tensors allowed deriving analytical results for the stationary states and estimates for their stability. Using computer algebra software to analytically calculate the geometry tensors for fixed geometries, including a spherocylinder, an ellipsoid, and a curved cylinder, then allowed us to perform classical bifurcation analysis, using changes to the underlying geometry as a control parameter. The most important result was that axisymmetric shapes often have only one stable solution: to rotate in place. Breaking this axial symmetry by curving the cylinder leads to productive translation, previously unstable, becoming a stable solution. This offers a plausible explanation to a long open problem in apicomplexan parasitology: Not only *Plasmodium* sporozoites, but also ookinetes and *Toxoplasma* tachyzoites have a curved,

non-axisymmetric geometry. Our theory suggests that this supports organizing their surface flow for productive migration. Of course there are many other factors that could contribute to the evolutionary selection of curved shapes, including more efficient spatial exploration or association with the curvature of target blood vessels. Turning away from apicomplexans, the theory developed here can also be applied to gliding bacteria and diatoms. For bacteria, which are axisymmetric, we find that they do retain a rotational component and might avoid only rotating by fixed helical tracks restricting their adhesins. Diatoms have an even more reduced active gliding motility zone: only the small raphe slit in their hard silicate shells allows force transmission to the substrate. Our theory can be adapted to study the relation between raphe shape and resulting trajectory, and because of the simplification the raphe's fixed shape brings, diatoms are a promising model system for more stochastic extensions of our geometric theory of gliding.

With the experimental observations of *Plasmodium* sporozoite trajectories and the theoretical understanding of how their surface flow and geometry relate to the resulting motion, we finally developed a comprehensive numerical model of apicomplexan gliders, and specifically sporozoites, in **Chapter 5**. This model extended the analytical theory by including the adhesin concentration as a second dynamic field and allowing some degree of deformability of the cell in reaction to the acting forces. Most importantly, however, it presented us with conceptual access to probe possible origins of the very peculiar chirality behavior seen in the experiments. This included the 3D right-handed chirality of the parasites' helical trajectories, but also extended to 2D motion on glass slides. Underneath the gel, reaching the glass slide from above, the parasites circle clockwise—opposite from their known preference for counterclockwise circling on established 2D motility assays, i.e. a glass slide in medium. Besides delivering important information on the origin of chirality, this implies that in these 2D assays sporozoites do not attempt to invade the glass slide, but instead move on their backs, aiming to climb into the medium above. We investigated this further by introducing two alternative models for chirality generation, the chiral flow and asymmetric adhesion model. The combination of 2D and 3D chirality observations alone was sufficient to distinguish between the two, with only the asymmetric adhesion model in agreement with the observed sporozoite chirality. Strikingly, the previously reported chirality behavior of *Plasmodium* ookinetes and *Toxoplasma* is different, precisely pointing toward the chiral flow model. For sporozoites, we corroborated our hypothesis by

an advanced two-sided traction force microscopy assay and 3D STED super-resolution microscopy. Mirko Singer once more performed these experiments, and I performed the analysis, which allowed us to confirm that the driving force of sporozoite migration is asymmetrically distributed as expected, and the apical ring tilted in the direction of expected higher adhesin concentration and hence higher force. With this, a comprehensive picture of sporozoite chirality emerged: The structurally encoded tilt of the apical polar ring produces an asymmetric release of adhesins, which leads to stronger force generation on one side of the sporozoite. In 3D migration, the sporozoite is bent away from this side, such that the more adhesive side forms the back, or dorsal, side. On the classical 2D assay, the sporozoite attaches more reliably with this more adhesive side, such that it runs on its back and a right-handed helix would lead it upward, instead of invading the gel. Furthermore, ookinetes and *Toxoplasma* tachyzoites plausibly generate chirality by the chiral flow model: their apical rings are not tilted, their chiral microtubule corset may serve as a director, and their thicker shape makes the chiral flow model overall more effective and more easily controlled. The striking geometric feature of sporozoites—their very slender cell body forced by the necessity to fit through the mosquitoes' salivary ducts—might have forced them to attain a different strategy. Because the chiral flow acts via the lever arm given by the cell radius, the slender sporozoites might have developed the tilted apical ring as a more effective alternative given their slender shape.

The work presented in this thesis constitutes multiple significant advancements. First, it deepens our understanding of apicomplexan and in particular sporozoite motility. We make the first rigorous connection between the local organization of the glideosome, the cell shape, and the resulting motion. This understanding offers insights into the curvature of sporozoites, as a tool to help self-organize the surface flow and use the stabilizing effect of helical trajectories, and in particular into their chirality. The discovered distinction in the chirality between *Plasmodium* sporozoites and *Toxoplasma* tachyzoites is consequential, because in many aspects these systems are treated as similar, and results from one are often extrapolated to the other. In terms of chirality and glideosome self-organization, our work cautions that there might be some fundamental differences in how these parasites organize their surface flow machinery. The experimental assays developed, supported by the image and data analysis software, are a second major contribution: The 3D assay is more sensitive to quantify motility in mutant sporozoites, which are routinely used to study

the effects of certain protein changes introduced by gene editing. For some such mutants, the standard 2D assay produces just a negative result, i.e. the parasites are unable to glide. But they can recover some motility in the 3D gel assay, allowing more accurate quantitative measurements. Coupled with image analysis and the theoretical framework developed here, we aim to link changes in observed migration to functional changes in the mechanism of the glideosome. The more general theoretical models, i.e. the active chiral Ornstein-Uhlenbeck particle and the geometric glider theory, provide significant theoretical advances, applicable to more general situations than just apicomplexan parasites. One application in particular is the design of synthetic microgliders, which are candidates for targeted drug delivery through tissues. The theories presented in this thesis can be applied to optimize trajectory and shape design for maximal persistence and velocity.

There are numerous points where the investigations herein can be continued and improved. The 3D imaging was designed to observe many sporozoites and be able to track them, which was accomplished and allowed definitive statements about trajectory shape and chirality. However, it did limit the spatial and temporal resolution achieved. Concerning time, we were in particular unable to investigate whether previously observed stop-and-go behavior on 2D substrates is still present or changed in the 3D environment, because the typical stop times correspond to only one frame in our 3D imaging setup. Faster imaging would answer if the fact that sporozoites seem to get stuck with their rear end and thus slow down is an artifact of the non-physiological 2D assay, or a general feature of their gliding motility. Higher spatial resolution would allow us to extract more quantitative information from the reconstructed shapes of individual sporozoites. Where we previously just observed a kink as sporozoites transition from 3D to 2D motility, this might allow us to resolve at which positions sporozoites kink how often and in which direction, yielding a more precise model of their elastic properties. This could be used to improve the very simple deformability model we introduced, in which we allowed only the torsion to vary, and only via a simple relaxation. To dynamically deform the shape simultaneously with adapting the surface flow and moving according to overdamped dynamics is a challenging problem on its own. For predictive power in understanding how sporozoites navigate complex environments, such a model must be informed by the complex elastic properties of the sporozoite. By its architecture (microtubules extend only to the nucleus behind the cell center), it seems likely that the elastic properties of the sporozoite are changing along the

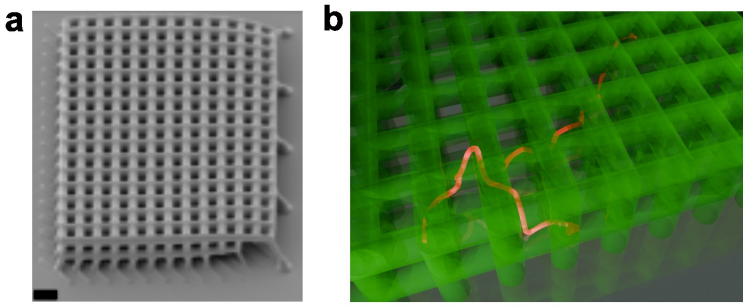

Figure 5.19: Sporozoite motility probed by configurable spofold, a 3D microprinted scaffold, developed by Zeynab Tavasolyzadeh in the group of Prof. Christine Selhuber-Unkel, in preparation for publication 8. **a:** SEM image of a 2-layer spofold. Scale bar 10 µm. **b:** Rendering of observed trajectories, overlaid with reconstructed spofold position.

length of the cell. In this thesis, we mostly considered equilibrium configurations of the motion and the optimal helical trajectories followed in the homogeneous 3D assay. Here, shape changes were not too crucial, and the equilibration method was sufficient. But it also means that there are dynamical parameters within the theory, for example the time scale with which the surface flow reacts to external perturbations, that we cannot constrain by these experiments. One way to address both the elastic model and the dynamic time scales is to observe sporozoites in more complex, but still well-controlled, environments. To this end, Zeynab Tavasolyzadeh from the group of Christine Selhuber-Unkel at the IMSEAM, Heidelberg University, developed a microprinted scaffold, called spofold. This regular cubic lattice with adjustable pillar spacing and diameter presents a configurable 3D environment that can be embedded in medium or a hydrogel. The presence of the structure makes imaging and analysis even more challenging, but we now possess a setup of experimental conditions and image analysis that allows us to systematically test and analyze sporozoite motility in different spofolds (Fig. 5.19).

The results of this project exemplify the power of interdisciplinary collaboration, beyond just applying the tools of one field to another. In our experimental collaboration between biophysicists and parasitologists, we designed experiments, developed image analysis code, and built theoretical models that allowed us to further our understanding of apicomplexan parasites, their gliding, how it interacts with the cell architecture, and in particular how their chirality is generated. The methods and ideas developed during this project are much more general. The experimental assays are not limited to the analysis performed here, but can now serve as a baseline to probe mutant parasite

motility, learning in more detail how introduced mutations affect motility. The theoretical frameworks, inspired by sporozoite biology, can be extended to other microbes, including bacteria and diatoms, but also to the design of synthetic microgliders.

Appendix A

Experimental and technical details

A.1 Infection of *Anopheles* mosquitoes with *P. berghei* and *P. falciparum*

Experiments for *P. berghei* were performed with a selection-marker-free ANKA strain that constitutively expressed eGFP and mCherry in sporozoites (R/G) [239], whereas for the *P. berghei* controls for *P. falciparum* an mCherry ANKA strain was used [240]. On day -7, a CD1 Swiss mouse was injected i.p. with a stabilate of (R/G). On day -3, 20 million parasites each were transferred into two naive mice by i.p. injection. On day 0, exflagellation of both mice was tested by taking a small drop of blood from the tip of the tail, placing it on an objective slide, and covering it with a cover slide. After 10 minutes at 20 °C, exflagellation was evaluated on an inverted microscope with a 40x objective in phase-contrast. Both mice were anesthetized and placed on top of a mosquito cage with approximately 400 female *Anopheles stephensi*. Feeding took place at room temperature (RT) for 20–30 minutes in the dark, then both mice were sacrificed and the mosquito cage was incubated at 21 °C and 80 % humidity.

Mosquito infection with *P. falciparum* tdTomato [241] was performed as previously described [242]. Asexual cultures were maintained in vitro in O+ erythrocytes at 4 % hematocrit in RPMI 1640 supplemented with 2.1 mM L-glutamine, 25 mM HEPES, 0.72 mM hypoxanthine, 0.21 % (wt/vol) sodium bicarbonate, and 10 % (vol/vol) heat-inactivated human serum. Cultures were maintained at 37 °C in a candle jar and gametocyte cultures were initiated at 0.5 % parasitemia and 4 % hematocrit. Medium was changed daily for up to 15 to 18 days without the addition of fresh blood to promote gametocytogenesis. Adult *An. stephensi* mosquitoes (3 to 7 days after emergence) were allowed to feed through a glass membrane feeder for up to 30 minutes on gametocyte cultures at 40 % hematocrit containing fresh O+ human serum and O+ erythrocytes. Infected mosquitoes were maintained for up to 19 days at 25 °C with

80 % humidity and were provided with a 10 % (wt/vol) sucrose solution.

A.2 Hydrogel assays and spinning-disk microscopy for high-throughput 3D sporozoite imaging

Hydrogels were prepared as in [116], soft hydrogels were prepared with 3 % acrylamide (AA) and 0.03 % bisacrylamide (BIS). For reference and traction force measurements, fluorescent beads (0.02 µm 660/680 nm) were added prior to activation by APS and TEMED. After polymerization, gels were stored in PBS at 4 °C. For standard hydrogel assays, hydrogels were incubated for 30 minutes with RPMI medium with 3 % BSA. Around 20 mosquitoes were aspirated, cooled on ice, rinsed in ethanol, and then dissected in PBS to remove the salivary glands. Salivary glands were transferred onto a 22x22 mm glass cover slide with 30 µL of RPMI/3 % BSA and cut 1–2 times each using 27G needles. The excess medium on top of the hydrogel was then removed and the hydrogel inverted onto the prepared slide with cut salivary glands. The slide was sealed with a 1:1:1 mixture of lanolin/vaseline/paraffin and imaged with a 20x oil-immersion objective at the spinning-disk confocal (PerkinElmer with Nikon Ti series). Single-channel 4D stacks were acquired with 20–60 z-slices with a spacing of 1 µm, and 2–6 s per frame depending on the number of z-slices.

Imaging of *P. falciparum* and *P. berghei* control sporozoite motility in hydrogels was performed using a 20x objective on a Zeiss LSM 880 confocal microscope. Focus was maintained using the Definite Focus system. Single-channel 4D image stacks were acquired, consisting of 14 z-slices with a spacing of 1.546 µm. Images were captured every 4.17 s for a total of 120 frames.

A.3 Hydrogel sandwich assay for 2-way invasion

For two-sided hydrogel invasion, hydrogels were prepared as for the high-throughput sporozoite imaging with 3 % acrylamide (AA) and 0.03 % bisacrylamide (BIS) with fluorescent beads (0.02 µm 660/680 nm). The salivary glands of 50 infected mosquitoes were collected in 100 µL of RPMI on ice. Salivary glands were physically disrupted with a plastic pestle inside a 1.5 mL tube for

one minute, then 900 µL of RPMI was added and the sample transferred into a 15 mL Falcon tube. The solution was carefully underlaid with 3 mL of 17 % (w/vol) Accudenz solution in water and centrifuged for 20 minutes at 2500 g without braking. The interphase and top liquid was collected with a Pasteur pipette and centrifuged for 3 minutes at 10000 g [243]. The pellet containing the sporozoites was resuspended in 2 µL of RPMI/3 % BSA and placed on the hydrogel with no excess buffer that had been incubated with RPMI/3 % BSA for 30 minutes. The hydrogel was then covered by a second hydrogel and the sample sealed at the edges and imaged at the spinning-disk confocal. The sandwich invasion assay was imaged with a 20x oil objective.

A.4 Hydrogel sandwich assay for two-sided traction force

For two-sided hydrogel traction force imaging of sporozoites, stiff hydrogels with 5 % AA and 0.3 % BIS and fluorescent beads (0.02 µm 660/680 nm) were prepared and stored in PBS at 4 °C. Sporozoite purification and sandwich assembly was performed as for the 2-way invasion hydrogel sandwich assay. Imaging was performed at the spinning-disk confocal with a 60x 1.49 NA objective. Areas were selected where the distance of the two hydrogels was between 1–2 µm. Using the beads, the two focal planes of the hydrogel surfaces were selected and imaging was performed in the order of red to far-red for both z-layers so that tension in the glass coverslip/hydrogel sandwich caused by focal changes has relaxed by the time the far-red beads are imaged.

A.5 STED sporozoite preparation

For STED microscopy of subpellicular microtubules in living sporozoites, the standard hydrogel assay was set up, the 30 µL of RPMI/3 % BSA to collect the salivary glands was supplemented with a 1 µM concentration of SiR-tubulin (Spirochrome). The sample was sealed and incubated at RT for 3 h. During that time, sporozoites entered the hydrogel, reached the bottom, and, over time, reduced motility. Imaging was performed with a 100x 1.4 NA objective at the Abberior SLM 2D/3D STED using the 3D STED mode.

A.6 Decorrelation of body-frame for the OUP model

We want to find the decorrelation of $\langle \mathbf{n}_2 \rangle$ in the regime where $\mathbf{\Omega}_0$ dominates the noise of the OUP. For that, we can use that the rotational problem possesses axial symmetry around the z axis, and that the translational problem is deterministic given a solution of the rotational problem. Therefore, the z components of moments must be invariant under rotation of $\mathbf{n}_1$ and $\mathbf{n}_2$, forcing many expectation values to vanish. From the previous solution, Eq. 13, we obtain

$$\mathrm{d}\langle \mathbf{n}_1 \rangle = \langle \mathbf{\Omega} \times \mathbf{n}_1 \rangle \, \mathrm{d}t = -\lambda \langle \mathbf{n}_1 \rangle \, \mathrm{d}t \ . \tag{A.1}$$

The analogous equation for $\mathbf{n}_2$ can be expanded by introducing the vector $\mathbf{n}_3$, which completes $\mathbf{n}_1$ and $\mathbf{n}_2$ to an orthonormal basis, and using the Jacobi identity,

$$\begin{aligned} \mathrm{d}\langle \mathbf{n}_2 \rangle / \mathrm{d}t = \ & \langle \mathbf{\Omega} \times \mathbf{n}_2 \rangle = \langle \mathbf{\Omega} \times (\mathbf{n}_3 \times \mathbf{n}_1) \rangle \\ = \ & - \langle \mathbf{n}_3 \times (\mathbf{n}_1 \times \mathbf{\Omega}) \rangle - \langle \mathbf{n}_1 \times (\mathbf{\Omega} \times \mathbf{n}_3) \rangle \end{aligned} \tag{A.2}$$

In the first term, we can write $\mathbf{n}_1 \times \mathbf{\Omega} = \langle \mathbf{n}_1 \times \mathbf{\Omega} \rangle + \mathbf{\Delta}$, where by rotational symmetry $\mathbf{\Delta}$ is isotropic in the x, y-plane, and hence $\langle \mathbf{n}_3 \times \mathbf{\Delta} \rangle = 0$ (at least to first order in Δ), such that, with the previous result,

$$- \langle \mathbf{n}_3 \times (\mathbf{n}_1 \times \mathbf{\Omega}) \rangle = - \langle \mathbf{n}_3 \times (\lambda \langle \mathbf{n}_1 \rangle) \rangle = -\lambda \langle \mathbf{n}_2 \rangle \ , \tag{A.3}$$

where the last step follows a similar argument (introducing an isotropic $\mathbf{\Delta}$ and computing the cross product $\mathbf{n}_3 \times \mathbf{n}_1 = \mathbf{n}_2$ through the averages). For the second term, similar logic can be applied, yielding

$$- \langle \mathbf{n}_1 \times (\mathbf{\Omega} \times \mathbf{n}_3) \rangle = \ - \langle \mathbf{n}_1 \times (\mathbf{\Omega} \times (-\mathbf{n}_2 \times \mathbf{n}_1)) \rangle \tag{A.4}$$

$$\begin{aligned} = \ & - \langle \mathbf{n}_1 \times (\mathbf{n}_2 \times (\mathbf{n}_1 \times \mathbf{\Omega})) \rangle - \langle \mathbf{n}_1 \times (\mathbf{n}_1 \times (\mathbf{\Omega} \times \mathbf{n}_2)) \rangle \\ = \ & - \lambda \langle \mathbf{n}_2 \rangle - \langle \mathbf{n}_1 \times (\mathbf{n}_1 \times (\mathbf{\Omega} \times \mathbf{n}_2)) \rangle \ . \end{aligned} \tag{A.5}$$

Now, with an analogous argument as used in the truncation in deriving Eq. 15, for the last term in Eq. A.5 only the $\mathbf{n}_1$-orthogonal part of $\Omega \times \mathbf{n}_2$ is relevant, which is generated by the $\mathbf{n}_1$-parallel component of $\mathbf{\Omega}$. We approximate this as

$\boldsymbol{\Omega}^{\parallel} \approx \Omega_0 \mathbf{n}_1$ to obtain

$$-\langle \mathbf{n}_1 \times (\mathbf{n}_1 \times (\boldsymbol{\Omega} \times \mathbf{n}_2)) \rangle = \Omega_0 \langle \mathbf{n}_3 \rangle \ , \tag{A.6}$$

which ultimately combines to give

$$\mathrm{d} \langle \mathbf{n}_2 \rangle / \mathrm{d}t = -2\lambda \langle \mathbf{n}_2 \rangle + \Omega_0 \langle \mathbf{n}_3 \rangle \ . \tag{A.7}$$

An analogous equation can be derived for $\langle \mathbf{n}_3 \rangle$, giving decay with twice the original eigenvalue λ while rotating with angular speed Ω_0. The two terms in the expansion of Eq. A.4 can be interpreted as the aforementioned decorrelation of the plane on the one hand, and rotation and decorrelation within the plane, on the other hand.

List of Publications

The following manuscripts, which contain part of the work presented in this thesis, have been prepared, submitted, or published during the course of this thesis.

1.	Leon Lettermann, Falko Ziebert, Ulrich S. Schwarz **A geometrical theory of gliding motility based on cell shape and surface flow** *Proceedings of the National Academy of Sciences* **121**30 (2024) https://doi.org/10.1073/pnas.2410708121 Parts reproduced with permission under license by PNAS, © 2024 PNAS	Chapter 4
2.	Leon Lettermann, Falko Ziebert, Mirko Singer, Friedrich Frischknecht, Ulrich S. Schwarz **Three-dimensional chiral active Ornstein-Uhlenbeck model for helical motion of microorganisms** *Physical Review Letters* **135** (2025) https://doi.org/10.1103/4kxb-h6p4 Parts reproduced with permission under license by the American Physical Society, © 2025 American Physical Society	Chapter 3
3.	Leon Lettermann†, Mirko Singer†, Smilla Steinbrück, Falko Ziebert, Sachie Kanatani, Photini Sinnis, Friedrich Frischknecht, Ulrich S. Schwarz, †: contributed equally **Chirality of malaria parasites determines their motion patterns** *Nature Physics*, in press (2025) Parts reproduced with permission under license by Springer Nature, © 2025 Springer Nature	Chapter 2 Chapter 5

The following manuscripts, which I contributed to but are on topics not presented in this thesis, have been prepared, submitted, or published during the course of this thesis.

---

4. Leon Lettermann, Alejandro Jurado, Timo Betz, Florentin Wörgötter, Sebastian Herzog
Tutorial: a beginner's guide to building a representative model of dynamical systems using the adjoint method
Communications Physics **7** (2024)
https://doi.org/10.1038/s42005-024-01606-9

---

5. Katharina Scholz, Marianne Papagrigorakes, Leon Lettermann, Federica Pennarola, Pintu Patra, Anil Kumar Dasanna, Cecilia P. Sanchez, Jessica Kehrer, Elisabetta Ada Cavalcanti-Adam, Ulrich S. Schwarz, Motomu Tanaka, Michael Lanzer
Contact Dynamics of Cytoadhering Plasmodium falciparum-Infected Erythrocytes in Flow
ACS Infectious Diseases **11**(9) (2025)
https://doi.org/10.1021/acsinfecdis.5c00594

---

6. Johanna Charlotte Neubauer, Anna Kaiser, Leon Lettermann, Tobias Volkert, Alexander Häge
Performance of large language models ChatGPT and Gemini in child and adolescent psychiatry knowledge assessment
PLOS One **20**(9) (2025)
https://doi.org/10.1371/journal.pone.0332917

---

7. Rachel Zeng†, Omar Al-Bourini†, Leonie Lettermann†, Leon Lettermann, Ulrike Olgemöller, Sabine Hofer, Matthias Boentert, Tim Friede, Manuel Nietert, Dirk Voit, Jens Frahm, Martin Uecker, Ali Seif Amir Hosseini, Jens Schmidt, †: contributed equally
Real-time MRI with deep learning for efficient evaluation of neuromuscular breathing impairment
Revision submitted

---

8. Zeynab Tavasolyzadeh, Leon Lettermann, Mirko Singer, Ulrich S. Schwarz, Friedrich Frischknecht, Christine Selhuber-Unkel
Hydrogel-Based 3D Microfabricated Scaffolds for Investigation of Plasmodium Sporozoite Motility
In preparation

---

9. Federica Pennarola, Leon Lettermann, ..., Ulrich S. Schwarz, Elisabetta Ada Cavalcanti-Adam
Dynamic and super resolution imaging of recurrent clathrin recruitment reveals constraints of coat sizes
In preparation

10. Johannes Dreckhoff, Leon Lettermann, Falko Ziebert, Ulrich S. Schwarz
Agent-based kinetic Monte Carlo simulations reveal dynamical coat stiffening during clathrin assembly
In preparation

11. Djordje Salai, ..., Leon Lettermann, ..., Ulrich S. Schwarz, ..., Hans-Georg Kräusslich
Super-resolution microscopy of HIV-1 Gag assembly-induced lipid domains
In preparation

12. Kim-Loreen Carlstedt, Martin Würtz, Annett Neuner, Violeta Pancakova, Svenja de Buhr, Leon Lettermann, Niccolo Banterle, Cecilia P. Sanchez, Elmar Schiebel, Ulrich S. Schwarz, Michael Lanzer
Identification of an oligomerization domain in KAHRP of *Plasmodium falciparum* and its structural and functional analysis
In preparation

13. Stefan Golfier, Veikko F. Geyer, Leon Lettermann, Ulrich S. Schwarz, Nicole Poulsen, Stefan Diez
Dynamic switching of cell-substrate contact sites allows gliding diatoms to modulate the curvature of their paths
In preparation

List of Chapter Covers

Chapter 1	Scanning electron micrograph of a sporozoite, from the lab of Freddy Frischknecht.
Chapter 2	Rendering of experimentally observed trajectories, color illustrates time progression. Red sporozoites are artificially input for visualization.
Chapter 3	Rendering of simulated trajectories for the active chiral Ornstein-Uhlenbeck particle, at different parameter values that result in different persistence of the trajectories.
Chapter 4	Rendering of the surface flow on the curved spherocylinder. Background is a z and time projection of a spinning disk experiment observing sporozoites in 3D.
Chapter 5	Rendering of the simulation results for the equilibrated configurations of shape and surface flow for a sporozoite (left) and *Toxoplasma*/ookinete (right).

List of Figures

List of Tables

Bibliography

[1] E. M. Purcell. Life at low Reynolds number. *Am. J. Phys.*, 45(1):3–11, January 1977.

[2] Howard C Berg and Edward M Purcell. Physics of chemoreception. *Biophys. J.*, 20(2):193–219, 1977.

[3] World Health Organization. *World malaria report 2024*. World Health Organization, 2024.

[4] Alan F Cowman, Julie Healer, Danushka Marapana, and Kevin Marsh. Malaria: biology and disease. *Cell*, 167(3):610–624, 2016.

[5] Georgina N. Montagna, Kai Matuschewski, and Carlos A. Buscaglia. Small heat shock proteins in cellular adhesion and migration: Evidence from Plasmodium genetics. *Cell Adhes. Migr.*, 6(2):78–84, March 2012.

[6] Eduardo Aliprandini, Joana Tavares, Raquel Hoffmann Panatieri, Sabine Thiberge, Marcio Massao Yamamoto, Olivier Silvie, Tomoko Ishino, Masao Yuda, Sylvie Dartevelle, François Traincard, Silvia Beatriz Boscardin, and Rogerio Amino. Cytotoxic anti-circumsporozoite antibodies target malaria sporozoites in the host skin. *Nat. Microbiol.*, 3(11):1224, 2018.

[7] Yevel Flores-Garcia, Gibran Nasir, Christine S. Hopp, Christian Munoz, Amanda E. Balaban, Fidel Zavala, and Photini Sinnis. Antibody-Mediated Protection against Plasmodium Sporozoites Begins at the Dermal Inoculation Site. *mBio*, 9(6):e02194–18, November 2018.

[8] Jessica Kehrer, Pauline Formaglio, Julianne Mendi Muthinja, Sebastian Weber, Danny Baltissen, Christopher Lance, Johanna Ripp, Janessa Grech, Markus Meissner, Charlotta Funaya, Rogerio Amino, and Friedrich Frischknecht. Plasmodium sporozoite disintegration during skin passage limits malaria parasite transmission. *EMBO Rep.*, 23(7):e54719, July 2022.

[9] Manuela C. Aguirre-Botero, Lawrence T. Wang, Pauline Formaglio, Eduardo Aliprandini, Jean-Michel Thiberge, Arne Schön, Yevel Flores-Garcia, Shamika Mathis-Torres, Barbara J. Flynn, Lais da Silva Pereira,

Yann Le Duff, Mathew Hurley, Adéla Nacer, Paul W. Bowyer, Fidel Zavala, Azza H. Idris, Joseph R. Francica, Robert A. Seder, and Rogerio Amino. Cytotoxicity of human antibodies targeting the circumsporozoite protein is amplified by 3D substrate and correlates with protection. *Cell Rep.*, 42(7):112681, July 2023.

[10] Lawrence T. Wang, Azza H. Idris, Neville K. Kisalu, Peter D. Crompton, and Robert A. Seder. Monoclonal antibodies to the circumsporozoite proteins as an emerging tool for malaria prevention. *Nat. Immunol.*, 25(9):1530–1545, September 2024.

[11] Patrick E. Duffy, J. Patrick Gorres, Sara A. Healy, and Michal Fried. Malaria vaccines: a new era of prevention and control. *Nat. Rev. Microbiol.*, 22(12):756–772, December 2024.

[12] Sundar Ram Naganathan, Sebastian Fürthauer, Masatoshi Nishikawa, Frank Jülicher, and Stephan W Grill. Active torque generation by the actomyosin cell cortex drives left–right symmetry breaking. *eLife*, 3:e04165, December 2014.

[13] U. Seifert. Stochastic thermodynamics of single enzymes and molecular motors. *Eur. Phys. J. E*, 34(3):26, March 2011.

[14] Tamás Vicsek and Anna Zafeiris. Collective motion. *Phys. Rep.*, 517(3):71–140, August 2012.

[15] Előd Méhes and Tamás Vicsek. Collective motion of cells: from experiments to models. *Integr. Biol.*, 6(9):831–854, September 2014.

[16] Youyuan Deng and Herbert Levine. Introduction to Models of Cell Motility. In Krastan B. Blagoev and Herbert Levine, editors, *Physics of Molecular and Cellular Processes*, pages 173–212. Springer International Publishing, Cham, 2022.

[17] J F Joanny, F Jülicher, K Kruse, and J Prost. Hydrodynamic theory for multi-component active polar gels. *New J. Phys.*, 9(11):422, November 2007.

[18] J. Prost, F. Jülicher, and J.-F. Joanny. Active gel physics. *Nat. Phys.*, 11(2):111–117, February 2015.

[19] William Gilpin, Matthew Storm Bull, and Manu Prakash. The multiscale physics of cilia and flagella. *Nat. Rev. Phys.*, 2(2):74–88, January 2020.

[20] Takuji Ishikawa. Fluid Dynamics of Squirmers and Ciliated Microorganisms. *Annu. Rev. Fluid Mech.*, 56(Volume 56, 2024):119–145, January 2024.

[21] Jonathan R. Howse, Richard A. L. Jones, Anthony J. Ryan, Tim Gough, Reza Vafabakhsh, and Ramin Golestanian. Self-Motile Colloidal Particles: From Directed Propulsion to Random Walk. *Phys. Rev. Lett.*, 99(4):048102, July 2007.

[22] Howard C Berg. *Random walks in biology*. Princeton University Press, September 1993.

[23] P. Romanczuk, M. Bär, W. Ebeling, B. Lindner, and L. Schimansky-Geier. Active Brownian particles. *Eur. Phys. J. Spec. Top.*, 202(1):1–162, March 2012.

[24] Clemens Bechinger, Roberto Di Leonardo, Hartmut Löwen, Charles Reichhardt, Giorgio Volpe, and Giovanni Volpe. Active Particles in Complex and Crowded Environments. *Rev. Mod. Phys.*, 88(4):045006, November 2016.

[25] Andreas Zöttl and Holger Stark. Emergent behavior in active colloids. *J. Phys.: Condens. Matter*, 28(25):253001, May 2016.

[26] Benno Liebchen and Demian Levis. Chiral active matter. *Europhys. Lett.*, 139(6):67001, September 2022.

[27] Debajyoti Debnath, Pulak K. Ghosh, Yunyun Li, Fabio Marchesoni, and Baowen Li. Diffusion of eccentric microswimmers. *Soft Matter*, 12(7):2017–2024, 2016.

[28] Juan Ruben Gomez-Solano, Alex Blokhuis, and Clemens Bechinger. Dynamics of Self-Propelled Janus Particles in Viscoelastic Fluids. *Phys. Rev. Lett.*, 116(13):138301, March 2016.

[29] Francisco J Sevilla. Diffusion of active chiral particles. *Phys. Rev. E*, 94(6):062120, December 2016.

[30] Juan Ruben Gomez-Solano and Francisco J. Sevilla. Active particles with fractional rotational Brownian motion. *J. Stat. Mech.: Theory Exp.*, 2020(6):063213, June 2020.

[31] Alexander R. Sprenger, Lorenzo Caprini, Hartmut Löwen, and René Wittmann. Dynamics of active particles with translational and rotational inertia. *J. Phys.: Condens. Matter*, 35(30):305101, April 2023.

[32] Sven van Teeffelen and Hartmut Löwen. Dynamics of a Brownian circle swimmer. *Phys. Rev. E*, 78(2):020101, August 2008.

[33] R. Ledesma-Aguilar, H. Löwen, and J. M. Yeomans. A circle swimmer at low Reynolds number. *Eur. Phys. J. E*, 35(8):70, August 2012.

[34] Felix Kümmel, Borge ten Hagen, Raphael Wittkowski, Ivo Buttinoni, Ralf Eichhorn, Giovanni Volpe, Hartmut Löwen, and Clemens Bechinger. Circular Motion of Asymmetric Self-Propelling Particles. *Phys. Rev. Lett.*, 110(19):198302, May 2013.

[35] Nathan A. Marine, Philip M. Wheat, Jesse Ault, and Jonathan D. Posner. Diffusive behaviors of circle-swimming motors. *Phys. Rev. E*, 87(5):052305, May 2013.

[36] Hartmut Löwen. Chirality in microswimmer motion: From circle swimmers to active turbulence. *Eur. Phys. J. Spec. Top.*, 225(11):2319–2331, November 2016.

[37] Amir Nourhani, Stephen J Ebbens, John G Gibbs, and Paul E Lammert. Spiral diffusion of rotating self-propellers with stochastic perturbation. *Phys. Rev. E*, 94(3):030601, 2016.

[38] Lorenzo Caprini, Hartmut Löwen, and Umberto Marini Bettolo Marconi. Chiral active matter in external potentials. *Soft Matter*, 19(33):6234–6246, August 2023.

[39] Benjamin Lindner. Diffusion of particles subject to nonlinear friction and a colored noise. *New J. Phys.*, 12(6):063026, June 2010.

[40] Christian Weber, Paul K. Radtke, Lutz Schimansky-Geier, and Peter Hänggi. Active motion assisted by correlated stochastic torques. *Phys. Rev. E*, 84(1):011132, July 2011.

[41] Pulak K. Ghosh, Yunyun Li, Giampiero Marchegiani, and Fabio Marchesoni. Communication: Memory effects and active Brownian diffusion. *J. Chem. Phys.*, 143(21):211101, December 2015.

[42] N Narinder, Clemens Bechinger, and Juan Ruben Gomez-Solano. Memory-Induced Transition from a Persistent Random Walk to Circular Motion for Achiral Microswimmers. *Phys. Rev. Lett.*, 121(7):078003, August 2018.

[43] Parvin Bayati and Amir Nourhani. Memory effects in spiral diffusion of rotary self-propellers. *Phys. Rev. E*, 105(2):024606, February 2022.

[44] Alexander R. Sprenger, Soudeh Jahanshahi, Alexei V. Ivlev, and Hartmut Löwen. Time-dependent inertia of self-propelled particles: The Langevin rocket. *Phys. Rev. E*, 103(4):042601, April 2021.

[45] David A. Morrison. Evolution of the Apicomplexa: where are we now? *Trends Parasitol.*, 25(8):375–382, August 2009.

[46] Norman D. Levine. Progress in Taxonomy of the Apicomplexan Protozoa. *J. Protozool.*, 35(4):518–520, 1988.

[47] Nicholas J. Katris, Giel G. van Dooren, Paul J. McMillan, Eric Hanssen, Leann Tilley, and Ross F. Waller. The Apical Complex Provides a Regulated Gateway for Secretion of Invasion Factors in Toxoplasma. *PLoS Pathog.*, 10(4):e1004074, April 2014.

[48] Matthew B Heintzelman. Gliding motility in apicomplexan parasites. In *Seminars in Cell & Developmental Biology*, volume 46, pages 135–142. Elsevier, October 2015.

[49] Michael W. White and Elena S. Suvorova. Apicomplexa Cell Cycles: Something Old, Borrowed, Lost, and New. *Trends Parasitol.*, 34(9):759–771, September 2018.

[50] J. P. Dubey. Advances in the life cycle of Toxoplasma gondii. *Int. J. Parasitol.*, 28(7):1019–1024, July 1998.

[51] Sonja Rueckert, Emma L. Betts, and Anastasios D. Tsaousis. The Symbiotic Spectrum: Where Do the Gregarines Fit? *Trends Parasitol.*, 35(9):687–694, September 2019.

[52] Yamei Jin, Chahnaz Kebaier, and Jerome Vanderberg. Direct Microscopic Quantification of Dynamics of Plasmodium berghei Sporozoite Transmission from Mosquitoes to Mice. *Infect. Immun.*, 75(11):5532–5539, November 2007.

[53] Rogerio Amino, Sabine Thiberge, Béatrice Martin, Susanna Celli, Spencer Shorte, Friedrich Frischknecht, and Robert Ménard. Quantitative imaging of Plasmodium transmission from mosquito to mammal. *Nat. Med.*, 12(2):220–224, February 2006.

[54] Kent E. Kester, James F. Cummings, Opokua Ofori-Anyinam, Christian F. Ockenhouse, Urszula Krzych, Philippe Moris, Robert Schwenk, Robin A. Nielsen, Zufan Debebe, Evgeny Pinelis, Laure Juompan, Jack Williams, Megan Dowler, V. Ann Stewart, Robert A. Wirtz, Marie-Claude Dubois, Marc Lievens, Joe Cohen, W. Ripley Ballou, and D. Gray Heppner, Jr. Randomized, Double-Blind, Phase 2a Trial of Falciparum Malaria Vaccines RTS,S/AS01B and RTS,S/AS02A in Malaria-Naive Adults: Safety, Efficacy, and Immunologic Associates of Protection. *J. Infect. Dis.*, 200(3):337–346, August 2009.

[55] Miguel Prudêncio, Ana Rodriguez, and Maria M. Mota. The silent path to thousands of merozoites: the Plasmodium liver stage. *Nat. Rev. Microbiol.*, 4(11):849–856, November 2006.

[56] Severina Klaus, Patrick Binder, Juyeop Kim, Marta Machado, Charlotta Funaya, Violetta Schaaf, Darius Klaschka, Aiste Kudulyte, Marek Cyrklaff, Vibor Laketa, Thomas Höfer, Julien Guizetti, Nils B. Becker, Friedrich Frischknecht, Ulrich S. Schwarz, and Markus Ganter. Asynchronous nuclear cycles in multinucleated Plasmodium falciparum facilitate rapid proliferation. *Sci. Adv.*, 8(13):eabj5362, March 2022.

[57] Nicholas J White, Sasithon Pukrittayakamee, Tran Tinh Hien, M Abul Faiz, Olugbenga A Mokuolu, and Arjen M Dondorp. Malaria. *Lancet*, 383(9918):723–735, February 2014.

[58] Shigeharu Sato. Plasmodium—a brief introduction to the parasites causing human malaria and their basic biology. *J. Physiol. Anthropol.*, 40:1, January 2021.

[59] Chris J. Janse, Blandine Franke-Fayard, Gunnar R. Mair, Jai Ramesar, Corinna Thiel, Sabine Engelmann, Kai Matuschewski, Geert Jan van Gemert, Robert W. Sauerwein, and Andrew P. Waters. High efficiency transfection of *Plasmodium berghei* facilitates novel selection procedures. *Mol. Biochem. Parasitol.*, 145(1):60–70, January 2006.

[60] David A. Baker. Malaria gametocytogenesis. *Mol. Biochem. Parasitol.*, 172(2):57–65, August 2010.

[61] Sylvia Münter, Benedikt Sabass, Christine Selhuber-Unkel, Mikhail Kudryashev, Stephan Hegge, Ulrike Engel, Joachim P Spatz, Kai Matuschewski, Ulrich S Schwarz, and Friedrich Frischknecht. Plasmodium sporozoite motility is modulated by the turnover of discrete adhesion sites. *Cell Host Microbe*, 6(6):551–562, December 2009.

[62] Sebastian Håkansson, Hiroshi Morisaki, John Heuser, and L. David Sibley. Time-Lapse Video Microscopy of Gliding Motility in *Toxoplasma gondii* Reveals a Novel, Biphasic Mechanism of Cell Locomotion. *Mol. Biol. Cell*, 10(11):3539–3547, November 1999.

[63] Makoto Miyata. Unique Centipede Mechanism of Mycoplasma Gliding. *Annu. Rev. Microbiol.*, 64(Volume 64, 2010):519–537, October 2010.

[64] Mark J. McBride. Bacterial Gliding Motility: Multiple Mechanisms for Cell Movement over Surfaces. *Annu. Rev. Microbiol.*, 55(1):49–75, 2001.

[65] Tâm Mignot, Joshua W Shaevitz, Patricia L Hartzell, and David R Zusman. Evidence that focal adhesion complexes power bacterial gliding motility. *Science*, 315(5813):853–856, 2007.

[66] Karen Grace Bondoc-Naumovitz, Emanuele Crosato, and Kirsty Y. Wan. Functional morphology of gliding motility in benthic diatoms. *Proc. Natl. Acad. Sci. U.S.A.*, 122(12):e2426910122, March 2025.

[67] Stefan Golfier, Veikko F. Geyer, Nicole Poulsen, and Stefan Diez. Dynamic switching of cell-substrate contact sites allows gliding diatoms to modulate the curvature of their paths. *bioRxiv*, March 2025. Preprint.

[68] M S Cooper and M Schliwa. Motility of cultured fish epidermal cells in the presence and absence of direct current electric fields. *J. Cell Biol.*, 102(4):1384–1399, April 1986.

[69] Tatyana M. Svitkina, Alexander B. Verkhovsky, Kyle M. McQuade, and Gary G. Borisy. Analysis of the Actin–Myosin II System in Fish Epidermal Keratocytes: Mechanism of Cell Body Translocation. *J. Cell Biol.*, 139(2):397–415, October 1997.

[70] M. J. Potel and S. A. Mackay. Preaggregative cell motion in Dictyostelium. *J. Cell Sci.*, 36:281–309, April 1979.

[71] Anh N. Hoang, Caroline N. Jones, Laurie Dimisko, Bashar Hamza, Joseph Martel, Nikola Kojic, and Daniel Irimia. Measuring neutrophil speed and directionality during chemotaxis, directly from a droplet of whole blood. *Technol.*, 1(01):49–57, November 2013.

[72] Graeme Lowe, Markus Meister, and Howard C. Berg. Rapid rotation of flagellar bundles in swimming bacteria. *Nature*, 325(6105):637–640, February 1987.

[73] V. A. Vladimirov, M. S. C. Wu, T. J. Pedley, P. V. Denissenko, and S. G. Zakhidova. Measurement of cell velocity distributions in populations of motile algae. *J. Exp. Biol.*, 207(7):1203–1216, March 2004.

[74] Jose A. Rodríguez, Miguel A. Lopez, Michelle C. Thayer, Yunzhe Zhao, Michael Oberholzer, Donald D. Chang, Neville K. Kisalu, Manuel L. Penichet, Gustavo Helguera, Robijn Bruinsma, Kent L. Hill, and Jianwei Miao. Propulsion of African trypanosomes is driven by bihelical waves with alternating chirality separated by kinks. *Proc. Natl. Acad. Sci. U.S.A.*, 106(46):19322–19327, November 2009.

[75] Nuno M. Oliveira, Kevin R. Foster, and William M. Durham. Single-cell twitching chemotaxis in developing biofilms. *Proc. Natl. Acad. Sci. U.S.A.*, 113(23):6532–6537, June 2016.

[76] Vasily Zaburdaev, Nicolas Biais, Michael Schmiedeberg, Jens Eriksson, Ann-Beth Jonsson, Michael P. Sheetz, and David A. Weitz. Uncovering the Mechanism of Trapping and Cell Orientation during Neisseria gonorrhoeae Twitching Motility. *Biophys. J.*, 107(7):1523–1531, October 2014.

[77] C. A. King. Cell motility of sporozoan protozoa. *Parasitol. Today*, 4(11):315–319, November 1988.

[78] Anthony Keeley and Dominique Soldati. The glideosome: a molecular machine powering motility and host-cell invasion by Apicomplexa. *Trends Cell Biol.*, 14(10):528–532, October 2004.

[79] Karine Frénal, Jean-François Dubremetz, Maryse Lebrun, and Dominique Soldati-Favre. Gliding motility powers invasion and egress in Apicomplexa. *Nat. Rev. Microbiol.*, 15(11):645–660, November 2017.

[80] Karine Frénal, Valérie Polonais, Jean-Baptiste Marq, Rolf Stratmann, Julien Limenitakis, and Dominique Soldati-Favre. Functional Dissection

of the Apicomplexan Glideosome Molecular Architecture. *Cell Host Microbe*, 8(4):343–357, October 2010.

[81] Vojtěch Pražák, Daven Vasishtan, Kay Grünewald, Ross G Douglas, and Josie L Ferreira. Molecular architecture of glideosome and nuclear F-actin in Plasmodium falciparum. *EMBO Rep.*, pages 1–13, March 2025.

[82] Richard J. Wall, Mohammad Zeeshan, Nicholas J. Katris, Rebecca Limenitakis, Edward Rea, Jessica Stock, Declan Brady, Ross F. Waller, Anthony A. Holder, and Rita Tewari. Systematic analysis of *Plasmodium* myosins reveals differential expression, localisation, and function in invasive and proliferative parasite stages. *Cell. Microbiol.*, 21(10), October 2019.

[83] Johanna Ripp, Xanthoula Smyrnakou, Marie-Therese Neuhoff, Franziska Hentzschel, and Friedrich Frischknecht. Phosphorylation of myosin a regulates gliding motility and is essential for Plasmodium transmission. *EMBO Rep.*, 23(7):e54857, July 2022.

[84] Ross G. Douglas, Prajwal Nandekar, Julia-Elisabeth Aktories, Hirdesh Kumar, Rebekka Weber, Julia M. Sattler, Mirko Singer, Simone Lepper, S. Kashif Sadiq, Rebecca C. Wade, and Friedrich Frischknecht. Inter-subunit interactions drive divergent dynamics in mammalian and Plasmodium actin filaments. *PLoS Biol.*, 16(7):e2005345, July 2018.

[85] Corinna Opitz and Dominique Soldati. 'The glideosome': a dynamic complex powering gliding motion and host cell invasion by Toxoplasma gondii. *Mol. Microbiol.*, 45(3):597–604, 2002.

[86] K. J. Robson, U. Frevert, I. Reckmann, G. Cowan, J. Beier, I. G. Scragg, K. Takehara, D. H. Bishop, G. Pradel, and R. Sinden. Thrombospondin-related adhesive protein (TRAP) of Plasmodium falciparum: expression during sporozoite ontogeny and binding to human hepatocytes. *EMBO J.*, 14(16):3883–3894, August 1995.

[87] Ali A. Sultan, Vandana Thathy, Ute Frevert, Kathryn J. H. Robson, Andrea Crisanti, Victor Nussenzweig, Ruth S. Nussenzweig, and Robert Ménard. TRAP Is Necessary for Gliding Motility and Infectivity of Plasmodium Sporozoites. *Cell*, 90(3):511–522, August 1997.

[88] My-Hang Huynh and Vern B. Carruthers. Toxoplasma MIC2 Is a Major Determinant of Invasion and Virulence. *PLoS Pathog.*, 2(8):e84, August 2006.

[89] Stefan Kappe, Thomas Bruderer, Soren Gantt, Hisashi Fujioka, Victor Nussenzweig, and Robert Ménard. Conservation of a Gliding Motility and Cell Invasion Machinery in Apicomplexan Parasites. *J. Cell Biol.*, 147(5):937–944, November 1999.

[90] D. G. Russell and R. E. Sinden. The role of the cytoskeleton in the motility of coccidian sporozoites. *J. Cell Sci.*, 50(1):345–359, August 1981.

[91] M. B. Heintzelman and J. D. Schwartzman. Myosin Diversity in Apicomplexa. *J. Parasitol.*, 87(2):429–432, April 2001.

[92] Guillaume Salbreux, Guillaume Charras, and Ewa Paluch. Actin cortex mechanics and cellular morphogenesis. *Trends Cell Biol.*, 22(10):536–545, October 2012.

[93] Naomi S. Morrissette and L. David Sibley. Cytoskeleton of Apicomplexan Parasites. *Microbiol. Mol. Biol. Rev.*, 66(1):21–38, March 2002.

[94] Ramiro Tomasina, Fabiana C. González, and Maria E. Francia. Structural and Functional Insights into the Microtubule Organizing Centers of Toxoplasma gondii and Plasmodium spp. *Microorganisms*, 9(12):2503, December 2021.

[95] Pengge Qian, Xu Wang, Cuirong Guan, Xin Fang, Mengya Cai, Chuanqi Zhong, Yong Cui, Yanbin Li, Luming Yao, Huiting Cui, Kai Jiang, and Jing Yuan. Apical anchorage and stabilization of subpellicular microtubules by apical polar ring ensures Plasmodium ookinete infection in mosquito. *Nat. Commun.*, 13(1):7465, December 2022.

[96] P. C. C. Garnham, R. G. Bird, and J. R. Baker. Electron microscope studies of motile stages of malaria parasites III. The Ookinetes of Haemamoeba and Plasmodium. *Trans. R. Soc. Trop. Med. Hyg.*, 56(2):116–120, March 1962.

[97] Mary Louise Chiappino, Barbara A. Nichols, and G. Richard O'connor. Scanning Electron Microscopy of Toxoplasma gondii: Parasite Torsion

and Host-Cell Responses during Invasion1. *J. Protozool.*, 31(2):288–292, May 1984.

[98] Barbara A. Nichols and Mary Louise Chiappino. Cytoskeleton of Toxoplasma gondii. *J. Protozool.*, 34(2):217–226, 1987.

[99] P.C.C. Garnham, R.G. Bird, and J.R. Baker. Electron microscope studies of motile stages of malaria parasites. I. The fine strucutre of the Sporozoites of Haemamoeba (=Plasmodium) gallinacea. *Trans. R. Soc. Trop. Med. Hyg.*, 54(3):274–278, May 1960.

[100] P.C.C Garnham, R.G Bird, J.R Baker, and R.S Bray. Electron microscope studies of motile stages of malaria parasites II. The fine structure of the sporozoite of Laverania (= Plasmodium) falcipara. *Trans. R. Soc. Trop. Med. Hyg.*, 55(1):98–IN7, January 1961.

[101] Jerome Vanderberg, Johannes Rdodin, and Meir Yoeli. Electron Microscopic and Histochemical Studies of Sporozoite Formation in Plasmodium berghei. *J. Protozool.*, 14(1):82–103, 1967.

[102] Mikhail Kudryashev, Simone Lepper, Rebecca Stanway, Stefan Bohn, Wolfgang Baumeister, Marek Cyrklaff, and Friedrich Frischknecht. Positioning of large organelles by a membrane- associated cytoskeleton in Plasmodium sporozoites. *Cell. Microbiol.*, 12(3):362–371, 2010.

[103] Benjamin Spreng, Hannah Fleckenstein, Patrick Kübler, Claudia Di Biagio, Madlen Benz, Pintu Patra, Ulrich S Schwarz, Marek Cyrklaff, and Friedrich Frischknecht. Microtubule number and length determine cellular shape and function in Plasmodium. *EMBO J.*, 38(15):e100984, August 2019.

[104] Mikhail Kudryashev, Sylvia Münter, Leandro Lemgruber, Georgina Montagna, Henning Stahlberg, Kai Matuschewski, Markus Meissner, Marek Cyrklaff, and Friedrich Frischknecht. Structural basis for chirality and directional motility of Plasmodium sporozoites. *Cell. Microbiol.*, 14(11):1757–1768, 2012.

[105] Georgios Pavlou, Bastien Touquet, Luis Vigetti, Patricia Renesto, Alexandre Bougdour, Delphine Debarre, Martial Balland, and Isabelle Tardieux. Coupling Polar Adhesion with Traction, Spring, and Torque Forces Allows High-Speed Helical Migration of the Protozoan Parasite *Toxoplasma*. *ACS Nano*, 14(6):7121–7139, June 2020.

[106] Eloïse Bertiaux, Aurélia C. Balestra, Lorène Bournonville, Vincent Louvel, Bohumil Maco, Dominique Soldati-Favre, Mathieu Brochet, Paul Guichard, and Virginie Hamel. Expansion microscopy provides new insights into the cytoskeleton of malaria parasites including the conservation of a conoid. *PLoS Biol.*, 19(3):e3001020, March 2021.

[107] Josie L. Ferreira and Friedrich Frischknecht. Parasite microtubule arrays. *Curr. Biol.*, 33(16):R845–R850, August 2023.

[108] Jerome P. Vanderberg. Studies on the Motility of Plasmodium Sporozoites. *J. Protozool.*, 21(4):527–537, 1974.

[109] Ijeoma Ejigiri, Daniel R. T. Ragheb, Paco Pino, Alida Coppi, Brandy Lee Bennett, Dominique Soldati-Favre, and Photini Sinnis. Shedding of TRAP by a Rhomboid Protease from the Malaria Sporozoite Surface Is Essential for Gliding Motility and Sporozoite Infectivity. *PLoS Pathog.*, 8(7):e1002725, July 2012.

[110] Stephan Hegge, Mikhail Kudryashev, Ashley Smith, and Friedrich Frischknecht. Automated classification of Plasmodium sporozoite movement patterns reveals a shift towards productive motility during salivary gland infection. *Biotechnol. J.*, 4(6):903–913, 2009.

[111] Jamie A. Whitelaw, Fernanda Latorre-Barragan, Simon Gras, Gurman S. Pall, Jacqueline M. Leung, Aoife Heaslip, Saskia Egarter, Nicole Andenmatten, Shane R. Nelson, David M. Warshaw, Gary E. Ward, and Markus Meissner. Surface attachment, promoted by the actomyosin system of Toxoplasma gondii is important for efficient gliding motility and invasion. *BMC Biol.*, 15(1):1, December 2017.

[112] Luis Vigetti, Bastien Touquet, Delphine Debarre, Thierry Rose, Lionel Bureau, Dima Abdallah, Galina V. Dubacheva, and Isabelle Tardieux. Submicrometre spatiotemporal characterization of the Toxoplasma adhesion strategy for gliding motility. *Nat. Microbiol.*, 9(12):3148–3164, December 2024.

[113] Jacqueline M. Leung, Mark A. Rould, Christoph Konradt, Christopher A. Hunter, and Gary E. Ward. Disruption of TgPHIL1 Alters Specific Parameters of Toxoplasma gondii Motility Measured in a Quantitative, Three-Dimensional Live Motility Assay. *PLoS One*, 9(1):e85763, January 2014.

[114] Rachel V Stadler, Shane R Nelson, David M Warshaw, and Gary E Ward. A circular zone of attachment to the extracellular matrix provides directionality to the motility of toxoplasma gondii in 3d. *eLife*, 11:e85171, December 2022.

[115] Andrey Kan, Yan-Hong Tan, Fiona Angrisano, Eric Hanssen, Kelly L. Rogers, Lachlan Whitehead, Vanessa P. Mollard, Anton Cozijnsen, Michael J. Delves, Simon Crawford, Robert E. Sinden, Geoffrey I. McFadden, Christopher Leckie, James Bailey, and Jake Baum. Quantitative analysis of plasmodium ookinete motion in three dimensions suggests a critical role for cell shape in the biomechanics of malaria parasite gliding motility. *Cell. Microbiol.*, 16(5):734–750, May 2014.

[116] Johanna Ripp, Jessica Kehrer, Xanthoula Smyrnakou, Nathalie Tisch, Joana Tavares, Rogerio Amino, Carmen Ruiz de Almodovar, and Friedrich Frischknecht. Malaria parasites differentially sense environmental elasticity during transmission. *EMBO Mol. Med.*, 13(4):e13933, April 2021.

[117] Christina L Hueschen, Li-av Segev-Zarko, Jian-Hua Chen, Mark A LeGros, Carolyn A Larabell, John C Boothroyd, Rob Phillips, and Alexander R Dunn. Emergent actin flows explain distinct modes of gliding motility. *Nature Physics*, 20(12):1989–1996, 2024.

[118] Annie Z. Tremp and Johannes T. Dessens. Malaria IMC1 Membrane Skeleton Proteins Operate Autonomously and Participate in Motility Independently of Cell Shape. *J. Biol. Chem.*, 286(7):5383–5391, February 2011.

[119] Zhenhui Liu, Songman Li, Pooja Anantha, Tassanee Thanakornsombut, Lintong Wu, Junjie Chen, Ryohma Tsuchiya, Abhai K Tripathi, Yun Chen, and Ishan Barman. Plasmodium sporozoite shows distinct motility patterns in responses to three-dimensional environments. *iScience*, 27(8), August 2024.

[120] Catherine A. Moreau, Saligram P. Bhargav, Hirdesh Kumar, Katharina A. Quadt, Henni Piirainen, Léanne Strauss, Jessica Kehrer, Martin Streichfuss, Joachim P. Spatz, Rebecca C. Wade, Inari Kursula, and Friedrich Frischknecht. A unique profilin-actin interface is important for malaria parasite motility. *PLoS Pathog.*, 13(5):e1006412, May 2017.

[121] Katharina A. Quadt, Martin Streichfuss, Catherine A. Moreau, Joachim P. Spatz, and Friedrich Frischknecht. Coupling of retrograde flow to force production during malaria parasite migration. *ACS Nano*, 10(2):2091–2102, February 2016.

[122] Albert K. Harris, Patricia Wild, and David Stopak. Silicone Rubber Substrata: A New Wrinkle in the Study of Cell Locomotion. *Science*, 208(4440):177–179, April 1980.

[123] Benedikt Sabass, Margaret L. Gardel, Clare M. Waterman, and Ulrich S. Schwarz. High Resolution Traction Force Microscopy Based on Experimental and Computational Advances. *Biophys. J.*, 94(1):207–220, January 2008.

[124] Ulrich S. Schwarz and Jérôme R. D. Soiné. Traction force microscopy on soft elastic substrates: A guide to recent computational advances. *Biochim. Biophys. Acta Mol. Cell Res.*, 1853(11, Part B):3095–3104, November 2015.

[125] Christian Albrecht, Kerstin Blank, Mio Lalic-Mülthaler, Siegfried Hirler, Thao Mai, Ilka Gilbert, Susanne Schiffmann, Tom Bayer, Hauke Clausen-Schaumann, and Hermann E. Gaub. DNA: A Programmable Force Sensor. *Science*, 301(5631):367–370, July 2003.

[126] Masatoshi Morimatsu, Armen H. Mekhdjian, Arjun S. Adhikari, and Alexander R. Dunn. Molecular Tension Sensors Report Forces Generated by Single Integrin Molecules in Living Cells. *Nano Lett.*, 13(9):3985–3989, September 2013.

[127] Johanna Ripp, Dimitri Probst, Mirko Singer, Ulrich S. Schwarz, and Friedrich Frischknecht. Traction force generation in Plasmodium sporozoites is modulated by a surface adhesin. *J. Microsc.*, n/a(n/a), 2025.

[128] Daan Vorselen, Yifan Wang, Miguel M. de Jesus, Pavak K. Shah, Matthew J. Footer, Morgan Huse, Wei Cai, and Julie A. Theriot. Microparticle traction force microscopy reveals subcellular force exertion patterns in immune cell–target interactions. *Nat. Commun.*, 11(1):20, January 2020.

[129] Otger Campàs, Tadanori Mammoto, Sean Hasso, Ralph A. Sperling, Daniel O'Connell, Ashley G. Bischof, Richard Maas, David A. Weitz,

L. Mahadevan, and Donald E. Ingber. Quantifying cell-generated mechanical forces within living embryonic tissues. *Nat. Methods*, 11(2):183–189, February 2014.

[130] Alejandro Jurado, Jonas Isensee, Arne Hofemeier, Lea Johanna Krüger, Raphael Wittkowski, Ramin Golestanian, Philip Bittihn, and Timo Betz. 3d multiscale shape analysis of nuclei and in vivo elastic stress sensors allows force inference. *Biophys. J.*, 2025.

[131] Wesley R. Legant, Jordan S. Miller, Brandon L. Blakely, Daniel M. Cohen, Guy M. Genin, and Christopher S. Chen. Measurement of mechanical tractions exerted by cells in three-dimensional matrices. *Nat. Methods*, 7(12):969–971, December 2010.

[132] Leanna M Owen, Arjun S Adhikari, Mohak Patel, Peter Grimmer, Natascha Leijnse, Min Cheol Kim, Jacob Notbohm, Christian Franck, and Alexander R Dunn. A cytoskeletal clutch mediates cellular force transmission in a soft, three-dimensional extracellular matrix. *Mol. Biol. Cell*, 28(14):1959–1974, 2017.

[133] Oliver M. Drozdowski, Kim E. Boonekamp, Ulrike Engel, Michael Boutros, and Ulrich S. Schwarz. Fully three-dimensional force inference in intestinal organoids reveals ratchet-like bud stabilization. *bioRxiv*, April 2025. Preprint.

[134] Jonathan Munera Lopez, Isadonna F. Tengganu, Jun Liu, John M. Murray, Luisa F. Arias Padilla, Ying Zhang, Peter T. Brown, Laurence Florens, and Ke Hu. An apical protein, Pcr2, is required for persistent movement by the human parasite Toxoplasma gondii. *PLoS Pathog.*, 18(8):e1010776, August 2022.

[135] J. Hiroshi Morisaki, John E. Heuser, and L. David Sibley. Invasion of Toxoplasma gondii occurs by active penetration of the host cell. *J. Cell Sci.*, 108(6):2457–2464, June 1995.

[136] Juliana Portes, Emile Barrias, Renata Travassos, Márcia Attias, and Wanderley de Souza. Toxoplasma gondii Mechanisms of Entry Into Host Cells. *Front. Cell. Infect. Microbiol.*, 10, June 2020.

[137] Markus Meissner, Dirk Schlüter, and Dominique Soldati. Role of Toxoplasma gondii Myosin A in Powering Parasite Gliding and Host Cell Invasion. *Science*, 298(5594):837–840, October 2002.

[138] Annie S. P. Yang, Sash Lopaticki, Matthew T. O'Neill, Sara M. Erickson, Donna N. Douglas, Norman M. Kneteman, and Justin A. Boddey. AMA1 and MAEBL are important for Plasmodium falciparum sporozoite infection of the liver. *Cell. Microbiol.*, 19(9):e12745, 2017.

[139] Anna Battista, Friedrich Frischknecht, and Ulrich S. Schwarz. Geometrical model for malaria parasite migration in structured environments. *Phys. Rev. E*, 90(4):042720, October 2014.

[140] Pintu Patra, Konrad Beyer, Astha Jaiswal, Anna Battista, Karl Rohr, Friedrich Frischknecht, and Ulrich S. Schwarz. Collective migration reveals mechanical flexibility of malaria parasites. *Nat. Phys.*, 18(5):586–594, May 2022.

[141] John Toner and Yuhai Tu. Flocks, herds, and schools: A quantitative theory of flocking. *Phys. Rev. E*, 58(4):4828, 1998.

[142] Christina L. Hueschen, Alexander R. Dunn, and Rob Phillips. Wildebeest herds on rolling hills: Flocking on arbitrary curved surfaces. *Phys. Rev. E*, 108(2):024610, August 2023.

[143] John Oreopoulos, Richard Berman, and Mark Browne. Chapter 9 - Spinning-disk confocal microscopy: present technology and future trends. In Jennifer C. Waters and Torsten Wittman, editors, *Methods in Cell Biology*, volume 123 of *Quantitative Imaging in Cell Biology*, pages 153–175. Academic Press, January 2014.

[144] Daniel B. Allan, Thomas Caswell, Nathan C. Keim, Casper M. van der Wel, and Ruben W. Verweij. soft-matter/trackpy: v0.6.4, July 2024.

[145] Rana Chattopadhyay, Soundarapandian Velmurugan, Chinnamma Chakiath, Lucy Andrews Donkor, Wilbur Milhous, John W. Barnwell, William E. Collins, and Stephen L. Hoffman. Establishment of an In Vitro Assay for Assessing the Effects of Drugs on the Liver Stages of Plasmodium vivax Malaria. *PLoS One*, 5(12):e14275, December 2010.

[146] Sandra March, Shengyong Ng, Soundarapandian Velmurugan, Ani Galstian, Jing Shan, David J. Logan, Anne E. Carpenter, David Thomas, B. Kim Lee Sim, Maria M. Mota, Stephen L. Hoffman, and Sangeeta N. Bhatia. A Microscale Human Liver Platform that Supports the Hepatic Stages of Plasmodium falciparum and vivax. *Cell Host Microbe*, 14(1):104–115, July 2013.

[147] H. S. Jennings. On the Significance of the Spiral Swimming of Organisms. *Am. Nat.*, 35(413):369–378, May 1901.

[148] Hugh C. Crenshaw. A New Look at Locomotion in Microorganisms: Rotating and Translating. *Am. Zool.*, 36(6):608–618, December 1996.

[149] James G Mitchell and Kazuhiro Kogure. Bacterial motility: links to the environment and a driving force for microbial physics. *FEMS Microbiol. Ecol.*, 55(1):3–16, 2006.

[150] Johannes M Keegstra, Francesco Carrara, and Roman Stocker. The ecological roles of bacterial chemotaxis. *Nat. Rev. Microbiol.*, 20(8):491–504, 2022.

[151] Ken F Jarrell and Mark J McBride. The surprisingly diverse ways that prokaryotes move. *Nat. Rev. Microbiol.*, 6(6):466–476, 2008.

[152] Ulrich S Schwarz. Physical constraints for pathogen movement. In *Semin. Cell Dev. Biol.*, volume 46 of *Biomineralisation & Motorisation of pathogens*, pages 82–90. Elsevier, October 2015.

[153] Daniel B Kearns. A field guide to bacterial swarming motility. *Nat. Rev. Microbiol.*, 8(9):634–644, 2010.

[154] H. C. Berg and L. Turner. Chemotaxis of bacteria in glass capillary arrays. Escherichia coli, motility, microchannel plate, and light scattering. *Biophys. J.*, 58(4):919–930, October 1990.

[155] Roland Thar and Tom Fenchel. True Chemotaxis in Oxygen Gradients of the Sulfur-Oxidizing Bacterium Thiovulum majus. *Appl. Environ. Microbiol.*, 67(7):3299–3303, July 2001.

[156] Tom Fenchel and Nicholas Blackburn. Motile Chemosensory Behaviour of Phagotrophic Protists: Mechanisms for and Efficiency in Congregating at Food Patches. *Protist*, 150(3):325–336, October 1999.

[157] Gáspár Jékely, Julien Colombelli, Harald Hausen, Keren Guy, Ernst Stelzer, François Nédélec, and Detlev Arendt. Mechanism of phototaxis in marine zooplankton. *Nature*, 456(7220):395–399, November 2008.

[158] Kyriacos C Leptos, Maurizio Chioccioli, Silvano Furlan, Adriana I Pesci, and Raymond E Goldstein. Phototaxis of chlamydomonas arises from a

tuned adaptive photoresponse shared with multicellular volvocine green algae. *Phys. Rev. E*, 107(1):014404, 2023.

[159] Andrew D. Rutenberg, Andrew J. Richardson, and Claire J. Montgomery. Diffusion of Asymmetric Swimmers. *Phys. Rev. Lett.*, 91(8):080601, August 2003.

[160] Nils B. Becker and Ralf Everaers. From rigid base pairs to semiflexible polymers: Coarse-graining DNA. *Phys. Rev. E*, 76(2):021923, August 2007.

[161] B. M. Friedrich and F. Jülicher. The stochastic dance of circling sperm cells: sperm chemotaxis in the plane. *New J. Phys.*, 10(12):123025, December 2008.

[162] Benjamin M. Friedrich and Frank Jülicher. Steering Chiral Swimmers along Noisy Helical Paths. *Phys. Rev. Lett.*, 103(6):068102, August 2009.

[163] Raphael Wittkowski and Hartmut Löwen. Self-propelled Brownian spinning top: Dynamics of a biaxial swimmer at low Reynolds numbers. *Phys. Rev. E*, 85(2):021406, February 2012.

[164] Julius B Kirkegaard, Alan O Marron, and Raymond E Goldstein. Motility of colonial choanoflagellates and the statistics of aggregate random walkers. *Phys. Rev. Lett.*, 116(3):038102, 2016.

[165] Xiaomeng Ren and Hermes Bloomfield-Gadêlha. Swimming by spinning: Spinning-top type rotations regularize sperm swimming into persistently progressive paths in 3d. *Adv. Sci.*, 12(6):2406143, 2025.

[166] Grzegorz Szamel. Self-propelled particle in an external potential: Existence of an effective temperature. *Phys. Rev. E*, 90(1):012111, July 2014.

[167] Francisco J. Sevilla, Rosalío F. Rodríguez, and Juan Ruben Gomez-Solano. Generalized Ornstein-Uhlenbeck model for active motion. *Phys. Rev. E*, 100(3):032123, September 2019.

[168] Eric Woillez, Yariv Kafri, and Vivien Lecomte. Nonlocal stationary probability distributions and escape rates for an active Ornstein–Uhlenbeck particle. *J. Stat. Mech.: Theory Exp.*, 2020(6):063204, June 2020.

[169] David Martin, Jérémy O'Byrne, Michael E. Cates, Etienne Fodor, Cesare Nardini, Julien Tailleur, and Frederic van Wijland. Statistical mechanics of active Ornstein-Uhlenbeck particles. *Phys. Rev. E*, 103(3):032607, March 2021.

[170] David Martin and Thibaut Arnoulx de Pirey. AOUP in the presence of Brownian noise: a perturbative approach. *J. Stat. Mech.: Theory Exp.*, 2021(4):043205, April 2021.

[171] G. H. Philipp Nguyen, René Wittmann, and Hartmut Löwen. Active Ornstein–Uhlenbeck model for self-propelled particles with inertia. *J. Phys.: Condens. Matter*, 34(3):035101, November 2021.

[172] Andrea Crisanti and Matteo Paoluzzi. Most probable path of active Ornstein-Uhlenbeck particles. *Phys. Rev. E*, 107(3):034110, March 2023.

[173] Sandipan Dutta. Most probable paths for active Ornstein-Uhlenbeck particles. *Phys. Rev. E*, 107(5):054130, May 2023.

[174] J. H. Fritz and U. Seifert. Thermodynamically consistent model of an active Ornstein–Uhlenbeck particle. *J. Stat. Mech.: Theory Exp.*, 2023(9):093204, October 2023.

[175] James Bradbury, Roy Frostig, Peter Hawkins, Matthew James Johnson, Chris Leary, Dougal Maclaurin, George Necula, Adam Paszke, Jake VanderPlas, Skye Wanderman-Milne, and Qiao Zhang. JAX: composable transformations of Python+NumPy programs, 2018.

[176] Patrick Kidger. *On Neural Differential Equations*. PhD Thesis, University of Oxford, 2021.

[177] Kristian Stølevik Olsen and Hartmut Löwen. Optimal diffusion of chiral active particles with strategic reorientations. *Phys. Rev. E*, 110(6):064606, 2024.

[178] Otto Kratky and Günther Porod. Röntgenuntersuchung gelöster fadenmoleküle. *Rec. Trav. Chim. Pays-Bas*, 68(12):1106–1122, 1949.

[179] Masao Doi, Sam F Edwards, and Samuel Frederick Edwards. *The theory of polymer dynamics*, volume 73. Oxford University Press, 1988.

[180] Crispin W Gardiner. Handbook of stochastic methods for physics, chemistry and the natural sciences. *Springer Ser. Synergetics*, 1985.

[181] Peter Hänggi and Peter Jung. Colored noise in dynamical systems. *Adv. Chem. Phys.*, 89:239–326, 1994.

[182] R. N. Bhattacharya. On the functional central limit theorem and the law of the iterated logarithm for Markov processes. *Z. Wahrscheinlichkeitstheorie Verw. Geb.*, 60(2):185–201, 1982.

[183] Ambarish Ghosh and Peer Fischer. Controlled Propulsion of Artificial Magnetic Nanostructured Propellers. *Nano Lett.*, 9(6):2243–2245, June 2009.

[184] Takaki Yamamoto and Masaki Sano. Chirality-induced helical self-propulsion of cholesteric liquid crystal droplets. *Soft Matter*, 13(18):3328–3333, 2017.

[185] Joaquin Llacer-Wintle, Antón Rivas-Dapena, Xiang-Zhong Chen, Eva Pellicer, Bradley J Nelson, Josep Puigmartí-Luis, and Salvador Pané. Biodegradable small-scale swimmers for biomedical applications. *Adv. Mater.*, 33(42):2102049, 2021.

[186] Laurent Blanchoin, Rajaa Boujemaa-Paterski, Cécile Sykes, and Julie Plastino. Actin Dynamics, Architecture, and Mechanics in Cell Motility. *Physiol. Rev.*, 94(1):235–263, January 2014.

[187] Janice M Dobrowolski and L David Sibley. Toxoplasma invasion of mammalian cells is powered by the actin cytoskeleton of the parasite. *Cell*, 84(6):933–939, 1996.

[188] LD Sibley. Intracellular parasite invasion strategies. *Science*, 304(5668):248–253, September 2004.

[189] Charles Wolgemuth, Egbert Hoiczyk, Dale Kaiser, and George Oster. How myxobacteria glide. *Curr. Biol.*, 12(5):369–377, 2002.

[190] Friedrich Braumann, Dennis Klug, Jessica Kehrer, Gaojie Song, Juan Feng, Timothy A Springer, and Friedrich Frischknecht. Conformational change of plasmodium trap is essential for sporozoite migration and transmission. *EMBO Rep.*, page e57064, 2023.

[191] Han Gao, Zhenke Yang, Xu Wang, Pengge Qian, Renjie Hong, Xin Chen, Xin-zhuan Su, Huiting Cui, and Jing Yuan. Isp1-anchored polarization of gcβ/cdc50a complex initiates malaria ookinete gliding motility. *Curr. Biol.*, 28(17):2763–2776, 2018.

[192] Nicolas Dos Santos Pacheco, Lorenzo Brusini, Romuald Haase, Nicolò Tosetti, Bohumil Maco, Mathieu Brochet, Oscar Vadas, and Dominique Soldati-Favre. Conoid extrusion regulates glideosome assembly to control motility and invasion in apicomplexa. *Nat. Microbiol.*, 7(11):1777–1790, 2022.

[193] Mingzhai Sun, Morgane Wartel, Eric Cascales, Joshua W Shaevitz, and Tâm Mignot. Motor-driven intracellular transport powers bacterial gliding motility. *Proc. Natl. Acad. Sci. U.S.A.*, 108(18):7559–7564, 2011.

[194] Daisuke Nakane, Keiko Sato, Hirofumi Wada, Mark J. McBride, and Koji Nakayama. Helical flow of surface protein required for bacterial gliding motility. *Proc. Natl. Acad. Sci. U.S.A.*, 110(27):11145–11150, July 2013.

[195] Abhishek Shrivastava, Pushkar P. Lele, and Howard C. Berg. A Rotary Motor Drives Flavobacterium Gliding. *Curr. Biol.*, 25(3):338–341, February 2015.

[196] Abhishek Shrivastava and Howard C Berg. Towards a model for flavobacterium gliding. *Curr. Opin. Microbiol.*, 28(3):93–97, 2015.

[197] Rajesh Balagam, Douglas B Litwin, Fabian Czerwinski, Mingzhai Sun, Heidi B Kaplan, Joshua W Shaevitz, and Oleg A Igoshin. Myxococcus xanthus gliding motors are elastically coupled to the substrate as predicted by the focal adhesion model of gliding motility. *PLoS Comput. Biol.*, 10(5):e1003619, 2014.

[198] Laura M Faure, Jean-Bernard Fiche, Leon Espinosa, Adrien Ducret, Vivek Anantharaman, Jennifer Luciano, Sébastien Lhospice, Salim T Islam, Julie Tréguier, Mélanie Sotes, et al. The mechanism of force transmission at bacterial focal adhesion complexes. *Nature*, 539(7630):530–535, 2016.

[199] Beiyan Nan and David R Zusman. Novel mechanisms power bacterial gliding motility. *Mol. Microbiol.*, 101(2):186–193, 2016.

[200] Benedikt Sabass, Matthias D. Koch, Guannan Liu, Howard A. Stone, and Joshua W. Shaevitz. Force generation by groups of migrating bacteria. *Proc. Natl. Acad. Sci. U.S.A.*, page 201621469, June 2017.

[201] Dobromir Szadkowski, Andrea Harms, Luis António Menezes Carreira, Manon Wigbers, Anna Potapova, Kristin Wuichet, Daniela Keilberg, Ulrich Gerland, and Lotte Søgaard-Andersen. Spatial control of the

gtpase mgla by localized romr–romx gef and mglb gap activities enables myxococcus xanthus motility. *Nat. Microbiol.*, 4(8):1344–1355, 2019.

[202] Navish Wadhwa and Howard C Berg. Bacterial motility: machinery and mechanisms. *Nat. Rev. Microbiol.*, 20(3):161–173, 2022.

[203] Beiyan Nan, Jigar N Bandaria, Amirpasha Moghtaderi, Im-Hong Sun, Ahmet Yildiz, and David R Zusman. Flagella stator homologs function as motors for myxobacterial gliding motility by moving in helical trajectories. *Proc. Natl. Acad. Sci. U.S.A.*, 110(16):E1508–E1513, April 2013.

[204] Guo Fu, Jigar N Bandaria, Anne Valérie Le Gall, Xue Fan, Ahmet Yildiz, Tâm Mignot, David R Zusman, and Beiyan Nan. Motab-like machinery drives the movement of mreb filaments during bacterial gliding motility. *Proc. Natl. Acad. Sci. U.S.A.*, 115(10):2484–2489, 2018.

[205] Tamás Vicsek, András Czirók, Eshel Ben-Jacob, Inon Cohen, and Ofer Shochet. Novel type of phase transition in a system of self-driven particles. *Phys. Rev. Lett.*, 75(6):1226, 1995.

[206] Katherine Copenhagen, Ricard Alert, Ned S Wingreen, and Joshua W Shaevitz. Topological defects promote layer formation in myxococcus xanthus colonies. *Nat. Phys.*, 17(2):211–215, 2021.

[207] Howard Brenner. The stokes resistance of an arbitrary particle. *Chem. Eng. Sci.*, 18(1):1–25, 1963.

[208] H. Brenner. The Stokes resistance of an arbitrary particle—II. *Chem. Eng. Sci.*, 19(9):599–629, September 1964.

[209] J. R. Dormand and P. J. Prince. A family of embedded Runge-Kutta formulae. *J. Comput. Appl. Math.*, 6(1):19–26, March 1980.

[210] Ahmet Nihat Simsek, Matthias D Koch, Joseph E Sanfilippo, Zemer Gitai, Gerhard Gompper, and Benedikt Sabass. Bacteria tune a trade-off between adhesion and migration to colonize surfaces under flow. *PRX Life*, 2(2):023003, 2024.

[211] Hirofumi Wada, Daisuke Nakane, and Hsuan-Yi Chen. Bidirectional bacterial gliding motility powered by the collective transport of cell surface proteins. *Phys. Rev. Lett.*, 111(24):248102, 2013.

[212] David G. Mann. The species concept in diatoms. *Phycologia*, 38(6):437–495, November 1999.

[213] E. Virginia Armbrust. The life of diatoms in the world's oceans. *Nature*, 459(7244):185–192, May 2009.

[214] Paul Tréguer, Chris Bowler, Brivaela Moriceau, Stephanie Dutkiewicz, Marion Gehlen, Olivier Aumont, Lucie Bittner, Richard Dugdale, Zoe Finkel, Daniele Iudicone, Oliver Jahn, Lionel Guidi, Marine Lasbleiz, Karine Leblanc, Marina Levy, and Philippe Pondaven. Influence of diatom diversity on the ocean biological carbon pump. *Nat. Geosci.*, 11(1):27–37, January 2018.

[215] Nicole C. Poulsen, Ilan Spector, Timothy P. Spurck, Thomas F. Schultz, and Richard Wetherbee. Diatom gliding is the result of an actin-myosin motility system. *Cell Motil.*, 44(1):23–33, 1999.

[216] Metin G. Davutoglu, Veikko F. Geyer, Lukas Niese, Johannes R. Soltwedel, Marcelo L. Zoccoler, Valeria Sabatino, Robert Haase, Nils Kröger, Stefan Diez, and Nicole Poulsen. Gliding motility of the diatom Craspedostauros australis coincides with the intracellular movement of raphid-specific myosins. *Commun. Biol.*, 7(1):1187, September 2024.

[217] Lesley A. Edgar and Jeremy D. Pickett-Heaps. Valve Morphogenesis in the Pennate Diatom Navicula Cuspidata. *J. Phycol.*, 20(1):47–61, 1984.

[218] Nicole Poulsen, Metin Gabriel Davutoglu, and Jirina Zackova Suchanova. Diatom Adhesion and Motility. In Angela Falciatore and Thomas Mock, editors, *The Molecular Life of Diatoms*, pages 367–393. Springer International Publishing, Cham, 2022.

[219] Janina Kristin Hellmann, Sylvia Münter, Mikhail Kudryashev, Simon Schulz, Kirsten Heiss, Ann-Kristin Müller, Kai Matuschewski, Joachim P Spatz, Ulrich S Schwarz, and Friedrich Frischknecht. Environmental constraints guide migration of malaria parasites during transmission. *PLoS Pathog.*, 7(6):e1002080, 2011.

[220] Andrea Valigurová, Naděžda Vaškovicová, Naďa Musilová, and Joseph Schrével. The enigma of eugregarine epicytic folds: where gliding motility originates? *Front. Zool.*, 10:1–28, 2013.

[221] T. Erdmann. Stability of Adhesion Clusters under Constant Force. *Phys. Rev. Lett.*, 92(10), 2004.

[222] Melanie J. I. Müller, Stefan Klumpp, and Reinhard Lipowsky. Tug-of-war as a cooperative mechanism for bidirectional cargo transport by molecular motors. *Proc. Natl. Acad. Sci. U.S.A.*, 105(12):4609–4614, March 2008.

[223] Stefano Palagi and Peer Fischer. Bioinspired microrobots. *Nat. Rev. Mater.*, 3(6):113–124, June 2018.

[224] Atsuko Uenoyama and Makoto Miyata. Gliding ghosts of Mycoplasma mobile. *Proc. Natl. Acad. Sci. U.S.A.*, 102(36):12754–12758, September 2005.

[225] Pengfei Zhan, Andreas Peil, Qiao Jiang, Dongfang Wang, Shikufa Mousavi, Qiancheng Xiong, Qi Shen, Yingxu Shang, Baoquan Ding, Chenxiang Lin, Yonggang Ke, and Na Liu. Recent Advances in DNA Origami-Engineered Nanomaterials and Applications. *Chem. Rev.*, 123(7):3976–4050, April 2023.

[226] Ryota Ibusuki, Tatsuya Morishita, Akane Furuta, Shintaro Nakayama, Maki Yoshio, Hiroaki Kojima, Kazuhiro Oiwa, and Ken'ya Furuta. Programmable molecular transport achieved by engineering protein motors to move on DNA nanotubes. *Science*, 375(6585):1159–1164, March 2022.

[227] Tyler D. Ross, Dino Osmanović, John F. Brady, and Paul W. K. Rothemund. Ray Optics for Gliders. *ACS Nano*, 16(10):16191–16200, October 2022.

[228] D. Terzopoulos and A. Witkin. Physically based models with rigid and deformable components. *IEEE Comput. Graph. Appl.*, 8(6):41–51, November 1988.

[229] Guillaume Salbreux and Frank Jülicher. Mechanics of active surfaces. *Phys. Rev. E*, 96(3):032404, September 2017.

[230] Kamran Mohseni and Tim Colonius. Numerical Treatment of Polar Coordinate Singularities. *J. Comput. Phys.*, 157(2):787–795, January 2000.

[231] Karen A. Beningo, Micah Dembo, and Yu-li Wang. Responses of fibroblasts to anchorage of dorsal extracellular matrix receptors. *Proc. Natl. Acad. Sci. U.S.A.*, 101(52):18024–18029, December 2004.

[232] Fatemeh Abbasi, Katharina Rieck, Matthias Brandt, Maja Matis, and Timo Betz. CFM: Confinement Force Microscopy-a dynamic, precise and stable microconfiner for traction force microscopy in spatial confinement. *bioRxiv*, August 2023. Preprint.

[233] Johannes W. Blumberg and Ulrich S. Schwarz. Comparison of direct and inverse methods for 2.5D traction force microscopy. *PLoS One*, 17(1):e0262773, January 2022.

[234] U. S. Schwarz, N. Q. Balaban, D. Riveline, A. Bershadsky, B. Geiger, and S. A. Safran. Calculation of Forces at Focal Adhesions from Elastic Substrate Data: The Effect of Localized Force and the Need for Regularization. *Biophys. J.*, 83(3):1380–1394, September 2002.

[235] S. Lepper, M. Merkel, A. Sartori, M. Cyrklaff, and F. Frischknecht. Rapid quantification of the effects of blotting for correlation of light and cryo-light microscopy images. *J. Microsc.*, 238(1):21–26, 2010.

[236] Ludek Koreny, Mohammad Zeeshan, Konstantin Barylyuk, Eelco C. Tromer, Jolien J. E. van Hooff, Declan Brady, Huiling Ke, Sara Chelaghma, David J. P. Ferguson, Laura Eme, Rita Tewari, and Ross F. Waller. Molecular characterization of the conoid complex in Toxoplasma reveals its conservation in all apicomplexans, including Plasmodium species. *PLoS Biol.*, 19(3):e3001081, March 2021.

[237] Catherine A. Moreau, Katharina A. Quadt, Henni Piirainen, Hirdesh Kumar, Saligram P. Bhargav, Léanne Strauss, Niraj H. Tolia, Rebecca C. Wade, Joachim P. Spatz, Inari Kursula, and Friedrich Frischknecht. A function of profilin in force generation during malaria parasite motility that is independent of actin binding. *J. Cell Sci.*, 134(5):jcs233775, April 2020.

[238] Pauline Formaglio, Marina E. Wosniack, Raphael M. Tromer, Jaderson G. Polli, Yuri B. Matos, Hang Zhong, Ernesto P. Raposo, Marcos G. E. da Luz, and Rogerio Amino. Plasmodium sporozoite search strategy to locate hotspots of blood vessel invasion. *Nat. Commun.*, 14(1):2965, May 2023.

[239] Kartik S. Bane, Simone Lepper, Jessica Kehrer, Julia M. Sattler, Mirko Singer, Miriam Reinig, Dennis Klug, Kirsten Heiss, Jake Baum, Ann-Kristin Mueller, and Friedrich Frischknecht. The Actin Filament-Binding

Protein Coronin Regulates Motility in Plasmodium Sporozoites. *PLoS Pathog.*, 12(7):e1005710, July 2016.

[240] Christine S Hopp, Kevin Chiou, Daniel RT Ragheb, Ahmed M Salman, Shahid M Khan, Andrea J Liu, and Photini Sinnis. Longitudinal analysis of Plasmodium sporozoite motility in the dermis reveals component of blood vessel recognition. *eLife*, 4:e07789, August 2015.

[241] Kyle Jarrod McLean, Judith Straimer, Christine S. Hopp, Joel Vega-Rodriguez, Jennifer L. Small-Saunders, Sachie Kanatani, Abhai Tripathi, Godfree Mlambo, Peter C. Dumoulin, Chantal T. Harris, Xinran Tong, Melanie J. Shears, Johan Ankarklev, Björn F. C. Kafsack, David A. Fidock, and Photini Sinnis. Generation of Transmission-Competent Human Malaria Parasites with Chromosomally-Integrated Fluorescent Reporters. *Sci. Rep.*, 9(1):13131, September 2019.

[242] Abhai K Tripathi, Godfree Mlambo, Sachie Kanatani, Photini Sinnis, and George Dimopoulos. Plasmodium falciparum Gametocyte Culture and Mosquito Infection Through Artificial Membrane Feeding. *J. Vis. Exp.*, page e61426, July 2020.

[243] Mark Kennedy, Matthew E. Fishbaugher, Ashley M. Vaughan, Rapatbhorn Patrapuvich, Rachasak Boonhok, Narathatai Yimamnuaychok, Nastaran Rezakhani, Peter Metzger, Marisa Ponpuak, Jetsumon Sattabongkot, Stefan H. Kappe, Jen CC Hume, and Scott E. Lindner. A rapid and scalable density gradient purification method for Plasmodium sporozoites. *Malar. J.*, 11(1):421, December 2012.

Acknowledgments

Many people have contributed to the work leading to this thesis and supported me in different ways over the past three and a half years, and I am tremendously grateful, all of you made my PhD time a great adventure!

I am grateful to everyone in the Schwarz group for consistently sharp discussions and a working atmosphere where problems get solved.

At our home base BioQuant, thanks to Valentin Wössner and Ian Mense for everyday help, quick feedback, and countless hallway exchanges. My office crew, Oliver Drozdowski, who was there from my first day, with many useful conversations about work (and the occasional beer). Nils Winkler, a worthy successor to Oliver, and Devika Magan, who evened the odds against the mammalian cell people for the malaria subgroup.

Falko Ziebert has been an invaluable sparring partner on involved mathematical details and also orthography. Most importantly, I am very grateful to my supervisor Ulrich Schwarz, who provided exactly the right balance of freedom and guidance: he encouraged independent ideas and backed them with a broad command of the literature across physics and biology.

I also had the chance to work with excellent students. Master students Johannes Lamers and Johannes Dreckhoff, who worked on my most favorite non-malaria project, clathrin mediated endocytosis, and Anna-Maria Lorinser who recently started to include stochasticity in the gliding-motility model.

As a theorist, I owe a lot to collaborators. First and foremost, Freddy Frischknecht and Mirko Singer, experts on sporozoite motility, whom I worked with throughout the thesis and hopefully will continue for quite some time. Our exchanges meandering from physics of solids to parasite omics were not only highly productive, but always great fun! The wider framework for this collaboration was given by the "Physics of Parasitism" special priority program, funded by the DFG as SPP 2332. The interface of biologists bringing their in-depth knowledge of different parasites on the one hand, and physicists bringing their mathematical toolbox on the other hand, was always inspiring and exciting at our annual meetings. Furthermore, I want to thank Smilla Steinbrück, Sachie Kanatani, and Photini Sinnis, who joined from Johns Hopkins University, Baltimore, and enabled us to extend experiments from rodent to human malaria. Zeynab Tavasolyzadeh and Christine Selhuber-Unkel from IMSEAM, Heidelberg University, who, together with Mirko, brought

engineering and nanoprinting into the project to work towards the next frontier, sporozoites interacting with artificial structures, with Zeynab and Mirko finally managing to overcome the tricky combination of experiments and analysis. The monthly malaria meeting, though more on blood stage than sporozoites, was always exciting. Thanks to Katharina Scholz and Motomu Tanaka for the work on footprinting rolling red blood cells, and to Kim-Loreen Carlstedt and Michael Lanzer for the interesting work on KAHRP and also finding helices and circles there.

Lastly, for the clathrin project, that saw far too little attention in this thesis but did not connect well with all the sporozoite motility: Federica Pennarola and Elisabetta Ada Cavalcanti-Adam, who introduced me to this fascinating system with a bunch of great experiments combining live imaging and MINFLUX.

I also want to thank my examination committee for being part of the final chapter of my PhD, Christine Selhuber-Unkel and Tristan Bereau, and in particular Peer Fischer, who agreed to serve as the second referee.

Outside the lab, I want to thank my parents and brothers for their steady support. To my friends—the DnD group among the Heidelberg PhD students; Tobias Volkert (co-founder in the next project); and everyone else—for always being there. And lastly, but most importantly, to my wife, Leonie Lettermann, for her support, critical questions, and everything!